Alma Mater Studiorum · Università di Bologna

DOTTORATO DI RICERCA IN FISICA
Ciclo XXXII

Settore Concorsuale: 02/A1
Settore Scientifico Disciplinare: FIS/01

Measurement of ZH(H$\to b\bar{b}$) with Z$\to \ell^+\ell^-$ in pp collisions at $\sqrt{s}$ = 13 TeV with the ATLAS Experiment at LHC

Presentata da: Grazia Cabras

Coordinatrice Dottorato:
Prof.essa Silvia Arcelli

Supervisore:
Dott. Benedetto Giacobbe
Co-supervisori:
Prof.essa Laura Fabbri
Dott.essa Camilla Vittori

Esame finale anno 2020

"Mi piacerebbe ogni tanto averti qui per mostrarti le cose che ho di te." Massimo Volume
Dedicata a mio padre Giorgio.

"I can live with anything you've got to throw in my face but I can't live without my mother's embrace." M. Kozelek
Dedicata a mia madre Rosa.

"[...] è stato a Bologna che ho scoperto che ci si poteva stringere tra amici e mostrare la propria inadeguatezza senza imbarazzo." E. Clementi
Dedicata alla mia colorata e scarmigliata famiglia acquisita:
i miei amici.

Abstract

The signal strength measurement of the $pp \rightarrow VH(H \rightarrow b\bar{b})$ at a center of mass energy of pp collision of 13 TeV is presented in this thesis. The data have been collected with the ATLAS detector in 2015, 2016 and 2017 data taking corresponding to an integrated luminosity of 79.8 fb^{-1}. The analysis has been performed in three different channels distinguished according to the number of charged leptons in the final state coming from the leptonical decay of the associated vector boson. The measured signal strength, with respect to the Standard Model expectation, is $\mu_{VH(H\rightarrow b\bar{b})}$=1.08$^{+0.27}_{-0.31}$ (from the combination of three analysis channels) with an observed significance with the background-only hypothesis, of 4.9 σ, with respect to an expected value of 4.3.
The iteration of the analysis with the full Run2 statistics (139 fb^{-1}) is also treated, with particular attention to the main innovations introduced with respect to the previous analyisis.
A description of a phenomenological study of the total proton-proton cross section and ρ-parameter (defined as the ratio of the real to imaginary part of the elastic scattering amplitude in the forward direction) is also presented.
LUCID-2 is the reference detector for online and offline luminosity measurements for ATLAS. It is described with particular attention to the PMT gain monitoring system where I developed a code for the analysis of the calibration data.

Sommario

Il tema principale di questa tesi è la misura della *signal strength* del canale di produzione associata dell'Higgs con un bosone vettore $pp \rightarrow VH(H \rightarrow b\bar{b})$, con l'Higgs che decade in due quark b, ad un'energia nel centro di massa di 13 TeV. I dati sono stati raccolti con l'esperimento ATLAS nel 2015, 2016 e 2017, per una luminosità integrata di 79.8 fb^{-1}. L'analisi è stata effettuata in tre diversi canali, distinti tra loro in base al numero di leptoni carichi nello stato finale, derivanti dal decadimento leptonico del bosone vettore associato. La *signal strength* misurata dalla combinazione dei tre canali è $\mu_{VH(H\rightarrow b\bar{b})}$=1.08$^{+0.27}_{-0.31}$, con un significanza di 4.9σ, rispetto ad un valore atteso di 4.3.
Viene trattata anche l'iterazione dell'analisi con l'intera statistica del Run2 di LHC (139 fb^{-1}), sottolineando i principali cambiamenti rispetto alla strategia precedentemente adottata.
E' fornita una descrizione del LUCID-2, il rivelatore di riferimento per le misure *online* e *offline* di luminosità, con particolare attenzione al sistema di monitoraggio del guadagno dei fotomoltiplicatori, per cui mi sono occupata dell'analisi dei dati di calibrazione raccolti.
E' inoltre presentata una descrizione dei miei studi fenomenologici sull'evoluzione della sezione d'urto totale adronica e del parametro ρ (definito come il rapporto tra la parte reale e immaginaria dell'ampiezza di scattering elastico nella direzione *forward*).

Contents

List of Figures

List of Tables

Introduction

The concept of an underlying ultimate constituent of matter seem to be inborn in the human nature and its search has always been of great interest for phylosophers and scientist across the centuries. Starting from the end of 18th to the *Golden Age* of particle physics with the advent of accelerators, the intuition was confirmed: nature is very simple and general principles can bring order to the chaos. Everything in the Universe is found to be made of very fundamental building blocks, the *fundamental particles*, governed by *four fundamental forces*. The best understanding of how these particles and three of the four forces are related to each other is given by the Standard Model of Particle Physics. It was mainly developed in 1970s and, during the years, it has successfully been supported by the experimental results. However, until 2012, the most important piece of the puzzle was still missing: the *Higgs* boson, which existence was postulated by Thomas W.B. Kibble, Peter Higgs, Robert Brout and François Englert and considered as the responsible of the *spontaneous symmetry breaking*, known as *Higgs Mechanism*, giving mass to all the massive particles of the Standard Model.
The Large Hadron Collider, located at CERN near to Geneva, has been carried out for the search of undiscovered processes, such as the Higgs production. The LHC is the largest particle accelarator ever built and it has been designed to reach a center of mass energy of 14 TeV in proton-proton collisions. On 2012 4th of July, ATLAS and CMS Collaborations announced an excess of 5σ at a mass if 125 GeV, claiming the discovery of a particle consistent with the Standard Model Higgs.
The measurement of the Higgs properties is of highest interest for the LHC physics program since it is essential to confirm the Standard Model or to give hints about new physics beyond it.
Among these properties, the decay mode in two b-quarks is of particular interest. The Higgs coupling to fermions is proportional to their mass and, for a Standard Model Higgs with m_H=125 GeV, the $H \rightarrow b\bar{b}$ channel has the largest branching ratio $\sim$ 58%. As a consequence, the study of this process is important to confirm that the new particle discovered in 2012 is the predicted Standard Model Higgs and, moreover, would give a prove of Higgs coupling to the quark sector. The most promising channel to perform the search is the associated production with a vector boson V = (W, Z) decaying in two leptons. Despite being the third production mode in terms of cross section at LHC, it has the advantage to have a clear signature in the final state thanks to the leptonic decay of the vector boson, favouring the rejection of the overwhelming QCD induced background. The analysis is performed in three different channels depending on the number of charged leptons in the final state, resulting in three different signals $ZH \rightarrow \nu\nu b\bar{b}$ (*0-lepton*), $WH \rightarrow \ell^{\pm}\nu b\bar{b}$ (*1-lepton*) and $ZH \rightarrow \ell^{\pm}\ell^{\mp}b\bar{b}$ (*2-lepton*).
The analysis presented in this thesis is mainly focused on the 2-lepton channel for two different data-takings recorded by the ATLAS detector: the first one corresponding to an integrated luminosity of 79.8 fb^{-1}, the second one to the full Run2 statistics ($\sim$ 139 fb^{-1}). The former has already been published in 2018 and it has to the observation of the VH associated production and of the $H \rightarrow b\bar{b}$. The 139 fb^{-1} iteration of the analysis is still on going and the first results look promising, giving a confirmation of the previous results. Important upgrades has been introduced with respect to the previous analysis which are expected

to increase the sensitivity to signal and to result in a better precision on the signal strength, also thanks to the use of the Full Run2 statistics.
The thesis is organized as follows.
In Chapter 1, a picture of the Standard Model theoretical framework is provided with particular attention to the Higgs boson and to the $VH(H \to b\bar{b})$ channel, main subject of the analysis.
In Chapter 2, the LHC and the ATLAS detector are presented.
Chapter 3 is dedicated to the description of the reconstruction of the physical objects of main interest in the purpose of this analysis, with particular attention to electrons, muons and jets (b-tagged ones) which are the signature of the final state of the 2-lepton channel.
In Chapter 4, the general analysis strategy is presented with a description of the data and Monte Carlo used, the object and event selection, the estimation of the signal and background modelling systematic uncertainties, the Multivariate analysis (MVA) and the signal extraction through a global profile likelihood fit performed on MVA output. The analysis is performed in different p_T^V, the transverse momentum of the vector boson, bins in order to maximize the significance.
In Chapter 5, the results of the 79.8 fb^{-1} analysis are treated together with the status and the further step of the on going Full Run2 iteration.
My personal involvement has covered different topics and stages of the analysis workflow:

- For the 79.8 fb $^{-1}$ analysis, I have performed Monte Carlo driven studies on the $Z + jets$ background, one of the irreducible background for the 2-lepton channel, with the purpose to estimate the related systematic uncertainties which enter in the fit. The Z+jets background contribution is splitted in three contributions, depending on the flavour composition of the events. The $Z + HF$ (HF =*heavy flavour*) is left floating in the fit and it is determined from the fit on data. Systematic uncertainties related to the flavour composition are assessed and enter the fit to better constrain the $Z + jets$ systematic uncertainty.
  A systematic uncertainty related to acceptance between the 0- and 2-lepton analysis is also estimated.
  I have estimated the residual multijet background contribution in the 2-lepton channel with a fit on data, using the default *template procedure*.

- For the 139 fb^{-1} analysis iteration, I have perfomed performance studies in the context on the Multivariate analysis. Two important innovations have been introduced with respect to the previous analysis: an additional cut in high p_T^V region (p_T^V>150 GeV) at 250 GeV and the adoption of hybrid truth tagging method for the b-jet identification. My analysis for the 2-lepton channel of the MVA performances introducing these changes has been a fundamental contribution to outline the better strategy to adopt.
  I have also performed a study to see the understand the effects of the change of isolation working point for electrons and muons on the event selection both for data and Monte Carlo samples.

In Chapter 6, a phenomenological studies on total proton-proton cross section and ρ-parameter (defined as the ratio of the real to the imaginary part of the elastic scattering amplitude in the forward direction) evolution with energy are presented. There are processes within the Standard Model not completely understood or which cannot be properly calculated due to the lack of theory. In particular, due to the non-Abelian nature of the QCD, soft terms are not properly calculable and, as a consequence, the total hadronic cross section is not predictable in the theoretical framework. However, there are very general principles which comes to the aid such as the Optical Theorem and the Dispersion Relations. The Optical

Theorem relates the total cross section σ_{tot} to the imaginary part of the elastic scattering in the forward direction. The Dispersion Relations are a very general physics theorem with lots of applications which give a relation between the real and the imaginary part of an analytic function. The combination of this two concepts allow to give prediction on the evolution of σ_{tot} and ρ with energy. Up until now, the general strategy has been to use a particular expression of the dispersion relations, *single-subtracted*, to perform a global fit of σ_{tot} and ρ to obtain prediction on the total hadronic cross section evolution at higher energies with respect the ones at which it is measured. Such approach is based on the validity of the single-subtracted dispersion relations, which postulate the non-existence of the Odderon. However, the most recent TOTEM ρ measurement has changed the scenarios opening the gates to two possibilities: the Odderon manifestation or a drastic change in the total cross section evolution above LHC energy regime. The purpose of my studies has been the investigation of the second possibility.
In Appendix A, a description of the LUCID-2 detector is provided. LUCID is the reference detector for online and offline luminosity measurements for the ATLAS detector. After Run1, it was completely redesigned in terms of detector components and electronics to cope with the new experimental challenging conditions imposed by Run2. One of the main innovation, it is an original photomultiplier (PMT) gain monitoring system based on the deposition of Bismuth-207 radioactive sources on the PMTs quartz windows. The electrons from ^{207}Bi internal conversion produce light above the Cherenkov threshold. In order to have a precise and reliable luminosity measurement, the monitoring of the PMT gain is fundamental. Dedicated runs were performed at the end of each physics fill to monitor and evaluate gain changes. During my ATLAS qualification task I have personally developed a code for the analysis of the data collected during the dedicated calibration runs and produced the relevant results on a daily basis, needed to adjust the working conditions of LUCID PMTs to ensure its stability over time.

Chapter 1

The Higgs Boson and the Standard Model

The Higgs boson was the most long-awaited missing piece to the puzzle of the Standard Model, the theoretical framework of modern particle physics.
The Standard Model was mainly developed in the 1970s and it lists and describes the fundamental matter components with their properties and the interactions among each others, taking into account electromagnetic, weak and strong forces. In the early 1960s, thanks to the joint effort of Glashow, Salam and Weinberg, electromagnetic and weak interaction had been unified as two sides of the same coin: the electroweak interaction. The theoretical outcome of the massless nature of the mediating bosons was in contrast with the experimental observation.
The solution to this problem was proposed, indipendently, in 1964, by Peter Higgs, Robert Brout and François Englert who postulated the existence of a scalar field, responsible for the spontaneous symmetry breaking that provides mass to the particles: this was the birth of the so-called *Higgs Mechanism*.
This chapter tells the long route from the birth of the Standard Model, through the Higgs postulation, to the discovery of such an important particle, with the description of its production and decay modes.
Among them, the associated production with a vector boson V together with the Higgs decay in a b-quarks pair is of great importance and it will be the main subject of the present thesis.

1.1 The Standard Model of Particle Interactions

The first idea of a fundamental constituent of matter comes from afar and it has roots in Ancient Greece. In 6th century B.C., the philosophers of the Milesian school were the first ones in history to try to explain what the Universe is made of without looking for answers in their Pantheon of Gods. They postulated the idea of *arché* as "ultimate underlying substance". According to Thales, *arché* should be the water. According to Anaximander, the origin should be the *apeiron*, a sort of unlimited and indefinite chaos, where all the things are born from the separation from their own opposite. According to Anaximenes, the air is what underlies everything and our world is nothing but the transformation of this element.
Then comes Democritus who, together with his mentor Leucippus, first stated the word *atom*, which means indivisible. He believed that *atoms* were infinite, uncreated and eternal and that different qualities of the objects depend on the kind of atom they are made of.
The ancient concept of underlying ultimate constituent of matter was really appreciated in the next centuries.
John Dalton discoveries at the end of 18th century gave a confirmation of what was just a naive intuition of the Ancient Greece philosophers.

The birth of the modern particle physics can be set with the discovery of the electron by Sir Joseph John Thompson in 1897: atoms are no longer the smallest division of matter.
During the next centuries, from the discovery of proton and neutron by Rutherford, many another particles has been discovered through cosmic rays and accelarator measurements putting the basis to the birth of the Standard Model and to the LHC era.

1.1.1 The Fundamental Particles

As said in the introduction to this chapter, the Standard Model (SM) lists the fundamental elementary particles, see Fig.1.1, [1], [2]. Twelve are accounted: 3 leptons, 3 neutrinos and

FIGURE 1.1: Visual sketch of the Standard Model.

6 quarks (all of them associated with their corresponding anti-particles).
In addition, there are four types of gauge bosons: photon, $W^{\pm}$ and Z^0, gluons, mediating, respectively, electromagnetic, weak and strong forces. Gravitational interaction does not enter. Finally, there is the Higgs boson, the particle responsible for the spontaneous symmetry breaking, as will be explained in Sec.1.2.2.
At first, SM particles can be divided according to their spins, a quantum number representing an intrinsic form of angular momentum, expressed in quantized units of $\hbar$. The distinction is in the statistics that different particles follow which determine how their wavefunction behaves. The wavefunction ψ tells about the behaviour of a particle system after the interchange of a pair of indistinguishable particles. The *spin-statistics theorem* is one of the cornerstones of quantum field theory and according to it, the wavefunction ψ:

- is symmetric under the exchange of identical bosons: $\psi \rightarrow \psi$
- is antisymmetric under the exchange of identical fermions: $\psi \rightarrow -\psi$

In the Standard Model we have:

- *Fermions*: carrying fractional spin, they follow the Fermi-Dirac statistics. In particular, all the SM fermions have $1/2\hbar$.
- *Bosons*: carrying integer spin, they follow the Bose-Einstein statistics. Between the SM bosons, we have:

- *scalar* bosons with spin 0 (Higgs is the only known)
- *vector* bosons with spin 1 (gauge bosons)

1.1.2 Fermions

Standard Model fermions can be divided into two groups depending on the interaction they undergo and their quantum numbers: *leptons* and *quarks*.

Leptons

Leptons undergo electromagnetic and weak interaction. There are three charged leptons: electrons, muons and taus (e, μ, τ). Three corresponding neutral leptons exist, known as *neutrinos* (ν_e, ν_μ, ν_τ). Electrons are stable and carry an integer charge Q=*e*. Muons and taus are both unstable and decay in electrons and neutrinos, with taus also decaying in other particles. Neutrinos are paired to the charged leptons, because of the weak interaction, according to a quantum number called *flavour*. They interact only via weak force. In this formulation, neutrinos are supposed to be massless, which is in contradiction with the recent experimental evidences. However, neutrinos masses have not been measured and they only an upper limit can be set.
In this sector, the fermions are divided in three families.

$$\begin{pmatrix} e \\ \nu_e \end{pmatrix} \begin{pmatrix} \mu \\ \nu_\mu \end{pmatrix} \begin{pmatrix} \tau \\ \nu_\tau \end{pmatrix} \tag{1.1}$$

A leptonic number is associated to each family (L_e, L_μ, L_τ) and it has to be conserved in all the interactions involving leptons.

Quarks

Quarks interact via electromagnetic, weak and strong interaction. They are the fundamental constituents of hadrons and, due to a property of strong force called *confinement*, they are never observed as free particles. Their charge is a fraction of the electron charge *e*: three of them with Q=+2/3|*e*| and three with Q=-1/3|*e*|.
Just like the leptons, they are divided in three families of increasing mass.

$$\begin{pmatrix} u \\ d \end{pmatrix} \begin{pmatrix} c \\ s \end{pmatrix} \begin{pmatrix} t \\ b \end{pmatrix} \tag{1.2}$$

Up and down (u and d) quark are so named because of the strong isospin symmetry. The idea of isospin came from what suggested by Heisenberg in 1932: proton and neutron are different charge states of the same particle: the nucleon. The isospin *I* is a quantum number with value *I*=1/2, differing in its third component I_3 which can have values +1/2 and -1/2. It is related to the charge by the relation:

$$Q/e = \frac{1}{2} + I_3 \tag{1.3}$$

assigning to proton I_3=+1/2 and to neutron I_3=-1/2. Isospin is an important quantum number because is conserved by strong interaction. The first evidence of this property came from the observation of the equivalence between *p-p*, *n-p* and *n-n* forces, once the Coulomb interaction is subtracted. Such a property can be connected to the quark sector considering that the valence quark composition of the proton is uud, while the neutron's one is udd. Proton and neutron masses are really similar and the reason is the closeness of u and

d masses.
Similarly to the strong isospin, it is possible to define a weak isospin T (as it will be explained better in Sec.1.1.3), which allow us to divide all the quarks in weak isospin pairs. The weak isospin T assumes the value of 1/2, while its projection $T3$ can assume the value of +1/2 and -1/2: pair of each quark family will have a quark with T_3=+1/2 and one with T_3=-1/2.
To each quark is also associated a *baryonic* number which must be conserved in every interaction. B=+1/3 for quarks and B=-1/3 for antiquarks: it must be 1 for baryons (composite states with three valence quarks) and 0 for mesons (with two valence quarks).
Quarks undergo strong interaction which is associated to the *colour* charge. All the quark flavours comes in three colours: *red*, *blue* and *green*. The colour must be conserved in all the interactions and it is responsible of the confinement: quarks can be observed just in colourless bounded states, as it will be explained in the following (see 1.1.3).

1.1.3 The fundamental interactions

The Standard Model includes three of the four fundamental interactions in Nature: electromagnetic, weak and strong forces. The attempt to incorporate gravitation clashes with the difficulty in harmonizing general relativity with quantum mechanics but however, at the scale of fundamental particle interaction due to the mass scales, is negligible (coupling constant of the order of 10^{-40}) compared to the other coupling constants.
All the mathematical framework is based on quantum mechanics and special relativity. The three interactions take their basis in the concept of local symmetries and so far they are described by gauge theories.
The Standard Model contains spin-1 particles, the vector bosons, quanta of vector fields. Vector bosons are the mediators of the three fundamental forces and the theory of local "gauge" symmetry help us describing them and their behaviour.
Let's go through the concept of symmetry considering a complex scalar field ϕ and its Hermitian conjugate $\phi^\dagger$ [3]. The field ϕ annihilates a particle with positive energy or creates an antiparticle with negative energy, while $\phi^\dagger$ annihilates an antiparticle with positive energy or creates a particle with negative energy. The Lagrangian is:

$$\mathscr{L} = \partial_\mu \phi^\dagger \partial^\mu - V(\phi^\dagger \phi) \tag{1.4}$$

For the U(1) symmetry, $\phi \to \phi' = e^{i\alpha}\phi$, with α constant parameter. For infinitesimal transformation of the fields and the Lagrangian:

$$\delta\phi = \phi' - \phi = i\alpha\phi \quad \delta\phi^\dagger \tag{1.5}$$

neglecting $\mathcal{O}(2)$ terms. To find the Noether's current, it is necessary to calculate the variation of the Lagrangian under this transformation:

$$\begin{aligned}
\delta\mathscr{L} &= \frac{\partial\mathscr{L}}{\partial\phi}\delta\phi + \frac{\partial\mathscr{L}}{\partial\phi^\dagger}\delta\phi^\dagger + \frac{\partial\mathscr{L}}{\partial(\partial_\mu\phi)}\delta(\partial_\mu\phi) + \frac{\partial\mathscr{L}}{\partial(\partial_\mu\phi^\dagger)}\delta(\partial_\mu\phi^\dagger) \\
&= \left(\frac{\partial\mathscr{L}}{\partial\phi} - \partial_\mu\frac{\partial\mathscr{L}}{\partial(\partial_\mu\phi)}\right)\delta\phi + \left(\frac{\partial\mathscr{L}}{\partial\phi^\dagger} - \partial_\mu\frac{\partial\mathscr{L}}{\partial(\partial_\mu\phi^\dagger)}\right)\delta\phi^\dagger + \partial_\mu\left(\frac{\partial\mathscr{L}}{\partial(\partial_\mu\phi)}\delta\phi + \frac{\partial\mathscr{L}}{\partial(\partial_\mu\phi^\dagger)}\delta\phi^\dagger\right) \\
&= \alpha\partial_\mu\left(i\partial^\mu\phi^\dagger\phi - i\phi^\dagger\partial^\mu\phi\right) \\
&= -\alpha\partial_\mu j^\mu
\end{aligned}$$

The first two terms of the second line are equal to zero by equation of motion. The Lagrangian is invariant so we have $\delta\mathscr{L}$=0. What we have obtained is a conserved current:

$$\partial_\mu j^\mu = 0 \tag{1.6}$$

A symmetry in the Lagrangian implies a conserved current, i.e. a conserved quantity. There are two types of symmetry:

- global: transformations leave the Langrangians invariant omogenously in all the space (like in the general example above).
- local: gauge transformations which leave the Lagrangiangs invariant point to point.

As said before, particle physics relies on last ones, since they are associated with forces as it will be explained in the following. The Standard Model is based on the group symmetry:

$$SU(3)_C \otimes SU(2)_L \otimes U(1)_Y \tag{1.7}$$

where $SU(3)_C$ is related to strong interaction and $SU(2)_L \otimes U(1)_Y$ to the electroweak interactions.

Quantum Electrodynamics: U(1) Local Gauge Invariance

Quantum Electrodynamics (QED) is the field theory of electromagnetic interaction. If we consider the Lagrangian in Eq.1.4 and a transformation $\phi \rightarrow \phi^{'} = e^{i\alpha}\phi$ with $\delta\phi = \phi^{'} - \phi = i\alpha\phi$, assuming that α is a space-time dependent parameter, the Lagrangian will be no more invariant.
What we want is to come up to a gauge symmetry. The way to save the invariance of the Lagrangian is to introduce a gauge field.
In Electrodynamics, $\overrightarrow{E}$ and $\overrightarrow{B}$ are respectively electric and magnetic fields, while ρ and $\overrightarrow{j}$ are the charge and current densities. They are connected by the well-known Maxwell's equations:

$$\overrightarrow{\nabla} \times \overrightarrow{E} + \frac{\partial \overrightarrow{B}}{\partial t} = 0 \qquad \overrightarrow{\nabla} \times \overrightarrow{B} = 0 \tag{1.8a}$$

$$\overrightarrow{\nabla} \times \overrightarrow{B} - \frac{\partial \overrightarrow{E}}{\partial t} = \overrightarrow{j} \qquad \overrightarrow{\nabla} \cdot \overrightarrow{E} = \rho \tag{1.8b}$$

Introducing two potentials, ϕ and $\overrightarrow{A}$:

$$\overrightarrow{E} = -\overrightarrow{\nabla}\phi - \frac{\partial \overrightarrow{A}}{\partial t} \qquad \overrightarrow{B} = \overrightarrow{\nabla} \times \overrightarrow{A} \tag{1.9}$$

We have a solution for the first two equations in Eq.(1.8b) but the correspondence between fields and potential is not unique. If we take transformed potential, with Λ as a scalar field:

$$\overrightarrow{A}^{'} = \overrightarrow{A} + \overrightarrow{\nabla}\Lambda \qquad \phi^{'} = \phi - \frac{\partial \Lambda}{\partial t} \tag{1.10}$$

they will give the same fields of the potentials 1.9.
This is an example of *gauge transformation*. It is a local transformation since Λ changes in space and time and the solutions to the equations of motion for the electromagnetic fields are invariant.
In terms of Lagrangian, the way to restore the invariance is to combine the two potentials ϕ and $\overrightarrow{A}$ in a four-vector potential $A^\mu = (\phi, \overrightarrow{A})$. Introducing a transformation of A^μ

$$A_\mu(x) \rightarrow A^{'}_\mu(x) = A_\mu(x) - \frac{1}{e}\partial_\mu \alpha(x) \tag{1.11}$$

and of the derivative in a *covariant derivative*:

$$D_\mu \phi = (\partial_\mu + ieA_\mu)\phi \tag{1.12}$$

we have an invariant form of the Lagrangian using the field and the covariant derivative:

$$\mathscr{L} = (D_\mu \phi)^\dagger (D^\mu \phi) - V(\phi^\dagger \phi) \tag{1.13}$$

To reconnect to QED, let's consider a fermion ψ with a local gauge transformation:

$$\psi \to \psi^{'} = e^{i\alpha}\psi \tag{1.14}$$

Replacing the derivative with the covariant one in the Lagrangian:

$$\mathscr{L} = i\bar{\psi}\gamma_\mu \partial^\mu \psi - m\bar{\psi}\psi \tag{1.15}$$

We get:

$$\mathscr{L} = i\bar{\psi}\gamma^\mu D_\mu \psi - m\bar{\psi}\psi \tag{1.16}$$

$$= \bar{\psi}(i\gamma^\mu \partial_\mu - m)\psi + e\bar{\psi}\gamma^\mu \psi A_\mu \tag{1.17}$$

In the case of QED, A_μ is the gauge field which couples to the Dirac particle with charge *e*. If we want it to correspond to the physical photon field, we have to introduce a kinetic term, representing the free propagation of the field. From the commutator of the covariant derivatives, we construct the field strenght tensor to ensure the invariance with respect to a local gauge transformation:

$$F_{\mu\nu} = -\frac{1}{e}[D_\mu, D_\nu] = -\frac{i}{e}[(\partial_\mu + ieA_\mu), (\partial_\nu + ieA_\nu] \tag{1.18}$$

$$= -\frac{i}{e}([\partial_\mu, \partial_\nu] + [\partial_\nu, ieA_\nu] + [ieA_\mu, \delta_\nu] - e^2[A_\mu, A_\nu] \tag{1.19}$$

$$= \partial_\mu A_\nu - \partial_\nu A_\mu \tag{1.20}$$

The field strenght gauge invariance can be demonstrated:

$$\delta F_{\mu\nu} = \partial_\mu \delta A_\nu - \partial_\nu \delta A_\mu = -\frac{1}{e}(\partial_\mu \partial_\nu - \partial_\nu \partial_\mu)\alpha(x) = 0 \tag{1.21}$$

Basically the antisymmetry in μ and ν ensures the gauge invariance.
The kinematic term is the square of the field strenght tensor:

$$-\frac{1}{4}F_{\mu\nu}F^{\mu\nu} \tag{1.22}$$

Finally the Lagrangian of the QED is:

$$\mathscr{L} = \bar{\psi}(i\gamma^\mu \partial_\mu - m)\psi + e\bar{\psi}\gamma^\mu A_\mu \psi - \frac{1}{4}F_{\mu\nu}F^{\mu\nu} \tag{1.23}$$

The gauge particle is the photon, which is *massless*, and it is the generator of U(1) symmetry group.
In QED, a charged particle is surrounded by a cloud of virtual photons and electron-positron pairs. Because of the electromagnetic force, virtual positrons tends to be close to the electron: this effect is known as *screening* or *vacuum polarization*. A visual representation of the

effect together with an example of the Feynmann diagram of virtual photons and e^+e^- production by a free electron are shown in Fig.1.2.

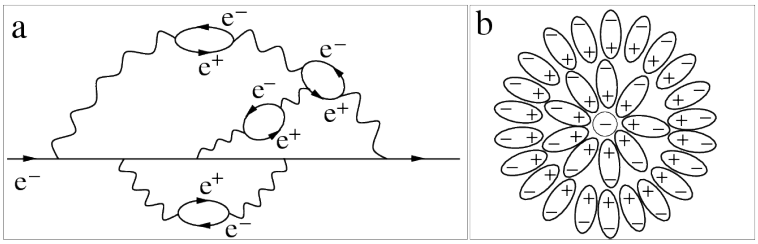

FIGURE 1.2: Vacuum polarisation effect. (a) Feynmann diagram for a free electron. (b) Visual represantation of the effect where it can be noted how the virtual positrons dispose themself around the electron, screening its bare charge.

This property lead to the concept of *running coupling constant*.
The attempts to define *bare* coupling (or mass or charge) led to infinities due to the mo-

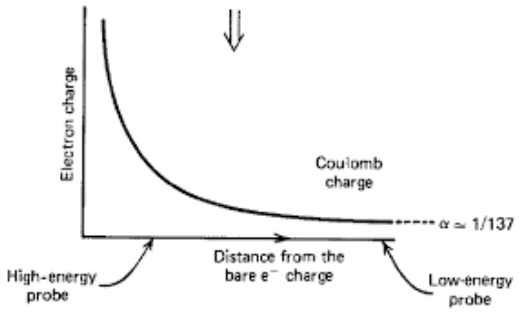

FIGURE 1.3: Electron charge as a function of the distance from the *bare* charge.

menta of the virtual particles which can go to infinity. A quantum field theory like QED requires the feature of *renormalisability* which allows to solve consequent divergences in the calculation. The general expression for the running coupling constant is:

$$\alpha(Q^2) = \frac{\alpha(\mu^2)}{1 + \alpha(\mu^2) b_0 ln\left(\frac{Q^2}{\mu^2}\right)} \tag{1.24}$$

b_0 is equal to -1/3π, taking into account three lepton families (they correspond to 3 degree of freedom), Q^2 is the transferred momentum and μ is the renormalisation scale. The choice of the scale is arbitrary. At the lowest energies, for example at μ=1 MeV, α=1/137. If we choose μ near to the Z^0 mass, the effective value will be $\alpha(M_Z)$=1/129: the effective coupling increases (but very slowly) with the energy-momentum transfer. From Fig.1.3, it can be seen how the effective charge of the electron increases with decreasing distance, together with the coupling.

Quantum Chromodynamics: SU(3) Local Gauge Invariance

To derive the Quantum Chromodynamics Lagrangian from local gauge invariance, we can extend what said in the previous sections but considering that the symmetry group is now

SU(3)$_C$, the group of phase transformation on the quark color fields.
The free Lagrangian in this case is:

$$\mathscr{L} = \bar{q}_j(i\gamma^\mu\partial_\mu - m)q_j \tag{1.25}$$

where q_j stands for the three color fields q_1, q_2 and q_3. Taking into account just one color flavour, the next step is requiring gauge symmetry. The transformation has the form:

$$q(x) \to Uq(x) \equiv e^{i\alpha_a(x)T_a}q(x) \tag{1.26}$$

In Eq.1.26, U is a 3 $\times$ 3 unitary matrix , T_a, with a=1,...,8 are a set of linearly traceless 3 $\times$ 3 matrices and α_a are the group parameters. Usually the choice for T_a is of hermitian matrices. The SU(3)$_C$ group is non-Abelian since not all the generators commute with each other:

$$[T_a, T_b] = if_{abc}T_c \tag{1.27}$$

where f_{abc} are the structure constant of the group.
Considering a local phase transformation:

$$q(x) \to [1 + i\alpha_a(x)T_a]q(x) \tag{1.28}$$
$$\partial_\mu \to (1 + i\alpha_a T_a)\partial_\mu + iT_a q\partial_\mu\alpha_a \tag{1.29}$$

Exactly as for QED, eight gauge fields G^a_μ are introduced with a transformation:

$$G^a_\mu \to G^a_\mu - \frac{1}{g}\partial_\mu\alpha_a - f_{abc}\alpha_b G^c_\mu \tag{1.30}$$

and a covariant derivative:

$$D_\mu = \partial_\mu + igT_a G^a_\mu \tag{1.31}$$

Note that the choice of the form of the fields in Eq.1.30 is due to the non-Abelian nature of the SU(3) group. Introducing the kinematic term we obtain the gauge invariant QCD Lagrangian:

$$\mathscr{L} = \bar{q}(i\gamma^\mu\partial_\mu - m)q - g(\bar{q}\gamma^\mu T_a q)G^a_\mu - \frac{1}{4}G^a_{\mu\nu}G^{\mu\nu}_a \tag{1.32}$$

The Eq.1.32 describes the interaction between colored quarks q and the vector bosons G_μ, called *gluons*, with coupling g. Just like the photons, the gluons are required to be *massless*. The non-Abelian nature of the SU(3)$_C$ group lead to the fact that also gluons carry color charge (differently from photons which are neutral), so QCD gauge bosons can interact with each other.
This particular property reflects also on the behaviour of the coupling constant. Just like for QED, also in this case we can talk about running coupling constant, although their behaviour is different.
Since the gluons carry themselves color charge, we have to consider loops due to the production of virtual particles that are both q$\bar{q}$ and gg couples, as can be seen in Fig.1.4. On the contrary of what happens in QED, a red (blue, green) charge is preferentially surrounded by other red (blue, green) charges. This has effect of the behaviour of the α_S coupling constant, as can be seen in Fig.1.5. Just like for QED, we can give a parametrisation of the running coupling constant, exploiting the renormalisability of the quantum fields theories.

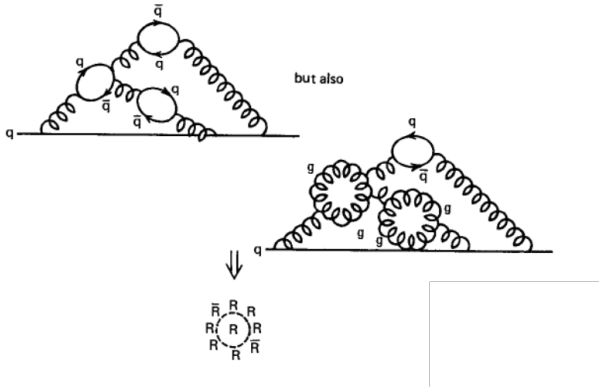

FIGURE 1.4: Antiscreening effect. Due to the non-neutral nature of the gluons, it is necessary to consider $q\bar{q}$ virtual couples but also virtual gluon couples.

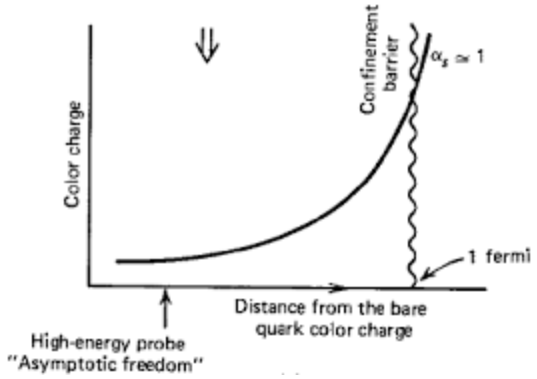

FIGURE 1.5: Behaviour of QCD running coupling constant.

Also in this case, it has to depend on a free parameter which as to be determined experimentally. Considering the parametrization:

$$\alpha_S(Q^2) = \frac{12\pi}{(11N_c - 2N_f)ln\left(\frac{Q^2}{\Lambda^2_{QCD}}\right)} \tag{1.33}$$

Λ^2_{QCD} (≈200 MeV) is the free parameter and corresponds to the QCD scale. This value has to be used at a scale above the bottom quark mass of about 5 GeV, [4]. N_c is the number of colors (3) and N_f is the number of active quark flavours which depends on the value of Q^2: for example, if $Q^2 = M^2_Z$, N_f=5, since the top quark mass is higher then the mass of the Z^0 boson.
When $Q^2 \to \infty$, $\alpha_S \to$0: this is the *asymptotic freedom* and quarks behave as free particles. On the contrary, when Q^2 is low, for example when it tends to Λ^2_{QCD}, α_S increases bringing to the phenomenon of *confinement*: free color charges cannot be observed. As can be seen from Fig.1.5, for distances from the quark around r=1fm, α_S approaches a constant value: this is known as *infrared slavery*.
The charge antiscreening property in its influence on the strong running coupling constant is the reason of the hadronisation.

Weak Interaction

The Weak Interactions involves all the fermions of the Standard Model. The reason for *weak* came from the comparison between the lifetime of the particles decaying via this force with the ones decaying through electromagnetic and strong interaction. The typical lifetime of a weak decaying particle is $\sim 10^{-8}$ s, long if compared to the ones electromagnetic-decaying with $\sim 10^{-16}$s and strong-decaying 10^{-23} s.
It was discovered by Enrico Fermi in 1934 during his studies on the decay of neutron, the nuclear β-decay (neutrino was not yet been discovered but its existence was postulated by Pauli in order to explain the continuous energy spectrum of the electron in the β decay):

$$n \to p + e^- + \bar{\nu}_e \tag{1.34}$$

He interpreted it as a point-like interaction, without assuming the existence of a mediator of the weak force (four-fermion contact interaction). Fermi expressed the Lagrangian of the weak interaction introducing a vector (V) current to represent the creation of the couple $e^- \bar{\nu}_e$:

$$\mathscr{L} = G_F(\bar{u}_p \gamma^\mu u_n)(\bar{u}_e \gamma_\mu u_\nu) \tag{1.35}$$

G_F is the coupling constant associated with the weak interaction. It was measured for the first time by Fermi himself from the neutron β-decay: $G_F = 2 \cdot 10^{-5} GeV^{-2}$. However, the best estimation was the one obtained exploiting the muon decay [5]:

$$G_F = 1.16639 \cdot 10^{-5} GeV^{-2} \tag{1.36}$$

Soon, the evidence that different processes due to weak interaction have similar coupling constant led to the idea of the *universality of weak interactions*.
Later in the years, with the Lee and Yang studies on the K particles and the Madame Wu experiment on β-decay of $^{60}_{27}$Co, became clear that weak interactions do not conserve *parity*. Another important outcome of the Wu's experiment was that in weak interaction *left-handed* fermions were favored.
It was in 1958, when Goldhaber, Grodzins and Sunyar discovered that neutrinos are pure helicity states $H = \pm 1$ that became evident what should be the nature of the weak current. The helicity measures the sign of the component of the spin ($\overrightarrow{\sigma}$) of the particle ($j_z = \pm \frac{1}{2}\hbar$), in the direction of the motion z. It is defined as:

$$H = \frac{\overrightarrow{\sigma} \cdot \overrightarrow{p}}{|\overrightarrow{p}|} - 1 \tag{1.37}$$

For massless fermions, the corresponding projector operator is:

$$P_{R,L} = \frac{1}{2}\Big(1 \pm \frac{\overrightarrow{\sigma} \cdot \overrightarrow{p}}{E}\Big) \tag{1.38}$$

If applied to a two component spinor, it will produce an helicity state from a superposition of positive and negative states:

$$P_R \psi = \frac{1}{2}\Big(1 + \frac{\overrightarrow{\sigma} \cdot \overrightarrow{p}}{E}\Big)(\psi_L + \psi_R) = \psi_R \tag{1.39}$$

$$P_L \psi = \frac{1}{2}\Big(1 - \frac{\overrightarrow{\sigma} \cdot \overrightarrow{p}}{E}\Big)(\psi_L + \psi_R) = \psi_L \tag{1.40}$$

While for the massive fermions, the anologous is the *chirality* operator, which acts on four-component Dirac spinor:

$$P_{R/L} = \frac{1}{2}(1 \pm \gamma^5) \tag{1.41}$$

where γ^5 is:

$$\gamma^5 = i\gamma^0\gamma^1\gamma^2\gamma^3 \tag{1.42}$$

with γ^i ($i = 0, 1, 2, 3$) being the so-called *Dirac matrices*, [6].
Considering the matrix element for the β-decay:

$$\mathcal{M} = GJ^{weak}_{baryon}J^{weak}_{lepton} = G(\bar{\psi}_p O_i \psi_n)(\bar{\psi}_e O \psi_\nu) \tag{1.43}$$

O_i can be equal to five possible operators, allowed by relativistic invariance. They are classified by their properties with respect to spatial transformation: scalar S, vector V, tensor T, axial vector (or pseudovector) A and pseudoscalar P. In the Fermi ansatz, O_i is assumed to be a vector operator but this turned to be an incomplete description since it is incompatible with parity violation and helicity behaviour. Due to the evidence that leptons and antileptons have opposite helicities, the choice of the operators was V and A.
We can write the leptonic current J^{weak}_{lepton} as a combination of vector and axial terms:

$$J^{weak}_{lepton} \equiv J^\mu_\ell = (c_V V^\mu_\ell + c_A A^\mu_\ell) \tag{1.44}$$

Assuming c_V and c_A equal to unity and opposite in sign, using the definitions of the operators, Eq.1.44 becomes:

$$J^\mu_\ell = \bar{\psi}_e\gamma^\mu\psi_\nu - \bar{\psi}_e\gamma^\mu\gamma^5\psi_\nu = \bar{\psi}_e\gamma^\mu(1-\gamma^5)\psi_\nu \tag{1.45}$$

Which turns out to be, exploiting the γ matrices properties and using the chirality operator definition in Eq.1.41:

$$J^\mu_\ell = 2\bar{\psi}_e\Big(\frac{1+\gamma^5}{2}\Big)\gamma^\mu\Big(\frac{1-\gamma^5}{2}\Big)\psi_\nu = 2(\bar{\psi}_e)_L\gamma_\mu(\psi_\nu)_L \tag{1.46}$$

Eq.1.46 is the expression of the *charged weak current* and it gives a formal expression of the coupling of charge vector bosons $W^\pm$ with the left-handed component of the fermions. In the same way, it has been shown how they couple with right-handed components of the anti-fermions.
This is the V-A theory of weak interactions. Standard Model fermions are divided, due to the weak interactions, in left-handed doublets (with weak isospin T_3 = 1/2) and right-handed singlets (with weak isospin T_3=0). For example, in the first lepton family, e will be paired to a ν_e because by the exchange of a W^+, it will become a neutrino and viceversa by the exchange of a W^-.
The massive nature of the weak force carriers explained the short range of weak interactions and causes a modification of G_F as follows:

$$\frac{g^2}{8M^2_W} \equiv \frac{G_F}{\sqrt{2}} \tag{1.47}$$

which represents the relation between the weak coupling constant g and the Fermi constant G_F.
During the 70s, at CERN, *neutral currents* were discovered from the evidence of interactions involving neutrinos and no charged leptons. A new vector boson, Z^0, was the mediator of these phenomena. Theoretically, weak neutral currents are really important since they

represent a fundamental milestone in the path towards electroweak unification, as we will see in the next section.

1.2 The Higgs Boson

The hunt for the Higgs boson started with Tevatron and LEP and it was one of the main motivation for the construction of the Large Hadron Collider at CERN in Geneva.
The Higgs boson existence was postulated in the framework of *spontaneous symmetry breakdown* of the SU(2)$_L\otimes$ U(1)$_Y$ giving mass to the Standard Model fermions and massive gauge bosons.
After 40 years since its theorization, during a famous seminar, on 2012 4th July, ATLAS and CMS (the LHC two multipurpose experiment) spokepersons announced to have discovered an excess around 5σ at a mass of 125 GeV.
At the end of the session, the CERN General Director Rolf Heuer stated "I think we have it." Peter Higgs and François Englert were sitting in the room and later on, in 2013, they were awarded with the Nobel Price.

1.2.1 The Electroweak Interactions

Late 60s: Weinberg, Salam and Glashow came out with an ambitious idea. Analogously to what achieved by Clerk Maxwell in 19th century with unification of electric and magnetic forces, they built a theory to treat electromagnetic and weak interaction as a whole.
The *electroweak interaction* would have taken its basis from the symmetry between the two at large momentum transfer ($q^2 >> 10^4$ GeV^{-2}), while at low energies a broken symmetry occurs. The broken symmetry would cause one of the four mediating bosons to be massless (photon) and the others (Z^0 and $W^{\pm}$) to be massive, causing the difference in the interaction range.
As said in the previous sections, a quantum field theory must have the essential feature of renormalisability, to save its predictive power. In other words, it has to avoid divergences at high energies and at high orders of the coupling constant.
Early weak interaction theories well behaved at low energies and to the first order but occurred in divergences not well absorbed by adding arbitrary constant.
The first step towards the cancelation of the divergences was the introduction of the concept of *neutral current* mediated by a brand new spin-1 particle: the neutral vector boson Z^0. It is assumed to have a weak coupling g similar in magnitude to the electromagnetic one, e. This was the first real step toward the unification.
The unified theory postulated the idea of four massless bosons, grouped in a triplet and a singlet of *weak isospin* T and *hypercharge* Y. The two quantum numbers are respectively the generators of the symmetry groups SU(2)$_L$ and U(1)$_Y$. The resulting symmetry group is SU(2)$_L\otimes$U(1)$_Y$.
The relation between the third component of weak isospin T_3 and the hypercharge Y is the well-know Gell-Mann-Nishijima formula:

$$Q = T_3 + \frac{Y}{2} \tag{1.48}$$

where Q is the electric charge.
The triplet, with T=1, includes the three bosons $\mathbf{W}_\mu$ = $W_\mu^{(1)}$, $W_\mu^{(2)}$, $W_\mu^{(3)}$, belonging to the group SU(2), while the singlet has the fourth boson B_μ of the U(1) group. For this reason,

the model is referred as SU(2)×U(1).
W_μ^+, W_μ^- and Z_μ^0 are the massive bosons, A_μ is the massless photon.
Z_μ^0 and A_μ are a mixing combination of the states $W_\mu^{(3)}$ and B_μ, as can be seen from Eq.1.51, 1.52 and 1.53.
The Lagrangian energy density, Eq.1.49, is a formal relativistically invariant form of the interaction energy of the fermions with the mediators.

$$L = g\mathbf{J}_\mu \cdot \mathbf{W}_\mu + g^{'} J_\mu^Y B_\mu \tag{1.49}$$

$\mathbf{J}_\mu$ and J_μ^Y are the weak isospin and hypercharge currents of the fermions, while $\mathbf{W}_\mu$ and B_μ are the 4-potential associated with the boson fields. The two coupling constant g and $g^{'}$ are not independent (see below). Eq.1.49 is a generalization of the interaction energy $e\mathbf{J}_\mu^Y A_\mu$ of an electric current with the electromagnetic field. Taking into account the relation in Eq.1.48, we get the relation between the weak isospin and hypercharge current:

$$J_\mu^Y = J_\mu^{EM} - J_\mu^{(3)} \tag{1.50}$$

where J_μ^{em} is the electromagnetic current, coupling to charge Q and J_μ^3 is the third component of the isospin current $\mathbf{J}_\mu$. The physical bosons consists of the charged particles $W_\mu^\pm$ and the neutrals Z_μ and A_μ.

$$W_\mu^\pm = \frac{1}{\sqrt{2}}[W_\mu^{(1)} \pm W_\mu^{(2)}] \tag{1.51}$$

$$W_\mu^{(3)} = \frac{gZ_\mu + g^{'} A_\mu}{\sqrt{g^2 + g^{'2}}} \tag{1.52}$$

$$B_\mu = \frac{-g^{'} Z_\mu + gA_\mu}{\sqrt{g^2 + g^{'2}}} \tag{1.53}$$

Combining together Eqs.1.49, 1.50, 1.51, 1.52 and 1.53 we get:

$$L = \frac{g}{\sqrt{2}}(J_\mu^- W_\mu^{'} + J_\mu^+ W_\mu^{'}) + \frac{g}{cos\theta_W}(J_\mu^{(3)} - sin^2\theta_W J_\mu^{em})Z_\mu + gsin\theta_W J_\mu^{em} A_\mu \tag{1.54}$$

where $J_\mu^\pm = J_\mu^{(1)} \pm iJ_\mu^{(2)}$. The ratio between the two coupling constants is $\frac{g'}{g} = tan\theta_W$.
In Eq.1.54, which represents the electroweak lagrangian energy density, we recognize in the first term the contribution of weak charge-changing current, in the second one the weak neutral current and in the third one the electromagnetic neutral current. Since the EM coupling is e, $e = gsin\theta_W$, where θ_W is the Weinberg weak mixing angle, [5].
Analogously to what has been said for QED and QCD, we want to ensure local gauge invariance. As said above, the group symmetry of electroweak interaction is $SU(2)_L \otimes U(1)_Y$. For $U(1)_Y$, the local transformation is expressed as:

$$\psi(x) \to e^{i\frac{Y}{2}\beta(x)}\psi(x) \tag{1.55}$$

where $\beta(x)$ is a parameter varying in space and time. We also know that weak interaction favors left-handed particles whose field expression is:

$$u_L = e^{i\frac{\sigma_i}{2}\alpha_i(x)} \tag{1.56}$$

where $\alpha_i(x)$ are space-time dependent parameters and σ_i are the Pauli matrices, generators of the SU(2) group. Taking into account the four boson fields defined above, the covariant

derivative to save the local symmetry invariance will be:

$$D_\mu = \partial_\mu + ig^{'}\frac{Y}{2}B_\mu(x) + ig\frac{\sigma_i}{2}W_\mu^i(x) \tag{1.57}$$

Finally, the Lagrangian of the Electroweak unified theory will be:

$$\mathscr{L} = \sum_j^3 i\bar{\psi}_j(x)\gamma^\mu D_\mu \psi_j(x) - \frac{1}{4}B_{\mu\nu}B^{\mu\nu} - \frac{1}{4}W_{\mu\nu}^i W_i^{\mu\nu} \tag{1.58}$$

In Eq.1.58, the first term represents the interaction with the fermions, while the last two terms are the free field propagation.
Within this theoretical formulation, the four gauge bosons are still massless. Adding a quadratic mass term to the Eq.1.58 is not possible without spoiling the gauge invariance, meaning that it is not possible to add the mass of three of the four bosons *by hand*.
The idea of the spontaneous symmetry breaking comes in help to explain the boson mass generation, experimentally evident from the short-range nature of the weak interaction.

1.2.2 The Higgs Mechanism

A possible solution to the riddle of massive boson in the Electroweak theoretical framework was proposed by Higgs, Brout and Englert in 1964, [7] [8]. They postulated the existence of scalar potential that can be added to the electroweak lagrangian to save the gauge invariance and the renormalisability, assuming the presence of a spontaneous symmetry breaking.
To give an idea of what a spontaneous symmetry breaking is, we can take a brilliant example by Sir Thomas W.B. Kibble, a British theoretical physicist, [9].
Suppose that we have a perfectly concave bowl and a marble to throw in it: the marble's trajectory would be complex but the rest position it's clear and it will be the center of the bowl bottom, see Fig.1.6a. If we suppose to have a different bowl with a bottom really similar to the one of a wine bottle, our marble will not sit in the end on the center, but somewhere in the circle of lowest points, see Fig.1.6b. This simple example leads to an easy example of spontaneous symmetry breaking: "[..] the ground or lowest-energy state does not share the symmetry of the underlying physics." In other words, we cannot say which ground state will be chosen at the end.

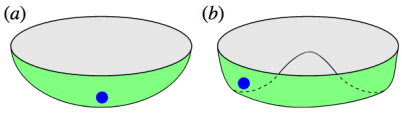

FIGURE 1.6: Final equilibrium point in a perfectly concave bowl (a) and in a "wine bottle"-shaped bottom bowl (b).

Let's consider a scalar self-interacting field ϕ, [2]. The corresponding Lagrangian is:

$$L = T - V = \frac{1}{2}(\partial_\mu\phi)^2 - \frac{1}{2}\mu^2\phi^2 \tag{1.59}$$

If we want to generalize it to scalar particles interacting with each others, the potential V must contain a term ϕ^4: this choice allows that the symmetry of the Lagrangian under the transformation $\phi \to -\phi$ is ensured (note that ϕ^6 terms and higher powers are excluded by

renormalisability requirements). μ is the mass and the Lagrangian will become:

$$L = T - V = \frac{1}{2}(\partial_\mu \phi)^2 - \frac{1}{2}\mu^2\phi^2 - \lambda\phi^4 \tag{1.60}$$

λ is a dimensionless constant representing the 4-boson vertex coupling.
The potential V has a minima ($\phi = \phi_{min}$) when $\frac{\partial V}{\partial \phi}$ = 0:

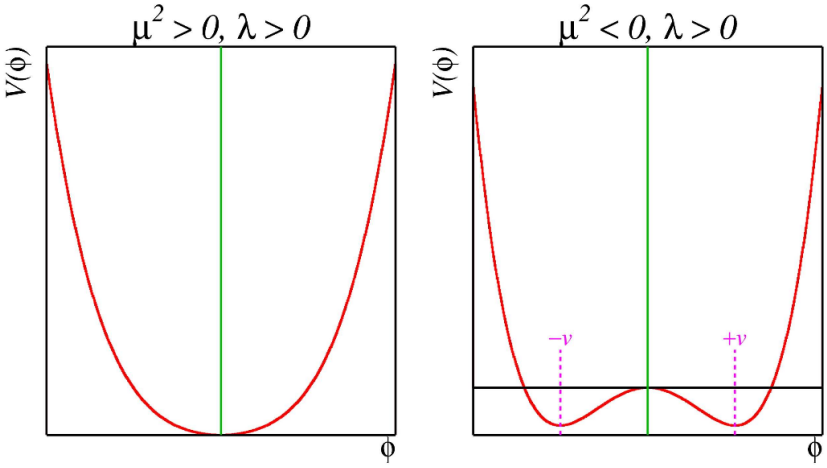

FIGURE 1.7: Higgs potentia for two values of μ^2.

$$\phi(\mu^2 + \lambda\phi^2) = 0 \tag{1.61}$$

Depending on the μ^2 values, two situations are possible:

- if μ^2>0, ϕ=ϕ_{min} where ϕ_{min}=0 corresponding to the lowest energy vacuum state V=0 (see Fig.1.7 on the left).
- if μ^2<0, we have two relative minima (see Fig.1.7 on the right).

$$\phi = \phi_{min} \qquad \text{where} \qquad \phi = \pm v = \pm\sqrt{\frac{-\mu^2}{\lambda}} \tag{1.62}$$

Expanding the field potential about one of the two vacuum minimum (we arbitrary choose +v):

$$\phi = v + \sigma(x) \tag{1.63}$$

where $\sigma(x)$ is the variation of the field about the minimum. Putting 1.63 in 1.60, we get:

$$L = \frac{1}{2}(\partial_\mu \sigma)^2 - \lambda v^2\sigma^2 - \lambda v\sigma^2 - (\lambda v\sigma^3 + \frac{1}{4}\lambda\sigma^4) + \text{constant} \tag{1.64}$$

What do we learn from Eq.1.64? The first term represents the kinetic one, the cubic term (σ_3) represents the self-interaction of the field σ and the constants contain the v^2 and v^4 terms. What remains is the *mass*-term., which assumes the positive value:

$$m = \sqrt{2\lambda^2} = \sqrt{-2\mu^2} \tag{1.65}$$

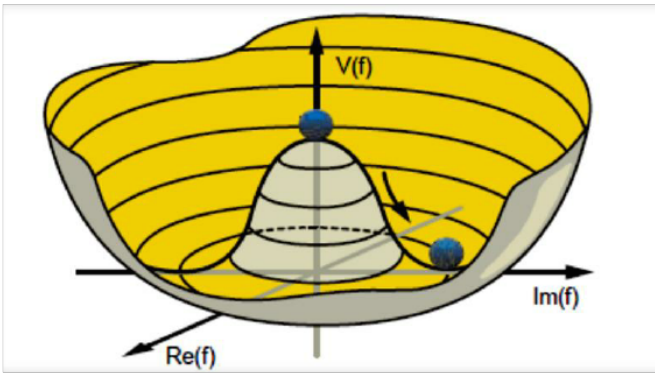

FIGURE 1.8: "Mexican Hat" potential.

So, following a simple perturbative approach, doing an expansion around one of the two local minima, we have obtained a real mass term. We are in front of a clear example of *spontaneous symmetry breaking*.
Coming back to our specific purpose and to the Electroweak sector, let's take first the example of the mass generation for a generic gauge boson. Suppose we have a Lagrangian:

$$\mathscr{L} = (\partial_\mu \phi)^*(\partial^\mu \phi) - \mu^2 \phi^* \phi - \lambda(\phi^* \phi)^2 \tag{1.66}$$

invariant with respect to a global U(1) symmetry with transformation $\phi \rightarrow \phi^{'} = e^{i\alpha\phi}$. The chosen potential will be a complex scalar field:

$$\phi = \frac{\phi_1 + i\phi_2}{\sqrt{2}} \tag{1.67}$$

In this case, while for μ^2>0, the minimum is always in the center at zero, when μ^2<0, the minimum is along a circle of radius v, with $\phi_1^2 + \phi_2^2 = -\frac{-\mu^2}{\lambda}$, as can be seen in Fig.1.8. As seen before, we take an expansion about a local minimum of this form:

$$\phi(x) = \frac{v + \eta(x) + i\rho(x)}{\sqrt{2}} \tag{1.68}$$

where $\eta(x)$ and $\rho(x)$ are the vacuum fluctuations around the ψ_1 and ψ_2 directions. Putting Eq.1.68 in the Lagrangian we obtain:

$$\mathscr{L} = \frac{1}{2}(\partial_\mu \rho)^2) + \frac{1}{2}(\partial_\mu \eta)^2 + \mu^2 \eta^2 + \text{cubic and quadratic terms + constants} \tag{1.69}$$

Really important conclusions came out from this formula. The first two terms are the kinetic contributions, while $\mu^2\eta^2$ is our mass term so the η field corresponds to a massive particle.
It is worth to note that there is no quadratic term for ρ: massless spin 0 Goldstone's boson disappears and it turns out not be a physical particle.
In the particular case of SU(2) symmetry, we choose to introduce four real scalar fields ϕ_i to be added to the $SU(2)_L$ and $U(1)_1$ Lagrangian, see Eq.1.58. To save the gauge invariance, the most proper way to act is to group the four field potentials in isospin doublets with

hypercharge Y=1.

$$\phi = \begin{pmatrix} \phi^+ \\ \phi^0 \end{pmatrix} \tag{1.70}$$

where:

$$\phi^+ \equiv \frac{(\phi_1 + i\phi_2)}{\sqrt{2}} \tag{1.71}$$

$$\phi^0 \equiv \frac{(\phi_3 + i\phi_4)}{\sqrt{2}} \tag{1.72}$$

The Lagrangian:

$$\mathscr{L} = (\partial_\mu \phi)^\dagger (\partial_\mu \phi) - V(\phi) \tag{1.73}$$

$$= (\partial_\mu \phi)^\dagger - \frac{1}{2}\mu^2 \phi^\dagger \phi - \frac{1}{4}\lambda(\phi^\dagger \phi)^2 \tag{1.74}$$

The Lagrangian is invariant under local SU(2) transformation $\phi \rightarrow \phi^{'} = e^{\frac{i\alpha_a(x)\tau_a}{2}}\phi$ if we replace ∂_μ with a covariant derivative:

$$D_\mu = \partial_\mu + ig\frac{\tau_a}{2}W_\mu^a \tag{1.75}$$

W_μ^a are the three gauge fields. If we apply to them a local gauge transformation:

$$\phi(x) \rightarrow \phi^{'}(x) = e^{(1+i\alpha_a(x)\frac{\tau_a}{2})}\phi(x) \tag{1.76}$$

where $\alpha_a(x)$ are the group parameters and τ_a are 3×3 traceless matrices.
Eq.1.74 becomes:

$$\mathscr{L} = \Big(\partial_\mu + ig\frac{1}{2}\boldsymbol{\tau}\cdot\mathbf{W}_\mu\Big)\phi\Big(\partial^\mu + ig\frac{1}{2}\boldsymbol{\tau}\cdot\mathbf{W}^\mu\Big)\phi^\dagger - V(\phi) - \frac{1}{4}\mathbf{W}_{\mu\nu}\mathbf{W}^{\mu\nu} \tag{1.77}$$

with $V(\phi) = \mu^2\phi^\dagger\phi + \lambda(\phi^\dagger\phi)^2$ and the last term is kinetic energy of the gauge fields.
We are interested to the case when μ^2<0 (when μ^2>0 we have a system of four scalar particles ϕ_i interacting with three massless vector bosons). The potential $V(\phi)$ has its minimum where:

$$\phi^\dagger\phi \equiv \frac{1}{2}(\phi_1^2 + \phi_2^2 + \phi_3^2 + \phi_4^2) = -\frac{\mu^2}{2\lambda} \tag{1.78}$$

As seen in the two general examples above, it is necessary to choose a particular minimum about which expand the potential.

$$\phi_1 = \phi_2 = \phi_4 = 0 \qquad \phi_3 = -\frac{\mu^2}{\lambda} \equiv v^2 \tag{1.79}$$

The expansion is:

$$\phi(x) = \sqrt{\frac{1}{2}}\begin{pmatrix} 0 \\ v + h(x) \end{pmatrix} \tag{1.80}$$

about this chosen vacuum state:

$$\phi_0 \equiv \sqrt{\frac{1}{2}}\begin{pmatrix} 0 \\ v \end{pmatrix} \tag{1.81}$$

where v is the vacuum expectation value.
As seen above, putting the expansion in the Lagrangian, the remaining field is $h(x)$, the *Higgs field*.

To get the masses of the gauge bosons W^a_μ, it is necessary to introduce ϕ_0 in the Lagrangian, where the corresponding relevant term is:

$$\left|ig\frac{1}{2}\boldsymbol{\tau}\cdot\mathbf{W}_\mu\phi\right| = \frac{g^2}{8}\left|\begin{pmatrix} W^3_\mu & W^1_\mu - iW^2_\mu \\ W^1_\mu + iW^2_\mu & W^3_\mu \end{pmatrix}\begin{pmatrix} 0 \\ v \end{pmatrix}\right|^2 \tag{1.82}$$

$$= \frac{g^2v^2}{8}\left[(W^1_\mu)^2 + (W^2_\mu)^2 + (W^3_\mu)^2\right] \tag{1.83}$$

here $|\ |^2$ has been used in place of $()^\dagger()$. This term describes three massive gauge boson fields with mass M=$\frac{1}{2}gv$. Basically, Goldstone massless bosons has been eaten and become massive: the scalar degrees of freedom has become the longitudinal polarizations of the massive vector bosons [2].
The final expression for Lagrangian of the SU(2)$_L$⊗U(1)$_Y$ is:

$$\mathscr{L} = |(i\partial_\mu - g\mathbf{T}\cdot\mathbf{W}_\mu - g'\frac{Y}{2}B_\mu)\phi|^2 - \frac{1}{2}\mu^2\phi^\dagger\phi - \frac{1}{4}(\phi^\dagger\phi)^2 \tag{1.84}$$

where the operators $\mathbf{T}$ and Y are the generators of the SU(2)$_L$ and U(1)$_Y$ groups of gauge transformations, respectively.
About the mass of the gauge bosons, it is worth to underline that the choice of ϕ_0 (see Eq.1.72) has been crucial. Indeed, if ϕ_0 is left invariant by one of the two subgroups, the corresponding boson remains massless. The choice of ϕ_0 implies T=1/2, T_3=-1/2 and Y=1. Since ϕ_0 is neutral the U(1) remains unbroken having as generator Q=T_3 + $\frac{Y}{2}$. The associated gauge boson, the photon, has m=0.
Knowing that $W^\pm = \frac{(W^1 \pm W^2)}{\sqrt{2}}$ and comparing the expression with obtained expanding the last term of Eq.1.83, we get that:

$$M_W = \frac{1}{2}vg \tag{1.85}$$

With similar calculation, we obtain also that:

$$M_Z = \frac{1}{2}v\sqrt{g^2 + g'^2} \tag{1.86}$$

The Higgs field gives mass also to the Standard Model fermions. As it regards leptons, we include the following SU(2)×U(1) gauge invariant term in the Lagrangian:

$$\mathscr{L}^{leptons} = -\lambda_e\left[(\bar{\nu},\bar{e})_L\begin{pmatrix}\phi^+ \\ \phi\end{pmatrix}e_R + \bar{e}_R(\phi^-,\phi^0)\begin{pmatrix}\nu_e \\ e\end{pmatrix}_L\right] \tag{1.87}$$

Eq.1.87 describes the Higgs coupling to the Standard Model left-handed doublets and right-handed singlets. Note that neutrinos, which exist just left-handed cannot, consequently, interact with the Higgs field (the reason for their masses must be due to another effect). The lepton mass term is:

$$\mathscr{L} = -m_e\bar{e}e - \frac{m_e}{v}\bar{e}eh \tag{1.88}$$

where m_ℓ is the mass of the lepton.
The same operation can be done for the quark masses but the Higgs doublet must be modified to take into account the massive nature of both the components of the quark doublet:

$$\phi_C = -i\tau_2\phi^* = \begin{pmatrix}-\bar{\phi}^0 \\ \phi^-\end{pmatrix} \to \sqrt{\frac{1}{2}}\begin{pmatrix}v+h \\ 0\end{pmatrix} \tag{1.89}$$

The resulting Lagrangian is:

$$\mathscr{L}^{quarks} = -\lambda_d^{ij}(\bar{u}_i, \vec{d}_j)_L \begin{pmatrix} \phi^\dagger \\ \phi^0 \end{pmatrix} d_{jR} - \lambda_u^{ij}(\bar{u}_i, \bar{d'}_j)_L \begin{pmatrix} -\bar{\phi}^0 \\ \phi^- \end{pmatrix} u_{jR} + \text{hermitian conjugate} \tag{1.90}$$

$i, j = 1, ..., N$ where N is the number of quark doublets.
The final quark Lagrangian matrix is:

$$\mathscr{L}^{quarks} = -m_d^i \bar{d}_i d_i \Big(1 + \frac{h}{v}\Big) - m_u^i \bar{u}_i u_i \Big(1 + \frac{h}{v}\Big) \tag{1.91}$$

In conclusion, the choice of an Higgs doublet generate masses for the gauge bosons and the fermions. However, the latter are free parameters and not predicted by the theoretical framework: as a consequence their experimental values are inputs for the Standard Model. Luckily, as we can notice, their Higgs coupling is proportional to their masses: a prediction that can be tested when a Higgs particle is observed.

1.2.3 The Higgs Mass Measurements

The Higgs boson discovery has been announced by ATLAS [10] and CMS [11] collaborations on 4th July 2012. They both observed an excess of events in the invariant mass plots of different Higgs decay channels combining the measurements of the 2011 at $\sqrt{s}$=7 TeV (corresponding to integrated luminosities of 4.8 fb^{-1} and 5.1 fb^{-1} for ATLAS and CMS, respectively) and 2012 at $\sqrt{s}$=8 TeV (corresponding to integrated luminosities of 5.8 fb^{-1} and 5.3 fb^{-1} for ATLAS and CMS, respectively) data taking. The analyses were focused on different decay modes: $H \to \gamma\gamma$, $H \to WW^*$, $H \to ZZ^*$, $H \to \tau\tau$ and $H \to b\bar{b}$.
The results for ATLAS and CMS are shown in Fig.(1.9) for $H \to ZZ^*$ and for $H \to \gamma\gamma$, respectively.
The Standard Model Higgs is a scalar of spin 0. Its mass is given by:

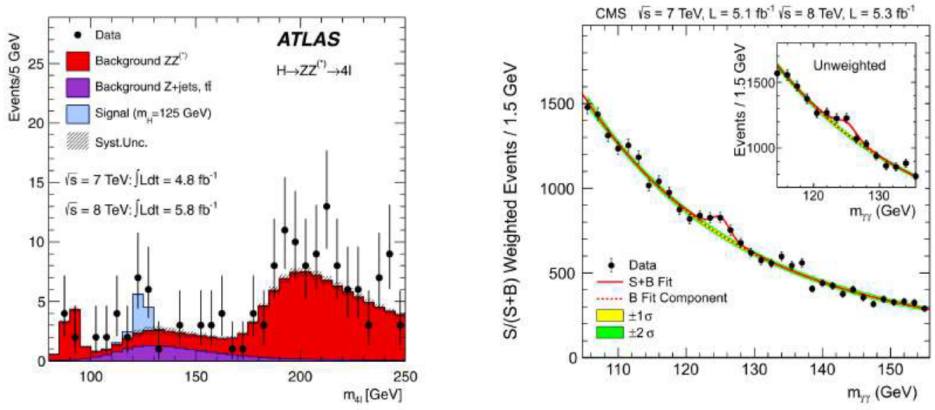

FIGURE 1.9: ATLAS (left) and CMS (right) Higgs boson evidence. The ATLAS distribution refers to the analysis of the $H \to ZZ^*$ decay analysis and it shows the four leptons invariant mass in the final state for the combined 7 TeV and 8 TeV data. The CMS distribution shows the diphoton invariant mass distribution for the $H \to \gamma\gamma$ decay channel.

$$m_H = \sqrt{2\lambda}v \tag{1.92}$$

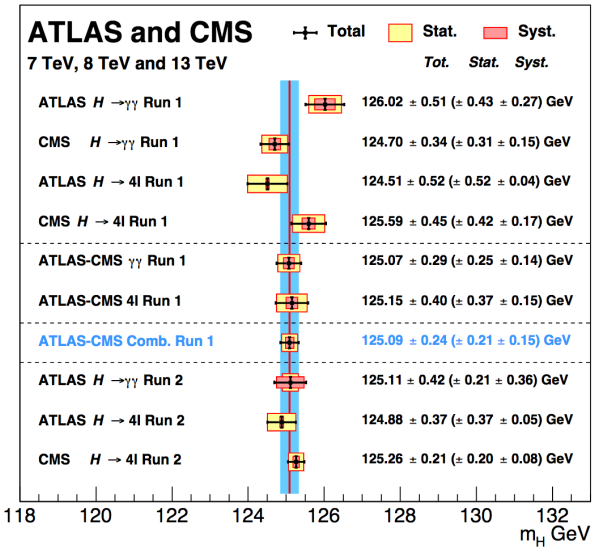

FIGURE 1.10: Summary of the ATLAS and CMS mass measurements in the $\gamma\gamma$ and ZZ channels in Run1 and Run2.

where λ is the Higgs self-coupling in the potential $V(\phi)$. The expectation value of the Higgs field is calculated from the Fermi constant G_F as $v = (\sqrt{2}G_F)^{-1/2}$. It is important to note that the Standard Model is not predictive about the value of the Higgs mass since the quartic term of the Higgs self-coupling λ^4 is a free parameter.
The first try to measure the Higgs mass was by the LEP (*Large Electron-Positron Collider*), opearated at CERN from 1989 to 2000. LEP was the first facility to reach the potential range of the Higgs mass: the most important conclusion reached at that time was that it must be larger than 114 GeV [12].
In those years, the first seed for the idea and realization of the Large Hadron Collider was there: the possibility to have a large proton-proton accelarator, with an energy range of 10-20 TeV and with high luminosity, to explore and study a large mass-range. Meanwhile, in the 1990s, at the Fermi National Accelarator Laboratory, the Tevatron collaboration (CDF and D0) started to have the first possible evidences for an Higgs boson with a mass around 160 GeV, in proton-antiproton collisions.
The LHC era began in 2008 with the first beam injection. During the 2011 data-taking, after the observation of an excess for a mass around 140 GeV found both in the WW boson and diphoton decay channel, it was found that the SM Higgs mass should be in small window around 125 GeV. This was the first step towards what happened in 2012 with the announcement of the discovery.
Both ATLAS and CMS collaboration concentrate on two high mass resolution channels to measure the Higgs mass: ZZ and $\gamma\gamma$. The mass resolution in these two channels is from 1.4 GeV to 2.0 GeV for ATLAS and 1.0 GeV to 2.8 GeV for CMS.
Fig.1.10 summarise all the Higgs mass measurements performed in Run 1, with preliminary Run 2 results. It accounts both the diphoton and the 4ℓ lepton decay channels. All the Run 1 measurements and the combination between ATLAS and CMS brought to the result of

$$m_H = (125.09 \pm 0.24) GeV \tag{1.93}$$

1.2.4 Higgs Production Modes at LHC

The main production modes at LHC are (ordered in decreasing rate):

a. gluon fusion (ggF).

b. weak-boson fusion (*VBF*, mostly ud initial states).

c. associated production with a gauge boson (VH with $V = W, Z$).

d. associated production with a $t\bar{t}$ pair.

The corresponding diagrams for these processes at the Leading Order are shown in Fig.(1.11). Tab.(1.1) summarizes the Higgs production cross-section with respect to center of mass en-

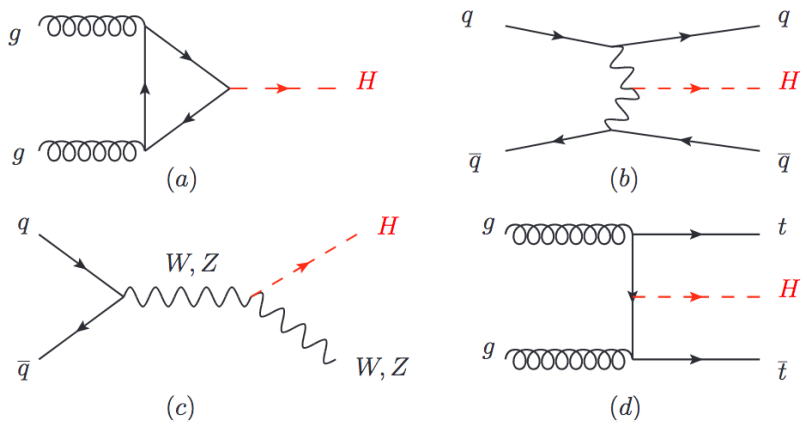

FIGURE 1.11: Leading order Feynmann diagrams for the main Higgs production modes at hadron colliders. (a) gluon fusion. (b) vector-boson fusion. (c) associated production with a gauge boson. (d) associated production with a a $t\bar{t}$ pair.

ergy $\sqrt{s}$, considering m_H=125 GeV at the LHC energy range. Fig.(1.12) shows the various

TABLE 1.1: The Standard Model predicted Higgs boson production cross section [pb] for m_H=125 GeV in pp collisions at 7, 8, 13 TeV. The prediction for the LHC energies are taken from [13], [14], [15], [16].

$\sqrt{s}$ [GeV]	ggF	VBF	WH	ZH	$t\bar{t}$	total
7	$16.9^{+5\%}_{-5\%}$	$1.24^{+2\%}_{-2\%}$	$0.58^{+3\%}_{-3\%}$	$0.34^{+4\%}_{-4\%}$	$0.09^{+8\%}_{-14\%}$	19.1
8	$21.4^{+5\%}_{-5\%}$	$1.60^{+2\%}_{-2\%}$	$0.70^{+3\%}_{-3\%}$	$0.42^{+5\%}_{-5\%}$	$0.13^{+8\%}_{-13\%}$	24.2
13	$48.6^{+5\%}_{-5\%}$	$3.78^{+2\%}_{-2\%}$	$1.37^{+2\%}_{-2\%}$	$0.88^{+5\%}_{-5\%}$	$0.50^{+9\%}_{-13\%}$	55.1
14	$54.7^{+5\%}_{-5\%}$	$4.28^{+2\%}_{-2\%}$	$1.51^{+2\%}_{-2\%}$	$0.90^{+5\%}_{-5\%}$	$0.60^{+9\%}_{-13\%}$	62.1

production cross section with the theoretical errors represented as bars [17].

Gluon-gluon Fusion (ggF)

At hadron colliders, the Higgs boson production mode with the highest cross section is the gluon-gluon fusion (ggF), as can be seen from the Fig.1.12. The process:

$$gg \rightarrow H + X \tag{1.94}$$

is mediated by the exchange of a virtual heavy top quark [18]. The contributions from lighter quarks are suppressed thanks to the mass dependency of the coupling of the fermions

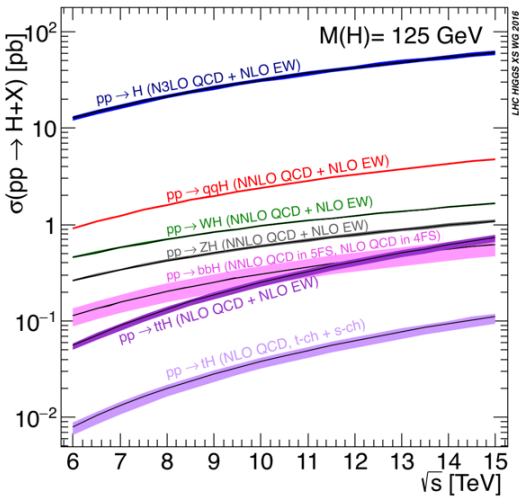

FIGURE 1.12: The Standard Model production cross section as a function of the center of mass energy.

with the Higgs field, see Eq.1.91. The cross section has been calculated to the next-to-leading order (NLO) in α_S, including the full dependence on the quark (top, bottom, charm) and Higgs boson masses [19]. The calculation of the cross section is known at NLO [20], NNLO [21] and N^{3}LO [22]. The LO and NLO QCD corrections amounts to about 80% of the total cross section calculated at N^{3}LO. The NNLO corrections enhance the cross section by approximately 30%

Vector Boson Fusion (VBF)

Vector Boson Fusion (VBF) is the process with the second largest cross section at LHC energy range. VBF process:

$$qq \rightarrow qqH \tag{1.95}$$

is the scattering of two quarks (or antiquarks) mediated by the exchange of a vector boson V(=W,Z), where the Higgs is radiated by the weak boson. Once scattered, the quark gives rise to a pair of hard jets in the forward and backward region of the detector. This particular feature of VBF, together with the strong suppression of the gluon emission in the central rapidity region, results in a clear signature in the final states, allowing the distinction from the overwhelming QCD background. The VBF scenario offers a clean search region not only for the search of Higgs boson but also the possibility to study the Higgs couplings. The VBF cross section has been calculated at the NNLO order of calculation with proper EW corrections [23].

WH and ZH associated production: *Higgs-Strahlung*

The third most relevant process is the associated production with a vector boson, W$^{\pm}$ and Z^0. It is also the main subject of this thesis and so far it will be described with more details in the following section and chapters.
The *Higgs-Strahlung* mechanism occurs when an Higgs boson is emitted through an *off-shell* vector boson.
Since this process in association with the $H \rightarrow b\bar{b}$ decay is the main core of this thesis, it will be treated in details in Sec.1.3.

$t\bar{t}H$ associated production

The associated production $t\bar{t}H$ pair allows to study the Yukawa coupling with the top quark. The cross section for this production mode has been calculated at LO with NLO QCD corrections [24], evaluated yielding an increase in the total cross section of 20%. The theoretical errors, estimated by combining all the main sources, amount to 10-15%. NLO calculation for $t\bar{t}H$ production with parton-shower Monte Carlo programs are provided in [25].

1.2.5 Higgs Decays

The understanding and interpretation of the Higgs decays allow us to study its coupling to many SM particles. The most relevant decay modes are $H \to b\bar{b}$, $H \to WW^*$, $H \to gg$, $H \to \tau^+\tau^-$ and $H \to c\bar{c}$, $H \to ZZ^*$, followed by the ones with smallest Branching Ratios (BR) $H \to \gamma\gamma$, $H \to \gamma Z$ and $H \to \mu^+\mu^-$ (the decay in electrons is highly suppressed). Decay to diphoton, gg and $Z\gamma$ are clearly loop-induced but provide anyway indirect information about the couplings to WW, ZZ and $t\bar{t}$. The different predicted BRs can be seen from Fig.1.13 and listed in the Tab.1.2, [15].

The partial widths at the leading order for the fermions are:

$$\Gamma(H \to ff) = \frac{G_F}{4\pi\sqrt{2}} m_f^2 m_H \left(1 - 4\frac{m_f^2}{m_H^2}\right)^{1/2} \tag{1.96}$$

$$\Gamma(H \to WW) = \frac{G_F}{8\pi\sqrt{2}} m_H^3 \left(1 - 4\frac{m_W^2}{m_H^2}\right)^2 \left(12\frac{m_W^4}{m_H^4} - \frac{m_W^2}{m_H^2} - 1\right) \tag{1.97}$$

$$\Gamma(H \to ZZ) = \frac{G_F}{16\pi\sqrt{2}} m_H^3 \left(1 - 4\frac{m_Z^2}{m_H^2}\right)^2 \left(12\frac{m_Z^4}{m_H^4} - \frac{m_Z^2}{m_H^2} - 1\right) \tag{1.98}$$

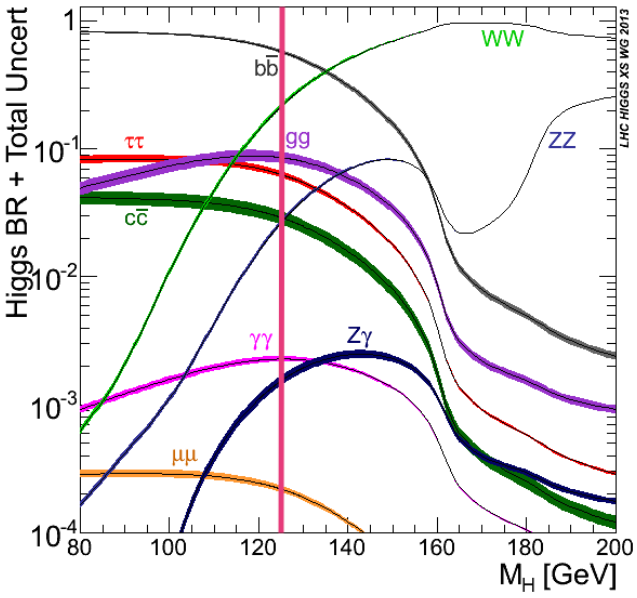

FIGURE 1.13: Branching Ratios for the main Higgs decay modes as a function of m_H. The magenta line points to the measured value of the Higgs mass.

TABLE 1.2: The predicted branching ratios and relative uncertainties for the decays of m_H = 125 GeV Standard Model Higgs.

Decay channel	Branching Ratio	Uncertainty
$H \to b\bar{b}$	5.84×10^{-1}	$^{+3.2\%}_{-3.3\%}$
$H \to W^+W^-$	2.14×10^{-1}	$^{+4.3\%}_{-4.2\%}$
$H \to \gamma\gamma$	2.27×10^{-3}	$^{+5.0\%}_{-4.9\%}$
$H \to \tau^+\tau^-$	6.27×10^{-2}	$^{+5.7\%}_{-4.7\%}$
$H \to c\bar{c}$	2.9×10^{-2}	$^{+12.2\%}_{-12.2\%}$
$H \to ZZ$	2.62×10^{-2}	$^{+4.3\%}_{-4.1\%}$
$H \to \gamma\gamma$	2.3×10^{-3}	$^{+9.0\%}_{-8.9\%}$
$H \to \gamma Z$	1.53×10^{-3}	$^{+5.0\%}_{-4.9\%}$
$H \to \mu^+\mu^-$	2.18×10^{-4}	$^{+6.0\%}_{-5.9\%}$

as can be seen, in the case of the fermions, it scales with m_f^2 meaning that heavier fermions are favored [26].
However, in the quark sector, it is necessary to consider an additional degree of freedom represented by the color charge. Eq.1.96 becomes:

$$\Gamma(H \to q\bar{q}) = \frac{3G_F}{4\pi\sqrt{2}} m_q^2 m_H \left(1 - 4\frac{m_f^2}{m_H^2}\right)^{3/2} \left[1 + \frac{4}{3}\frac{\alpha_S}{\pi}\Delta_H^{QCD}\right] \tag{1.99}$$

where m_q is the quark mass, Δ_H^{QCD} is the QCD correction and α_S is the strong coupling constant. In the limit $m_H >> m_q$, QCD corrections are not negligible. The decay width receives as many contributions which in the case of b quark decrease $H \to b\bar{b}$ decay width by more than 50%.

1.3 Higgs boson associated with a vector boson V and decaying in $b\bar{b}$

As can be seen for Tab.1.2 and from Fig.1.13, $H \to b\bar{b}$ has the largest branching ratio ($\sim$ 58%) for the Standard Model Higgs with m_H=125 GeV. The measurement of this decay is of great interest since it is important to prove the Yukawa coupling to the quark sector and to put constraints to the Higgs decaying width. The Higgs main production mode at LHC is via gluon-gluon fusion ggF:

$$gg \to H(H \to \bar{b}b) + X \tag{1.100}$$

However the sensitivity in the inclusive search for the Higgs boson with $H \to b\bar{b}$ is limited by the QCD overwhelming background from the inclusive production of $p\bar{p} \to b\bar{b} + X$.
The search for $H \to b\bar{b}$ has been performed in the VBF production mode. The signal is expected to be an enhancement in the two b-jet invariant mass distribution m_{bb} over the smoothly falling background distribution. Also in this case, the main difficulties come from the QCD induced background. The issue has been addressed by the requirement of an additional photon in the final state that reduces the background. The analyisis have been performed at ATLAS during Run1 [27], [28] and Run2 [29] and it is part of the combined result for $H \to b\bar{b}$ observation, as it will be seen in Chapter 5.
At LHC, the search for the decay of the Higgs boson to a pair of b-quark has the highest sensitivity in the associated WH and ZH production modes thanks to the leptonic decay of W and Z used for triggering and to purify signal and reject QCD background, see Fig.(1.14).

The Higgs boson candidates are reconstructed from exactly two b-tagged jets in the event.

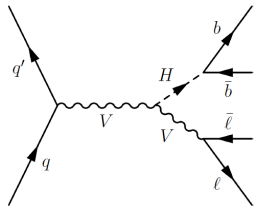

FIGURE 1.14: Feynmann Leading Order diagram of the VH production with the Higgs decaying in $b\bar{b}$.

At Tevatron, the vector boson associated production is the second in terms of largest rate and the $H \rightarrow b\bar{b}$ channel contributes the majority of the Higgs searches in the low mass range (m_H<130 GeV). The CDF and D0 have performed a combined analysis [30] in the mass range 115 GeV<m_H<140 GeV obtaining a significant excess of data events with respect to the background estimation. At m_H=125 GeV, the observed signal strenght (the ratio between Standard Model predicted and measured cross section) of μ=1.59$^{0.68}_{-0.72}$. Morever, the combination of the measurements enlightened that the excess is concentrated in the two b-quark decay channel, probing the presence of a low-mass Higgs boson, [1].

1.3.1 VH associated production

The search for a Higgs boson in the WH and ZH with the $H \rightarrow b\bar{b}$ is focused in a kinematic region where the Higgs and the vector boson are produced in association and are emitted at high p_T, i.e. in a topological configuration where they are back-to-back in the transverse plane and highly boosted. Fig.(1.15) shows the LO diagrams for the partonic process VH, with Fig.(1.15)c contributing just to ZH,.

The first consequence is that the intermediate virtual boson producing the Higgs and associated vector boson must be very massive and it will be produced centrally so that the kinematic acceptance of its decay products will be improved. The second consequence is the signal-to-background ratio significantly improved, reducing the impact of background uncertainties on the discovery significance.

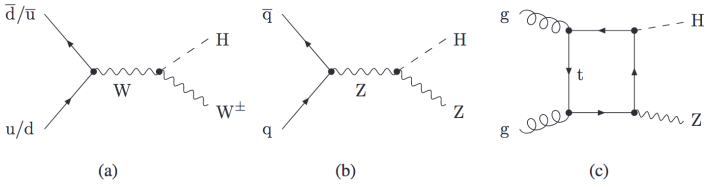

FIGURE 1.15: (a) and (b) LO diagrams for the partonic processes $pp \rightarrow VH(V = W, Z)$. (c) diagram contributes only contributes to $gg \rightarrow ZH$ channel.

A reliable prediction of the total cross section is fundamental to claim the observation of the $VH(H \rightarrow b\bar{b})$ channel. The inclusive partonic cross section can be written as:

$$\hat{\sigma}(\hat{s}) = \int_0^{\hat{s}} dk^2 \sigma\Big(V^*(k) - \frac{d\Gamma}{dk^2}(V^*(k) \rightarrow VH)\Big) + \Delta\sigma \qquad (1.101)$$

where $\sqrt{\hat{s}}$ is the partonic center of mass energy. The first term of the expression represents a virtual gauge boson V^* with momentum k produced in a Drell-Yan process, with then radiates a Higgs boson. The factor $\sigma(V^*)$ is the total cross section for producing the intermediate vector boson. The term $\Delta\sigma$ is referred to the other contributions (i.e., non Drell-Yan). The hadronic cross section is obtained convoluting Eq.1.101 with the parton density functions, [13].
The LO prediction from the process is derived from the Feynmann diagrams shown in Fig.1.15.
The QCD corrections are given to the Drell-Yan cross section $\hat{\sigma}(V^*)$ by NLO QCD corrections. For $V = W$, NNLO QCD correction are also applied to the intermediate boson. In the case of ZH, one has to consider the contribution from gluon-gluon fusion production mode which do not involve a virtual weak gauge boson. As can be seen from Fig.1.15c, both Z and H couple to the gluons via top-quark loop.
Also Electroweak correction at NLO are applied. It is important to note that they differ between the different leptonic decays.
The predicted cross section depends on the renormalization and factorization scales μ_R and μ_F which is set to $M_V + M_H$, [16].
The total Standard Model predicted cross section are listed below for $W^{\pm}H$ and for ZH, separated according to the possibile leptonic decays, see Tab.1.3.

TABLE 1.3: Total VH predicted cross sections at different center of mass energy. Different neutrino flavours contributions has been summed in $Z(\to)\nu\nu$. The percentage uncertainties are related to the scale variations.

	$\sqrt{s}[GeV]$	$W^+(\to \ell^+\nu)H$	$W^-(\to \ell^-\bar{\nu})H$	$Z(\to \nu\nu)H$	$Z(\to \ell^+\ell^-)H$
σ[fb]	7	$40.9^{+0.7\%}_{-0.8\%}$	$23.04^{+0.6\%}_{-0.8\%}$	$68.18^{+2.6\%}_{-2.4\%}$	$11.43^{+2.6\%}_{-2.4\%}$
σ[fb]	8	$49.52^{+0.8\%}_{-0.6\%}$	$23.62^{+0.6\%}_{-0.8\%}$	$84.56^{+2.9\%}_{-2.4\%}$	$14.18^{+2.6\%}_{-2.4\%}$
σ[fb]	13	$94.26^{+0.5\%}_{-0.7\%}$	$59.83^{+0.4\%}_{-0.7\%}$	$177.62^{+3.8\%}_{-3.1\%}$	$29.82^{+3.8\%}_{-3.3\%}$
σ[fb]	14	$103.36^{+0.3\%}_{-0.8\%}$	$66.49^{+0.5\%}_{-0.6\%}$	$198.12^{+3.8\%}_{-3.3\%}$	$33.27^{+3.8\%}_{-3.3\%}$

1.3.2 $VH(H \to b\bar{b})$

The main decays studied for the VH production are $H \to b\bar{b}$ and $H \to WW^*$. The former is the one of interest for this thesis and it is the dominant for the Standard Model Higgs. While, as it has been seen above, the vector bosons are reconstructed via their leptonic decays, the Higgs boson candidate is reconstructed from two tagged b-jets. A reliable and robust b-tagging strategy with high efficiency and low fake rate is crucial for an accurate estimate of the signal. The prescriptions and the strategy used in this analysis will be explained in Chapter 3 and 4.
As it regards the prediction of the $VH(H \to b\bar{b})$, the calculation of $H \to b\bar{b}$ is known at the NLO [16]. When including it, the predicted cross section at 13 TeV are for WH and ZH events:

$$\sigma^{NNLO\ \ QCD}(W^+H) = 24.18^{+0.36\%}_{-0.64\%} fb$$
$$\sigma^{NNLO\ \ QCD}(W^-H) = 15.87^{+0.26\%}_{-0.46\%} fb$$
$$\sigma^{NNLO\ \ QCD}(ZH) = 6.89^{+0.10\%}_{-0.16\%} fb$$

Differential predictions for the final state $ZH(\ell^1\ell^2)$ is presented below, since it will be the main focus of my studies. They are presented for different selection cut in the vector transverse momentum phase space. The red curve is the *inclusive* selection, while the other curves correspond to the following cuts:

- blue: 0 GeV < p_T^V < 150 GeV.
- green: 150 GeV < p_T^V < 250 GeV.
- magenta: p_T^V > 250 GeV.

The transverse momentum p_T of the Higgs boson candidate and the rapidity of the $b\bar{b}$ pair are shown in Fig.(1.16), while for the leading lepton of the vector boson decay are shown in Fig.(1.17).

It can be noted how the phase-space boundaries are damped due to the contribution of

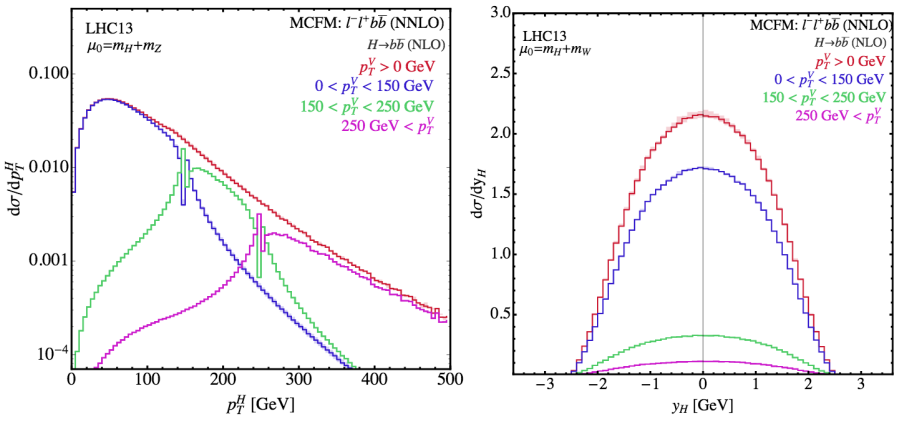

FIGURE 1.16: The transverse momentum and rapidity of the $b\bar{b}$ pair for ZH at the 13 TeV LHC.

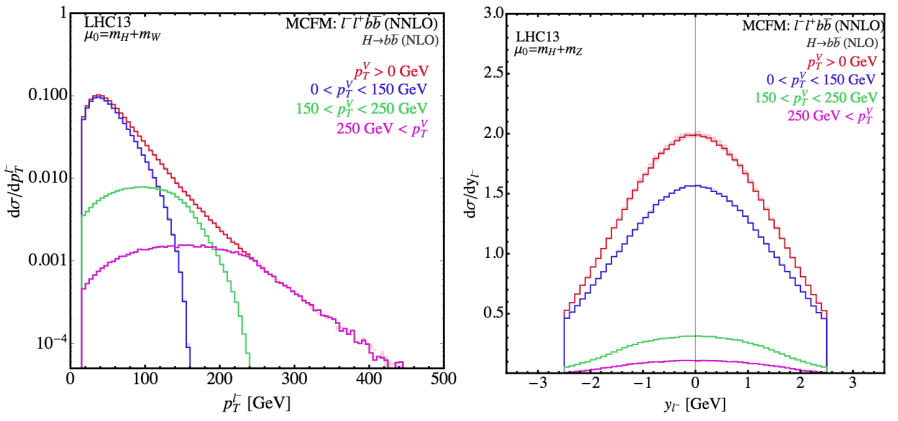

FIGURE 1.17: The lepton transverse momentum and rapidity for ZH at the 13 TeV LHC.

$gg \to ZH$. There is in particular an inflection in the Higgs transverse momentum around $p_T^H \approx m_t$, where the gluon-gluon fusion ZH production starts to become important.

Chapter 2

The LHC and the ATLAS Experiment at CERN

In 1954 the history of particle accelarators reached its climax with the foundation of the *Conseil Européen pour la Recherche Nucléare*, CERN, the largest subnuclear physics laboratory in the world.
It was May 1954 when the first shovel of earth was dug in the Meyrin site, closeby to Geneva: the choice of the host country was driven by the Swiss neutrality during the World Wars and by the central position of Switzerland in Europe.
Several facilities followed one another during the years: from the Proton Synchrotron (PS) to the Super Proton Synchrotron (SPS), with the discovery in 1983 of W and Z boson from proton-antiproton collisions.
In 1988, the 27 chilometers tunnel to host the Large Electron Positron (LEP) collider was completed: the facility started with an energy around 90 GeV (near to Z boson mass) to perform precision measurements for W and Z bosons. After that, the energy was increased to start the search for Higgs boson. However, it became soon evident that increasing the energy causes harsh energy losses due to synchrotron radiation. LEP was shut down and dismantled at the beginning of the new century in 2000 leaving place to the construction and installation of the Large Hadron Collider (LHC) in the same tunnel.

2.1 The Large Hadron Collider

The Large Hadron Collider is placed, as anticipated, in the ex-LEP circular tunnel at a depth ranging from 50 m to 175 m underground, at the Swiss-French border, see Fig.2.1. From the design energy, proton beams can reach 7 TeV energy resulting in a center of mass energy of $\sqrt{s}$=14 TeV. They travel in opposite directions in separate beam pipes, kept at ultra-high vacuum ($\sim 10^{-10}$ torr). Inside the tubes, the beams are deflected by a system of 1232 dipole electromagnets, built from coils of special electric cable, operating in superconducting state, inducing a medium magnetic field of 8.4 T. To ensure an efficient electricity conduction, the magnets are chilled to 1.9 K, via the connection of the accelerator system to a system which cools the magnets distributing liquid helium. A system of 392 quadripole magnet is used to keep under control the beam optics: in the usual data-taking, beams are *squeezed* to increase the chance to have a collision.
The parallel beams are allowed to collide in four main interaction points, where LHC experiments are placed. ATLAS (*A Toroidal LHC Apparatus*) and CMS (*Compact Muon Solenoid*) are the two multipurpose particle detectors, designed to search for heavy particles, especially the Higgs boson, and for Beyond Standard Model searches. LHCb is a dedicated experiment to study B mesons physics and CP violation. ALICE (*A Large Ion Collider Experiment*) exploits heavy ion collisions, during dedicated runs, to study the quark-gluon plasma. Three smaller experiments are present: TOTEM (*TOTal Elastic and diffractive cross section Measurements*, it

shares the interaction point with CMS and its physics program is mainly focused on total cross section, elastic and diffractive process measurements, as it will be seen in Appendix 6), LHCf (*Large Hadron Collider forward*, which uses the LHC beams to simulate and study high energy cosmic rays) and MoEDAL (*Monopole and Exotic Detector At LHC*, which shares the interaction point with LHCb and has as main purpose the study of the magnetic monopole).

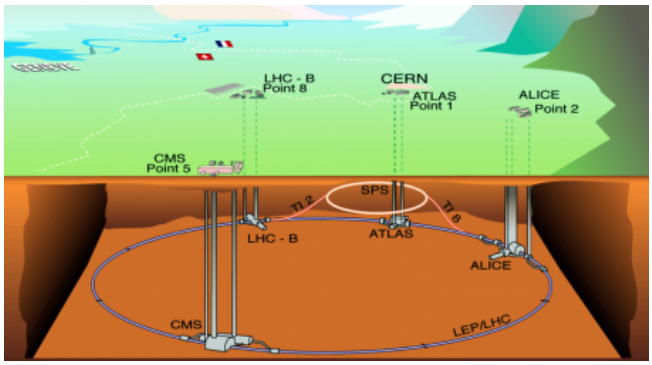

FIGURE 2.1: Pictorial view of the LHC complex at the Swiss-French border.

2.1.1 LHC Acceleration Chain

LHC is the final stage of a complex acceleration chain. Starting from its very beginning, proton source is a metal cylinder, called *Duoplasmatron*, filled with hydrogen gas, which is surrounded by an electric field used to strip hydrogen atoms from their electrons and eventually get protons. To leave the Duoplasmatron, particles are accelarated by a 90 kV supply and then they are sent to the first step of the chain by Radio-Frequency Quadrupole (QRF). Fig.2.2 shows the LHC injector complex (including the heavy ion route). The accelaration

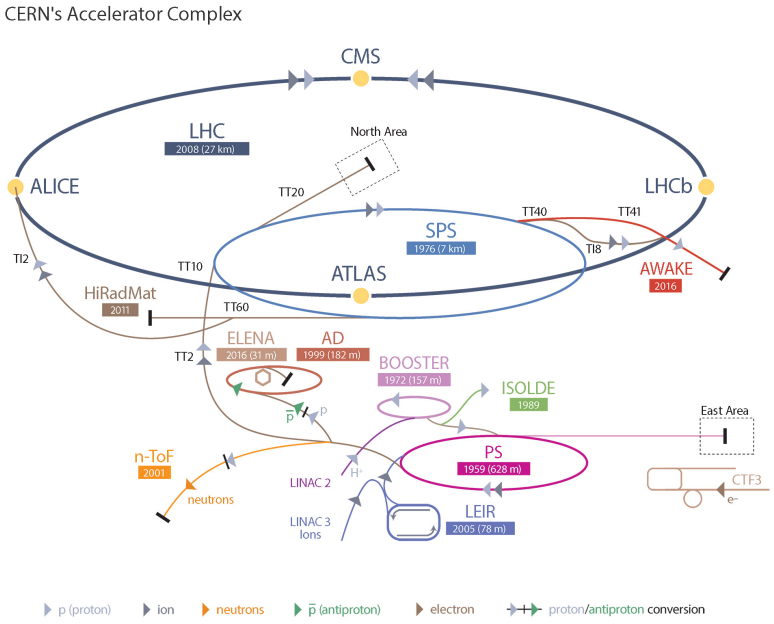

FIGURE 2.2: The LHC injector complex, including the heavy ion route.

follows different successive stages.

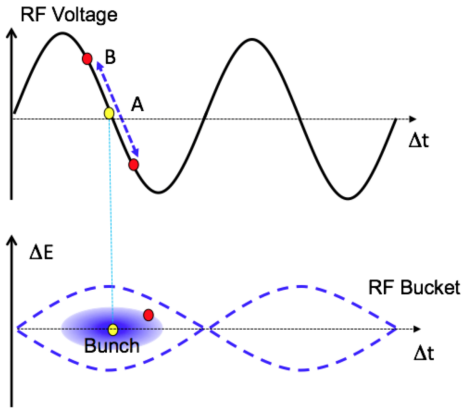

FIGURE 2.3: Scheme of the RF voltage (top) and the formation of RF buckets and bunches: A is the synchronous particle, B is the non-synchronous.

- LINAC2 is a linear accelerator for protons and ions. It accelerates beams up to an energy of 50 MeV and injects them in the following *ring of the chain* with a rate of 1 Hz.
- *Proton Synchrotron Booster* (PSB) is made of 4 superimposed rings. It accelerates the beam coming from LINAC2 to an energy of 1.4 GeV. The five bunches, circulating in each of the rings, are then sent through a magnet deflector into a single line for the injection to the next acceleration stage.
- *Proton Synchrotron* (PS) accelerates the protons up to an energy of 28 GeV.
- *Super Proton Synchrotron* (SPS) is the final injector that increases the energy from 28 GeV to 450 GeV.

Once they are injected in the LHC ring, particles are accelerated using a Radio Frequency (RF) system deployed in specially designed cavities. RFs are used to generate a longitudinal electric field and, at high energies, the passage to RF cavity induces a gain or a loss of energy, expressed as $\Delta E = q\Delta V$, with the effective gap voltage $\Delta V = V_0 sin(\omega_{RF} t + \phi)$, where ω_{RF} is the RF frequency, V_0 is the effective peak accelerating voltage and ϕ is the phase. The advantage to use RF cavities is that particles satisfy the *sychronization* requirement for the LHC energy regime. The particles always have to *see* the acceleration voltage so the number of RF cavities must be an integer multiple (h) of the revolution frequency to make them cross the electric field with a constant phase, i.e. experience a constant force.

$$f_{RF} = h \cdot f_{rev} \tag{2.1}$$

Eq.2.1 states that a particle with a speed β (in units of c) circulates in the accelarator with a period $T_{rev} = \frac{2\pi R}{\beta c}$ and a frequency $f_{rev} = \frac{\beta c}{2\pi R}$. At LHC, knowing that the RF frequency is 400.79 MHz, the revolution frequency f_{rev} is 11.245 kHz, the proton is relativistic with $v \sim c$ and the circumference is $2\pi R$ ∼26659 m, we have 35640 RF cavities. A particle exactly synchronized with the RF frequency is labelled as *synchronous particle* while the other ones oscillate longitudinally around her orbit, see Fig.2.3.

The effect of this behaviour makes the protons not spread uniformly around the accelerator, but "clumped" around the synchronous particle orbite: this is the so-called *bunch* of protons. In the nominal filling scheme of LHC Run2, the bunches are spaced by 25 ns which corresponds in terms of frequency to 40 MHz: the outcome is that, in a chain of 35640 RF-*buckets*, 3564 potential slots for a bunch of protons is available, each of them labelled with

a unique *bunch crossing identifier* (BCID).

2.2 LHC Status During Run 2

The LHC Run2 started in 2015 and it lasted until the last months of 2018. During 2018 August and early September, the integrated luminosity delivered to ATLAS and CMS reached 53.1 fb^{-1}, surpassing the 2017 value of 50 fb^{-1}.
Together with the available center of mass energy, luminosity is the second main figure of merit of any particle collider, since it quantifies its potentiality in providing a statistically significant sample of a class of events. It will be treated in details in Appendix A.
The instaneous luminosity $\mathscr{L}$ ([$cm^{-2}s^{-1}$]) reflects the instaneous performance of the collider. It is defined as the ratio of the rate R and of cross-section σ of a physical process: $\mathscr{L} = \frac{R}{\sigma}$. It decays exponentially, with a time constant at LHC of the order of hours.
The integrated luminosity is the instanteous luminosity integrated over a certain time interval, defined as the ratio between the total number of events N and the cross-section σ.
It is clear the importance of an accurate luminosity measurement from its relation with σ, since its related systematic uncertainty directly affects every cross section measurement. The ATLAS goal for Run2 has been to keep it at a 2% level, necessary to allow discrimination between Standard Model and Beyond Standard Model effects and to determine precisely the Higgs boson production cross-section.
Moreover, the high integrated luminosity recorded has allowed to count on a large data-set to study Higgs properties, such as its direct Yukawa coupling with the third sector quarks (the heaviest ones). Fig.2.4 shows the total integrated luminosity during Run2 as a function of time, [31]. Tab. 2.1 shows an overview of the LHC performance parameters luminosity

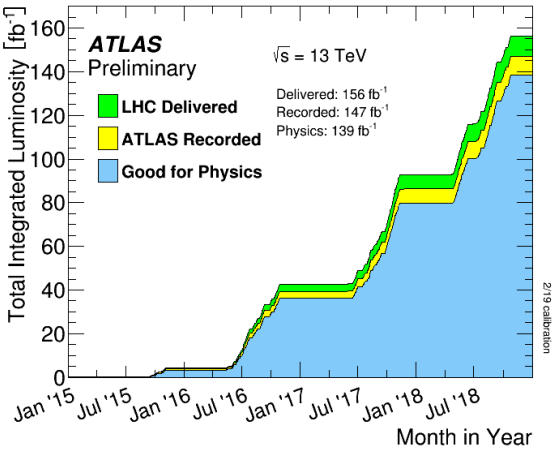

FIGURE 2.4: Total integrated luminosity versus time during Run2 during stable beams for pp collisions at 13 TeV in 2015-2018. Delivered luminosity (green) accounts the luminosity delivered from the start of stable beams until the LHC requests ATLAS to put detector in standby mode to allow beam dump and beam studies. Recorded luminosity (yellow) reflects the DAQ inefficiency and dead-time: when there is stable beam, tracking detectors undergo a ramp of the high-voltage. In blue, the Good for Physics data are shown: they have to respect good data quality requirements for all reconstructed objects.

related during whole Run2 data-taking, [32]. The total delivered integrated luminosity for

the full Run2 is 156 fb^{-1}.

TABLE 2.1: LHC performance parameters for pp collisions at $\sqrt{s}$ = 13 TeV for the whole Run2 data-taking (2015-2018), taking into account the best performances during normal operation. In 2017, LHC was operated in two modes: standard 25 ns with long trains and "8b4e" scheme with 8 bunches separated by 25 ns followed by four empty bunch slots. Values are listed for both.

Parameters	2015	2016	2017	2018
Maximum number of colliding bunch pairs	2232	2208	2544/1909	2545
Bunch spacing [ns]	25	25	25/8b4e	25
Bunch population [10^{11} protons]	1.1	1.1	1.1/1.2	1.1
β^*	0.8	0.4	0.3	0.3/0.25
Peak Luminosity $\mathscr{L}_{peak}$ [10^{33} cm^{-2}s^{-1}]	5	13	16	19
Peak number of inelastic interactions/crossing (<μ>)	~16	~41	~45/60	~55
Total delivered integrated luminosity [fb^{-1}]	4.0	38.5	50.2	63.4

2.3 The ATLAS Detector

The ATLAS detector is the largest volume detector ever built at a particle collider, with its 44 m length and 25 m height, with a 7000 tons weight. It sits in a cavern 100 m underground, [33]. Fig.2.5 shows the detector layout. ATLAS is forward-backward symmetric with respect to the interaction point. The nominal interaction point is defined as the origin of the coordinate system, while z-axis is the beam direction and xy-plane is transverse to the beam direction. The positive x-axis is defined as pointing from the interaction point to the centre of the LHC ring, while the positive y-axis points upwards. The volume is divided into a side-A corresponding to positive z-direction, and side-C corresponding to negative ones. The azimuthal angle ϕ is measured around the beam axis, while the polar angle θ is measured with respect to the beam axis. In Fig.2.6, the ATLAS right-handed coordinate system is depicted.

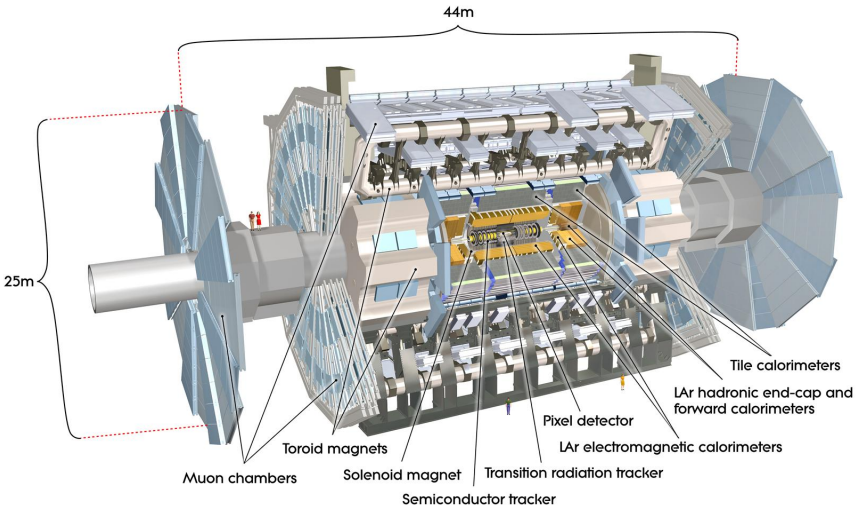

FIGURE 2.5: Sketch of the ATLAS detector.

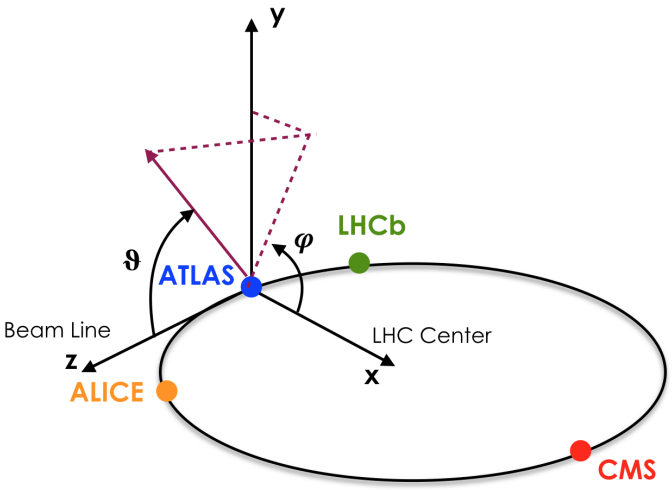

FIGURE 2.6: Skematization of the ATLAS coordinate system.

The trasverse momentum p_T (it is defined as $p_T = \sqrt{p_x^2 + p_y^2}$), the transverse energy E_T (i.e., the geometrical projection of the energy on its transverse component $E_T = E\sin\theta$) and the missing transverse energy E_T^{miss} are defined in the transverse plane. In case of non-negligible masses, the *rapidity* y is used:

$$y = \frac{1}{2} ln\left[\frac{(E + p_Z)}{(E - p_Z)}\right] \tag{2.2}$$

While in the relativisti case the *pseudorapidity* η is used:

$$\eta = -lntg\left(\frac{\theta}{2}\right) \tag{2.3}$$

In order to measure the angular separation a useful quantity to use is ΔR, the distance in the $\eta - \phi$ space:

$$\Delta R = \sqrt{(\Delta\eta)^2 + (\Delta\phi)^2} \tag{2.4}$$

The four major components of ATLAS are the Inner Detector, the Magnet and Calorimeter System and the Muon Spectrometer. Additional forward detectors are also present to measure the luminosity (LUCID), to perform elastic and diffractive physics measurements (ALFA and AFP) and to measure neutral particles (γ, n) in the forward direction (ZDC).
A thin superconducting solenoid surronds the Inner Detector cavity, while three large superconducting toroids (one barrel and two end-caps) are arranged around the calorimeters with an eight-fold azimuthal symmetry. This particular configuration has been the starting point for the development of the rest of the detector.
The Inner Detector, drowned in a 2 T solenoidal field, allows pattern recognition, momentum and vertex measurements and electron identification thanks to the combination of different technologies: high-resolution semiconductor pixel and strips in the core of the tracking volume and straw-tube for tracking generating and detecting transition radiation in the outer parts.
High granularity liquid-argon (LAr) electromagnetic sampling calorimeters cover the pseudorapidity range $|\eta|$<3.2, providing excellent performances in energy and position resolution. A scintillator-tile calorimeter covers the hadronic calorometry role in the range $|\eta|$<1.7. It is divided in large barrel with two smaller extended barrel cylinders at each side.

In the end-caps, LAr is exploited also as hadronic calorimeter and it extends the pseudorapidity coverage to $|\eta|$<4.9.
Muon Spectrometer surrounds the calorimeter system. The air-core *toroid system*, with its long barrel and the two end-cap magnets, causes a strong bending power in a large volume within a light and open structure. Multiple-scattering effects are minimised and three layers of high precision tracking chambers ensure an excellent muon momentum resolution. In addition, trigger chambers (timing resolution of the order of 1.5-4 ns) are included in the Muon System.

2.3.1 Physics Requirements

Before going through the complete description of the ATLAS detector components, it is important to underline the physics requirement at the roots of the choices for its realization. These requirements had been defined in late 90s to cover as much as possible all the new phenomena accessible for observation at the TeV scale, [33]. Indeed, high luminosity and increased cross-sections enable high precision tests on QCD, electroweak interactions and flavour physics, together with the possibility to explore Beyond Standard Model theories.
In particular, the search for the Standard Model Higgs boson has been used as a benchmark to estabilish the performance of all the sub-systems of ATLAS. As said in the prevoius chapter, there is a range of production and decay mechanisms, depending on the mass of the Higgs boson, which is not predicted by the theory but left as a free parameter.
Besides the advantages derived from the high LHC luminosity and the consequent interaction large rates (fundamental for processes characterized by small cross-section), the inelastic proton-proton collision at such a high-energy regime causes difficulties in the detection, mainly because QCD jet production dominate over the rare events, requiring specific identification methods of their typical signatures.
Further demands on the integrated luminosity and on the particle-identification have been imposed and then converted into a set of general requirements to follow:

- Due to the experimental conditions at LHC, detectors require fast, radiation-hard electronics and sensor elements. In addition, high detector granularity is needed to handle the particle fluxes and to reduce the influence of overlapping events.
- Large acceptance in pseudorapidity with an almost full azimuthal angle coverage.
- Good charged-particle momentum resolution and reconstruction efficiency in the inner tracker.
- Good resolution on the secondary vertex is essential for offline tagging of τ-leptons and b-jets
- Very good electromagnetic calorimetry for electron and photon identification and measurements together with the full-coverage hadronic calorimetry to ensure an accurate jet and missing transverse energy measurements related to undetected neutrinos. This is a very fundamental part for the measurements regarding rare events.
- Good muon identification and momentum resolution over a wide range of momenta. In addition, it is also needed the ability to determine unambiguosly the charge of high p_T muons.
- High efficient triggering on low p_T objects with sufficient background rejection is essential to have a trigger rate suitable for the physics processes of interest.

Tab.2.2 summarizes the performance goal of the ATLAS subsystem.

TABLE 2.2: General performance goals of the ATLAS detector. p_T and E are in GeV [33].

Detector Component	Required Resolution	η coverage Measurement	η coverage Trigger
Tracking	σ_{p_T}/p_T = 0.05%$p_T \oplus$1%	$\pm$ 2.5	
EM calorimetry	σ_E/E = 10%$\sqrt{E}\oplus$0.7%	$\pm$ 3.2	$\pm$ 2.5
Hadronic calorimetry (jets) barrel and end-cap forward	σ_E/E = 50%$\sqrt{E}\oplus$3% σ_E/E = 100%$\sqrt{E}\oplus$10%	$\pm$ 3.2 $\pm$ 3.1<$\lvert\eta\rvert$<4.9	$\pm$ 3.2 $\pm$ 3.1<$\lvert\eta\rvert$<4.9
Muon Spectrometer	σ_{p_T}/p_T = 10% at p_T=1 TeV	$\pm$2.7	$\pm$2.4

2.3.2 Inner Detector

The Inner Detector (ID) is the first part of ATLAS to see decay products of collisions [34]. Due to the large track density ($\sim$1000 particles every 25 ns in pseudorapidity range of $|\eta|$<2.5), a fine detector granularity is needed to ensure a precise momentum and vertex resolution. As can be seen from Fig.2.7, it is composed of *Insertable B-layer* (IBL), pixel system, *Silicon Conductor Tracker* (SCT) and *Transition Radiation Tracker* (TRT). The IBL has been added in 2015. The ID is 5.3 m long with a diameter of 2.5 m. In the barrel region it is arranged in concentric cylinders around the beam axis while in the end-cap regions sensors are located on disks perpendicular to the beam axis.

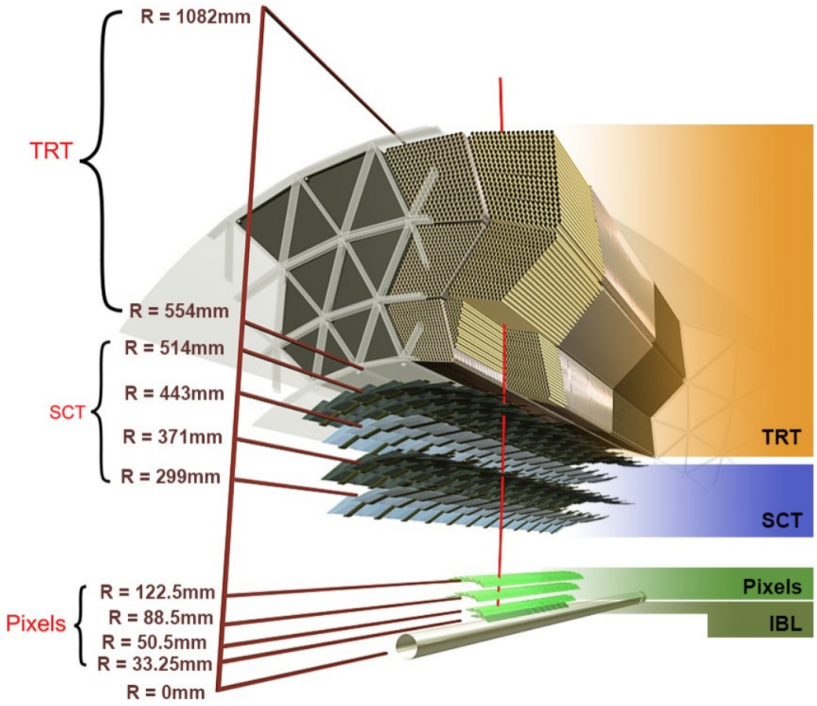

FIGURE 2.7: Sketch of the ATLAS Inner Detector with all its components, including IBL.

The Pixel Detector and the Silicon Conductor Tracker

Pixels and SCT are the precision tracking detectors and they cover the region $|\eta|$<2.5. Both exploit the silicon semiconductor technology but with different configuration.
The Silicon Pixel Detector allow to achieve the highest granularity around the vertex. It

consists in 1744 modules arranged in three barrel layers (approximately 67 millions of pixels) and three end-cap disks on each side (13 millions of pixels). The layers are segmented in R-ϕ and z and typically three of them are crossed by each track. All the sensors are identical, with a minimum size of (R-ϕ)$\times z$ of 50$\times$400 μm^2. The full system covers an area of 1.7 m^2. The intrinsic precision is of 10 μm for (R-ϕ) plane and 115 μm for z coordinate, both in the barrel and end-cap. Fig.2.8 shows the pixel detector in all its macro-components.
The SCT system is placed in the intermediate radial range to provide eight precision mea-

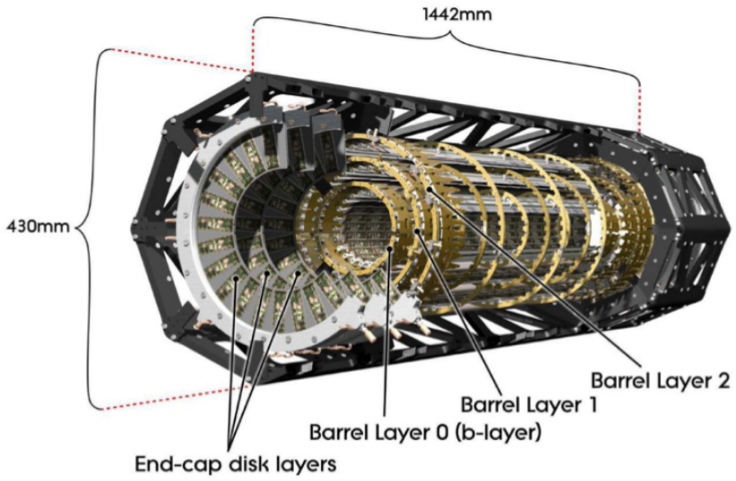

FIGURE 2.8: Sketch of the ATLAS pixel detector

surements for momentum, impact parameter and vertex position: eight strip layers are crossed by a particle. In the barrel region, SCT layers provide precision point in the in R-ϕ and z coordinates, using small angle stereo strips for both. They consist of two 6.4 cm long daisy-chained sensors with a strip pitch of 80 μm. In the end-cap region, the detector is arranged in a set of strips radially disposed and in a set of stereo strips at angle of 40 μrad. SCT has approximately 6.3 million of readout channels. Fig.2.9 shows the position of the barrel and end-cap SCT component. The intrisic precision per module is 17μm in the (R-ϕ) plane and 580 μm in z-coordinate, both for barrel and end-cap.
The radiation length for both the detectors is 0.1 X_0 at η=0.

The Transition Radiation Tracker

The TRT is the outermost component of the ATLAS ID. It consists in an hybrid detector: it is both a tracker thanks to the straw tubes which is made of and a Transition Radiation detector. The latter allows to distinguish a light and heavy particle thanks to the difference in the light emitted when they cross layers with different refractive index. Each component is made of straw tubes of Polymide drift tubes with 4 mm diameter. The barrel contains a 50000 straw tubes (with a maximum length of 144 cm). The end-caps contains 320000 radial straws, arranged in wheels, see Fig.2.9. The total number of read-out channels is 420000. Between the straw and the wire there is a gap filled with a gas mixture (70%Xe, 27%CO_2 and 3% O_2). A ionizing particle induces a low amplitude signal, while other particles crossing straws cause transition radiation emission absorbed by the Xenon inducing an high amplitude signal. Each TRT read-out channel has two independent thresholds which allow the detector to discriminate between tracking hits (lower threshold) and transition radiation

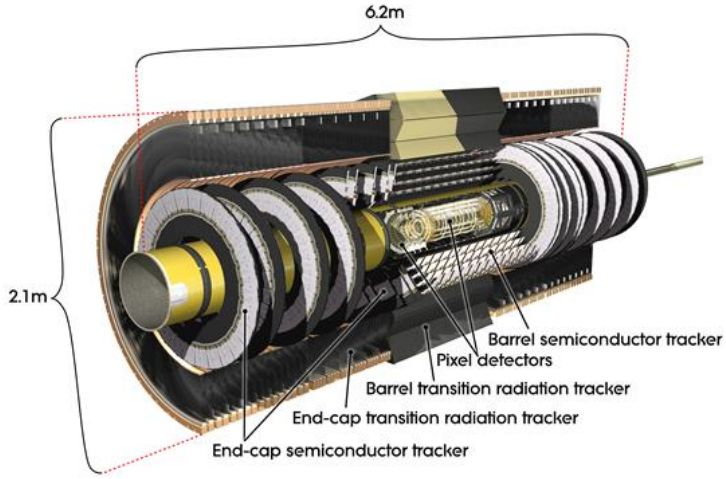

FIGURE 2.9: View of the ATLAS inner detector (no IBL) with SCT and TRT component enlightened.

hits (higher threshold). Tipically TRT provides 36 hits per track in the straw tubes covering a pseudorapidity range of $|\eta|$<2.0. TRT provides only R-ϕ information, with an intrinsic precision of 130 μm per tube. The radiation length is 0.2 X_0 at η=0.

Insertable B-Layer

The Insertable B-Layer (IBL) is the last and innermost part of the ATLAS ID to have been installed. Built during the first long shut-down, it was operated for the first time in 2015 at the beginning of LHC Run 2 [35]. A skematic view of the IBL is shown in Fig.2.10. It is positioned between the new Beryllium beam pipe and the B-Layer, the innermost part of existent pixel detector.

It consists in a barrel layer of 14 staves. The average radial distance of the sensitive area

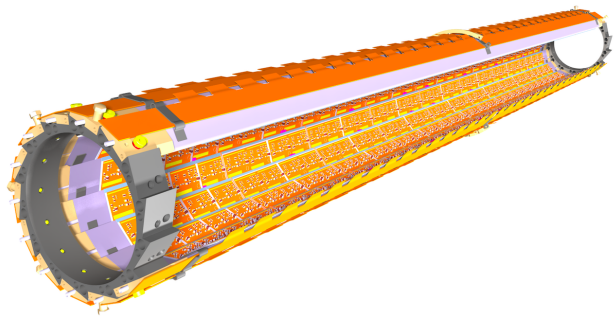

FIGURE 2.10: Skematic view of the Insertable B-Layer.

from the beam pipe is 33 mm, while its total envolope has a radius between 31-40 mm. 16 or 32 modules (depending on their size) are equipped on each module. In the first case, each module consist of 2 front-end chips on one common sensor tile, while in the second case each module is made of one front-end chip connected to a single sensor tile. The staves are tilted by 14^o degrees to ensure a full coverage in ϕ for high p_T tracks. However, its small radius limits the sensors at an angle between 0 and 27^o with respect to the radial direction. IBL is radiation harder than the pre-existent B-Layer and its small pixels (50$\times$250 μm^2) lower the occupancy in high-luminosity regime. The radiation length at η=0 is 1.43% of X_0. There are many reason which explains the need for its construction and installation.

Failures in the pre-existent B-layer and in other parts of the inner detector, whose inneficiencies cannot be compensated by reconstruction, are compensated by IBL, avoiding deterioration in impact parameter reconstruction, which directly affects the b-tagging: IBL is able to completely restore the full b-tagging efficiency even in case of complete B-layer failure. With the high-luminosity expected for the High Luminosity LHC (HL-LHC), event pile-up will increase leading to read-out inefficiencies due to the higher occupancy, since the current pixel detector was designed for a maximum peak luminosity of 10^{34} cm^{-2}s^{-1}. Since redundancy in track measurement with the increase of pile-up is necessary to keep fake rate under control, IBL is fundamental because helps to save the b-tagging efficiencies preserving from failures of B-layer, affected more than other layers by pile-up effects. Moreover, its closeness to the interaction point improves vertexing and b-tagging performance: this is crucial for reconstruction of the Higgs candidate in the channel VH(H$\rightarrow b\bar{b}$), as it will be explained in Chapter 3.

2.3.3 Magnet System

An efficient magnet system is fundamental to ensure enough bending power and good performance in track reconstrunction and momentum measuerements. Four large superconducting magnets make up the ATLAS magnet system, with 22 m diameter, 26 m lenght and 1.6 GJ of stored energy [36]. The spatial arrangement of the coils is shown in Fig.2.11. It pro-

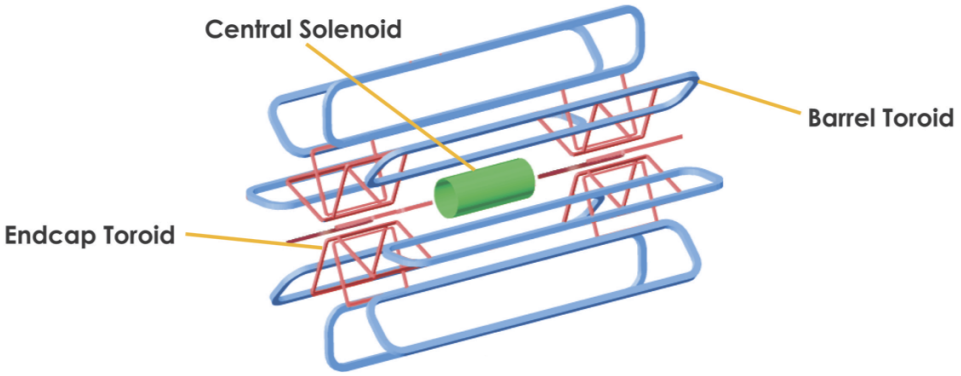

FIGURE 2.11: ATLAS magnet system.

vides magnetic field over a volume of approximately 12000 m^3, which is the region where the field exceeds 50 mT. The whole system consists in:

- a solenoid aligned to the beam axis and providing a 2 T axial magnetic field to the inner detector.
- a barrel toroid and two end-caps toroids which provide toroidal magnetic fields o 4 T for the muon detectors in the central and end-cap regions.

The central solenoid consists in one coil with a Al-stabilized NbTi conductor with 5.3 m length and 2.5 m diameter. At the nominal current of 7.730 kA, the magnetic field in the center is 1.998 T. The layout was carefully optimised to keep the material thickness of the calorimeter as low as possible, to achieve the desired performance. This results in the solenoid assembly contributin a total of 0.66 radiation lengths at normal incidence.
The barrel toroid consists in eigth coils with Al-stabilizedNbTi/Cu conductor in their own vacuum vessel, with 25.3 m length and an inner diameter of 9.4 m and outer of 20.1 m. Each of the two end-cap toroids is made of eight coils. They are 5 m long, with an inner diameter

of 1.65 m and outer of 10.7 m. All the toroid structure has been designed to minimize the uncertainty on the momentum measurements due to the multiple scattering. Barrel toroid covers the region $|\eta|$<1, while the end-caps toroids cover 1<$|\eta|$<2.7. The magnetic field significantly drops at $|\eta|$=1.5 which is the so-called *transition region*: here the bending power is ensured by the combination of barrel and end-cap fields.

2.3.4 Calorimetry System

ATLAS calorimeters cover the pseudorapidity range of $|\eta|$<4.9. The aim is to provide good containment of electromagnetic and hadronic showers and provide precision on energy and position measurements. ATLAS has both electromagnetic and hadronic calorimeters [37]. An important characteristics is the choice of their depth to contain showering of the particles. The total thickness of the EM calorimeter is more than 22 radiation lenghts in the barrel and more than 24 X_0 in the end-caps. The approximate 9.7 interaction lenghts λ of the Hadronic Calorimeter in the barrel (10 λ in the end-cap) in the end-caps ensure good resolution for high-energy jets. Furthermore, the total thickness, including 1.3 λ of the outer support, λ = 11 at η=0 allows good precision in E_T^{miss} measurements, which is important for many physics signatures involving neutrinos.
Both calorimeters use *sampling* tecniques, meaning that layers of passive and active material are arranged alternately. Particles cross a passive material (*absorber*) with high interaction cross-section which force them to shower *electromagnetically* or *hadronically* and the product particles are then detected in the active material.
Fig.2.12 shows the ATLAS calorimeter system.

Three cryostat host the calorimeters closest to the beam-line: electromagnetic barrel

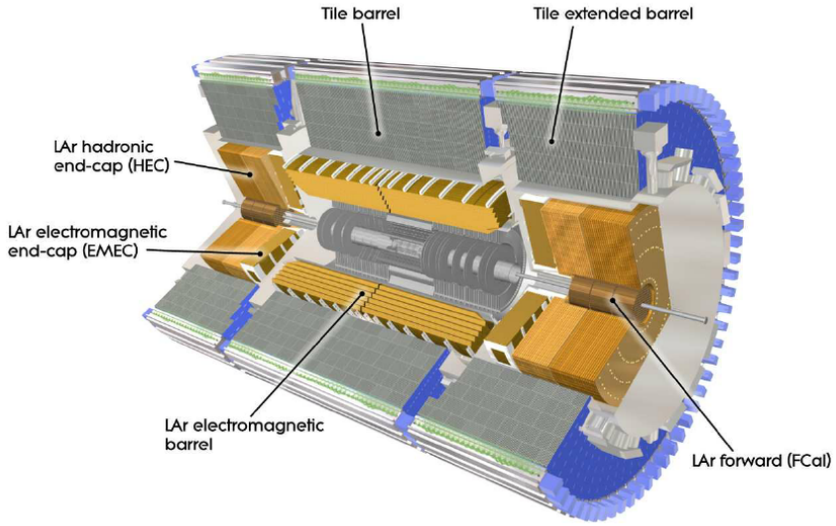

FIGURE 2.12: Cut away of the ATLAS calorimetry.

calorimeter and two electromagnetic end-caps calorimeters (EMEC). The end-caps cryostat contains also two end-cap hadronic calorimeters (HEC), placed near the EMECs, and a forward calorimeter (FCal) to cover the very forward region, the closest one to the beam line. All this elements are part of the complex of the Liquid Argon (LAr) calorimeter. Liquid Argon is the active detector medium, chosen for its intrinsic linear behaviour, stability response over time and intrinsic radiation hardness. Besides LAr, which acts both as electromagnetic and hadronic calorimeter, there is the Tile calorimeter, the purely ATLAS hadronic barrel calorimeter, which exploits scintillating tiles.

The Electromagnetic Calorimeter

LAr electromagnetic calorimeter uses liquid argon as active medium and lead as passive absorber, where the layers are disposed following an accordion geometry [38]. Such a choice provides the full coverage in ϕ and the fast extraction of the signal. As already anticipated, EM calorimeter is divided into a barrel and two end-caps components, covering, $|\eta|$<1.475 and 1.375<$|\eta|$<3.2, respectively. While the barrel is divided in two by a gap of 6 mm at z=0, the end-caps are divided in two coaxial wheels: an outer, covering 1.375<$|\eta|$<2.5 and an inner covering 2.5<$|\eta|$<3.2. The total thickness of the EM calorimeter is larger than 24 X_0 in the barrel and larger than 26 X_0 in the end-caps. Fig.2.13 shows the calorimeter segmentation in three longitudinal sections which allows high-granularity, especially in the pseudorapidity region $|\eta|$<2.5, of highest interest in many ATLAS analysis. The first section uses narrow

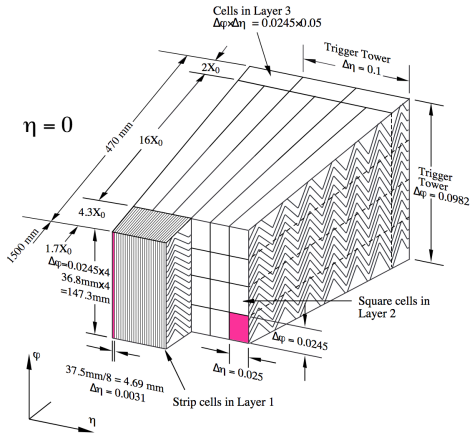

FIGURE 2.13: Sketch of a barrel module with different layers clearly visible. The η and ϕ granularity of the three layers cells is shown.

cells (5mm in the η direction) for particle identification and for highly precise angular measurements. The middle section is made of $\Delta\eta \times \Delta\phi$ = 0.025 $\times$ 0.025 square towers and its is used for measurement of released energy. The last section is characterized by a granularity of 0.05 in η and a thickness varying between $2X_0$ and $16X_0$. It measures the energy of those particles which have not been stopped in the previous segments, allowing the distinction between electromagnetic and hadronic showers because the majority of electrons and photons are stopped in the middle region.
The pseudorapidity range 1.375<$|\eta|$<1.52 is the transition region between barrel and end-caps where significant losses in energy and performance occurs: this is why in most of the analysis selecting photons and electrons it is discarded.
The energy resolution of LAr achieved for photons of 100 GeV, independently from η, is found to be 1.5%, considering that:

$$\frac{\Delta E}{E} = \frac{10\%}{\sqrt{E}} \oplus 0.1\% \tag{2.5}$$

The LAr readout system is composed by preamplifiers outside the cryostats, shapers, analog pipelines and an ADC system. The electrodes for readout are located in the gaps between the lead absorbers and consist of three conductive copper layers separated by polymide sheets. The two outer layers are at the high-voltage potential and the innser one is used for reading out the signal via capacitive coupling. Each barrel and end-cap between two absorbers is equipped with two electrodes.

The Hadronic Calorimeter

Tile Calorimeter (TileCal) is the purely hadronic calorimeter of the ATLAS detector [39]. It is placed in the barrel region, directly outside LAr. It is made of iron plates used as passive medium, while scintillating layers act as active material, covering the region $|\eta|$<1, divided into barrel ($|\eta|$<1) and extended barrel (1<$|\eta|$<1.7). The two macro-component are divided into 64 modules. In depth, TileCal is segmented in three layers, corresponding to 1.5, 4.1 and 1.8 interaction lengths for the barrel and 1.5, 2.6 and 3.3 for the extended barrel. The total thickness of the detector in terms of interaction length is 9.7 λ at η=0, at the outer edge of the tile-instrumented region. Photomultipliers are used for the read-out. The energy resolution of TileCal is:

$$\frac{\Delta E}{E} = \frac{50\%}{\sqrt{E}} \oplus 2.5\% \oplus \frac{5\%}{E} \tag{2.6}$$

in units of GeV.
The hadronic end-cap calorimeter (HEC) covers the region 1.5<$|\eta|$<3.2 and consists of two wheels per side, located in the same cryostat of the EMEC. Each wheel has 32 identical wedge-shaped modules and segmented in depth with a total of four layers per end-cap. Parallel copper plates are the passive medium, of 25 mm deep for the closest wheels, 50 mm for the further. Between copper plates, 8.5 mm gaps filled with LAr serve as active material.

Forward Calorimeter

The Forward Calorimeter (FCal) is both electromagnetic and hadronic. Its depth is approximately 10 λ and it is contained in the same cryostat as EMEC and HEC. It covers the region 3.1<$|\eta|$<4.9. Of the three modules constituting it, one is optimized for electromagnetic measurement, using copper as passive material, and two for hadronic measurements, exploiting tungsten. LAr is the active material.

2.3.5 Muon Spectrometer

The choice to put the Muon Spectrometer (MS) in the outer region of the ATLAS detector has been driven by the nature itself of the particle it has to detect [40]. Muons travel much more than any other charged particle in the ATLAS volume because they hardly interact with materials. They undergo *bremmstrahlung* less than electron and they have a lifetime of 2.2 μs. So far, since we expect the other particles to be *trapped* by the calorimeters, muons can be reconstructed from the combined information from ID and MS.
Fig.2.14 shows a section of the MS, with also barrel and end-cap toroids enlightened. All the system is based on the magnetic deflection due to the toroidal fields. MS has an outer diameter of 22 m and it is composed by trigger and precision chambers. The chambers in the barrel are arranged in three concentric cylindrical shells around the beam axis: inner station at a radius 5 m, middlestation at 7.5 m and outer station at 10 m. In the end-cap region, large wheels are located at a distance from the interaction point of z=7.4 m, z=10.8 m, z=14 m and z=21.5 m, perpendicularly to z-axis.
The subdetectors of the muon spectrometer are grouped into:

- Trigger Chambers: providing fast-response for online trigger and high granularity
- Precision Chambers: providing precise momentum measurements

Trigger Chambers

The Trigger Chambers are fast muon momentum measurement detectors [41], with two components:

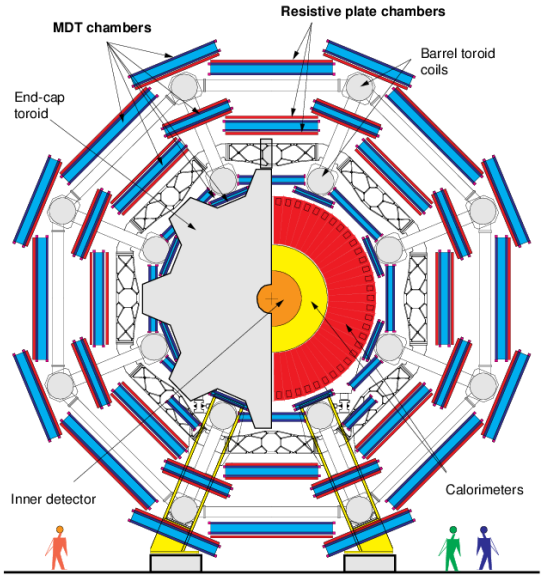

FIGURE 2.14: Cross view of the Muon Spectrometer.

- Resistive Plate Chambers (RPC) covering the range $|\eta|$<1.05
- Thin Gap Chambers (TGC) covering the range 1.05$|\eta|$<2.4

The trigger chambers serve to provide bunch-crossing identification, signal above a defined p_T threshold and to provide muon coordinate ortogonally to the precision chambers.
In the RPCs, crossing muon produce primary ionization electrons crossing in a gas mixture of 97% tetrafluoroethane ($C_2H_2F_4$)and 3% isobutane (C_4H_{10}). Electrons are multiplied by a 4.5 kV/mm electric field. They are detected by three layers (two in the middle, one in outer barrel station), which provide information on η and ϕ coordinates.
The TGC are installed in the end-cap region. They are thin multi-wire proportional chambers, filled with a highly quenching gas: 55% CO_2 and 45%n-pentane (n-C_5H_{12}). The anode-cathode spacing is smaller than the anode-anode spacing allowing short drift time. The geometry and the choice of the gas allow to work in quasi-saturation mode. Their precision is 4mm in the radial direction and 5 mm in the ϕ coordinate. In Fig.2.15, the trigger efficiency as a function of the reconstructed muon p_T is shown for the different years of the Run2 data taking. The efficiency has been stable over the years. The slight degradation of the plateau is due to the increase number of disable detector due to a high-voltage problem [42].

Precision Chambers

They measure the muon trajectory and they are composed by:

- Monitored Drift Tubes (MDT)
- Cathod Strip Chambers (CSC)

MDT chambers measure only the z-coordinate in barrel and end-cap region, with a coverage of $|\eta|$<2 [43]. They consist in multi-layer (3 or 4) drift tubes (30 mm diameter) and aluminum walls, filled with a gaseous mixture of argon and carbon dioxide, at 3 bar. The full muon trajectory is reconstructed by measuring muon momentum in the region 2<$|\eta|$<2.7, with a spacial revolution of 80 μm.
The CSC are multi-wire chambers measuring muon momentum in the same region, exploiting strip cathodes. The wires are made of parallel anodes perpendicular to strips of opposite

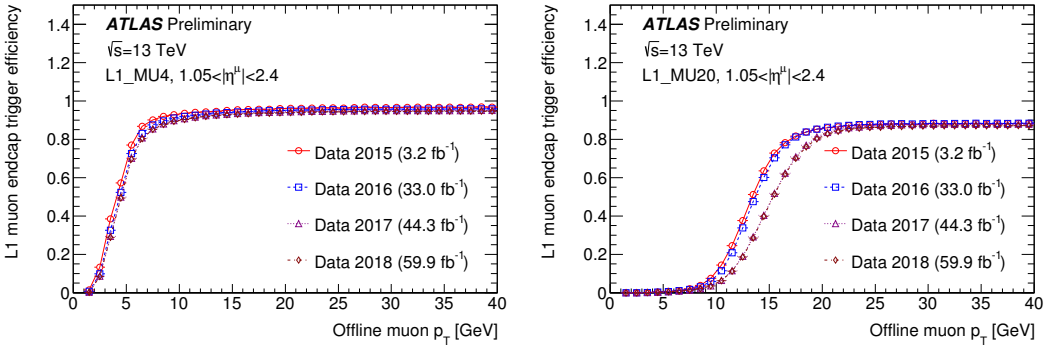

FIGURE 2.15: The trigger efficiencies of Level-1 single muon trigger for a threshold of 4 GeV (left) and 20 GeV (right) as a function of the transverse momentum of the reconstructed muon in the end-cap region, 1.05<$|\eta|$<2.4, for different years in Run2. The efficiency of the L1 muon trigger has been stable through the Run2.

polarity. Anode-cathode distance equals the one between anode wires, 2.5 mm. The time resolution is 7 ns, while the spacial is 60 μm in the ϕ direction and 1cm in η.

2.3.6 Forward Detectors

ATLAS is also equipped with LUCID, ZDC, ALFA and AFP detectors, which partially covers the forward rapidity region [44]. Their position with respect to the interaction point is sketched in Fig.2.16.

The total proton-proton cross-section σ_{tot} is a contribution elastic and inelastic cross-

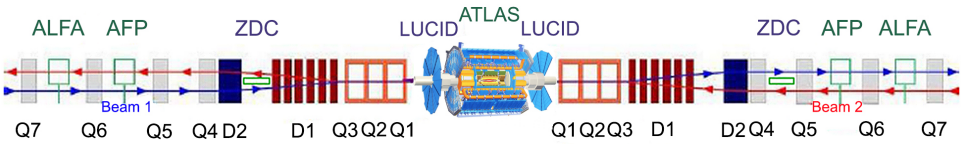

FIGURE 2.16: ATLAS Forward Detector Complex [45].

sections [46]. At LHC energies, σ_{el} contributes to 20% of σ_{tot}. The remaining 80% is due to inelastic contribution including Single Diffractive dissociations (SD), Double Diffractive dissociations (DD) , Central Diffractive production (CD) and non-diffractive processes.
In this sense, the importance to have a forward apparatus can be understood looking at the two plots in Fig.2.17. It can be seen, looking at the left plot, that about 40% of the parti-

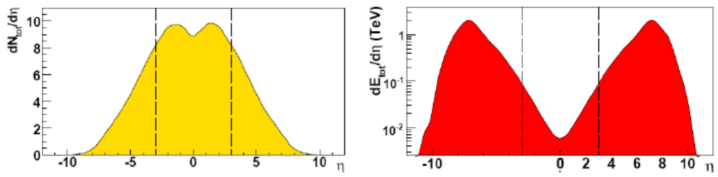

FIGURE 2.17: On the left particle flow, on the right energy flow as a function of pseudorapidity as obtained by DPMJET [47] for pp interactions at $\sqrt{s}$=14 TeV.

cles are produced outside the ATLAS central acceptance, while from the right one, we can conclude that the energy released there is a tiny fraction with respect to the total. Fig.2.18

shows the topology of elastic and diffractive events in the LHC pseudorapidity range.
The forward calorimeter coverage of $|\eta|$<4.9 does not allow to access to diffractive system

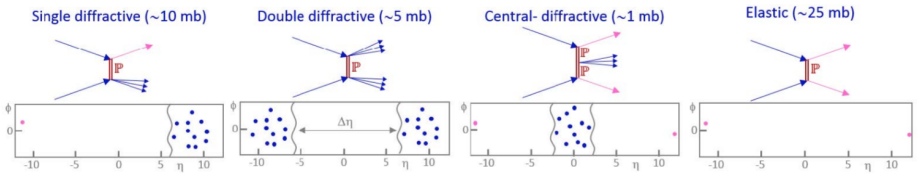

FIGURE 2.18: Topology in the central and forward detectors of each diffractive event class (azimuthal angle ϕ vs. pseudorapidity η). Pink dots represent diffractively scattered protons, while blue dots are the products of the diffractive interactions.

mass less than 10 GeV. The indirect measurement of ξ (i.e., the fractional longitudinal momentum loss of the protons) via the energy detected in the calorimeter is not precise due to invisible energy and it is available obly in limited ξ regions. Morever, the measurement of the transferred momentum t of the proton is not available in the central detector. The *proton tagging* is the only way out for a detailed probing of diffractioon. A study of the cross section as a function of the size of the rapidity gap as measured by the ATLAS central detector has been performed [48]. The forward rapidity gaps (Δ_η^F) are defined as forward rapidity gap region on detector edge devoid of particles having transverse momentum p_T>200 GeV. In Fig.2.19, the differential cross sections as a function of the size of the gap size are shown.

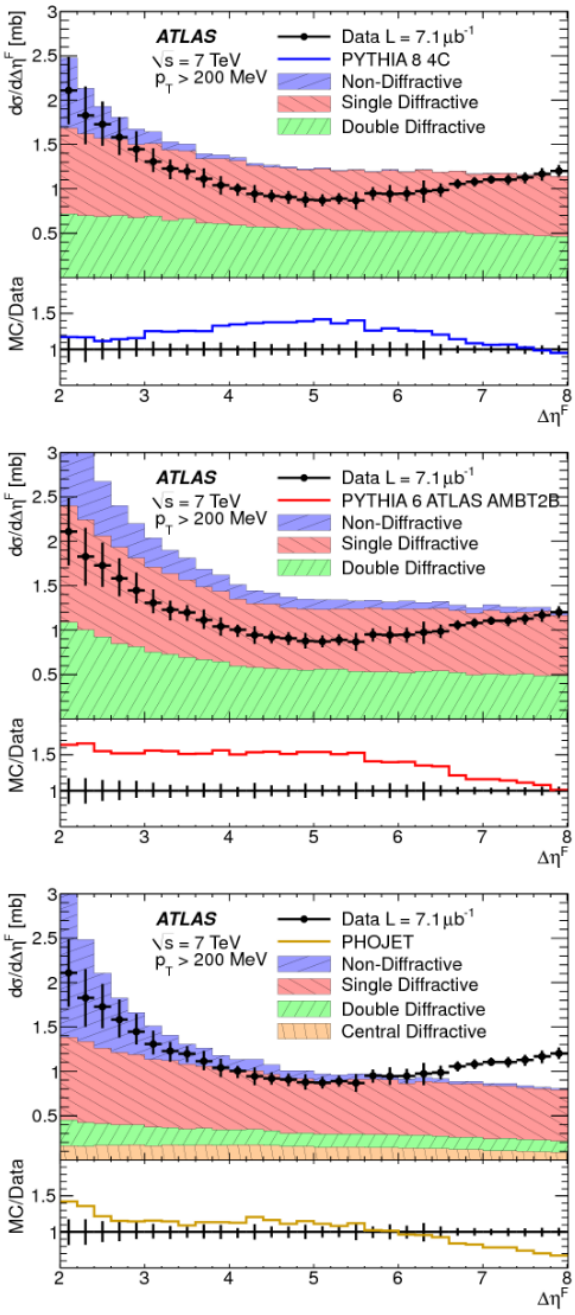

FIGURE 2.19: The black dots represent the measured inelastic cross section differential in forward gap size Δ_η^F for particles with p_T>200 GeV and Δ_η^F>2. The error bars indicated the total uncertainties. The colored areas report the MC predictions of the generators Pythia8 (top), Pythia6 (center) and Phojet (bottom) for ND, SD and DD (also CD for Phojet) contributions [48].

The black dots represent the measured inelastic cross section differential in forward gap size Δ_η^F for particles with p_T>200 GeV and Δ_η^F>2 with error bars indicating their total uncertainties. Colored areas report the Monte Carlo predictions of the three generators used Pythia8 (top), Pythia6 (center) and Phojet (bottom).
The possibility offered by the Forward detectors is to detect particles and processes not detectable in the central region.

Among them, there is LUCID (*LUminosity measurements using Cherenkov Integrating Detectors* [49], the reference detector for ATLAS online and offline Luminosity since the beginning of Run2. It will be discussed in details in Appendix A.

ZDC

ZDC (*Zero Degree Calorimeter*) consisted in two stations placed at 140 m distance to the interaction point, symmetrically [50]. With a pseudorapidity coverage of $|\eta|$>8.3, ZDC is designed to detect neutrons from heavy-ion collisions and to measure the centrality of the interaction counting the number of spectator neutrons. It can also be used to reduce the beam-halo and beam-gas background. Thanks to its time resolution of 100 ps, ZDC is able to determine IP position with a 3 cm precision in z coordinate. Each station contains one electromagnetic and three hadronic calorimeters module. Their layout is similar based on tungsten plates, placed normally to the beam direction, extended with steel plates. Series of quartz rods enter the plates parallel to z direction. Cherenkov light emitted is then converted by phototubes.

ALFA

ALFA (*A Absolute Luminosity For ATLAS*) is formed by two Roman Pots stations, symmetrically placed at 240 m distance from the IP [51]. The main purpose is to measure the total proton-proton cross section. Each station consists of 4+4 vertical pots detectors. ALFA measures the elastic scattering rate, from a back-to-back proton signature, see Fig.2.20. This mea-

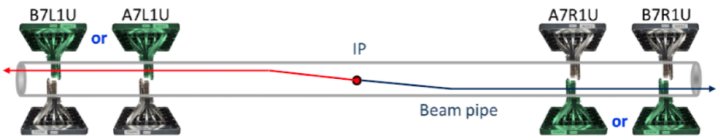

FIGURE 2.20: ALFA golden signature for reconstruction of elastic scattering events.

surements are performed in dedicated runs with a particular beam optics with high β^* and parallel-to-point focusing [52], [53]. The differential elastic cross section is then used to estimate the total cross section, through the Optical Theorem:

$$\sigma_{tot} \propto 4\pi Im(f_{el})_{t\to 0} \tag{2.7}$$

where t is the four momentum transfer and f_{el} is the elastic scattering amplitude. The strategy used by ALFA to measure σ_{tot} will be described in Appendix 6.

AFP

The AFP (*ATLAS Forward Proton*) detector consists of 2+2 horizontal stations placed at 210 m from the interaction point [54]. Each station provides a precise measurement of the position and proton trajectory, independently from the ATLAS central detector. One of the stations contains a silicon tracker system, while the other is also equipped with a Time of Flight detector, useful for measurements of proton pile-up and background rejection.
The general goal is to detect proton from diffractive interactions. Contrary to ALFA, AFP is designed to run in ATLAS standard luminosity conditions (i.e., high pile-up).

2.3.7 Trigger and Data Acquisition

As already said, LHC has a bunch crossing rate of 40 MHz, with an average size per event of 1.3 Mb: such a huge amount of data from collision cannot be completely stored. This issue, together with the fact that not all the bunch crossings contain a hard collision, lead to the deployment of a Trigger and Data Acquisition System (TDAQ), capable to reduce the event information rate to 1kHz, the maximum data storage rate [55].
Each sub-detector has its own sub-system of trigger, data-acquisition, all following the same building logic. As it regards the trigger used for the event selection for the purposes of this analysis presented in this thesis, they will be provide in Chapter 4.

Trigger

The ATLAS Trigger system can be divided into a detector based trigger called Level 1 (L1) and in a software based one, the High Level Trigger (HLT). Fig.2.21 shows the scheme of the ATLAS Trigger and Data Aquisition System [56]. Level 1 Trigger, with a fixed latency of

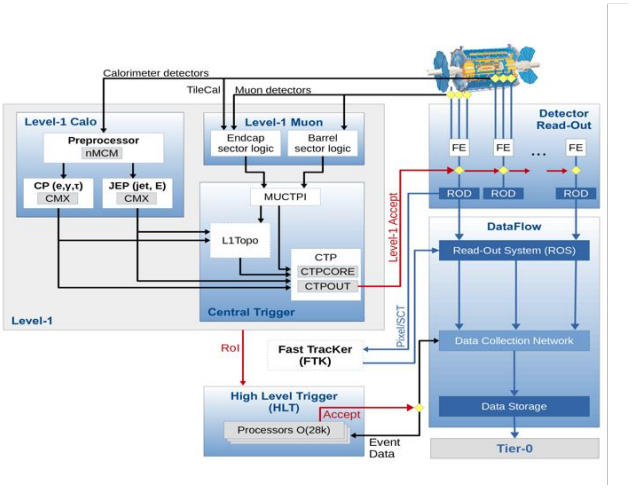

FIGURE 2.21

2.5 μs, searches for high-transverse momentum muons, electrons, photons, jets and events with large missing and total transverse energy, collecting information from Muon Spectrometer (L1Muon) and Calorimeters (L1Calo). In addition, during Run2, a new topological processor has been installed, L1Topo which implements global event-related variables.
The information collected are used by the Central Trigger Processor (CTP) to define the Region of Interest (RoIs) in the detector. This first step reduces the information rate from 400 MHz to 100 kHz, with a decision time of 2.5 μs. The RoIs represents the position of the triggered object in the η-ϕ plane. All this information are then sent to the High Level Trigger. The HLT (merged combination of Run1 Level2 and Event Filter), using all the available detector data, reduce the trigger rate to 1 kHz.

Data Acquisition

L1 trigger sends a triggered event to the detector Readout Drivers, the RODs. RODs are elements of the front-end systems which gather information from several data-streams. Analoug-to-digital components digitize the signals, formatting them in raw data before transferring them to the DAQ system. At first stage, the read-out system temporarly store them waiting for the HLT performing the final selection that definitively transfer them

to the permanent CERN storage. Besides the processing of data, DAQ also provides feedbacks on the status of the hardware and software components. Eventually, events stored by the TDAQ chain are provided to the analysis teams, which apply further selection to reject events of no interest.

2.3.8 The Detector Control System

The Detector Control System (DCS) allows safe operation of the ATLAS detector hardware and provides an homogeneous interface to all sub-detectors and to the technical infrastructure of the experiment [57]. It monitors and stores operational parameters, signals indicating abnormal behaviours to the operator and allows automatic or manual intervention. A bi-directional communication between the sub-detectors and other systems, such as LHC accelerator, ATLAS magnets and detector safety system, exists.

Chapter 3

Object Reconstruction and Identification

The starting points of any ATLAS analysis are the reconstruction and identification techniques of physics objects travelling through the detector volume, representing the observable characteristics of the particles coming from pp collisions. $VH(H \rightarrow b\bar{b})$ search is the main subject of this thesis and this chapter will be mainly focused on the description of the strategy used for the reconstruction and identification of the main objects of interest for this analysis, including electrons, muons, jets (b-tagged ones) and missing transverse energy (MET).
In particular, high importance will be given to leptons (green square) and b-jets (pink square) reconstruction and identification techniques, since they are the physics objects of higher interest for the ZH channel. In this chapter, a general description of the methods used during Run2 data-taking will be provided while the details about the tools used for the analysis described in this thesis will be given in Chapter 4.

3.1 Electrons

Typically, an electron can loose a significant amount of its energy when interacting with the material it goes through, due to *bremsstrahlung*. The radiated photon can convert into an electron-positron pair, which can interact with the detector material. This phenomenon results in the so-called *electromagnetic shower*, a cascade of very collimated positron, electrons and photons. These interactions can occur inside the inner detector volume (or even in the beam pipe), generating multiple tracks in the inner detector or downstream the inner detector, impacting in the calorimeter [58].
Fig.3.1 shows the ideal electron path and all the subdectors involved in reconstruction and identification.

3.1.1 Electron Reconstruction

An electron is reconstructed matching multiple tracks, all originating from the same primary electron, to the same electromagnetic cluster in the calorimeter. The procedure is based on the three characteristics of the electron signature: localised clusters of energy deposits found in the electromagnetic calorimeter, charge-particle tracks in the inner detector and the close matching of the two in the η-ϕ space to form the candidate. These three charecteristics corresponds to three steps of electron reconstruction in the precision region of the ATLAS detector.
Recalling what said in Sec.2.3.4, the η-ϕ space of the EM calorimeter is divided into a grid of 200x256 elements of size $\Delta\eta \times \Delta\phi$=0.025$\times$0.025, corresponding the granularity of the second layer. The energy collected in the first, second and third layer are summed to form the energy of a tower. A *seed-cluster* algorithm searches for electron clusters, whose transverse

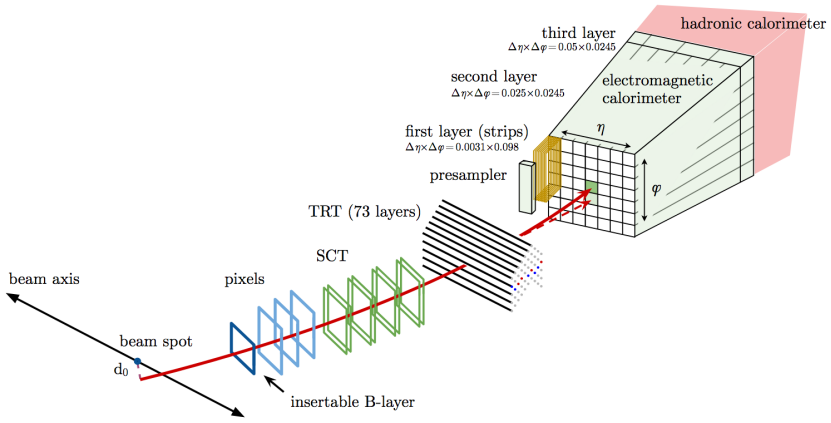

FIGURE 3.1: An illustration of the path of an electron through the detector. The red trajectory shows the hypothetical path of an electron: first, it traverse the tracking system going throug pixel detector, silicon-strip and lastly TRT, then it enters the electromagnetic calorimeter. Dashed red line represents the trajectory of a photon produced by the interaction of the electron with the tracking system material [58].

energy exceeds 2.5 GeV. Two seed-clusters can be found close to each other, i.e. if their towers overlap within an area of $\Delta\eta \times \Delta\phi$=5×9 units of 0.025×0.025. In this case, the candidate with the higher E_T is retained if E_T is 10% higher than the other, otherwise the highest-E_T central tower candidate is kept, with the duplicate removed. The reconstruction efficiency depends in general on η and E_T. As can be seen from the triangles in Fig.3.2, it ranges from 65% at E_T=4.5 GeV to more than 99% above E_T=15 GeV.
The second step is the clustering of the hits in the pixel and SCT detectors. The track seeds are formed from sets of three space-points in the silicon detectors. The pattern-recognition algorithm, using the pion hypotesis for the energy loss $\frac{dE}{dx}$, fails for a track seed with p_T>1 GeV, since it cannot be extended to a full track of at least seven silicon hits per candidate track. A second attempt is made with a modified pattern recognition which allows up to 30% energy loss for bremsstrahlung: it is the electron hypothesis. Track candidates with p_T>400 MeV are fitted, with an efficiency from 80% at p_T = 1 GeV to 98% at p_T>10 GeV, as can be seen from open circles in Fig.3.2.

Another fitting procedure, using an optimised Gaussian-sum filter (GSF), is applied for tracks with at least four silicon hits and that are matched to an EM calorimeter cluster in the η-ϕ space. It is designed to better account for energy losses of charged particles. The efficiency ϵ is higher than 60% at p_T>4.5 GeV, see Fig.3.2.
The final step of the electron reconstruction is the matching between GSF-track candidate to the calorimetr seed cluster. When several tracks fulfil the criteria, a *primary track* is selected using an algorithm that takes into account the distance in η and ϕ between the extrapolated tracks and the cluster barycenters in the calorimeter second layer and the number of hits in the silicon detectors and in the innermost silicon layer. An *electron candidate* is selected when it is associated with at least four hits in the silicon layers and no association with a vertex from photon conversion. Further criteria based on energy and transverse momentum are applied to provide a better discrimination with respect to a potential photon candidate (e.g., in case the primary candidate track is matched to a secondary vertex and has no pixel hits).

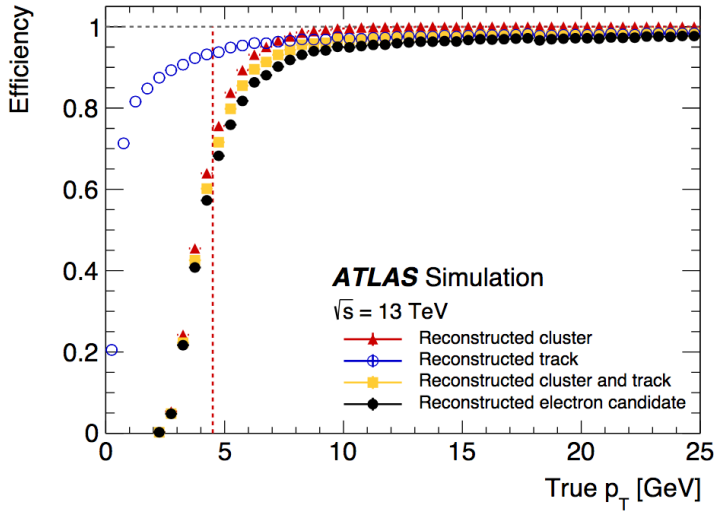

FIGURE 3.2: Total reconstruction efficiency for simulated electrons as a function of the true transverse momentum p_T for each step of the electron reconstruction assembly line: seed-cluster reconstruction (red triangles), track reconstruction of the first stage fit (blue open circles), GSF tracking candidates (yellow squares) and the final electron candidate, after the matching procedure (black circles) [58].

3.1.2 Electron Identification

Electron identification is likelihood (LH) based, with a large set of measurements contributing, including information from tracking and calorimeter system and their combination [58]. The electron LH is based on the product for signal ($\mathcal{L}_S$) and for backgroung ($\mathcal{L}_B$) of n probability density functions (pdfs), P:

$$\mathcal{L}_{S(B)}(\mathbf{x}) = \prod_{i=1}^{n} P_{S(B),i}(x_i) \tag{3.1}$$

where $\mathbf{x}$ is the vector of the various quantities, $P_{S,i}(x_i)$ is the value of the signal pdf for the quantity i at x_i value and $P_{B,i}(x_i)$ is the corresponding for the background pdf. The signal is the electron hypothesis, while the background is the ensamble of the events that mimic its signature, such as combination of jets, or electrons from photon conversion or hadron decays with heavy flavours.
The electron LH identification is based on a discriminat, built as follows:

$$d_L = \frac{\mathcal{L}_S}{\mathcal{L}_S + \mathcal{L}_B} \tag{3.2}$$

The advantage of the LH-based method with respect to *cut-based* algorithm is that it provides a better background rejection since the selection criteria are applied sequentially on each variable. Three identification working points are used to address the various requirements of signal efficiencies and background rejection factors: *Loose*, *Medium* and *Tight*. Fig.3.3 shows the LH electron-identification efficiencies as a function of E_T and η for such 3 cases.

The operating working points have been optimized in η and E_T bins because the distributions of shower shapes depend on the amount of detector material electrons pass through (varying with pseudorapidity) and changes in shower shapes and tracks have to be accounted

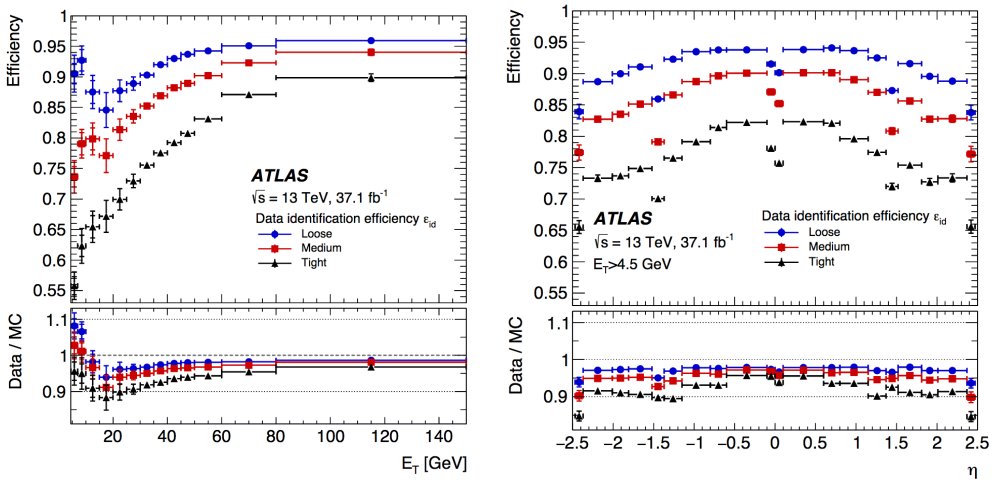

FIGURE 3.3: Measured LH electron-identification efficiencies in $Z \rightarrow ee$ events at 37.1 fb^{-1} for *Loose*, *Medium* and *Tight* operating points as a function of E_T (left) and η (right). The bottom panel shows the data-to-simulation ratios.

with increasing energies (varying with E_T).
As can be seen from Fig.3.3, for *Tight* operating point, the identification efficiency varies from 55% at 4.5 GeV (minimum transverse energy for electron identification in Run2) to 90% at 100 GeV, while *Loose* operating working point ranges from 85% at E_T=20 GeV to 96% at E_T=100 GeV. The lower efficiencies for *Tight* result, of course, in higher background rejection.

3.1.3 Electron Isolation

A challenging point at the LHC is to differentiate prompt electron production in signal processes (from hard-scattering vertex or from the decay of heavy resonances as Higgs, vector bosons, etc.) from overwhelming backgrounds (semileptonic decays, misidentified hadrons, electron-positron pairs from photons, etc.). A characteristic signature which can be exploited is the activity surrounding the candidate object in the $\eta - \phi$ space. Variables are constructed to quantify the amount of activity by summing transverse energies in the calorimeter clusters or the transverse momenta of tracks in a cone of radius $\Delta R = \sqrt{(\Delta\eta)^2 + (\Delta\phi)^2}$ around the candidate direction but excluding it. So, it is possible to distinguish two kinds of isolation variables, based on calorimeter or tracking measurements.
A cone of size ΔR is defined around the candidate cluster position to build the calorimeter-based isolation variable. Differently with respect to Run1, the topological cluster energy is used with the advantage of the noise suppression. Indeed, topological clusters are seeded by cells with a deposited electromagnetic energy more than four times higher than the expected noise-threshold of the cell (including both electronic noise and pile-up effects). After that, the clusters are expanded adding neighbouring cells containing a deposited energy more than twice the noise level.
The procedure is stopped by the lack of cells satisfying the requirement with the addition of a final shell surrounding the resulting cell complex. The core energy (corresponding to the candidate) is subtracted removing the cells included in a $\Delta\eta \times \Delta\phi$=0.125×0.175 rectangle. The procedure is schematized in Fig.3.4. Eventually, leakage corrections have to be applied to account possible out-of-core energy deposit by the candidate. The final variable is called $E^{iso}_{T,cone}$.

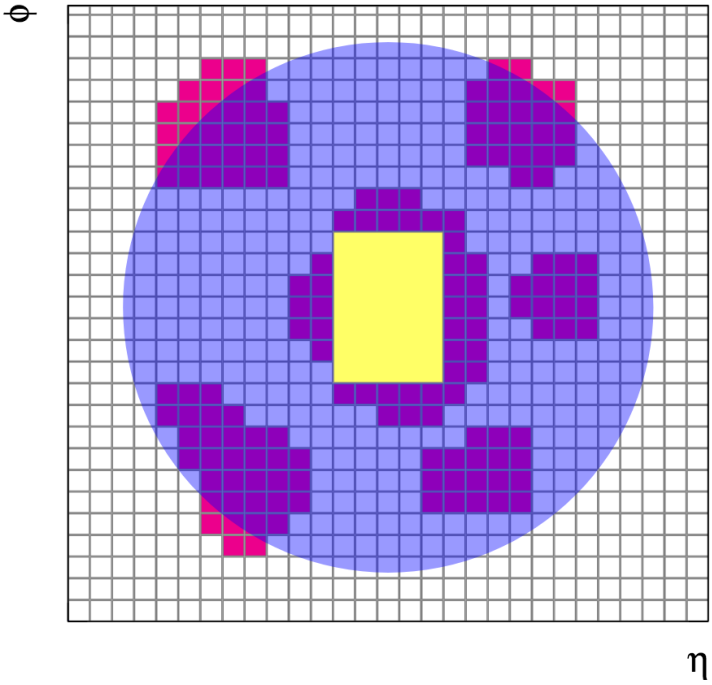

FIGURE 3.4: Calorimeter isolation method. The grid represents the second-layer calorimeter cells in the η-ϕ space. The electron candidate is located at the center of the isolation cone (purple circle). The topological clusters (red) falling in the isolation cone are included in the isolation variable computation. The yellow rectangle correspond to the core subtracted.

The method for the track-based isolation variables construction uses tracks with p_T>1 GeV, reconstructed in the fiducial region of the inner detector ($|\eta|$<2.5). They have to satisfy track quality requirements, considering a minimum number of hits identified in the silicon detectors and a minimum number of detector regions crossed by tracks. A requirement on longitudinal impact parameter z_0, corrected for position of the primary vertex and multiplied by the $sin\theta$ (track polar angle sine), allows to minimize pile-up and to select the relevant vertex of the process. Typically, track-based isolation variable calculation takes as relevant vertex the one with the largest sum of the squares of the transverse momenta. The variables are constructed taking the p_T of the tracks found in a cone of radius ΔR, around the candidate direction, excluding its own contribution. Contributions from secondary electrons deriving from bremsstrahlung photons are taken as part of the initial electron's energy. An extrapolation to the second layer of the EM calorimeter: all extrapolated tracks within a $\Delta\eta \times \Delta\phi$=0.05×0.1 window around the cluster position are treated as part of the electron candidates and discarded. The final track-isolation variable is called p_T^{iso}.

The implementation of isolation criteria is peculiar for the single analysis needs. Several operating points were estabilished using cones of radius ΔR=0.2 for the calorimeter-based ones and cones of variable size with a maximum of 0.2 or 0.4. They can be divided in three categories:

- targeting a fixed value of the isolation efficiency ϵ_{iso}, uniform in η and p_T: *Loose* isolation
- targeting a fixed value of the isolation efficiency ϵ_{iso}, dependent on the p_T of the electron but uniform in η: *Gradient* isolation
- imposing fixed requirements on the value of the isolation variable: *Fix* isolation

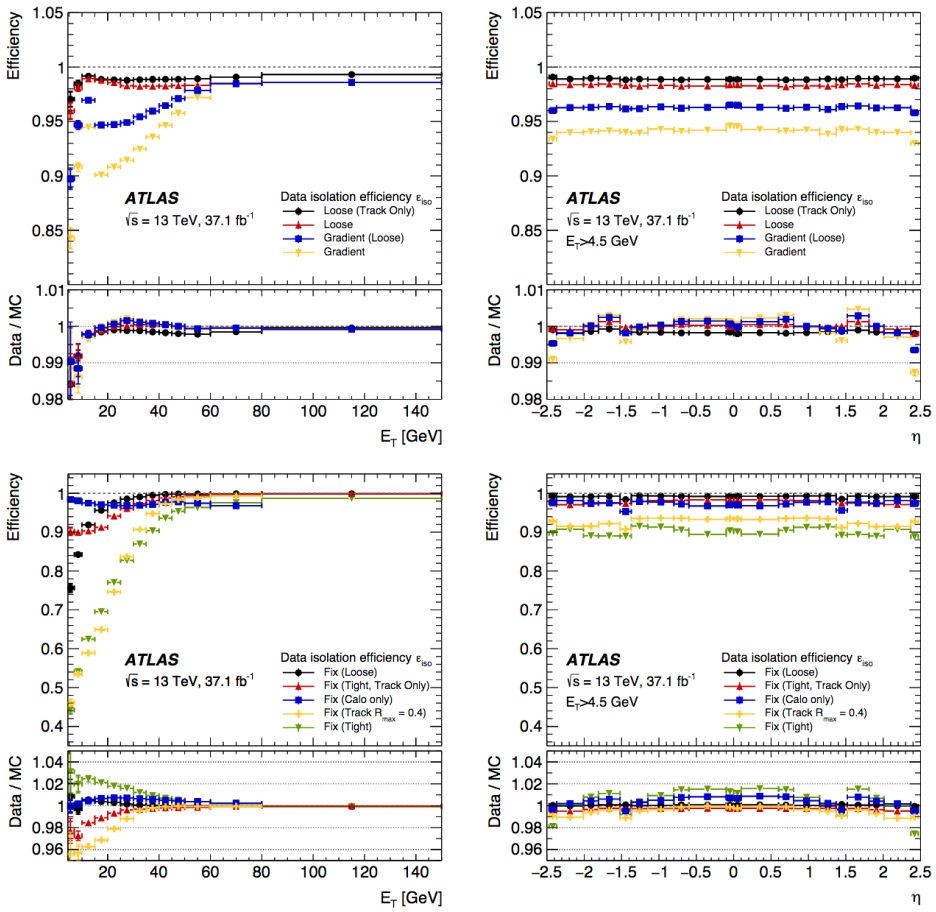

FIGURE 3.5: Isolation efficiencies for data and the ratio to the simulation in the lower panel for the ATLAS isolation operating points as a function of the electron candidate transverse energy (left) and pseudorapidity (right) in $Z \rightarrow ee$ events. Top plots show ϵ_{iso} for operating points targeting specific efficiencies. Bottom plots show operating points when applying fixed requirements on isolatation variables.

TABLE 3.1: Definition of electron isolation operating points and isolation efficiencies ϵ_{iso}. All operating points use a cone size of ΔR=0.2 for calorimeter-based variables and a R_{max}=0.2 for track-based ones, except for the final element *Fix (Track)* which uses R_{max}=0.4. The values refer to simulated $Z \rightarrow ee$ samples, witch electrons satisfying Tight identification criteria. For *Gradient*, the units of p_T are in GeV.

Operating points	$E^{iso}_{T,cone}$	$p^{iso}_{T,var}$	**Total** ϵ_{iso}
Loose (Track Only)	-	ϵ_{iso}=99%	99%
Loose	ϵ_{iso}=99%	ϵ_{iso}=99%	98%
Gradient	ϵ_{iso} = 0.1143 × p_T + 92.14%	ϵ_{iso} = 0.1143 × p_T + 92.14%	90(99)% at 25(60) GeV
Gradient (Loose)	ϵ_{iso} = 0.057 × p_T + 95.57%	ϵ_{iso} = 0.057 × p_T + 95.57%	95(99)% at 25(60) GeV
Fix (Loose)	$E^{iso}_{T,cone}/p_T$<0.20	$p^{iso}_{T,var}$<0.15	-
Fix (Tight)	$E^{iso}_{T,cone}/p_T$<0.06	$p^{iso}_{T,var}$<0.06	-
Fix (Tight Track Only)	-	$p^{iso}_{T,var}$<0.06	-
Fix (Calo Only)	$E^{iso}_{T,cone}$<3.5 GeV	-	-
Fix (Track R_{max} = 0.4)	$E^{iso}_{T,cone}/p_T$<0.11	$p^{iso}_{T,var}$<0.06	-

Tab 3.1 listed the electron isolation operating points with their respective efficiencies (see also Fig.3.5).

3.2 Muons

The first step of the muon reconstruction is performed with independent measurements in the Inner Detector and in the Muon Spectrometer. The information is then combined to get muon tracks, used in physics analyses. Given that reconstruction process in the ID is the same of any charged particle, next section will be focused on the description of muon MS and combined muon reconstruction.

Muon Reconstruction

The very starting point is the search for hit patterns in each muon chamber in the Muon Spectrometer in order to form segments [59]. In each MDT chamber and nearby trigger chamber, a Hough transform [60] is used to find hits aligned on a trajectory in the bending plane of the detector. Segments are obtained performing a straight-line fit to the hits found in each layer. The RPC or TGC hits measure the coordinate orthogonal to the bending plane. In the CSC detectors, segments derive from a combinatorial search in the η and ϕ planes. Such segments are selected using criteria based on hit multiplicity and fit quality and then matched using relative positions and angles. At least two matching segments are required to build a track, with exception in the barrel-endcap transition region where a single high-quality segment with η and ϕ information can be used. A single segment can be used to build several track candidates. An overlap removal algorithm is then applied to provide the best assignment to a single track of to allow for the segment to be shared between two tracks.
Four muon types are defined after the combined ID-MS reconstruction, depending on which subdetector has been involved in the procedure, as shown in Fig.3.6.

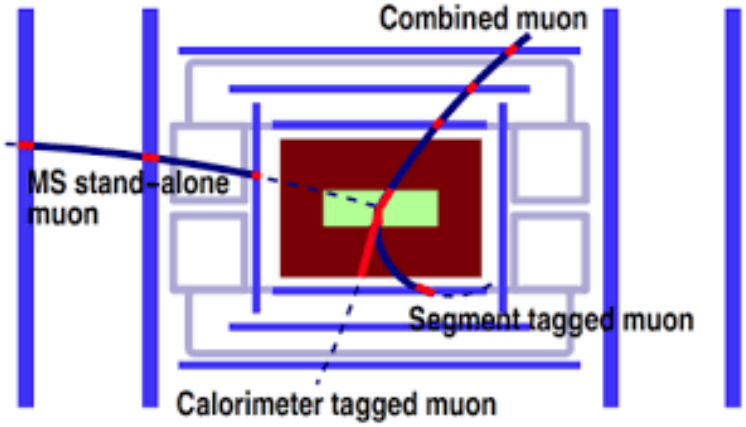

FIGURE 3.6: Muon reconstruction in ATLAS.

- *Combined (CB) muon.* Track reconstruction is performed independently in the ID and MS. The combined track is built with a global refit that used the hits from both ID and MS subdetectors. Most muons are reconstructed following an outside-in pattern recongnition, in which muons are first reconstructed in MS and then extrapolated inward to be matched to an ID track. The complementary approach estabilish and outward extrapolation from the ID to the MS.

- *Segment-tagged (ST) muons.* A track in the ID is classified as muon if, once extrapolated to the MS, it is associated with at least one local track segment in the MDT or CSC chambers. They are used when a candidate crosses only one layer of the MS chamber, because of their low p_T or because they fall in reduced acceptance regions.

- *Calorimeter-tagged (CT) muons.* An ID track is considered a muon if it can be matched to an energy deposit in the calorimeter compatible with a minimum-ionizing particle. The identification criteria for CT muons are optimised for the region $|\eta|$<0.1 (momentum range is 15 GeV<p_T<100 GeV), where the MS is only partially instrumented for cabling to the calorimeter and inner detector. Although they have the lowest purity with respect to the other types, they allow to recover the acceptance in this region.

- *Extrapolated (ME) muons* or *Standalone muons.* The muon trajectory is reconstructed based only on the MS track and a loose requirement on compatibility with originating from the IP. Muons are required to traverse at least two layers of the MS chambers to provide track measurements, while three layers are required in the forward region. They allow to extend acceptance in the region 2.5<$|\eta|$<2.7, not covered by ID.

3.2.1 Muon Identification

Muon identification is performed by applying quality requirements in order to suppress background, mainly due to pion and kaon decays, and to select prompt muons with high efficiency and ensure better momentum measurements. The procedure exploits typical signature of background muon candidates allowing to discriminate them from the prompt muon candidate [59].
Four muon identification selections are provided to address the requirements of different analyses.

- *Loose muons.* The Loose criteria has been specifically designed to maximise the reconstruction efficiency to provide good quality muon tracks. They have been optimised especially for the search of Higgs boson candidate decaying in a four-lepton final state. All muons are used and CB and ME candidates, satisfying Medium requirements, are included. CT and ST are restricted to the $|\eta|$<0.1 region. In the region $|\eta|$<2.5, 97.5% of the Loose muons are combined, 1.5% are CT and 1% are ST.

- *Medium muons.* The Medium criteria is the default selection used in ATLAS. Only CB and ME tracks are used. The former are required to have $\geq$3 hits in at least two MDT layers, except for tracks in the $|\eta|$<0.1 region. The latter must have at least three MDT/CSC layers and they are used only in the 2.5<$|\eta|$<2.7 acceptance region. In the pseudorapidity region $|\eta|$<2.5, about 0.5% of the muons are classified as Medium originate from the inside-out combined reconstruction strategy.

- *Tight muons.* The Tight identification criteria is optimised to maximise the purity of muons at the cost of efficiency. Only CB muons with hits in at least two stations of MS and satisfying Medium selection criteria are kept.

- *High-p_T muons.* The last identification criteria have to maximise the momentum resolution for tracks with transverse momentum higher than 100 GeV. CB muons passing Medium selection and having at least three hits in the three MS stations are selected. The latter requirement helps to improve of 30% the p_T resolution above 1.5 TeV at the cost of an efficiency reconstruction reduction of 20%.

Fig.3.7 shows the muon reconstruction efficiency corrected for the ID efficiency for the Loose (no CT component) identification operating point for the whole Run2 data-taking as a function of p_T and η, per year. They are measured from $J/\Psi \rightarrow \mu^+\mu^-$ decays using the tag-and-probe technique.

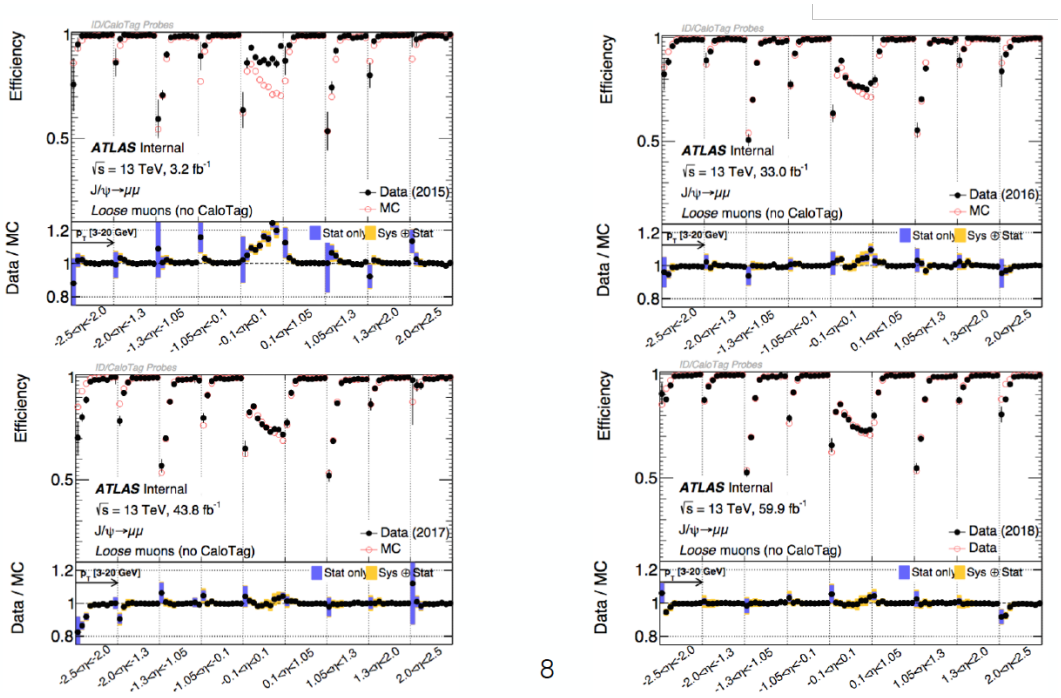

FIGURE 3.7: Muon reconstruction efficiency in Run2 data-taking [59].

3.2.2 Muon Isolation

Similarly to what said in previous section for electrons, the measurement of the detector activity around the muon candidate is a powerful and helpful tool for background rejection in many physics analyses. Muons coming from heavy particle decays, such as W, Z or Higgs, are often produced isolated from other particles. On the contrary to what happens for muons from semileptonic decays who are embedded in jets [59].
Two kinds of variables are defined: track-based and calorimeter-based.

- The track-based isolation variable is $p_T^{varcone30}$. It is defined as the scalar sum of the transverse momenta of the tracks with p_T>1 GeV in a cone of size ΔR=min(10 GeV/p_T^{μ}, 0.3) around the muon of transverse momentum p_T^{μ}, excluding the muon track itself. The p_T-dependent nature of the cone size has been chosen to improve the performance for muons produced in the decay of high-energy particles.

- The calorimeter-based isolation variable is defined as the sum of the transverse energy of topological clusters in a cone of size ΔR=0.2 around the muon, after the subtraction of the contribution of the muon candidate to the energy deposit and the pile-up correction.

The isolation criteria are determined using the relative isolation variables, defined as the ratio of the isolation variables to the muon transverse momentum.
Seven isolation criteria (*isolation working points*) are defined and optimised for different physics analyses, see Tab. 3.2 for the entire list with respective definition and requirements.

TABLE 3.2: Definition of the seven isolation working points. Second column reports their definition, third column the criteria used.

Isolation Working Points	Discriminating variables	Definition
LooseTrackOnly	$p_T^{varcone30}/p_T^{\mu}$	99% efficiency constant in η and p_T
Loose	$p_T^{varcone30}/p_T^{\mu}$, $E_T^{topocone20}/p_T^{\mu}$	99% efficiency constant in η and p_T
Tight	$p_T^{varcone30}/p_T^{\mu}$, $E_T^{topocone20}/p_T^{\mu}$	96% efficiency constant in η and p_T
Gradient	$p_T^{varcone30}/p_T^{\mu}$, $E_T^{topocone20}/p_T^{\mu}$	$\geq$90%(99%) efficiency at 25(60) GeV
GradientLoose	$p_T^{varcone30}/p_T^{\mu}$, $E_T^{topocone20}/p_T^{\mu}$	$\geq$95%(99%) efficiency at 25(60) GeV
FixedCutTightTrackOnly	$p_T^{varcone30}/p_T^{\mu}$	$p_T^{varcone30}/p_T^{\mu}$<0.06
FixCutLoose	$p_T^{varcone30}/p_T^{\mu}$, $E_T^{topocone20}/p_T^{\mu}$	$p_T^{varcone30}/p_T^{\mu}$<0.15 and $E_T^{topocone20}/p_T^{\mu}$<0.30

The efficiencies for the seven isolation working points are measured in data and simulation in $Z \to \mu\mu$ decays, using tag-and-probe method.

3.3 Missing Transverse Momentum

Conservation of transverse energy in the transverse plane implies that the sum of contribution of all collision products should be zero. Deviation from this result is known as *missing transverse energy* E_T^{miss}. This is considered an hint to weak-interacting neutral and stable particles in the final state, the Standard Model neutrinos. Also other objects which can escape the acceptance of the detector or poorly reconstructed can contribute to E_T^{miss} reconstruction.
The reconstructed missing transverse energy has two main contributions [61]. The *hard* term contains fully reconstructed objects such as electrons, muons, taus, photon and jets. The *soft* term, coming from underlying event activity and soft radiation from the hard event, consist of signals not associated with any reconstructed object. It is defined as the magnitude of the negative vector sum p_T:

$$\overrightarrow{E}_T^{miss} = -\Big(\sum_{i\in e}\overrightarrow{p}_{T,i} + \sum_{i\in\mu}\overrightarrow{p}_{T,i} + \sum_{i\in\tau}\overrightarrow{p}_{T,i} + \sum_{i\in jets,i} p_{T,i} + \sum_{i\in\gamma}\overrightarrow{p}_{T,i} + \sum_{i\in\text{soft term}}\overrightarrow{p}_{T,i}\Big) \tag{3.3}$$

Several methods are used at ATLAS to quantify the missing transverse energy:

- CST (*Calorimeter-based Soft Term*) E_T^{miss} is based on the energy deposit in the calorimeter, not associated with hard objects. However, calorimeter-based approach suffers from pile-up effects which affect the soft term.
- Track E_T^{miss} is based on Inner Detector measurements and it offers higher resilience to pile-up effect because ID tracks can be associated to vertices, i.e. to a particular pp collision. The advantage of a purely track-based reconstruction method is the large independence from pile-up but, on the other hand, it has limitations due limited acceptance and insensitivity to neutral particles.
- TST (*Track-based Soft Term*) E_T^{miss} is a compromise between the previous two reconstruction methods and it is the preferred one for Run2. It uses a track-based soft term combined with calorimeter-based measurements for the hard objects.

3.4 Jets

Almost immediately after being produced, quarks and gluons undergo to fragmentation and hadronization, which lead to a collimated spray of energetic hadrons.

Jets represent the characteristic signature of these phenomena and the measurements of their direction and energy provide information about the originating fundamental particle. Jets need to be defined by a set of rules, containing the prescription on how to group particle and assign momentum to the resulting object: the *jet reconstruction algorithms*.
As stated by Gavin P. Salam, this subject can be called *jetography* [62]. Like in photography, where the understanding of optics and of the subject properties helps the better choice of focus, aperture and length of exposure, jets definition and reconstruction methods can be adapted to the specific physics analysis and detector peculiarities. Following the analogy, as it happens in photography where photons are not what we want to see, in jetography, jets are of interest in the way that they helps up to visualize the objects they are arised from, in our case, the Higgs boson.

3.4.1 Jet Reconstruction: anti-k_t algorithm

The most important feature of a jet reconstruction algorithm is the *infrared* and *collinear* safety (IRC) which means that modifying an event by a collinear splitting or the addition of a soft emission should not change the set of hard jets.
There are two possible choices about the first requirement for jet reconstruction:

- *soft-resilient* jet: it provides regular jets but implies a certain rigidity in the ability to adapt a jet to the branching nature of QCD radiation.
- *soft-adaptable* jet: it provides adaptability at the cost of having less regular jets.

It is not yet clear if a best choice between them exists, however, nowadays, the most common approach is of a soft-resilient algorithm because it allows to simplify theoretical calculations and to eliminate momentum-resolution losses. Moreover, the knowledge of the typical shape of the jets facilatates experimental reconstruction and calibration.
Examples of IRC safe and soft-resilient jet algorithm are k_t, Cambridge/Aachen and anti-k_t. ATLAS preferred one is anti-k_t algorithm [63], with which the jets of the present analysis have been reconstructed. It consists in an iterative procedure, considering the distance d_{ij} between two clusters or *pseudojets* and the distance d_{iB} between the pseudojet i and the beam (B).
The clusters are locally calibrated three-dimensional topological clusters (*topo-clusters*), built from cells of the calorimeter, both electromagnetic and hadronic. The topo-clustering procedure starts with the identification of seed cells that should have energy significance at least 4σ above the noise level, where noise is defined as quadratic sum of electronic and pile-up signals. Neighbouring cells with energy significance higher than 2 σ with respect to the noise are then iteratively added together with a final extra ring of closest cells. Afterwards, the topoclusters are divided in energy categories using local energy maxima criteria. Each of them is then calibrated according to its local properties, such as energy density, calorimeter depth and isolation with respect to nearby clusters. This procedure is known as *Local Cluster Weighting* (LCW). The reconstructed jets are calibrated through the ATLAS LCW+JES (*Jet Energy Scale resolution*), which applies corrections as a function of the jet energy and pseudorapidity to the jets reconstructed at the electromagnetic scale [64].
Then, the anti-k_t algorithm acts by the sequential recombination of the reconstructed clusters:

- for each of them, it evaluates the distance between cluster i and cluster j, defined as follows:

$$d_{ij} = \min(p_{T,i}^{2p}, p_{T,j}^{2p}) \frac{\Delta R_{ij}^2}{R^2} \tag{3.4}$$

where ΔR_{ij}^2 is the angular distance between i and j in the η-ϕ space:

$$\Delta R_{ij}^2 = (\eta_i - \eta_j)^2 - (\phi_i - \phi_j)^2 \tag{3.5}$$

$p_{T,i(j)}$, $\eta_{i(j)}$ and $\phi_{i(j)}$ are the transverse momentum, the pseudorapidity and the azimuthal angle of i and j, while R is the radius parameter whose value is R=0.4 for this analysis. Finally, p is a parameter characterizing sequential recombination algorithms, equal to -1 in the case of anti-k_t.

- for each cluster i, the distance d_{iB} from the beam is also evaluated as:

$$d_{iB} = p_{T,i}^{2p} \tag{3.6}$$

- the minimum distance between d_{ij} and d_{iB} is found.
- if the minimum is d_{ij} then it is combined into a single *pseudo-jet* and all the procedure is repeated, otherwise it is considered as a final jet state and the iterations are stopped.

3.4.2 Jet Energy Calibration

A proper energy calibration is needed because the energy scale of the reconstructed jets does not correspond to the truth-particle jet energy scale (JES), which is defined as the energy of jets from hard interaction only, built from all stable particles in Monte Carlo simulation. Several effects cause the discrepancy:

- calorimeter non-compensation due to the difference in response between electromagnetic and hadronic showers
- inactive regions in the detector
- energy deposits below the noise thresholds
- energy left outsite the reconstructed jet (but belonging to the truth particle)
- longitudinal leakage from showers not fully contained in the calorimeter volume

In addition, *pileup* effects also have to be taken into account. Due to the high instantaneous luminosity achieved by LHC, multiple simultaneous pp interactions occurs within a single bunch crossing (pileup), causing a challenging condition for precise jet reconstruction and calibration. Indeed, pileup products in the same event (*in-time pileup*) contaminate jets, in a way proportional to the area of the jet. Morever, pileup interactions can mimic jet signatures, creating pileup jets from additional pp interactions, fake jets or random combinations of soft particles originating from multiple vertices (*stochastic pileup*). Calorimeters are also sensitive to collisions occurring in subsequent bunch-crossing (*out-of-time pileup*), due to the charge collection in ATLAS calorimeters (400-600 ns) which is long if compared to the LHC bunch-crossing duration of 25 ns. The issue is solved reducing sensitivity using a fast bipolar shaped calorimeter signal with net zero integral over time which allows the cancellation, on average, of in-time and out-of-time pileup effects.
Furthermore, three methods, based on the matching between tracks and jets, are used in ATLAS to suppress the remaining pileup jets:

- Jet Vertex Fraction (JVF), used mostly in Run1.
- improved variables (corrJVF and R_{p_T}) for the pileup jets identification.

- Jet Vertex Tagger (JVT), a new likelihood discriminant used in Run2.

In the context of $VH(H \rightarrow b\bar{b})$ analysis JVT is used but since it is a multivariate combination of corrJVF (JVF corrected for the vertex number) and R_{p_T}, all the three will be discussed.

Jet Vertex Fraction (JVF)

The Jet Vertex Fraction JVF is used to identify the primary vertex from the originating jet [65]. A cut on this variable can help to remove jets which are not associated with it. Once it has been identified, the JVF variable can be used to select jets having a high probability of originating from that vertex. Tracks are assigned to calorimeter jets following the ghost-association procedure, which basically consists in associating tracks with small p_T to the jet clustering process.
The JVF is calculated as the ratio of the scalar transverse momentum (p_T) sum of the tracks that are associated to the jet, originated by the hard-scatter vertex PV divided by the scalar p_T sum of all associated tracks indipendently of their origin. For a given jet i, its JVF with respect to the primary vertex PV_j is:

$$\mathrm{JVF}(\mathrm{jet}_i, \mathrm{PV}_j) = \frac{\sum_m p_T(track_m^{\mathrm{jet}_i}, \mathrm{PV}_j)}{\sum_n \sum_l p_T(track_l^{\mathrm{jet}_i}, \mathrm{PV}_n)} \tag{3.7}$$

where m runs over all the tracks coming from the primary vertex PV_j where jet_i has its origin, n runs over all the tracks in the event and l over all the tracks originating from PV_n. Only tracks with p_T>500 MeV are considered in JVF calculation, which is bounded to [0,1] interval and takes value -1 when jet is associated with no tracks.
The principal of the method is schematized in Fig.3.8a, while Fig.3.8b shows its discriminating power. It is important to note that the JVF-based pileup rejection has limits with

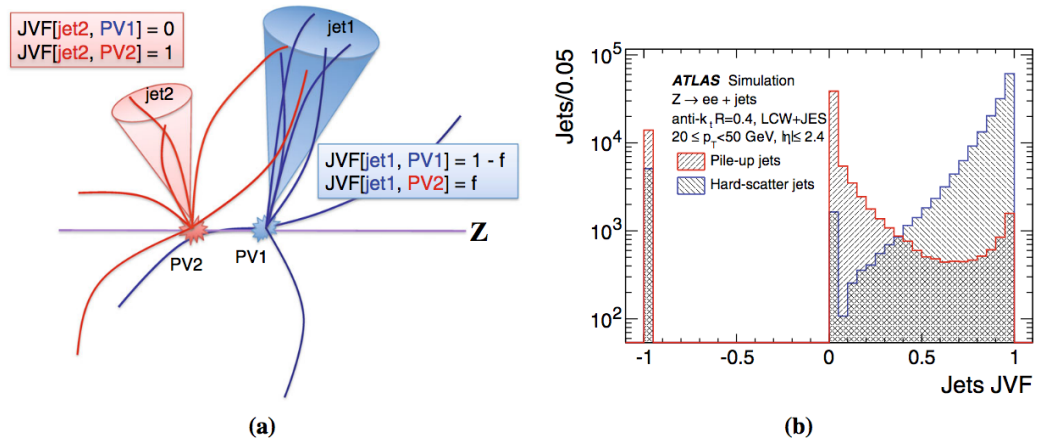

FIGURE 3.8: (a) Representation of the JVF principle where f stands for the fraction of track p_T contributed to jet1 due to the secondary vertex PV2. (b) Distribution for hard-scatter (blue) and pile-up (red) jets with 20<p_T<50 GeV and $|\eta|$<2.4 after pile-up subtraction in simulated Z+jets events [66].

increasing luminosities. This kind of selection is used only with $p_T \leq 50$ GeV jets.

Improved variables for pile-up vertex identification

As said before, JVF is a powerful tool in rejecting pileup jets but it shows its limit in high luminosity conditions. Looking at Eq.3.7, it can be seen that a denominator increasing, the mean JVF is shifted to smaller values. The pileup dependent nature of JVF is addressed in two ways, introducing two new variables.
The first one is JVF-like variable corrected for its pileup dependence [66]. It is defined as:

$$\text{corrJVF} = \frac{\sum_m p_{T,m}^{track}(\text{PV}_0)}{\sum_l p_{T,l}^{track}(\text{PV}_0) + \frac{\sum_{n\geq 1}\sum_l p_{T,l}^{track}(\text{PV}_n)}{(k\cdot n_{track}^{PU})}} \tag{3.8}$$

where $\sum_m p_{T,m}^{track}(\text{PV}_0)$ is the scalar sum of the p_T of the tracks associated with the jet which originate from the hard-scatter vertex. The $\sum_{n\geq 1}\sum_l p_{T,l}^{track}(\text{PV}_n)$ is the scalar sum of the p_T of the associated tracks generating from any of the pileup interaction. The corrJVF variable is based on a track-to-vertex association method, different from the one used for JVF. The new selection aims to improve efficiency for b-quarks.
It consists in two steps. First, a vertex is reconstructed and associated with tracks. If a track is associated to more than one vertex, vertex with lower $\sum(p_T^{track})^2$ is discarded. In the second step, if a track is not associated to a primary vertex after the first iteration but it is within $|z|$<3 mm with respect to the hard-scatter vertex, it is assigned to it. The $|z|$<3 mm requirement was chosen to target tracks from hadron decays in flight, not likely to be attached to any vertex. The new 2-step method has resulted in a significant increase in the hard-scatter jet efficiency and in a great pileup jets rejection, with large performance gain for jets originating from b-quarks.
The second variable is R_{p_T} is defined as the scalar sum of the p_T tracks that are associated with the jet and orginate from the hard-scatter vertex divided by the fully calibrated jet p_T, which includes pileup subtraction:

$$R_{p_T} = \frac{\sum_k p_{T,k}^{track}(\text{PV}_0)}{p_T^{jet}} \tag{3.9}$$

From Fig.3.9a it can be seen that R_{p_T} is peaked at 0 and it falls for pileup jets, since tracks from the hard-scatter vertex rarely contribute. For hard-scatter jets, this varibale represents the charged p_T fraction and its mean value and spread are larger for pileup jets.
Fig.3.9b shows the hard scatter jet efficiency as a function of the number of primary vertices when imposing minimum requirements on R_{p_T} and JVF to obtain an inclusive efficiency of 90%.

Jet Vertex Tagger

The jet vertex tagger (JVT) is a new discriminant [66], constructed using R_{p_T} and corrJVF as two dimensional likelihood derived using simulated dijet events based on k-nearest neighbour (kNN) algorithm [67]. For each point in the two dimensional R_{p_T}-corrJVF plane, the relative probability for a jet to be of signal type is computed as the ratio of the number of hard-scatter jets to the number of hard-scatter plus pileup found in a local neighbourhood, using as training sample of signal and pile-up jets with 20 GeV<p_T<50 GeV and $|\eta|$<2.4. The neighbourhood is defined as the 100 nearest neighbours around the test point in the R_{p_T}-corrJVF space(using an Euclidean metric and rescaling variables to make them have the same range). Fig.3.10a shows the fake rate versus signal jets efficiency curves for JVF, corrJVF, R_{p_T} and JVT, representing the fraction of pileup jets passing the minimum requirements. The JVT performance is driven by corrJVF in the region of high signal jet efficiency

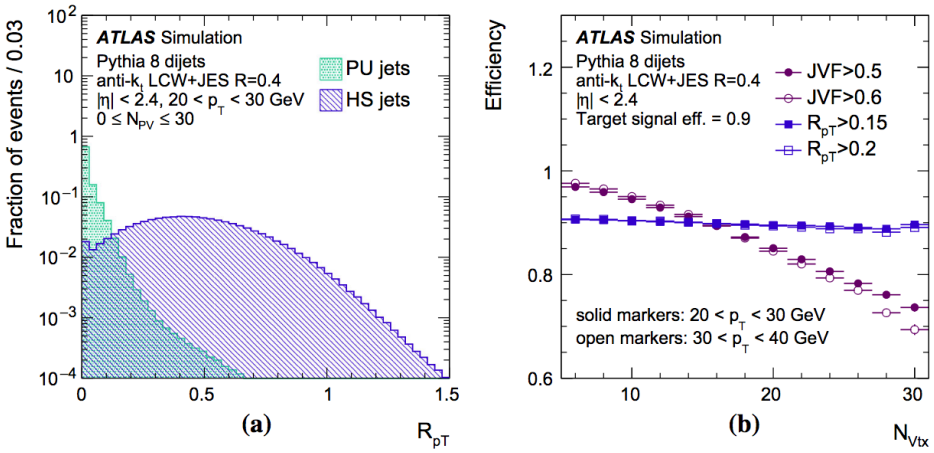

FIGURE 3.9: (a) Distribution of R_{p_T} for pileup (PU) and hard-scatter (HS) jets with 20 GeV<p_T<30 GeV. (b) Primary vertex dependence of the hard-scatter jets efficiency for 20 GeV<p_T<30 GeV (solid markers) and for 30 GeV<p_T<40 GeV (open markers) jets for fixed cut on R_{p_T} (blue) and JVF (violet). The cuts can be found in the legend [66].

and by R_{p_T} in the high pileup rejection region.

Using JVT the signal jet efficiency of 80, 90 and 95% are reached for fake rates of 0.4, 1.0 and 3%. It is even better with respect what happened with cuts on JVF where the same efficiencies are obtained but with pileup fake rates of 1.3, 2.2 and 4%.

Fig.3.10b show the dependence of hard-scater jet efficiencies on the number of primary vertex NPV. For the full range, the hard-scatter jet efficiencies after a selection based on JVT are stable around 1%. The better performance in pileup jet suppression of JVT-based approach is due to the differences in fragmentation and showering between jets initiated by gluons and light quarks which affect the corrJVF and R_{p_T} shapes. Fig.3.11 shows the fake rate curve versus efficiency for JVT with a comparison of the trends for light quarks, gluons and b-quarks. The performance is worse for light quarks. The better discrimination performance is for hard scatter jets generated by b-quarks. For this reason, this is the method used in the $VH(H \rightarrow b\bar{b})$ analysis.

Jet Energy Scale (JES)

The relation between the reconstructed jet energy (or jet p_T), after the pileup subtraction, and the truth-particle jet energy is mediated by a multiplicative factor. In ATLAS, the JES is obtained from the jet energy and has a strong dependence on η, reflecting the different detector technologies [68]. Typically, JES is derived from inclusive dijet events. As a consequence, it is extracted from a mixed quark gluon jet final state. The differences in fragmentation and in particle composition results in different jet response. In particular, gluons fragment into a large number of soft particles if compared to quark jets, leading to a lower response in the calorimeter, less sensitive at low p_T. This effect is known as *flavour dependence* of the jet response.

A track-based post-calibration correction is applied to reduce this effect and to improve jet energy resolution. The corrections in jet response are applied sequentially, in a manner that the average JES remains unchanged. For calibrated topoclusters, two corrections are applied. One is based on the number of tracks above p_T>1 GeV associated to the jet. The other one is based on the jet width, defined as the average $\Delta R = \sqrt{(\Delta\eta)^2 + (\Delta\phi)^2}$ distance between the tracks associated to the jet and the the calorimeter jet axis. A third

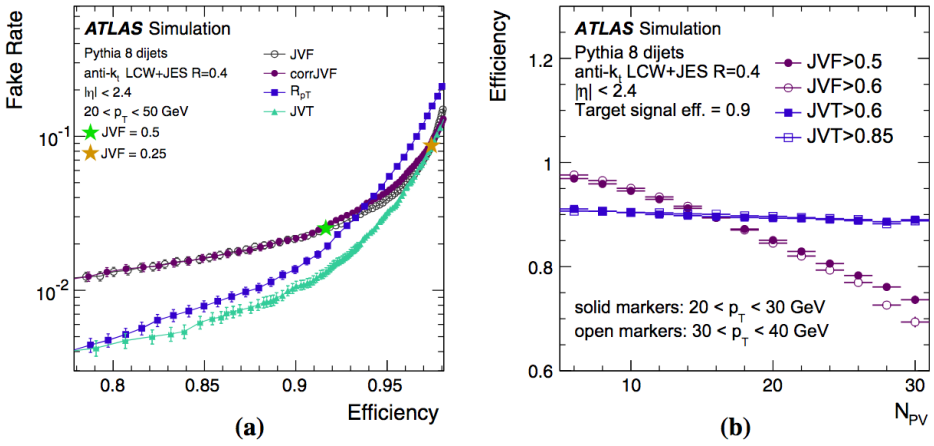

FIGURE 3.10: (a) Fake rates from pileup jets versys hard-scatter jet efficiency for JVF, corrJVF and JVT. The golden and green stars points the mostly used JVF working points, with values of 0.25 and 0.5. (b) Primary vertex dependency of the hard scatter jet efficiency for 20 GeV<p_T<30 GeV (solid markers) and for 30 GeV<p_T<40 GeV (open markers) for fixed cuts of JVT (blue) and JVF (violet) to get an inclusive efficiency of 90% [66].

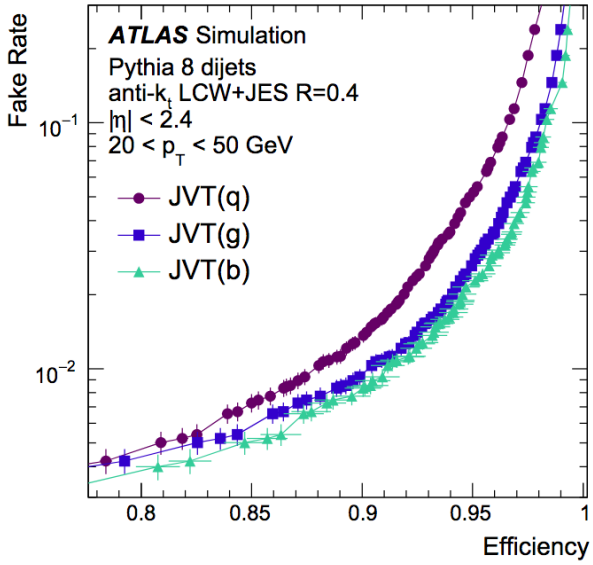

FIGURE 3.11: Fake rates from pileup jets versus hard-scatter jet efficiency curves for JVT separating jets initiated by light quarks, b-quarks and gluons [66].

correction, evaluated on Muon Spectrometer measurements matched to the jet, is applied to include energy leakage outside the calorimeter. A residual *in situ* calibration is applied exploiting the balance of physics objects in transverse plane to bring the jet response in data and MC to agreement.
The overview of the all jet calibration chain is shown in Fig.3.12.

3.4.3 b-tagging

An hadronic jet which originates from the production of a b-hadron is know as b-jet. The identification of this kind of physical object is a crucial factor in a wide range of physics

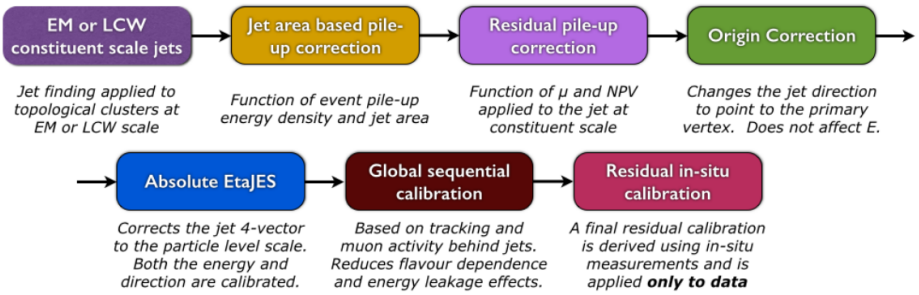

FIGURE 3.12: Overview of the ATLAS jet calibration steps.

analyses, going from Standard Model precision measurements to the study of heavy particles properties such as top quark and Higgs up to Beyond Standard Model searches. It is of course crucial in the present analysis where in the final state we want to select exactly two b-tagged jet to reconstruct the Higgs candidate.
b-tagging algorithms are specifically introduced for their identification and they are strictly based on the intrinsic properties of b-hadrons. Their lifetime is of the order of 1.5 ps and, for a p_T = 50 GeV, its mean flight path length allow it to travel in the detector volume about 3 mm before decaying, resulting in a typical topology with at least one vertex slightly displaced from the primary vertex, as can been in Fig.3.13.
The common basis of all the kinds of b-tagging algorithms is the exploitment of charged

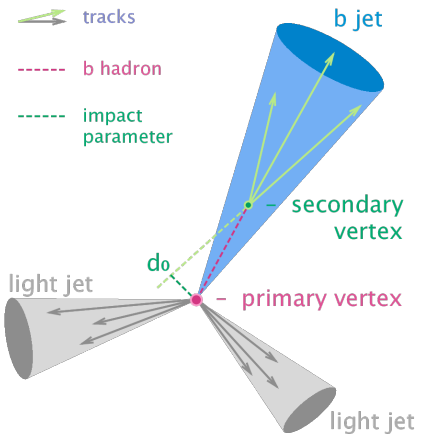

FIGURE 3.13: Common topology at the basis of b-jets identification.

particles tracks to produce a set of variables, useful for jet flavour discrimination. ATLAS uses three different types of algorithm.

- Impact parameter based algorithm.
- Inclusive secondary vertex reconstruction algorithm.
- Decay chain multivertex algorithm.

The output of these different way of approach to b-tagging are then recombined in a multivariate discriminant, which provides the best separation between jet flavours [69], [70]
.

Impact parameter based algorithms: IP2D and IP3D

IP2D and IP3D make use of the impact parameter significance of the tracks matched to the jet. They are labelled as *inclusive* since they do not completely displace the primary and secondary vertex in the reconstruction procedure. The sign of the impact parameter is defined depending on the position of the point of closest approach of the track to the primary vertex with respect to the jet direction: if it is in front of it the sign is taken positive, otherwise it is negative. The probability distribution functions (PDFs) for the single impact parameters are used to define the ratios between the $b-$ and light flavour jet hypotheses and then they are combined in a single log-likelihood discriminant (LLR). IP3D uses both the transverse d_0 and longitidinal z_0 impact parameters taking into account their correlations, while IP2D only uses the transverse one.
Fig.3.14 shows the transverse and longitudinal impact parameter distribution for the tracks

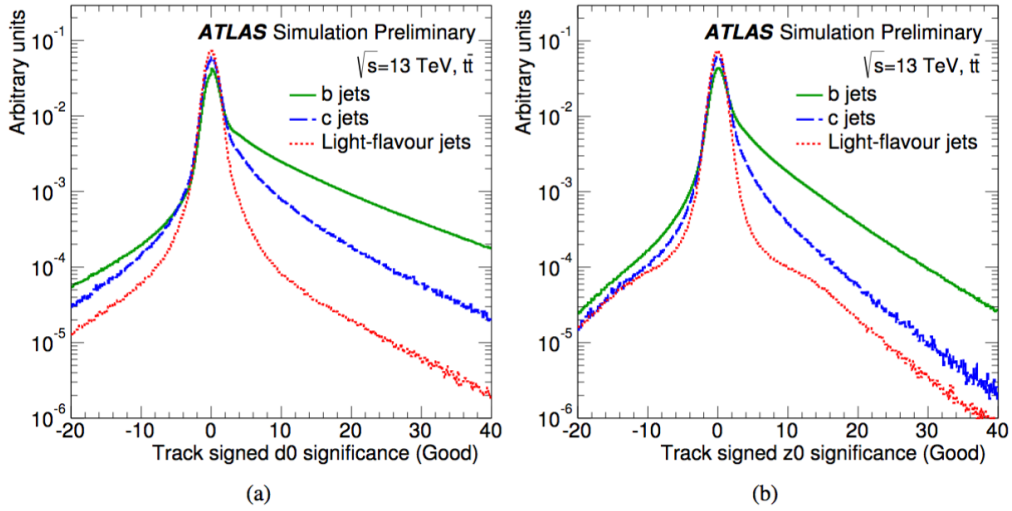

FIGURE 3.14: Distribution of (a) transverse and (b) longitudinal impact parameter [70].

from $b-$, $c-$ and light flavour jets. Typically, b-jets have high impact parameter and the cut on this value allow a good discrimination power.
IP2D is more robust, compared to IP3D, since it does not take into account z_0, more affected from pileup jets.

Secondary Vertex Finding Algorithm: SV

The aim of the secondary vertex based algorithm is to reconstruct the displaced secondary vertex within the jet. The procedure starts with the reconstruction of two tracks vertices. Tracks are rejected if they form a secondary vertex identified as originating from the decay of a long-lived particle, photon conversion or hadronic interactions with the detector material.
A second vertex is then reconstructed with the remaining tracks. Fig.3.15 shows the SV reconstruction efficiency with respect to jet p_T (a) and η (b).

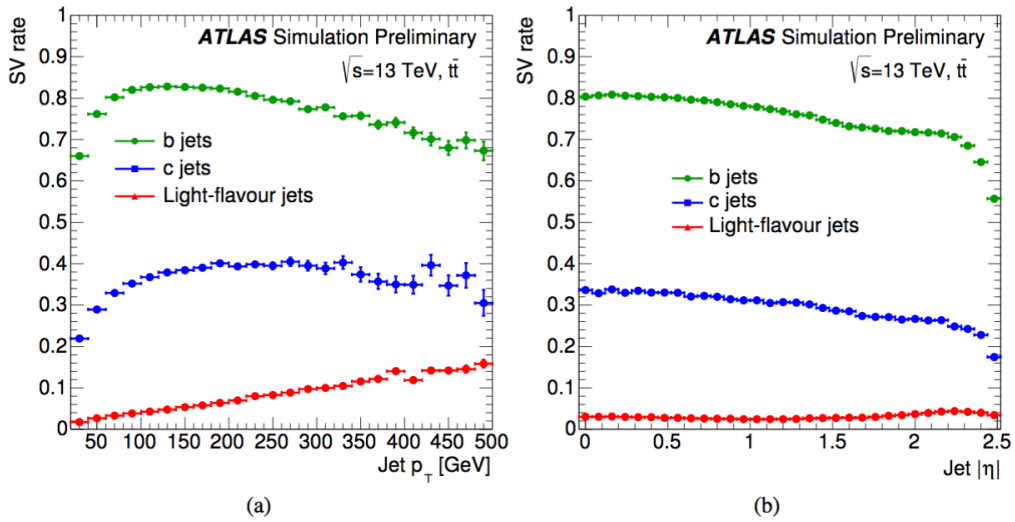

FIGURE 3.15: Secondary vertex reconstruction rates for Secondary Vertex Finding Algorithm.

Decay Chain Multivertex Algorithm: JetFitter

The exclusive algorithm JetFitter attempts to reconstruct the full primary vertex of b- and c- hadron decay chain, by exploiting the topological structure of the phenomena. A Kalman Filter is applied to find the common line on which the primary vertex and the bottom charm vertices lie as well as their positions, from considerations on the $b-$hadrons flight path. Following this approach, it is possible to resolve the $b-$ secondary vertices. Fig.3.16 shows the JetFitter reconstruction efficiency with respect to jet p_T (a) and η (b).

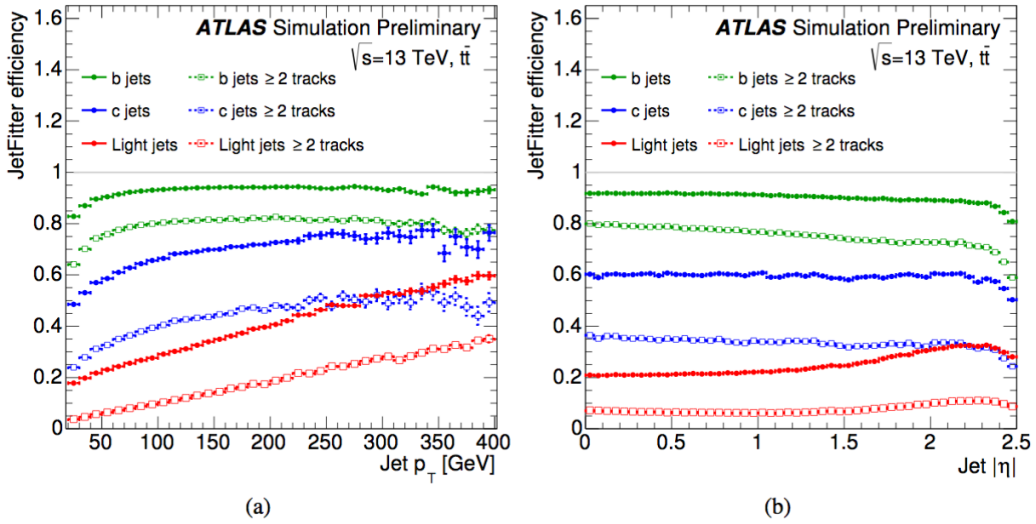

FIGURE 3.16: Secondary vertex reconstruction rates for JetFitter [70].

Multivariate Algorithm: MV

The inputs variables obtained from the three types of algorithms described above are combined in a boosted decision tree (BDT) algorithm to achieve an even better discrimination between $b-$quarks from c- and light flavour jets: the MV2 algorithm. It is a significant improvement of the previous MV1 used in Run1, not only for the better performance, but also because it has a significantly simpliflied machinery. In Tab.3.3 are listed and divided per originating algorithm all the discriminating variables entering in BDT construction and sensitive to jet flavour.

TABLE 3.3: The 24 input variables used in the multivariate algorithm MV2.

Input	Variable	Description
Kinematics	p_T^{jet}	Jet Transverse Momentum
	η_T^{jet}	Jet Pseudorapidity
IP2D, IP3D	$\log(P_b/P_{light})$	Likelihood ratio between $b-$ and light jet hypothesis
	$\log(P_b/P_c)$	Likelihood ratio between $b-$ and $c-$ jet hypothesis
	$\log(P_c/P_{light})$	Likelihood ratio between $c-$ and light jet hypothesis
SV	m(SV)	Invariant mass of tracks at the secondary vertex assuming pion masses
	f_E(SV)	Fraction of the charged jet energy in the secondary vertex
	$N_{TrkAtVtx}$(SV)	Number of tracks used in the secondary vertex
	$N_{2TrkAtVtx}$(SV)	Number of two track vertex candidates
	L_{xy} (SV)	Transverse distance between the primary and secondary vertices
	L_{xyz} (SV)	Distance between the primary and secondary vertices
	S_{xyz} (SV)	Distance between the primary and secondary vertices divided for its uncertainty
	ΔR (jet, SV)	ΔR between the jet axis and the direction of the secondary vertex relative to the primary vertex
JetFitter	$N_{2TrkAtVtx}$(JF)	Number of two track vertex candidates (prior to decay fit)
	m (JF)	Invariant mass of tracks from displaced vertices assuming pion masses
	S_{xyz}(JF)	Significance of the average distance between the primary and displaced vertices
	f_E (JF)	Fraction of charged jet energy in the secondary vertices
	$N_{1-trkvertices}$ (JF)	Number of displaced vertices with one track
	$N_{\geq 2-trkvertices}$ (JF)	Number of displaced vertices with more than one track
	$N_{TrkAtVtx}$(JF)	Number of tracks from displaced vertices with at least two tracks
	ΔR ($\overrightarrow{p}_{jet}$, $\overrightarrow{p}_{vtx}$)	ΔR between the jet axis and the vectorial sum of all the momenta of all the tracks attached to displaced vertices

Three variant of MV2 have been realesed: MV2c00, MV2c10 and MV2c20, where the differences in the names points to the c-flavour composition.
Fig.3.17 shows the MV2c10 BDT output from $t\bar{t}$ events.
The efficiency calibrations of the b-tagging algorithms are set by fixed values: *working points* WP. Working points are single cut values on the MV2 distribution and are chosen to provide target b-tagging efficiencies. In Tab.3.4, the values of the recommended working points are

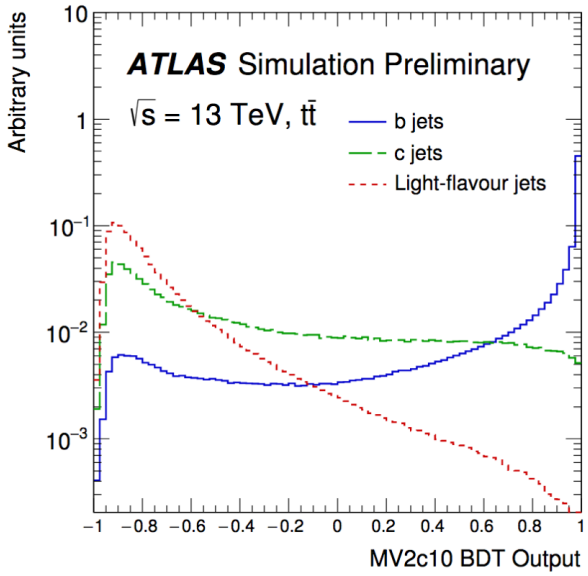

FIGURE 3.17: MV2c10 BDT output for b-(blue), $c-$ (green) and light-(red) flavour jets, evaluated in $t\bar{t}$ events, [70].

shown.

Later on, in the Chapter dedicated to event selection for this analysis, details will be pro-

TABLE 3.4: Operating points for the MV2c10 b-tagger. For a fixed cut on the BDT output, the resulting b-jet efficiency as well as charm, light and τ rejection are shown.

BDT cut value	**$b-$jet efficiency [%]**	**$c-$jet rejection**	**light-jet rejection**	**τ rejection**
0.9349	60	34	1538	184
0.8244	70	12	381	55
0.6459	77	6	134	22
0.1758	85	3.1	33	8.2

vided about the exact b-tagging strategy adopted.

A considerable enhancement in b-tagging performance is achieved thanks to the Insertable B-Layer, as anticipated in Chapter 2. Fig.3.18 and 3.19 show the performance comparison of the default b-tagging algorithm in Run1 (MV1c), with Run1 detector and reconstruction strategy, and MV2c20, with the Run2 detector and algorithm updates. Looking at the distribution, it can be seen that the light-flavour jet rejection is improved by a factor of 4 and the $c-$jet rejection by a factor 1.5-2 with a b-tagging efficiency of 70%. The advantage of the IBL lies in the improvement of the impact parameter resolution for the low-medium p_T jets.

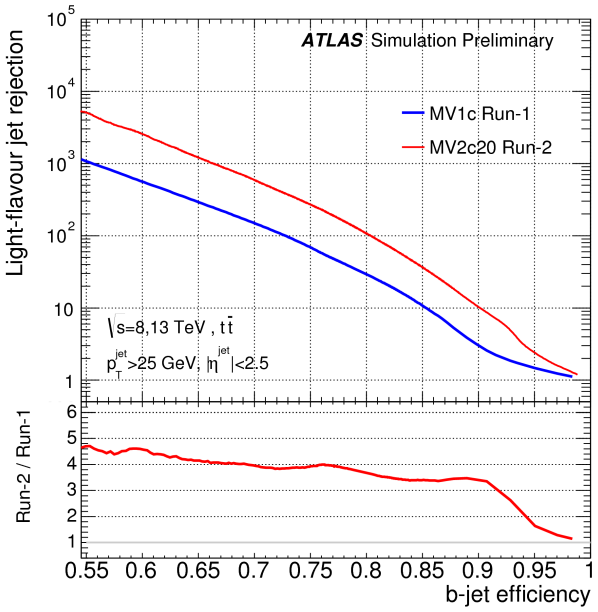

FIGURE 3.18: Light jet rejection with respect to $b-$jet efficiency for the MV1c b-tagging algorithm compared to the MV2c20 [70].

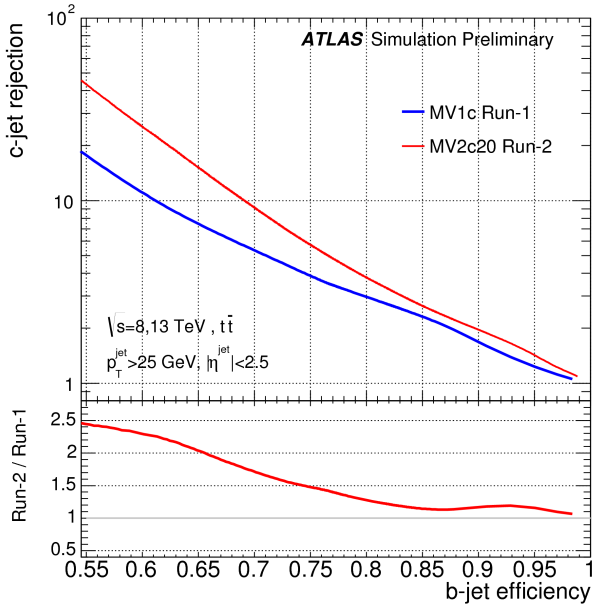

FIGURE 3.19: c- jet rejection with respect to $b-$jet efficiency for the MV1c b-tagging algorithm compared to the MV2c20 [70].

Chapter 4

The Measurement of $ZH(H \to b\bar{b})$ with $Z \to \ell^+\ell^-$

The search for the Standard Model VH(H$\to b\bar{b}$) is of high importance at LHC since it can directly prove the Higgs coupling to the quark sector. As said in Chapter 1, the Higgs decay mode in a pair of b-quarks has the largest branching ratio, 58%. The most sensitive production mode is the VH channel, known as Higgsstrahlung. At LHC, it is the third production mode with a predicted cross section of 2.3 pb at 13 TeV, [1]. Nevertheless, it is the preferred way to study the $b\bar{b}$ decay, which has always been so elusive due to the overwhelming QCD background. The advantage in using this channel is that the leptonic decay of the vector boson V provides a clear signature for the final state, helping the rejection of the multi-jet background.
The present thesis deals with the analysis performed combining the data collected in 2015, 2016 and 2017 (corresponding to an integrated luminosity of 79.8 fb^{-1} [71] and the following iteration with the full Run2 statistics (integrated luminosity of 139 fb^{-1}).

4.1 General Analysis Strategy

The goal of the $VH(H \to b\bar{b})$ analysis is the extraction of the *signal strength* μ with a global binned *Profile Likelihood* fit (*PFL*) of the data and Monte Carlo samples [72]. The signal strength is defined as production times the decay rates relative to the Standard Model prediction:

$$\mu = \frac{(\sigma \times BR)_{obs}}{(\sigma \times BR)_{SM}} \tag{4.1}$$

where σ_{obs} and σ_{SM} are observed and Standard Model expected cross section and BR is the branching ratio of the process of interest. From the signal strength measurement, one can obtain information about the couplings of the Higgs boson. The likelihood function, considering only statistical uncertainties is built as [73]:

$$\mathcal{L}(\mu) = \prod_{i=1}^{N_{bins}} = \frac{(\mu s_i + b_i)^{n_i}}{n_i!} e^{-(\mu s_i + b_i)} \tag{4.2}$$

where:

- μ is the signal strength.
- s_i are b_i are the expected number of events in the bin i, respectively for signal and background over a total numeber of bins N_{bins}.
- N_i is the total number of events in the bin i.

However, systematic uncertainties have to be introduced as a vector $\boldsymbol{\theta}$ of *nuisance parameters* NP to take into account possible Monte Carlo mismodelling in the simulation of data and detector response. Each systematic uncertainty corresponds to a i_{th} component of the vector $\boldsymbol{\theta}$. The profile likelihood function then becomes:

$$\mathcal{L}(\mu, \boldsymbol{\theta}) = \prod_{i=1}^{n_{bins}} = \frac{(\mu s_i(\boldsymbol{\theta}) + b_i(\boldsymbol{\theta}))^{n_i}}{n_i!} e^{-(\mu s_i(\boldsymbol{\theta}) + b_i(\boldsymbol{\theta}))} \times \mathcal{L}_{aux}(\boldsymbol{\theta}) \tag{4.3}$$

where $\mathcal{L}_{aux}(\boldsymbol{\theta})$ are functions representing auxiliary measurements with a likelihood function approximable to a Gaussian. They are defined as:

$$\mathcal{L}_{aux}(\boldsymbol{\theta}) = \prod_{j=1}^{n_{syst}} \frac{1}{\sqrt{2\pi}\sigma_j} e^{-\frac{(\hat{\theta_j} - \theta_j)^2}{2\sigma_j^2}} \tag{4.4}$$

where $\hat{\theta}_j$ is the central value of the Gaussian corresponding to nominal value of the systematic uncertainty j, n_{syst} is the total number of systematic uncertainties being considered, θ_j is the corresponding best fit value, σ_j the prior uncertainty of θ_j.
The auxiliary measurements act as costraint of the nuisance parameters within their uncertainties.
The flow of the analysis to come to the binned profile likelihood fit is described in the following.

1. **Events and object selection**.
   The signal we want to reconstruct is the VH decay which is characterized by the final state:

   - the leptonic decay of the vector boson V
   - the Higgs boson decay in two b-quarks

   In a first stage, the event phase space is divided upon the number of **charged** leptons from the V decay. This results in a *split* of the analysis in three different channels (ℓ=e, μ, not τ):

   - 0-lepton channel: ZH$\to \nu\bar{\nu}b\bar{b}$.
   - 1-lepton channel: W$^{\pm}$H $\to \ell^{\mp}\overset{(-)}{\nu}b\bar{b}$.
   - 2-lepton channel: ZH$\to \ell^+\ell^- b\bar{b}$.

   In each channel the events are then categorized according to the boson transverse momentum p_T^V which are later on divided by the multiplicity of jets in the final state, with exactly 2 b-tagged jets which corresponds to the Higgs candidate.
   As it regards the 79.8 fb^{-1} analysis, for the 0- and 1-lepton channel, one single p_T^V region is considered with p_T^V, splitted in 2 and 3 jet final states.
   For the 2-lepton channel, which is the main argument of this thesis, two p_T^V regions are considered:

   - 75 GeV <p_T^V<150 GeV (*medium* p_T region)
   - p_T^V>150 GeV (*high* p_T region)

   Both of them are splitted in two regions with 2 jets and $\geq$3 jets multiplicity. It is important to underline that it is possible to investigate the medium p_T^V region in the 2-lepton channel thanks to the peak of the Z boson decaying in two charged leptons.

These divisions of the phase space result in eight signal regions.
For the iteration of the analysis with the Full Run2 statistics ($\sim$139 fb^{-1}), an additional p_T^V cut at 250 GeV is introduced in region p_T^V>150 GeV, leading to a total number of 14 signal regions.
The object reconstruction is performed following the Combined Performance recommendation.
The details about the object and event selection are provided in 4.9.1 and in 4.9.2 for the 2-lepton channel.

2. **Multivariate Analysis**.
A Multivariate Analysis (MVA) is performed on simulated samples for signal and background to obtain the classifiers for the signal and background discrimination. The chosen classifier is the *Boosted Decision Tree* (BDT). The variables entering the MVA analysis are the ones with the highest discrimination power between signal and background.
The MVA analysis is performed in each VH signal region resulting from the event selection and the BDT_{VH} output are inputs for the signal strength by the PFL fit. Details are described in Sec.(4.10).
An MVA analysis is performed as a cross-check on VZ signal, 5.1.2. The signal strength of VZ is extracted with the same technique used for VH and it is used as consistency check of the MVA procedure.

3. **Systematic Uncertainties**. The systematic uncertainties enter in the profile likelihood fit as nuisance parameters, as stated above.
The largest background normalization NPs is left to be determined in the fit to data, without having priors. For $Z + HF$ and $W + HF$, the normalization factors are affected by theoretical uncertainties which are evaluated from comparisons of the nominal and the alternative Monte Carlo generators and from internal variation of the nominal Monte Carlo, see Sec.(4.4). The main sources of background are left floating and extracted from the fit.
Additional experimental systematic uncertainties are described in 5.2.1.

4. It is important to underline that, at this stage, the analysis is still blind. This procedure is performed to avoid the *experimenter's bias*, the unintended biasing of the result in a particular direction. It is typically applied in case of search for rare processes. When analyzing data, the data are *blinded* in the region where an excess of events of interests for the discovery is expected. Only when the analysis method, the selection cut and the background estimate is fixed, the region is *unblinded*.

5. The MVA output and the evaluated systematic uncertainties are input for the global profile likelihood fit leading to the signal strength extraction, which is described in Sec.(4.12). The statistical analysis procedure is described in Sec.(5.1).

Since my personal involvement is related to the 2-lepton channel, in the present Chapter, I will describe the main feature of the VH analyses in the 2-lepton channel describing the event selection, the data and Monte Carlo samples used and the main sources of background and how they are modelled. The last part of the Chapter is dedicated to the description of the Multivariate analysis tools used for the estimation of the signal strength.

4.2 Derivation Framework

The Run2 analysis model for ATLAS includes the centralised production of analyis specific data formats containing interesting events and, at the same time, reducing the problem of the large amount of data to be processed and stored.
A feature common to many physics analyses is the use of intermediate-sized data formats at some stage of the analysis procedure. Typically, these formats are made directly from the retained output of the reconstruction: known as Analysis Object Data or AOD in ATLAS. They have the following features:

- they have a size around a few percent to a few per mille of the input data.
- they are typically aimed at one analysis or perhaps a group of related analyses (for example, they share the same final state).
- they usually contain all of the information necessary to perform smearing, scaling, selection, calibration and other operations on reconstructed objects (known in ATLAS as combined performance operations) and evaluate the systematic uncertainties related to them.
- they are used privately by physicists or groups of physicists to produce their small n-tuples, on which the final analysis is performed.

The strategy has been changed during Run2 in order to solve these issues. The intermediate formats are produced from AOD using a common software: the *Derivation Framework*. The ATLAS definitions for the four standard operations for informal removal are:

- Skimming: the removal of whole events.
- Thinning: the removal of individual objects within an event.
- Slimming: the removal of not necessary variables within a given object type.
- Augmentation: the addition of information not found in the input data.

The derivations are performed starting from the output of the general reconstruction framework ATHENA. The ATLAS analysis model is shown in Fig.(4.1). The model is based on a new

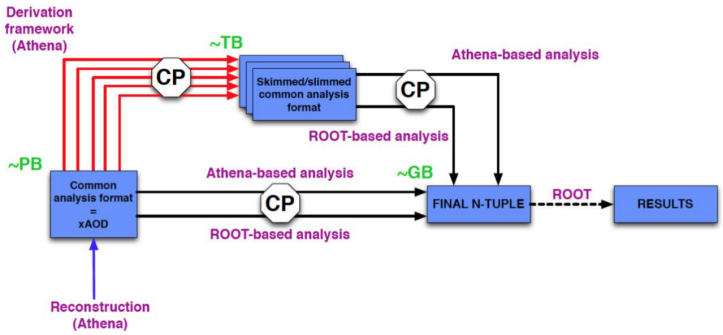

FIGURE 4.1: Scheme of the ATLAS Derivation Framework adopted for Run2. The data are reconstructed by ATHENA and derived by the Derivation Framework, under the ATHENA system. The data samples size decreases from the order of PB to few GB. The Combined Performances (CP) help the derivation giving information about the objects to use and the calibrations to apply on them.

format, xAOD, produced directly by reconstruction and which replaces the Run1 AOD. The derivation framework acts on them to create the intermediate data products by removing and adding, through the steps previously listed, information maintaining the structure and the Event Data Model (EDM), used in the original xAOD. The last component of the chain is the analysis framework, which is used to read the derived data formats, apply combined performance and tools and produce the final ntuples.
Derivation are usually defined by individual physics analysis teams according to specific analysis requirements. The derivation used for 2-lepton channel is HIGG2D4 for 2-lepton channel.
Later on, the CxAOD Framework acts on them using two algorithms. It is a general purpose analysis tool designed and devoloped by the *Hbb* group to serve as an interface to the wide variety of combined performance (CP) tools provided by the ATLAS Collaboration. The first algorithm is the CxAODMaker which runs on Derived xAODs (DxAODs) to produce slimmed dataset following the xAOD EDM called Calibrated xAOD (CxAOD), by applying object selections and low level event selections.
The second algorithm is the CxAODReader executes the analysis event selection on CxAODs to produce n-tuples or histograms. A schematic overview of the CxAODFramework used for this analysis is shown in Fig.(4.2).

FIGURE 4.2: Hbb CxAODFramework workflow.

4.3 Monte Carlo Samples

Monte Carlo samples are used to simulate signal and background processes, relevant for the analysis purposes.

The Event Generator

As said in Chapter 1, protons are composite objects made of partons which can be distinguished in *valance quarks*, *gluons* and *sea quarks*. Each proton has three valence quarks, two up quarks and one down quark, defining its fundamental properties. The interaction among them is mediated by gluons, which can create virtual quark/anti-quark couples (the sea quarks) eventually annihilating into a gluon. An hard-scattering must occur to have a new and high mass particles, i.e. at high momentum transfer: as we have already seen this corresponds to the asymptotic freedom scenario, where the partons, although bound inside the proton, can be considered as free particles in such reactions. The interacting partons in a hard scattering can be valence quarks, gluons or sea quarks and they carry a fraction x of the total proton's momentum.
The *factorization theorem* help us to describe what happens during a pp collision, splitting the event in several parts, all used separately in the event simulation. The differential cross section, with O representing a set of variables, for a process involving two partons carrying

momenta p_1 and p_2 can be, therefore, expressed by:

$$\frac{d\sigma_{pp\to X}}{dO} = \sum_{ij} \int dx_1 dx_2 \int d\Omega f_i(x_1,\mu) f_j(x_2,\mu) \frac{d\hat{\sigma}_{ij\to X}(x_1,x_2,\Omega,\alpha_s(\mu),\mu)}{d\hat{\Omega}} D_{x\to X(\Omega,\mu)} \tag{4.5}$$

where μ stands for both the factorisation (μ_F) and renormalisation (μ_R) scales, which are usually chosen at the same value, and α_S is the strong coupling constant. In Eq.(4.5) the different parts involved in a hard scattering can be identified.

- The parton content of the incoming protons are represented by the Parton Distribution Functions (PDFs) f_i and f_j. PDFs describe the probability of a parton i (j) to carry a fraction x of the proton momentum.
- The hard scattering event producing new particles is described by the Matrix Element (ME) which is represented by the partonic differential cross section $d\hat{\sigma}/d\hat{\Omega}$.
- The transistion function $D(x \to X(\Omega,\mu))$ represents the transition from partons to hadrons, which involves the parton shower (PS) and hadronisation.

Fig.(4.3) shows a sketch of a pp collision simulation.

The PDF describes the probability of a certain parton to take part in a hard scattering

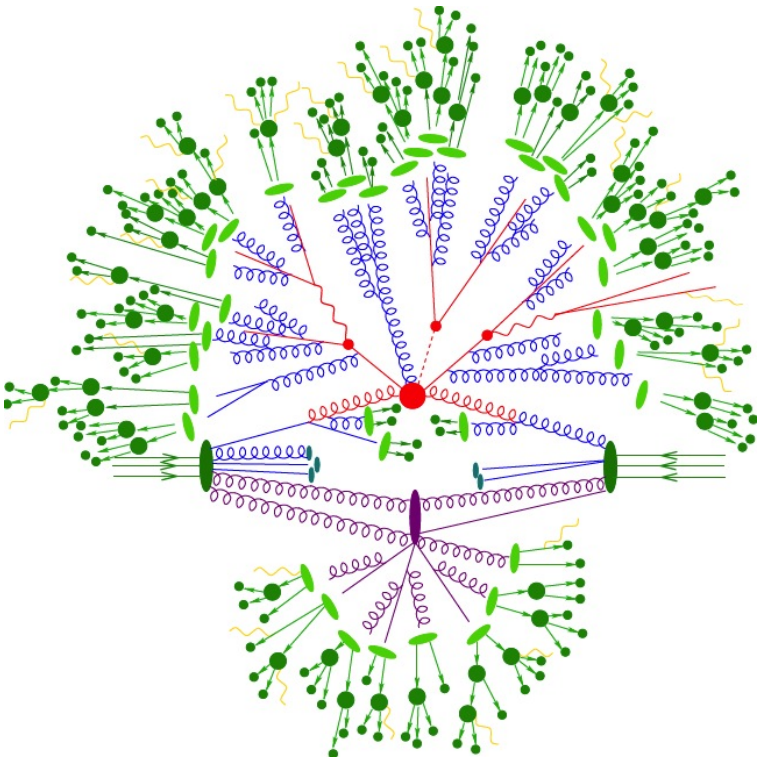

FIGURE 4.3: The hard scattering is shown in red, simulated by the Matrix Element generators. Multiple interaction models simulate secondary interactions, shown in purple. Parton Showers, in blue, produce bremsstrahlung. Fragmentation models describe the hadronisation of partons, shown in light green. Decays of unstable partons are shown in dark green.

collision, carrying a fraction x of the proton momentum. This information is essential to properly estimate the partonic cross section. Due to the lack of the QCD theory in describing low energy interactions, PDFs come out from several kind of measurements, sensitive

to the proton internal structure such as electron-proton collision, Drell-Yan and jet production in proton-proton collisions. The results are then combined into fits to extract the full distributions for all partons and x to extrapolate to the desired energy scale μ. These studies are carried by different collaborations which adopt several strategies to provide their PDF sets to be used in Monte Carlo simulations. As a consequence, the choice of the PDF set influences the predictions of the simulation. Together with the predictions, the errors on them are provided in order to correctly asses the systematic uncertainty for the chosen PDF set.
The Matrix Element (ME), as said above, describes the hard scattering at parton level. It is calculated from QED and QCD theory with the help of Feynman rules. The simulation programs which calculated the ME do not go beyond the Next-to-Leading Order (NLO) in order not to have routines too much time consuming. In the Leading Order (LO), the diagrams with the largest contribution to the process are taken into account, while at NLO loop radiative correction are introduced. All the diagrams are calculated at the same energy scale μ, so different ME simulations with the same precison can still be different upon the choice of μ.
The factorisation and renormalisation scales, respectively μ_F and μ_R, are two cut-off scales which separate short distance from long distance effects, meaning that loops and real emissions below them are only approximated. Most of the simulation models choose the same value for both scales. In general, the value μ assessed to the two scales is to an energy of the order of the hard scattering scale (the energy in the center of mass, the mass of the heavy particles produced, etc.). The choice of the scale changes the prediction but most of the simulators offer the variation of μ from its nominal value to properly estimate the systematic originating from its choice.
The parton shower (PS) connects the ME (parton level) to the produced and observable hadrons. The process described is the one which partons produced at ME undergo. Before hadronization, there are several stages of intermediate radiation until a certain scale is reached (typically 1 GeV). The evolution parameter, which is proportional to the energy scale, orders the evolution in a way that each additional branching of the parton is lower in t (Mandelstam variable for the square of the 4-momentum transfer) than the previous one. The choice of the evolution parameter strictly depends on the simulation model. PS simulators can be matched to ME ones with the caveat of resolving possible overlap between them: it can happen that in NLO ME generations the radiation of extra partons is already included so the same contribution from the PS has to be removed in order to avoid the probability exceed unity.
Above 1 GeV, the formation of hadrons, described by hadronization, occurs. The simulation models used at ATLAS use the *string fragmentation* model or the *cluster fragmentation* model, see Fig.(4.4). The string fragmentation model connects partons from PS via *color strings*, representing the field of strong force between the color charges. When two quarks move apart, the energy of the field grows until it becomes large enough to create a new $q\bar{q}$ pair, breaking the string. The process continues until the energy is absorbed and the quarks are grouped into hadrons. The cluster fragmentation breaks the gluon from PS into a $q\bar{q}$ pair. It then pairs each quark with an anti-quark forming clusters. The clusters decay into hadrons absorbing all the energy stored. In both the models, baryons are formed if *diquarks* (loosely bound states) pairs are formed. Several tunings are performed to properly model the observed fraction hadrons. The hadrons simulated may not be stable, meaning that they decay inside the detector volume. The decays are modelled inside the simulations using information about hadron lifetime, branching ratios and hadron decay width.
Beyond the main processes occurring in a hard scattering, additional interactions have to be considered. They are described by underlying event simulations. Since the energy scale is of the order of few GeV, small if compared to the energy of the hard scattering event, the

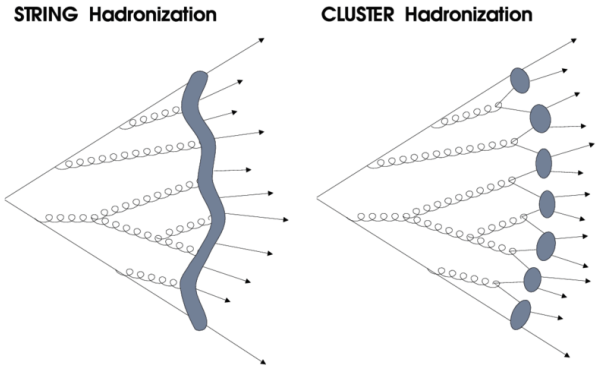

FIGURE 4.4: Representation of the string (left) and cluster (right) fragmentation models.

underlying events only produce a uniform underlying activity in form of hadrons but not additional jets. In order to introduce the additional interactions, a cut-off scale is introduced with an estimation based on proton radius and collision energy. It is usually tuned with results obtained from data.
Finally, an additional correction is implemented to take into account *pile-up* events, not emerging from the hard scattering between the two protons, due to the bunched configuration of the LHC beams. In the simulators, they do not include hard scattering events and they are modelled as exchange of gluons at small center of mass energies.

Monte Carlo Simulation for VH(H$\to b\bar{b}$)

In the context of the analyses presented in this thesis, several Monte Carlo generators are used, following the ATLAS recommendations on the choice for a particular process, in order to describe it with the best achievable precision. Alternative generators are used to evaluate systematic uncertainties. The list of the main generators used includes:

- POWHEG [74] MC generator only generates the ME at NLO precision. In the simulation used for this thesis, the default strategy is to interface with PYTHIA for the description of the PS for signal VH and $t\bar{t}$ background modelling.
- PYTHIA [75] provides LO ME calculation and it is able to provide PS and UE modelling by string fragmentation. Since it provides LO ME precision, it is usually interfaced with NLO precision simulators.
- SHERPA [76] is a stand-alone MC generator, providing NLO precision for a variety of processes. It is the preferred generator for processes with additional jets, which Sherpa can include in ME.

Tab.(4.1) shows the main Monte Carlo generators used to simulate signal and background processes in the 2-lepton channel.

TABLE 4.1: Monte Carlo generators used for the simulation of signal and background in 2-lepton channel. Tools used for the described simulation steps are specified together with the order of the cross section prediction.

Process	ME Generator	ME PDF	PS and Hadronization	UE Model Tune	Cross Section order
Signal for a SM Higgs with m_H=125 GeV and $b\bar{b}$ branching fraction to 50%					
$qq \to ZH \to \ell^+\ell^- b\bar{b}$	POWHEG-BOX2 + GOSAM + MiNLO	NNPDF3.0NLO	PYTHIA 8.212	ZNLO	NNLO(QCD)+NLO(EW)
$gg \to ZH \to \ell^+\ell^- b\bar{b}$	POWHEG-BOX2	NNPDF3.0NLO	PYTHIA 8.212	ZNLO	NNLO(QCD)+NLL
Top quark with m_t=172.5 GeV					
$t\bar{t}$	POWHEG-BOX2	NNPDF3.0NLO	PYTHIA 8.230	A14	NLO+NNLL
single t s-channel	POWHEG-BOX2	NNPDF3.0NLO	PYTHIA 8.230	A14	NLO
single t t-channel	POWHEG-BOX2	NNPDF3.0NLO	PYTHIA 8.230	A14	NLO
single t Wt	POWHEG-BOX2	NNPDF3.0NLO	PYTHIA 8.230	A14	Approximate NLO
Vector boson+jets					
$W \to \ell\nu$	SHERPA 2.2.1	NNPDF3.0NLO	SHERPA 2.2.1	Default	NNLO
$Z/\gamma^* \to \ell\ell$	SHERPA 2.2.1	NNPDF3.0NLO	SHERPA 2.2.1	Default	NNLO
$Z/\gamma^* \to \nu\nu$	SHERPA 2.2.1	NNPDF3.0NLO	SHERPA 2.2.1	Default	NNLO
Diboson					
qq → WW	SHERPA 2.2.1	NNPDF3.0NLO	SHERPA 2.2.1	Default	NLO
qq → WZ	SHERPA 2.2.1	NNPDF3.0NLO	SHERPA 2.2.1	Default	NNLO
qq → ZZ	SHERPA 2.2.1	NNPDF3.0NLO	SHERPA 2.2.1	Default	NNLO
gg → VV	SHERPA 2.2.2	NNPDF3.0NLO	SHERPA 2.2.2	Default	NNLO

The alternative Monte Carlo samples used for the assessment of systematic uncertainties are HERWIG [77] and MADGRAPH_aMC@NLO [78].
HERWIG is a multi-purpose generator which is no longer used as stand-alone. It is still used to provide the PS description for a simulation model. For the hadronization, it uses the cluster fragmentation model and special tunes for PS. It is used as alternative generator for PS for $t\bar{t}$ and single top, both interfaced with POWHEG and MADGRAPH for ME. In the case of signal and diboson background, it is interfaced just with POWHEG.
MadGraph5_aMC@NLO provides only ME calculations and it is interfaced with PYTHIA or to HERWIG for PS. It used as alternative generator for ME for all the background. It is interfaced with PYTHIA8 for PS in the case of $V + jets$ and $t\bar{t}$ and with HERWIG for $t\bar{t}$, single-t and diboson.

4.3.1 The Detector Simulation

After the event simulation, the interactions of the particles in final state with the detector are simulated to allow the comparison with real events. For the present analyses, GEANT4 (GEometry ANd Tracking) [79] software has been chosen. It provides a model for the particles interactions through matter. Each detector component is implemented as a separate piece, together with materials from support structures, to allow a constant update in case of changes. The final simulation of an event in the ATLAS detector, the outcome from the MC Event generator is putted into the detector simulator. The last step of the simulation chain is the digitization of the detector response to a particle interacting with it. The information is, by GEANT4 construction, available for each single detector module, allowing to pass the simulated event through the same trigger and reconstruction algorithms for the data event.

4.4 Signal and Background processes

The aim of the analyses presented in this thesis is to measure the associated production of the Higgs boson decaying into two b-quarks together with a vector boson decaying leptonically. In particular we are interested in the study of the final state events with two charged leptons corresponding to ZH$\to \ell^+\ell^- b\bar{b}$. It is also crucial to understand also all those events producing similar signatures and populating the same phase space of the signal process. As explained in the previous section, they are studied using MC simulation. The main sources of background for the 2-leptons channel are:

- V(Z,W)+$jets$
- $t\bar{t}$
- Diboson VV
- single top quark
- Multijet (QCD induced background)

4.4.1 Signal $ZH(H \to b\bar{b})$

For the ZH, two Feynman diagrams have to be considered, see Fig.(4.5).
The calculation of the ZH cross section is up to the NNLO QCD and NLO EW effect, see Tab.(4.1), resulting in two predicted values at 13 TeV:

- $\sigma(q\bar{q} \to ZH)$ = 0.76 pb. It corresponds to the diagram on the left in Fig.(4.5).
- $\sigma(gg \to ZH)$ = 0.12 pb. It corresponds to the diagram on the right in Fig.(4.5).

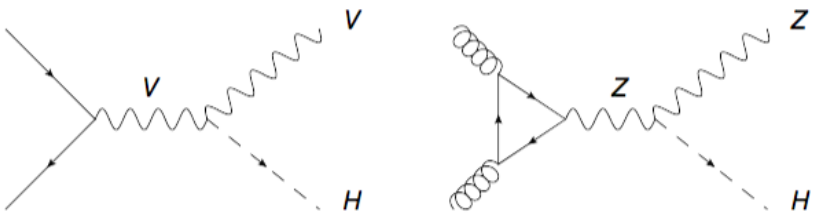

FIGURE 4.5: SM VH production. On the left, the quark induced production (*Higgsstrahlung*). On the right the gluon XH induced production.

4.4.2 V+jets

V+jets is an irreducible background for our signal when the vector boson decays into two leptons in association with two b-jets. It can happen when V=Z, but also when V=W if W decays into leptons. Moreover, there can be contamination also in the case of no b-jets due possible misidentification of the b-tagging algorithm. The cross section of a single V boson production is known at NNLO precision, at 13 TeV:

- $\sigma(pp \rightarrow Z + X)$ = 1906 pb
- $\sigma(pp \rightarrow W^{\pm} + X)$ = 20080 pb

However, most of these bosons are produced with no associated jets. The cross section with 2 or more additional jets has been measured to be 54 pb for Z+jets. Details about Z+jets samples and the systematic uncertainties related to its modelling are described with details in 4.5.

4.4.3 $t\bar{t}$

The second largest background is $t\bar{t}$, see Fig.(4.6). The production cross section is known at NNLO precision: $\sigma(pp \rightarrow t\bar{t} + X)$ = 831.76 pb at 13 TeV. A top quark decays into a W boson and a bottom quark with a branching ratio of 99%. If the two W bosons decay into $W^{\pm} \rightarrow \ell^{\pm}\overset{(-)}{\nu}$, the event mimics the Z decay into two charged leptons.

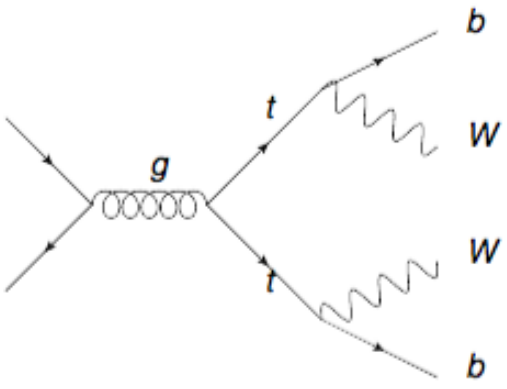

FIGURE 4.6: $t\bar{t}$ signal.

4.4.4 Diboson

Diboson production (ZZ, WZ or WW) is a subdominant background process. The cross sections at 13 TeV are low if compared to $V + jets$ and $t\bar{t}$ processes.

- σ(ZZ)=22.9 pb
- σ(WZ)=77.3 pb
- σ(WW)=117.5 pb

The ZZ events mimic the final state of ZH$\to \ell^+\ell^- b\bar{b}$ if one Z decays into a pair of charged leptons and the other one decays into a pair of quarks b (the invariant mass of the quark pair is in this case close to the one expected from an Higgs boson). Also the WZ events can enter the signal phase space if the Z boson decays leptonically and the W into two quarks due to the possible inefficiency of the b-tagging algorithms.

4.4.5 Single top quark

Single top production is another sub-dominant background. There are three different production channels: s, t and Wt, shown in Fig.(4.7). They lead to different final states. The

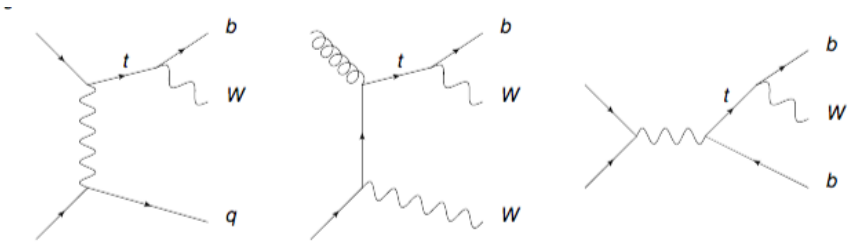

FIGURE 4.7: Single top production diagrams.

production cross section at 13 TeV for these processes are calculated up to NNLO precision:

- $\sigma(s-channel)$ = 10.3 pb (Fig.(4.7) left).
- $\sigma(t-channel)$ = 217.0 pb (Fig.(4.7) center).
- $\sigma(Wt-channel)$ = 71.7 pb (Fig.(4.7) right).

While s- and t- channels are almost negligible for the 2-lepton signal analysis, Wt can enter the phase space of interest in case the W boson decays leptonically and an additional jet is produced.

4.4.6 Multijet

Multijet is a QCD induced background including all processes with a final stat with partons without the presence of other particles. The analyses presented here suppress the amount of multijet events to a negligible level by the requirement of two isolated leptons (typically, in multijet events, non-isolated low p_T leptons come from hadron decays). An additional suppression is ensured by the requirement of two heavy flavour jets b since the production of them is usually suppressed with respect to light ones.
The strength of the suppression has been confirmed by data-driven studies as will be explained in 4.11.2.

4.5 Z+jets Monte Carlo samples and related systematic uncertainties

The production of Z in association with jets is one of the main sources of background for the 2-lepton channel. As can be seen from Tab.(4.1), the nominal Z+jets samples are simulated

using Sherpa 2.2.1., interfaced with NNPDF3, for ME calculation. Parton shower and underlying events are the ones provided internally by SHERPA. The generator adopts a full 5-flavour number scheme, with massless b-quarks and c-quarks in the matrix elements, while massive quarks are produced by parton shower or in the scattering process of the underlying event.
$Z + jets$ samples are splitted in slices of the vector boson and the H_T (defined as $H_T = \sum_{i \in FS} p_{T,i}$, i.e. the sum of the transverse momenta in the final state *FS*) of the event, introducing a cut at generation level. Samples are produced for different slices in max(H_T, p_T^V), where p_T^V is the transverse momentum of the truth lepton pair from the decay of the V boson. The split is performed in the following intervals:

$$\max(H_T, p_T^V) = [0-70, 70-140, 140-280, 280-500, 500-1000, >1000]\text{GeV}$$

It is necessary to generate the samples using these slices because of the rapidly falling p_T^V and H_T distributions.
Furthermore to obtain a sufficient number of heavy-flavour events, samples are generated with heavy flavour filters applied. Except for the highest max(H_T, p_T^V) slices, the filters applied are:

- *B-Veto*: at least 1 b-hadron present with p_T>0 GeV and $|\eta|$<4.
- *C-Veto*: at least 1 c-hadron present with p_T>4 GeV and $|\eta|$<3 and veto events which pass the B-filter.
- *B-Veto, C-Veto*: veto events which pass the b-filter and c-filter.

Nominal samples also include systematic variations, written as additional weights and corresponding to the following variations:

- factorization scale: $2\mu_F$.
- factorization scale: $0.5\mu_F$.
- renormalization scale: $0.5\mu_R$.
- renormalization scale: $2\mu_R$.
- PDF variation using MMHT2014nnlo68cl and CT14nnlo [80].

The alternative Monte Carlo samples provide a cross-check for the nominal prediction. They are useful to test how much the nominal prediction is reliable in describing single variables and phase space regions and can provide useful information about possible data/MC discrepancies or MC mis-modelling. For the presented analyses, the alternative samples considered for V+jets processes are generated using MADGRAPH which provides a LO (QCD) description of these processes for the ME, while for the parton shower its is obtained by the ATLAS A14 tune. They make use of NNPDF2.3 LO PDFs. MADGRAPH adopts the full 5-flavour number scheme with massless quarks in the ME calculation, while massive quarks are produced by the parton shower.
For $Z + jets$, the variable shape with the highest impact on the final fit for the signal strenght is m_{bb}. Fig.(4.8) shows the comparison between SHERPA, its internal variations (variations of μ_R and μ_F) and MADGRAPH. The alternative generator is well covered by the nominal internal variations but a mismodelling occurs at low energies.
The estimate of systematic uncertainties on the theoretical prediction of the Z+jets background relies on two main studies:

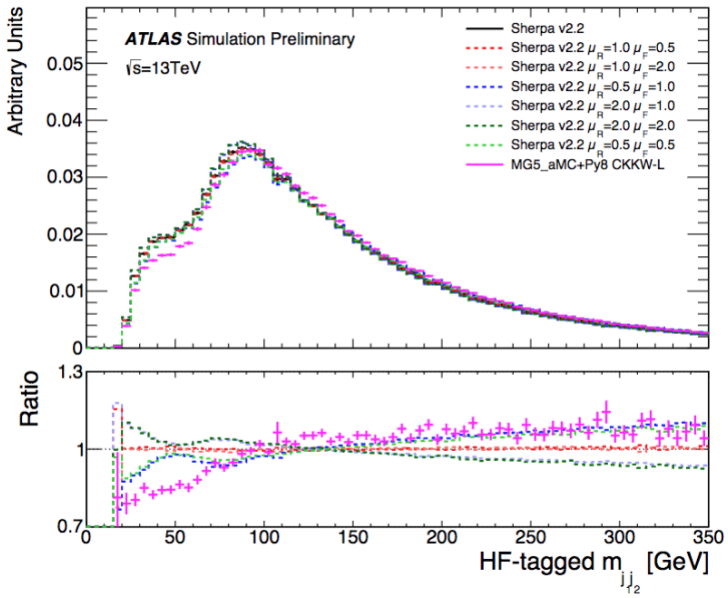

FIGURE 4.8: Shape comparison of the invariant mass of the two b-jets for $Z + jets$ for different MC predictions [81].

1. Particle-level studies of the nominal generator with varied scales to MadGraph (Monte Carlo based).

2. Data-driven comparison in high purity control regions.

As it regards the data driven approach, control regions are chosen in data which are dominated by $Z + jets$ background. In these regions, the total Monte Carlo background is compared to data [72]. The procedure is performed for m_{bb} and p_T^Z. The choice of the control region is chosen such that $Z+jets$ is the dominant background in order to consider possible data/MC differences due to modelling uncertainties due to this background. The 2-lepton channel has the highest purity due to the additional cut on the invariant mass of the Z boson and it is the chosen for the shape studies. An additional cut to reduce the $t\bar{t}$ contribution is applied by requiring a E_T^{miss} significance cut <3.5. The study is performed in different flavour compositions and for each of them in different jet multiplicity scenarios, 2jet or $\geq$3jet. They enter in the final fit as uncertainties on the m_{bb} and p_T^V shape distributions.

4.6 $t\bar{t}$, Diboson and single-t systematic uncertainties

As it regards the $t\bar{t}$, the normalisations in the 2- and $\geq$3jet regions are both left floating in the global fit and are determined in their respective $e\mu$ control regions. High purity control regions can be obtained by requiring different flavour of pair of dilepton ($e\mu$ or μe). Lepton flavour does not change the kinematics of $t\bar{t}$ between the signal region (same flavour) and the control region (different flavour). $t\bar{t}$ kinematic distributions using the control region are estimated by selecting same kinematic selection as signal region.

$$N_{top}^{SR} = \frac{N_{top}^{CR,data}}{N_{top}^{CR,MC}} \times N_{top}^{SR,MC} = \frac{N_{top}^{SR,MC}}{N_{data}^{CR,MC}} \times N_{top}^{CR,data} \tag{4.6}$$

As can be seen from Eq.(4.6), top background modelling in the signal region can be so constrained in the $e\mu$ control regions. Very pure control regions are obtained with more than 99% top contribution ($t\bar{t}$ and Wt), as can be seen also from the Data/MC comparisons in 4.11.6. The shape uncertainties of p_T^V and m_{bb} (most sensitive discriminant to constrain top background yields and shapes) distributions are estimated from the comparisons to alternative samples, see Tab.(4.1).
For the single top backgrounds, uncertainties are derived in the normalisation, acceptance and shapes of the m_{bb} and p_T^V distributions for Wt and t-channels. For Wt-channel, the modelling uncertainties are evalutated based on the flavour of the two b-tagged jets. The s-channel has only normalisation uncertainty since its contribution is overall negligible.
The diboson contribution is small, representing a 0.1% of the background. A normalization uncertainty is assessed and enters as input in the likelihood fit. WZ and ZZ have uncertainties derived for the overall normalisation, the relative acceptance between regions and for the m_{bb} and p_T^V shapes.

4.7 Truth Tagging

The b-tagging algorithm has a high rejection power against c- and $light$-jets. The downside is that the number of simulated background events after the b-tagging requirements, especially in case of background processes with c- and $light$-jets is highly reduced, causing instabilities in MVA training, modelling studies or in fit procedure. In 79.8 fb^{-1} analysis, the way chosen to circumvent the issue of the statistical fluctuation in the MC samples has been to remove events failing the b-tagging requirements and to apply a weight to each MC event: the *truth-tag* weight. The weights are based on the probability to have n tagged jets in the event. The truth tag weight is defined as the product of the b-tagging efficiency for each b-tagged jet times the complement of the b-tagging efficiency for each non b-tagged jet. All possible combinations of b-tagged and non b-tagged jets satisfying the analysis selection are considered and the total truth tag weight is defined as the sum of the truth tag weights of each combination.
Considering the example of a three jets event, requiring exactly 2 b-tagged jets with a b-tagging efficiency ϵ_i, the total truth tagging weight would be:

$$w_{tot} = \epsilon_1\epsilon_2(1-\epsilon_3) + \epsilon_1(1-\epsilon_2)\epsilon_3 + (1-\epsilon_1)\epsilon_2\epsilon_3 \tag{4.7}$$

The two jets selected as b-tagged are random chosen upon their tagging efficiency probability, following:

$$P_{1,2}^{tagged} = \frac{\epsilon_1\epsilon_2(1-\epsilon_3)}{w_{tot}} \tag{4.8}$$

which represents the probability to choose a certain combination, scaled by the total truth tagging weight. Following this approach, jets that are tagged are chosen randomly among all the possible combinations and independently from the real b-tagging score for the jets. For this reason, a new b-tagging weight is generated for each jet in the event. The tagged jets will have b-tagging scores sampled from the MV2c10 cumulative distribution above the 70% efficiency cut, the others will be assigned a b-tag score below 70%.
As it will be shown in Sec.4.11.5, I have worked to optimization studies in the context of the Multivariate analysis to check the performance of an alternative b-tagging method.

4.8 Data Samples

The two analysis described in this thesis are performed using data collected by the ATLAS detector in pp collisions at $\sqrt{s}$=13 TeV. Data used for the first analysis are the ones collected in 2015, 2016 and 2017, corresponding to a total integrated luminosity of 79.8 fb^{-1}. The second analysis is a subsequent iteration including 2018 data-taking for a total integrated luminosity of 139 fb^{-1}. The data quality is ensured by following the conditions outlined by the Good Runs List (GRL) tool provided by the ATLAS Data Quality Group, which helps in discarding samples one detectors experienced problems. The tool uses data-quality status flags from specific area of the detector to determine if an event within a given luminosity block is usable for physics analysis.
In the 2-lepton channel, the final state is characterized by the presence of two charged leptons, with opposite signs, coming form the Z decay: $e^{\pm}e^{\mp}$, $\mu^{\pm}\mu^{\mp}$, $e^{\pm}\mu^{\mp}$. The single lepton triggers used in each data collection period are listed in Tab.(4.2) and Tab.(4.3).

TABLE 4.2: Single Electron triggers used in 2015-2018 data collection period.

Trigger Name	Period	Threshold [GeV]	Description
HLT_e24_lhmedium_L1EM20VH	2015	24 GeV	Seeded using L1EM20VH level 1 trigger cali-brated at the EM scale with a threshold of 20GeV, and require medium ID quality.
HLT_e60_lhmedium	2015	60 GeV	Seeded using L1EM20VH level 1 trigger cali-brated at the EM scale with a threshold of 20GeV, and require medium ID quality.
HLT_e120_lhloose	2015	120 GeV	Seeded using L1EM20VH level 1 trigger cali-brated at the EM scale with a threshold of 20GeV, and require loose ID quality.
HLT_e26_lhtight_nod0_ivarloose	2016-2018	26 GeV	Tight likelihood ID required, and variable looseisolation required.
HLT_e60_lhmedium(_nod0)	2016-2018	60 GeV	Medium ID likelihood required.
HLT_e140_lhloose(_nod0)	2016-2018	140 GeV	Loose ID likelihood required.
HLT_e300_etcut	2018	300 GeV No ID requirements.	

TABLE 4.3: Single Muon triggers used in 2015-2018 data collection period.

Trigger Name	Period	Threshold [GeV]	Description
HLT_mu20_iloose_L1MU15	2015	20 GeV	Seeded using L1MU15 level 1 trigger witha threshold of 15 GeV, and requiring looseisolation requirements.
HLT_mu50	2015-2018	60 GeV	No isolation requirements.
HLT_mu26_ivarmedium	2016-2018	26 GeV	Variable cone medium isolation requirements.

4.9 Object and Event Selection

4.9.1 Object Identification

The criteria used by ATLAS for the object reconstruction has been already described in Chapter 3. In the 2-lepton channel, the criteria used for e, μ and jet reconstruction are summarized in Tab.(4.4), Tab.(4.5) and in Tab.(4.6). For the definition of the cuts refer to 3.1 and 3.2 respectively for electrons and muons. As said in the description of the analysis

TABLE 4.4: Electron selection requirements used in the 79.8 fb^{-1} and in the 139 fb^{-1} iteration. As can be seen, the criteria are the same with the exception of the chosen Isolation Working Point.

Electron Selection	p_T	η	ID	d_0^{sig} w.r.t. BL	$\lvert z_0 \sin\theta \rvert$	Isolation
Analysis with 79.8 fb^{-1}						
VH-*loose*	>7 GeV	$\lvert\eta\rvert$<2.47	LH Loose + B-layer cut	<5	<0.5 mm	LooseTrackOnly
ZH-*signal*	>27 GeV	$\lvert\eta\rvert$<2.47	LH Loose + B-layer cut	<5	<0.5 mm	LooseTrackOnly
Analysis with 139 fb^{-1}						
VH-*loose*	>7 GeV	$\lvert\eta\rvert$<2.47	LH Loose + B-layer cut	<5	<0.5 mm	FixedCutLoose
ZH-*signal*	>27 GeV	$\lvert\eta\rvert$<2.47	LH Loose + B-layer cut	<5	<0.5 mm	FixedCutLoose

TABLE 4.5: Muon selection requirements used in 79.8 fb^{-1} and in 140 fb^{-1} iteration. As can be seen, the criteria are the same with the exception of the chosen Isolation Working Point.

Muon Selection	p_T	η	ID	d_0^{sig} w.r.t. BL	$\lvert z_0 \sin\theta \rvert$	Isolation
Analysis with 79.8 fb^{-1}						
VH-*loose*	>7 GeV	$\lvert\eta\rvert$<2.7	Loose Quality	<3	<0.5 mm	LooseTrackOnly
ZH-*signal*	>27 GeV	$\lvert\eta\rvert$<2.5	Loose Quality	<3	<0.5 mm	LooseTrackOnly
Analysis with 139 fb^{-1}						
VH-*loose*	>7 GeV	$\lvert\eta\rvert$<2.7	Loose Quality	<3	<0.5 mm	FixedCutLoose
ZH-*signal*	>27 GeV	$\lvert\eta\rvert$<2.5	Loose Quality	<3	<0.5 mm	FixedCutLoose

strategy in Sec.4.1, events with 2 or $\geq$3 jets (*forward jets*) are selected for the 2-lepton channel, with the requirement of exactly 2 b-tagged jets (*signal jets*). The selection requirements are listed in Tab.(4.6).

4.9.2 Event Selection

The events are categorized by the exact number of VH-*Loose* leptons, as defined in Tab.(4.4) and (4.5) present in the final state. The 2-lepton channel is composed by events containg *exactly* 2 VH-*Loose* leptons. Events are divided according to the vector boson transverse momentum to improve the analysis sensitivity. In 79.8 fb^{-1} analysis, two p_T^V regions are considered:

- Low p_T^V region: [75, 150] GeV.
- High p_T^V region: >150 GeV.

In the analysis iteration with the full Run2 statistics, the high p_T^V region has been splitted further into two regions with an additional cut-off at 250 GeV, so three different regions are under investigation:

- p_T^V region: [75, 150] GeV (this region is included only for the 2 lepton analysis).
- p_T^V region: [150, 250] GeV.
- p_T^V region: pver 250 GeV.

Events are also required to contain at least two signal jets, as defined in Tab(4.6). In the 2-lepton channel, this results in two categories of events depending on the number of selected jets, before b-tagging:

TABLE 4.6: *AntiKt4EMTopoJets* selection requirements. A Jet Vertex Tagger (JVT) is used to remove jets associated to pile-up vertices for p_T<60 GeV and $|\eta|$<2.4. The jet cleaning criteria identify jet arising from non-collision backgrounds or noise in the calorimeters, with events containing such jets removed. The selection criteria are common to the two analyses.

Jet Category	Selection Requirements
Forward Jets	jet cleaning p_T>30 GeV 2.5$\leq$<$\|\eta\|$<4.5
Signal Jets	jet cleaning p_T>20 GeV and $\|\eta\|$<2.5 JVT$\geq$0.59 if (p_T<60 GeV and $\|\eta\|$<2.4)

- 2 jets events
- $\geq$3 jets events

The high jet multiplicity results in a 6% gain in expected signal significance. Only events with exactly two b-tagged jets are considered in the context of these analyses since they have the largest signal sensitivity. Signal jets in each event are labelled by the b-tagging and transverse momentum. The leading jet is the b-tagged one with highest transverse momentum, the sub-leading is the b-tagged one with lower p_T and, in the events with $\geq$3 events, the third jet is the one with the highest p_T among the non-b-tagged signal jets. The leading jet is required to have p_T>45 GeV. The invariant mass of the Higgs boson is reconstructed from the two b-tagged jets.
The b-tagging algorithm used in the analyses is the MV2c10 algorithm, described in 3.4.3. The output of the MV2c10 algorithm is a score between -1 and 1, which express the likelihood for a jet to be b-tagged. The working points are shown in Tab.(3.4). These analyses exploit the 70% fixed cut working point. Fig.(4.9) shows the corresponding b-tagging efficiency as a function of reconstructed calorimeter jet transverse momentum [82]. In the

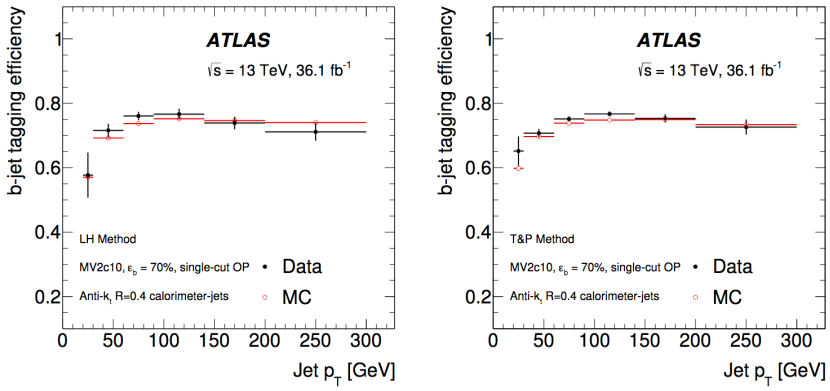

FIGURE 4.9: The b-tagging efficiency measured in data (full circles) and simulation (open circles), corresponding to the 70% b-tagging efficiency as a function of the jet p_T^V using the likelihood method (a) and the Tag&Probe method, for R=0.4 calorimeter jets [82].

2-lepton channel, a Z decaying to two same flavour leptons (ee, $\mu\mu$) needs to be reconstructed. Events with exactly two VH-*Loose* leptons of the same flavour with at least one satisfying the selection requirements listed in Tab.(4.4) and Tab.(4.5) are then selected. All

the events with additional VH-*Loose* leptons are discarded. For muons, the opposite charge requirements stands while this is not possible for electrons due to the higher rate of charge misidentification. Moreover, the invariant mass of the two selected final state leptons must be consistent with the Z boson mass in the window 81<$m(ee/\mu\mu)$<101 GeV.

4.10 Multivariate Analysis

As we have seen in Sec.(4.4), the ZH signal has a small production cross section if compared to the ones of the background events. Large contribution of events which mimic the signal enter the ZH phase space making the extraction of the signal challenging.
A Multivariate Analysis (MVA) approach is used instead of conventional cut-based analysis tools, with a gain in efficiency and precision [83].
The basic idea is that the variables describing an event or an object can be represented by a n-dimensional vector $\mathbf{x}$, called *feature variable* of n-dimensional feature space and representing a set of discriminating observables. The goal of running a machine learning algorithm is to obtain an outcome $\mathbf{y}(\mathbf{x})$, expressed as:

$$\mathbf{y}(\mathbf{x}) = f(\mathbf{x}) \quad \text{where} \quad \mathbf{x} = (x_1, x_2, ..., x_n) \tag{4.9}$$

where the form of the function $\mathbf{y}(\mathbf{x})$ is determined during the *training* (or *learning*) procedure on the basis of training data. Typically, correlation exists between the feature variables so, in order to determine the results with high precision a multivariate approach is used. The MVA methods help to solve the problem of the not precise knowloedge of the exact mathematical dependence between the variables of interest. In absence of a known model in describing it, statistical trainings give a better description of the data. While in the simplest example, it is possible to adopt a linear regression approach where $\mathbf{y}$ is a linear function of $\mathbf{x}$ and a prediction of it can be made knowing $\mathbf{x}$, in most of cases, such as in particle physics, the identification of the functionality is more complex since the parameter space has a high dimensionality. The prediction on $\mathbf{y}(\mathbf{x})$ becomes in these cases very complex and it can be only approximated from a given set of observables. What it can be done is to approximate the desired function with $\hat{\mathbf{y}} = f(\mathbf{y}, \mathbf{w})$, where $\mathbf{w}$ are adjustable parameters.
A MVA method has to address these three typical points:

- signal-to-background discrimination.
- selection of the variables with the highest signal/background discrimination.
- dimensionality reduction of the feature space (i.e., the multiple quantities characterizing an event) and simplification by the reduction of the number of variables.
- finding regions of interest in data.

Every MVA analysis is based on three steps:

- training or learning
- testing
- classification

The first step is the development of an algorithm for *learning from data* with the goal to be able to respond correctly to future data. While for conventional statistical methods the start point is a mathematical model to find parameters either analytically or numerically, in machine learning an approximating function is automatically inferred without any *a priori* assumption.
The training algorithms are of two types:

- *unsupervised algorithms*, where no *a priori* categories are given and the algorithm has to find them by itself.
- *supervised algorithms*, where a set of training events with correct category association is given.

The most powerful approach and the one used in this context is the second one. The training data set $\mathbf{y}, \mathbf{x}$, where $\mathbf{y}$ are the targets encodes information about the input-output relationship to be learned. In high energy physics, the training data are typically from Monte Carlo simulations. The goal of the training step is to determine the adjustable parameters $\mathbf{w}$ and to define the *classifier* that will be used in the classification step, to identify each real data event belonging to signal or to background.
The are two main types of classifiers: *linear* and *non-linear* classifiers.
The *linear* classifier is the most common tool to discriminate signal from background and it is based on the application of a group of rectangular cuts on selected variables. It is important to note that it is not properly a multivariate analyser but a *sequence* of univariate ones. No combination of the variables is achieved and a cut on a variable does not depend on another one. In case of two variables with correlation, a cut-based selection is not the best option since it produces a separation with a large overlap. A more effective cut can be obtained with a linear combination of two variables. For example:

$$\alpha x_1 + \beta x_2 < \gamma \tag{4.10}$$

where α, β and γ are three optimized parameters. This can be generalized to N variables by:

$$t = \sum_{i=1}^{N} \alpha_i x_i < t_{cut} \tag{4.11}$$

where t is the linear combination, α_i are the parameters to optimize the S/B separation and t_{cut} is the final cut to apply to the variable.
The *non-linear* classifiers use non-linear function: the single cut on a variable depends simultaneously on all the other variables cuts not necessarily in a linear way. The non-linear classifier used for this analysis is the *Boosted Decision Tree* (BDT) which will be described in 4.10.1.
The *testing* step is fundamental because it ensures that the definition of the classifier is not due to a specific feature of the training sample. In this case the discriminant variable distributions are obtained from other additional Monte Carlo samples. A possible inconsistency between the training and the test distributions would manifest itself in *overtraining*. Overtraining can lead to a false increase in performance, while the effective decrease is measured in test sample.
The last step is the *classification* which assigns events to one of the possible classes by the classifier from the training step achieving the splitting into signal and background.

4.10.1 Boosted Decision Tree

A decision tree is a binary tree structured classifier [84]. Repeated "yes"/"no" decisions are taken on one single variable at a time until a stop criterion is fulfilled. The phase space is split this way into many regions that are eventually classified as signal or background, depending on the majority of the training events that end up in the final node. Fig.(4.10) shows a schematic view of a decision tree.
The boosting of a decision tree extends the concept from one to several trees which form a forest. The trees are derived from the same training ensemble by reweighting events and

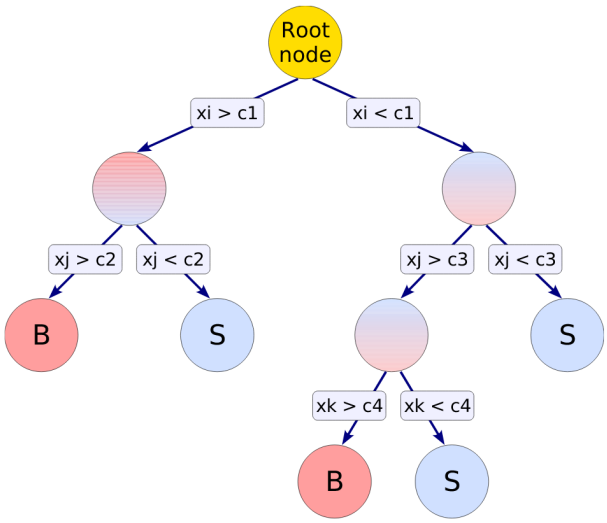

FIGURE 4.10: Schematic view of a decision tree. Starting from the root node, a sequence of binary splits using the discriminating variables x_i applied to the data. Each split uses the variable that at this node gives the best separation between signal and background when being cut on. The same variable may thus be used at several nodes, while others might not be used at all. The leaf nodes at the bottom end of the tree are labeled"S" for signal and "B" for background depending on the majority of events that end up in the respective nodes [84].

are finally combined into a single classifier which is given by an average of the individual decision trees. Boosting procedure stabilize the response of the decision trees with respect to fluctuations in the training sample and it is able to enhance the performance.

Description and implementation

Decision trees are classifiers that allow a straightforward intepretation as they can be visualized by a simple two-dimensional tree structure. They are able to split the phase space into a large number of hypercubes, each of which is identified as *signal-like* or *background-like*. For classification trees, the path down the tree to each leading node represents an individual cut sequence that selects signal or background depending on the leaf type. A shortcoming of decision trees is their instability with respect to statistical fluctuations in the training sample from which the tree structure is derived. For example, if two input variables exhibit similar separation power, a fluctuation in the training sample may occur, causing the tree growing algorithm to decide to split on one variable, while the other variable could have been selected without fluctuation. In cases like that, the whole tree results altered below this node, possibly giving a substantially different classifier response. This issue can be avoided by constructing a forest of decision trees and classifying an event on a majority vote of the classifications done by each tree in the forest. All the trees in the forest are derived from the same training sample, with the events being subsequently sujected to *boosting*, a procedure which modifies their weight in the sample, as will be explained in 4.10.1.

Training (or *growing*) a Decision Tree

The training, or *growing*, of a decision tree is the process that defines the splitting criteria for each node. The training starts with the root node, where an initial splitting criteria for the full training sample is determined. The two resulting subsets undergo the same algorithm and, after several iteration, the whole tree is built. At each step, the split in the single node is determined by finding the variable and the corresponding cut value providing the best separation between signal and background. Once the splitting is stopped, a leaf is classified as signal or background depending on the class the majority of events belongs to.
Several separation criteria are available to assess the performance of a node in terms of variable and the cut requirement. All separation criteria have a maximum where the samples are fully mixed, resulting in a purity p=0.5, and fall off to zero when the sample consists of one event class only. The purity of a node is given by the ratio of signal events to all events in that node. Pure background nodes have zero purity. The separation criteria are:

- *Gini index* (default one): $p \cdot (1 - p)$
- *Cross entropy*: -$p \cdot \ln(p) - (1 - p) \cdot \ln(1 - p)$
- *Misclassification error*: $1 - \max(p, 1 - p)$
- *Statistical significance*: $S\sqrt{S + B}$

The *Gini index* is the criteria adopted for the MVA analysis performed in the analysis presented here.
The splitting continues until each leaf node contains only signal or only background events, which could suggest that perfect discrimination is achievable. Such a decision tree would be strongly overtrained. To correct this, a *pruning* procedure is applied [84].
An example of overtraining is shown in Fig.(4.11). In Fig.(4.11)(a), the classifier has managed

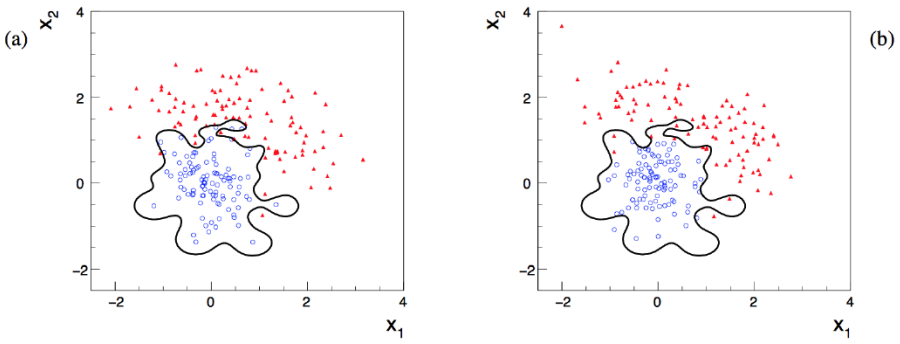

FIGURE 4.11: Scatter plot of two input variables for event classified as signal (blue circles) and background (red traingles). The decision boundary determined by the classifier is shown as a black line. The decision boundary is much performant on the training sample (left). If it is applied to a statistically independent data sample (right), the contortions that led to a good performances on the training samples do not lead to the same good discrimination.

to enclose all the signal events and exclude the background events. If this decision boundary is applied to a statistically independent data sample, the contortions that led to good performances on the training sample will not work so well, as can be seen from Fig.(4.11)(b).

Boosting a decision tree

Boosting is a way of enhancing the classification performance and increasing the stability with respect to statistical fluctuations in the training sample. It improves the separation performance compared to a single decision tree by sequentially applying an MVA algorithm to reweighted (*boosted*) versions of the training data and then taking a weighted majority vote of the sequence of MVA algorithms produced. The procedure applied to a decision tree consists in building a sequential list of trees each reweighted depending on the performances of the previous tree. The main boosting algorithms are [84]:

- AdaBoost
- Gradient Boost
- Bagging
- Randomised Trees

The chosen algorithm for this analysis is *AdaBoost*. In general, events considered in a classification problem can be misclassified during training and they are assigned a higher event weight in the training of the following tree. Starting with the original event weights when training the first decision tree, the subsequent tree is trained using a modified event sample where the weights of previously misclassified events are multiplied by a common boost weight α. The boost weight is derived from the misclassification rate, *err*, of the previous tree.

$$\alpha = \frac{1 - err}{err} \tag{4.12}$$

where $err = (\text{misclassified events})/(\text{total events})$. The weights of the entire event sample are then renormalized such that the sum of weights remain constant. The result of an individual classifier is $h(\mathbf{x})$, with $\mathbf{x}$ being the vector of input variables, which is equal to +1 for signal and -1 for background. The boosted event classification is given by:

$$y_{Boost}(\mathbf{x}) = \frac{1}{N_{Collection}} \cdot \sum_{i}^{N_{Collection}} \ln\alpha_i \cdot h_i(\mathbf{x}) \tag{4.13}$$

where the sum is over all classifiers in the collection. Small values for $y_{Boost}(\mathbf{x})$ indicate a background-like event, while large value a signal-like event.
The use of an alternative boosting, the *Gradient Boost*, is presently under study for the full Run2 statistics analysis. The idea of function estimation through boosting can be understood with an additive expansion approach. The function $F(\mathbf{x})$ is assumed to be weighted sum of parametrized base function $f(x; a_m)$, called *weak learners*. Decision trees benefit most from boosting and they implements *GradientBoost*. The function in this expansion corresponds to a decision tree:

$$F(\mathbf{x}; P) = \sum_{m=0}^{\infty} \beta_m f(x; a_m) \quad P \in \beta_m; {a_m}_0^M \tag{4.14}$$

The boosting procedure acts on the parameters P adjusting them such that the deviation between the model response $F(\mathbf{x})$ and the outcome y from the training is minimized. Deviations are measured by the *loss-function* $L(F, y)$, with the choice of squared error loss form $L(F, y) = (F(\mathbf{x}) - y)^2$. AdaBoost methods adopts an exponential loss of the form $L(F, y) = e^{-F(\mathbf{x})y}$. However exponential loss lacks in robustness in presence of outliers or mislabelled data points. Its performances are expected to degrade in noisy settings. The

GradientBoost algorithm attempts to cure this weakness using a binomial log-likelihood loss:

$$L(F, y) = \ln\left(1 + e^{-2F(\mathbf{x})y}\right) \tag{4.15}$$

The minimization is performed by calculating the current gradient of the loss function and then growing a regression tree whose leaf values are adjusted to match the mean value of the gradient in each region defined by the tree structure. The iteration of the procedure provides the set of decision trees which minimize the loss function.

4.10.2 Classification Performance Evaluation

In order to evaluate the classification performance, different benchmark quantities are available.

- The *signal efficiency at tree representative background efficiencies* (efficiency is equal to 1-rejection) obtained from a cut on the classifier output. It is also used the area of the background rejection versus the signal efficiency function, following the prescription that states that the larger the area the better the performance.
- The separation $< S^2 >$ of a classifier y, defined as:

$$< S^2 >= \frac{1}{2}\int \frac{(\hat{y}_S(y) - \hat{y}_B(y))^2}{\hat{y}_S(y) + \hat{y}_B(y)} dy \tag{4.16}$$

  where $\hat{y}_S$ and $\hat{y}_B$ are the signal and background *probability distribution functions* (PDFs) of y. The separation is zero for identical signal and background shapes and it is one for shapes with no overlap.
- The discrimination significance of a classifier, defined by the difference between the classifier means for signal and background divided by the quadratic sum of their root-mean-squares.

4.10.3 Multivariate Analysis in VH(H$\to b\bar{b}$) analyses

In the context of the two analyses presented in this thesis, a supervised learning Boosted Decision Tree technique has been used. The BDT has been defined and tuned using an implementation in the MVA Toolkit (TMVA), which can be integrated in the standard ROOT analysis code. The MVA ntuples have been produced from Monte Carlo signal and background samples using the CxAODReader (4.2). The default b-tagging strategy is the truth tagging, described in 4.7.
Different jet multiplicity and p_T^V dedicated training regions have been defined to enhance sensitivity. For the 2-lepton channel, the following training regions have been defined:

- 2 jets, 2 b-tags, 75 GeV<p_T^V<150 GeV
- $\geq$3 jets jets, 2 b-tags, 75 GeV<p_T^V<150 GeV
- 2 jets, 2 b-tags, p_T^V>150 GeV
- $\geq$3 jets jets, 2 b-tags, p_T^V>150 GeV

This four different trainings are adopted for both the analyses. In particular, it is important to note that the same choice occurs in the case of iteration at 139 fb^{-1}, contrary to the definition of the analysis regions entering the profile likelihood fit. Performance studies to verify if using two dedicated training splitting the high p_T^V region could increase or not

sensitivity, as I will explain in 4.11.4.
The input variables are chosen in order to maximize the separation in the VH search. The input variables have been studied in 0-,1- and 2-lepton analysis separately and chosen to maximize the signal/background separation. The common variables to them are defined as follows:

- m_{jj}: the invariant mass of the dijet system, constructed upon two b-tagged jets.
- $\Delta R(jet_1, jet_2)$: distance in $\eta - \phi$ space between the two b-tagged jets.
- p_T^{jet1}: transverse momentum of the leading b-tagged jet in the dijet system.
- p_T^{jet2}: transverse momentum of the subleading b-tagged jet in the dijet system.
- p_T^V: transverse momentum of the vector boson. In the 2-lepton channel it is defined as the vectorial sum of the transverse momenta of the two leptons.
- $\Delta\phi(Z, H)$: in the 2-lepton channel, the distance in ϕ between the di-lepton system (i.e., the vector boson candidate) and the Higgs boson candidate (i.e., the dijet system constructed from the two b-tagged jets).
- p_T^{jet3}: the transverse momentum of the signal jet with the highest transverse momentum among the signal jets that are not b-tagged, only used for events with 3 or more jets in the final state ($jet3$).
- m_{jjj}: invariant mass of the two b-tagged jets and $jet3$.

For the 2-lepton channel, four additional variables are used:

- E_T^{miss} significance: the *quasi*-significance of the E_T^{miss} in the event, defined as $E_T^{miss}/\sqrt{S_T}$ where S_T is defined as the scalar sum of the p_T of the leptons and jets in the event.
- $|\Delta\eta(Z, H)|$: the distance in η between the dilepton and dijet system of the b-tagged jets.
- $m_{\ell\ell}$: the invariant mass of the dilepton system.
- cosθ: angle between the negatively charged lepton and the Z-boson in the Z-boson rest frame.

The latter is about to be added for the full Run-2 analysis since a significant gain in the training performance when including this variable has been observed at earlier stage. It makes use of the difference in polarization between the signal and $Z + jets$ background.
Input variables used for the BDT training for the high p_T^V region (p_T^V>150 GeV) are shown both for jet multiplicity of 2 and $\geq$3, see Fig.(4.12), (4.13), (4.14) and (4.15).

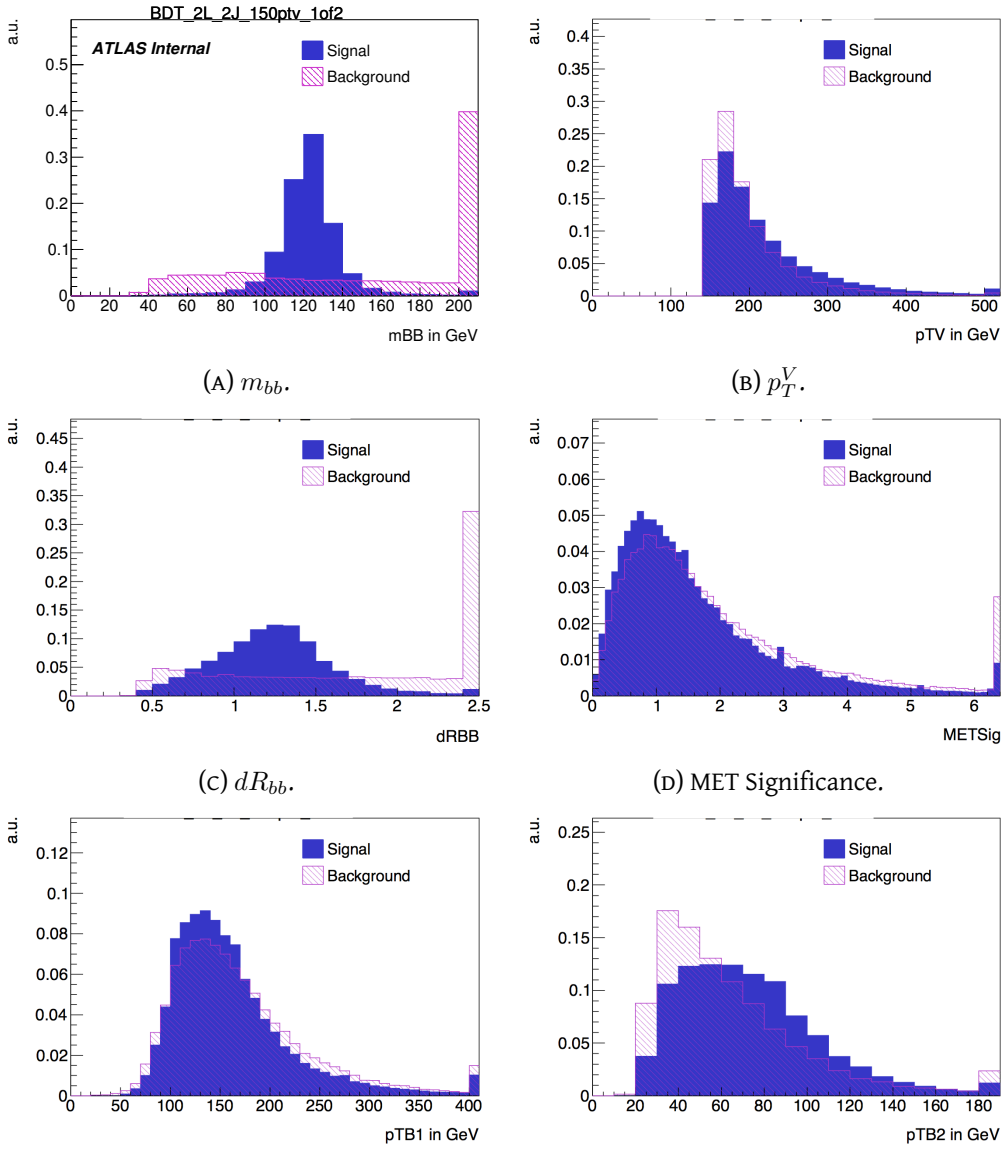

(A) m_{bb}. (B) p_T^V.

(C) dR_{bb}. (D) MET Significance.

(E) p_T^{b1}. (F) p_T^{b2}.

FIGURE 4.12: Input variables entering the training for signal (blue) and background (magenta) samples in the 2 lepton channel for the 2jet region with p_T^Z>150 GeV.

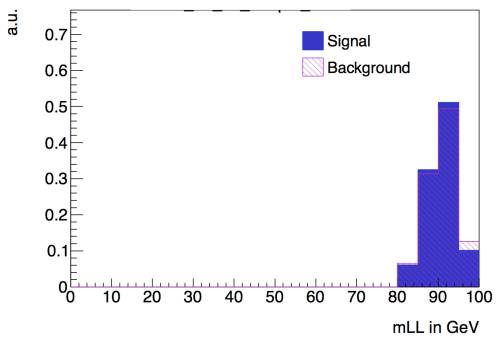

(A) $m_{\ell\ell}$.

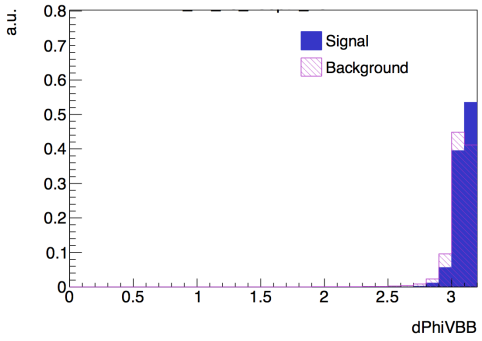

(B) $d\phi(V,H)$.

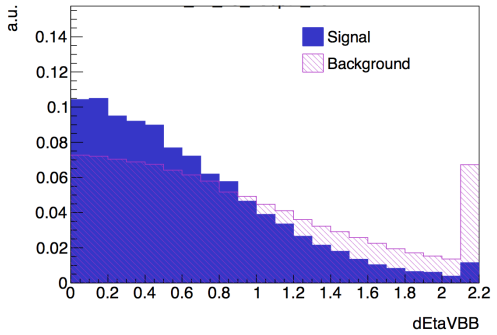

(C) $d\eta(V,H)$.

FIGURE 4.13: Input variables entering the training for signal (blue) and background (magenta) samples in the 2 lepton channel for the 2jet region with p_T^Z>150 GeV.

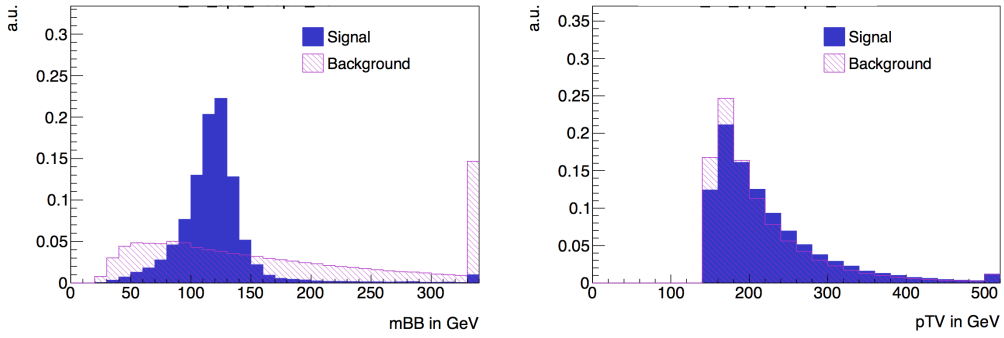

(A) m_{bb}.

(B) p_T^V.

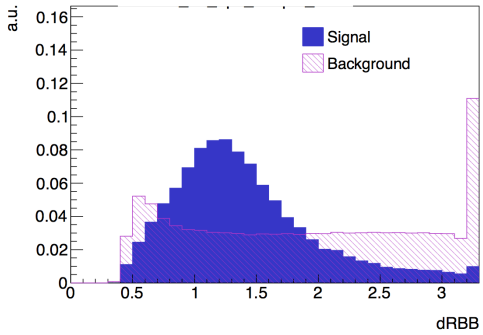

(C) dR_{bb}.

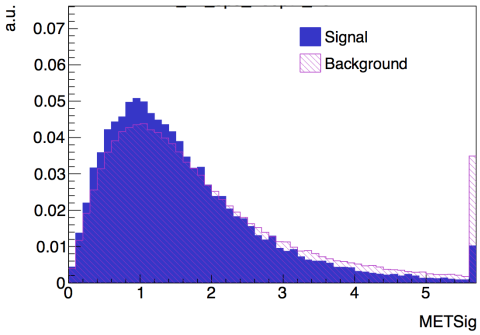

(D) MET Significance.

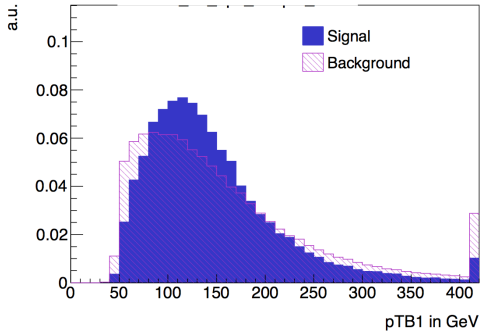

(E) p_T^{b1}.

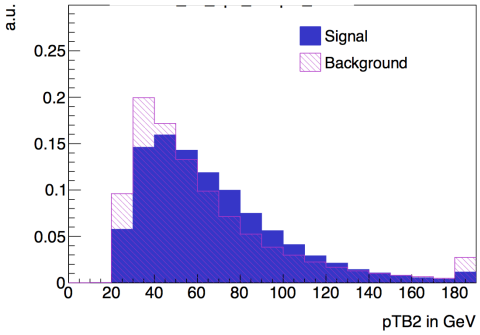

(F) p_T^{b2}.

FIGURE 4.14: Input variables entering the training for signal (blue) and background (magenta) samples in the 2 lepton channel for the $\geq$3jet region with p_T^Z>150 GeV.

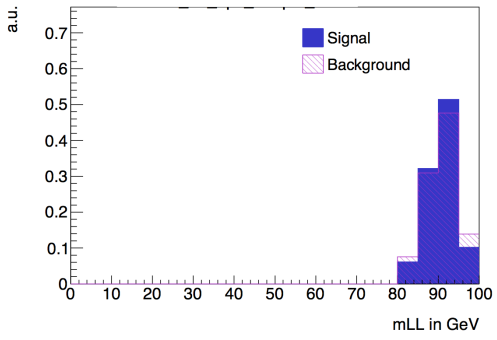

(A) $m_{\ell\ell}$.

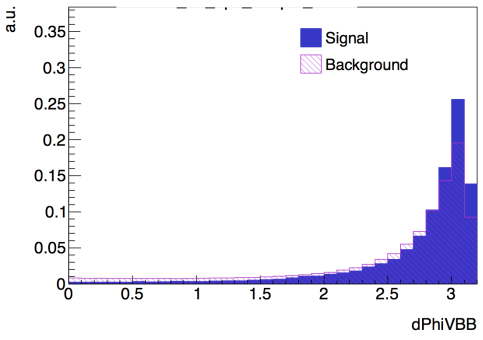

(B) $d\phi(V,H)$.

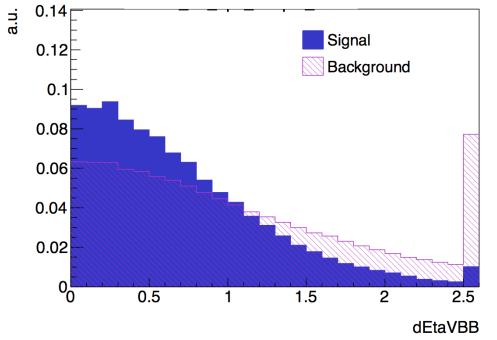

(C) $d\eta(V,H)$.

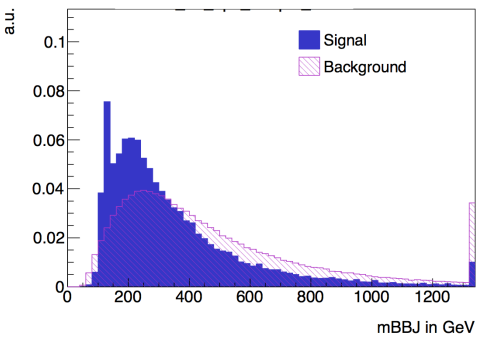

(D) m_{jjj}

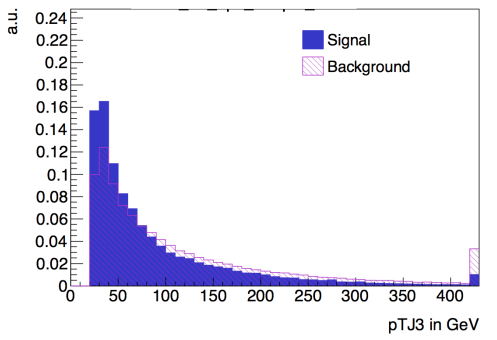

(E) $dp_T^{j_3}$.

FIGURE 4.15: Input variables entering the training for signal (blue) and background (magenta) samples in the 2 lepton channel for the $\geq$3jet region with p_T^Z>150 GeV.

The BDT output scores are shown in Fig.(4.16), for 2 jets and $\geq$3 jets events. These are used input to the profile likelihood fit, described in Sec.(5.1).

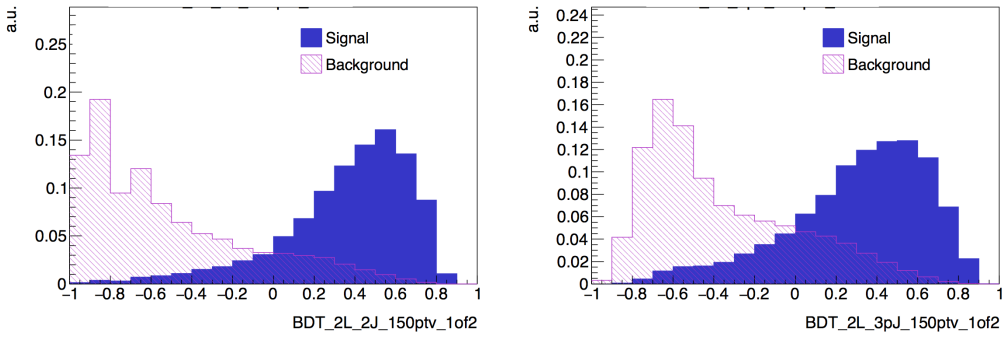

FIGURE 4.16: MVA output for 2 jets (left) and $\geq$3 jets (right) events.

Setup and Training

The BDT is trained using all nominal MC samples of the analyses.
The samples of mc16a, mc16d (79.8 fb^{-1} and 139 fb^{-1}) and mc16e (139 fb^{-1}) (see 4.11.6) production has been combined in the training. The signal template is given by the ZH samples, while the background template is given by the sum of all the background samples. The trainings has been splitted in two statistically independent samples to ensure an unbiased result and to keep under control possible overtrainings. One sub-training is performed using even numbered MC events used as training sample, one using odd-numbered ones used as testing sample, respectively applied on each other to ensure ortogonality. The final discriminant is then built by summing the multivariate discriminant of the even and odd events.
In the training, truth tagging is applied to all samples to maximise the amount of MC statistics in the training. Since the MC events entering the profile likelihood fit are hybrid truth tagged it was also tested to use hybrid truth tagging in the training, see 4.11.5
The hyperparameters used are listed in Tab(4.7).
For the iteration of the analysis with the full Run2 statistics, studies are currently under

TABLE 4.7: Hyperparameters used in BDT Trainings.

TMVA Settings	Value	Definition
BoostType	AdaBoost	Boost procedure
AdaBoostBeta	0.15	Learning rate
SeparationType	GiniIndex	Node separation gain
PruneMethod	NoPruning	Pruning method
NTrees	200	Number of trees
MaxDepth	4	Maximum tree depth
nCuts	100	Number of equally spaced cuts tested per variable per node
nEvents	Min5%	Minimum number of events in a node (in % of total number of events)

way. In particular, an update can be the substitution of the BoostType going from AdaBoost to Gradient Boosting. Moreover, increasing the number of trees can increase the performance.
Distributions in Fig.(4.17) and in Fig.(4.18) show the diagnostics plots I have produced to verify if overtraining was present in the two trainings for 2 jets multiplicity, in the medium and high p_T^V region.

These overtraining checks evaluate the trained BDT on the training data set and on the statistically independent evaluation data set (i.e. the testing sample). As can be seen, no significant difference in the BDT output score distribution is observed between the training and testing data set, both for signal and background template. It can also be appreciated in the signal and background efficiencies (see Figs.4.17B, 4.18B, 4.19B and 4.20B) and in the ROC

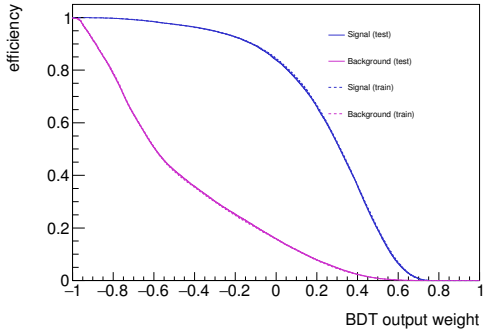

(A) BDT output score distributions.

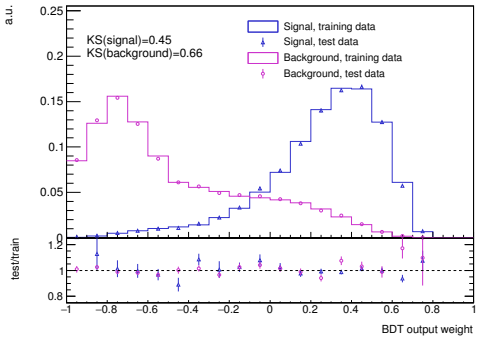

(B) Signal and Background efficiency as a function of BDT output score.

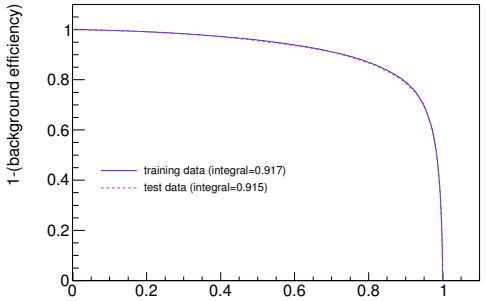

(C) ROC curve comparing the training data set and a statistically independent testing data set.

FIGURE 4.17: Overtraining checks for 2-lepton channel in the inclusive medium p_T^V region, 75 GeV<p_T^V<150 GeV for 2 jets multiplicity.

curve (*Receiver Operating Characteristic* curve [85]) where the corresponding area under the curve, which serves as a measure of the signal-to-background discrimination performance of the BDT show no overtraining, see Figs.4.18C, 4.19C and 4.20C. Overtraining would have resulted into a significant difference between the training and testing sample curve, in particular in a higher area for the training sample with respect the testing one.

The same can be seen for the two trainings with $\geq$3 jets multiplicity in the final state. Also in this case, no significant overtraining is observed.

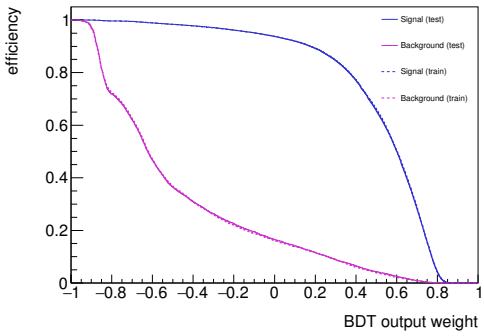

(A) BDT output score distributions.

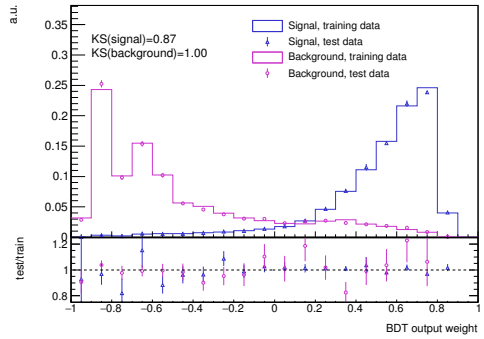

(B) Signal and Background efficiency as a function of BDT output score.

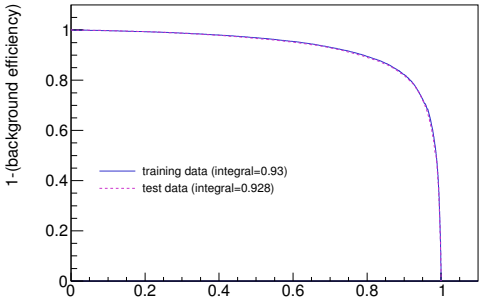

(C) ROC curve comparing the training data set and a statistically independent testing data set.

FIGURE 4.18: Overtraining checks for 2-lepton channel in the p_T^V>150 GeV region for 2 jets multiplicity.

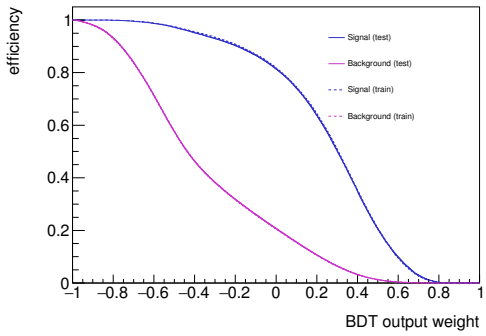

(A) BDT output score distributions.

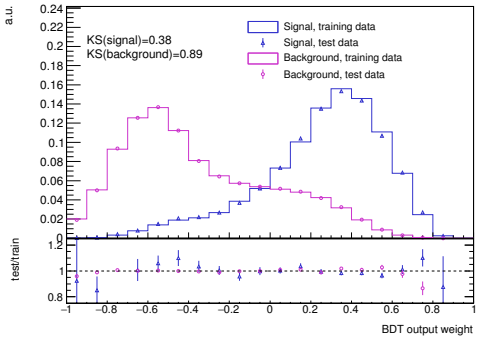

(B) Signal and Background efficiency as a function of BDT output score.

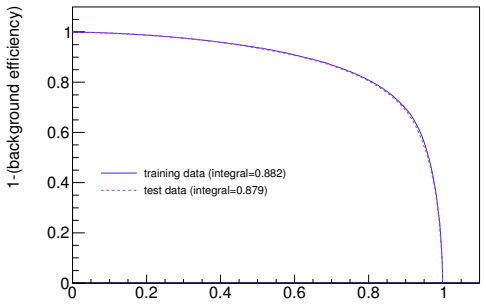

(C) ROC curve comparing the training data set and a statistically independent testing data set.

FIGURE 4.19: Overtraining checks for 2-lepton channel in the inclusive medium p_T^V region, 75 GeV<p_T^V<150 GeV for $\geq$3 jets multiplicity.

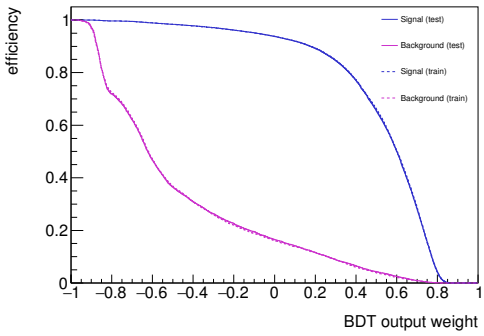

(A) BDT output score distributions.

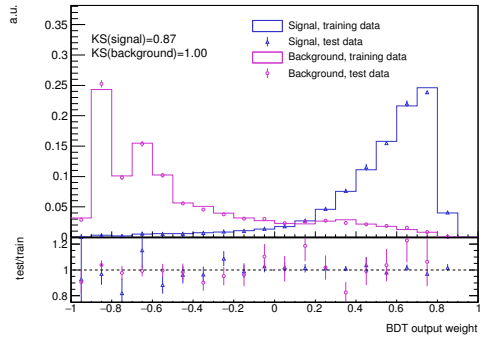

(B) Signal and Background efficiency as a function of BDT output score.

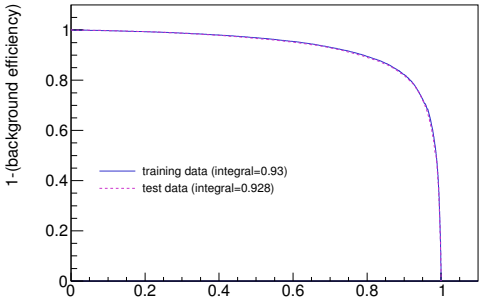

(C) ROC curve comparing the training data set and a statistically independent testing data set.

FIGURE 4.20: Overtraining checks for 2-lepton channel in p_T^V>150 GeV region for $\geq$3 jets multiplicity.

4.10.4 BDT Transformation

To maximize the separation of the signal and background, the BDT output are transformed with an optimal binning, taking into account that low BDT output scores are populated by background events, high BDT output scores have a good signal-to-background ratio and the statistical uncertainty of each bin [72]. The function used is:

$$Z(k,l) = z_s \frac{n_{s(k,l)}}{N_s} + z_b \frac{n_b(k,l)}{N_b} \tag{4.17}$$

called *transformation D*, where z_s and z_b are the tuning parameters and $n_s(k,l)$ and $n_b(k,l)$ the number of the signal and background events in the BDT output interval from bins k to l.
The rebinning follows the next steps:

- Starting from the last bin on the right of the original histogram, increase the range of the interval $I(k, last)$ by adding one after the other, the bins from the right to the left.
- Calculate the value of Z at each step.
- Once $Z(I[k_0, last]) > 1$, rebin all the bins in the interval $I(k_0, last)$ into a single bin.
- Repeat steps 1-3, starting this time from the last bin on the right, not included in the previous remap, until k_0 in the first bin.

If the statistical uncertainty of the new bin is larger than 100%, the second step is repeated until it becomes lower than 100%.

4.11 Contribution to 79.8 fb^{-1} and to 139 fb^{-1} Analysis

As anticipated in the introduction to the chapter, this thesis deals with to two different analysis, which share basically the same strategy (except for some changes in terms of optimization). In the present section, my main contribution are described.

- 79.8 fb^{-1}:
  - 4.11.1: a particle-level study of the Z+jets background systematic uncertainties.
  - 4.11.2: estimation of the multi-jet background through the *template method* procedure.
- 139 fb^{-1}:
  - 4.11.3: study of the change of the lepton isolation working points.
  - 4.11.4: optimization studies, in the context of the MVA analysis, about the introduction of an additional cut at p_T^V<250 GeV in the high-p_T^V region.
  - 4.11.5: optimization studies, in the context of the MVA analysis, about the change of b-tagging strategy.
  - 4.11.6: data/MC comparison.

4.11.1 Z+jets Modelling with Monte Carlo samples for the 79.8 fb^{-1} analysis

The particle-level study of the Z+jets background related systematic uncertainties has represented one of my initial contribution to $VH(H \to b\bar{b})$ analysis in the 2-lepton channel. The $Z + jets$ background is divided in three main components, depending on the flavour composition of the events. Simulated jets are labelled as b-, c- or light flavour (l) according to which hadron with p_T>5 GeV are found within a cone of size ΔR=0.3 around their axis. $V + jets$ events are categorized as follows:

- Z+HF (*Heavy Flavours*), including $Z + bb$, $Z + bc$, $Z + cc$ and $Z + bl$ events (where l stands for light flavours).
- $Z + cl$, including events labelled as $V + cl$
- $V + l$, including events labelled as $V +$ light flavours

The first step is to consider the relative variation in acceptance between different analysis regions at truth level, by comparing nominal and alternative Monte Carlo samples. For $Z + jets$, the acceptance uncertainties are evaluated in the following regions:

- 2-jets versus $\geq$3-jet events
- 0-lepton versus 2-lepton events (for Z+HF events)

The procedure is performed to understand the correlation between the different phase space regions in order to implement proper nuisance parameters in the Profile Likelihood Fit. Nuisance parameters are parametrized in the fit with a Gaussian PDF and these MC-driven studies are fundamental to provide a prior on this Gaussian constraint, helping the fit to determine the best value for the parameter. The acceptance are calculated with double ratios, as follows:

$$\frac{\text{Acceptance}\left[\text{Category}\, y_A\left(\text{nominal MC}\right)\right]}{\text{Acceptance}\left[\text{Category}\, y_B\left(\text{nominal MC}\right)\right]} \Bigg/ \frac{\text{Acceptance}\left[\text{Category}\, y_A\left(\text{internal variation or alternative MC}\right)\right]}{\text{Acceptance}\left[\text{Category}\, y_B\left(\text{internal variation or nominal MC}\right)\right]}$$

The final uncertainty is the result of the quadratic sum of the variations originating from this contribution:

- effect of varying factorization μ_F and renormalization μ_R scales in the Sherpa samples.
- sum in quadrature of the variation obtained from the different resummation scale (*qsf*, the scale used for the resummation of soft gluon emissions) and matrix element matching scale *ckkw*,the scale taken for the calculation for the overlap between jets from matrix elements and parton shower) from Sherpa 2.1 [86].
- maximal variation between the normal Sherpa prediction and the prediction obtained with alternative PDF.
- difference between Sherpa and MadGraph predictions.

Another systematic uncertainty to be assessed comes from the flavour composition. The Z+HF background is composed by the contribution from bb, bc, bl and cc backgrounds. The uncertainties are implemented as normalisation on each of the smaller components and they act as prior in the final fit.
The breakdown of the 2-lepton to 0-lepton Z+HF normalisation uncertainty is shown in

MC or internal variation change	Relative variation in p_T^V>150 GeV region [%]
μ_R=1, μ_F=0.5	0.5
μ_R=1, μ_F=2	-0.2
μ_R=0.5, μ_F=1	5.7
μ_R=2, μ_F=2	-4.8
μ_R=2, μ_F=2	-1.1
μ_R=0.5, μ_F=0.5	-5.7
ckkw	0.2
qsf	-0.4
MadGraph	-0.4
Combination	7

TABLE 4.8: Breakdown of the 2 to $\geq$3 jets Z+HF normalization uncertainty (see the text for the explanation of the various contributions).

Tab.(4.8). Only high p_T^V region has been considered since no medium p_T^V region was available in 0-lepton channel. The maximum variation is due to variation in the renormalization scale μ_R with a maximum of 6%. The breakdown of the uncertainty in flavour composition is shown separately for $Z + bc/Z + bb$, $Z + bl/Z + bb$ and $Z + cc/Z + bb$ respectively in Tab.(4.9), Tab.(4.10) and Tab.(4.11).

Relative internal variation	Relative variation-2jets [%]		Relative variation-$\geq$3 jets [%]	
	75 GeV<p_T^V<150 GeV region	p_T^V>150 GeV region [%]	75 GeV<p_T^V<150 GeV region	p_T^V>150 GeV region [%]
μ_R=1, μ_F=0.5	-0.6	-1.5	-0.4	-0.7
μ_R=1, μ_F=2	0	1	0	1
μ_R=0.5, μ_F=1	-2	-1	-2	-1
μ_R=1, μ_F=1	1	1	2	1
μ_R=2, μ_F=2	2	2	2	2
μ_R=0.5, μ_F=0.5	-1	-2	-2	-2
MadGraph	-40	-36	-27	-27
ckkw	-4	-2	1	1
qsf	-1	0	-3	0
Combination	40	36	28	27

TABLE 4.9: Breakdown of the Zbc/Zbb normalisation uncertainty in all the 2-lepton analysis region.

Relative internal variation	Relative variation-2jets [%]		Relative variation-$\geq$ 3jets [%]	
	75 GeV<p_T^V<150 GeV region	p_T^V>150 GeV region [%]	75 GeV<p_T^V<150 GeV region	p_T^V>150 GeV region [%]
μ_R=1, μ_F=0.5	0	-1.2	-0.4	-0.5
μ_R=1, μ_F=2	0	1	0	0
μ_R=0.5, μ_F=1	-2	-1	-2	-1
μ_R=2, μ_F=1	1	1	2	1
μ_R=2, μ_F=2	2	2	2	2
μ_R=0.5, μ_F=0.5	-1	-2	-2	-1
MadGraph	-27	-24	-20	-17
ckkw	-4	-1	1	2
qsf	1	-1	-3	-1
Combination	28	24	20	17

TABLE 4.10: Breakdown of the Zbl/Zbb normalisation uncertainty in all the 2-lepton analysis region.

Relative internal variation	Relative variation-2jets [%]		Relative variation-$\geq$ 3jets [%]	
	75 GeV<p_T^V<150 GeV region	p_T^V>150 GeV region [%]	75 GeV<p_T^V<150 GeV region	p_T^V>150 GeV region [%]
μ_R=1, μ_F=0.5	1.4	0.1	1.8	0.5
μ_R=1, μ_F=2	0	0	0	0
μ_R=0.5, μ_F=1	1	-1	-2	-3
μ_R=2, μ_F=1	0	1	4	3
μ_R=2, μ_F=2	-1	1	4	3
μ_R=0.5, μ_F=0.5	1	-1	-1	-3
MadGraph	-16	-16	-8	-13
ckkw	1	1	1	4
qsf	-3	0	-4	0
Combination	16	16	9	13

TABLE 4.11: Breakdown of the Zcc/Zbb normalisation uncertainty in all the 2-lepton analysis region.

As can be seen, the results of the estimate of the flavour normalization are largely dominated by Sherpa and MadGraph different predictions, while the Sherpa internal variations marginally contribute to the estimated systematic uncertainty.

4.11.2 Multijet Estimation in 2 Lepton channel for 79.8 fb^{-1} analysis

As anticipated, multijet background in 2-lepton channel is highly suppressed by requiring two isolated leptons in the final state and by the cut for a dilepton invariant mass close to that of a Z boson. For the 79.8 fb^{-1} analysis, I have contributed to the estimation of the residual QCD background. It is performed through the default procedure of *template method* [87]. First of all, a background enriched region is defined to model the multi-jet (MJ) background and the template is obtained from same-sign (SS) events to reduce the contamination of EW and top background. The multi-jet shape is modelled by an exponential function, with SS-data fit to the non-MJ background and to the exponential multi-jet model. The shape of the Z+jets background is taken from MC and it has a quite different shape with respect to MJ background. The *non-Z* background (mainly top) shape is more similar to MJ shape, meaning that with a freely floating normalization parameter, the non-Z background can be absorbed by the MJ contribution, resulting in an over-estimation of the MJ background.
Fig.(4.21) shows the di-electron mass distribution in SS events. Due to charge flipping of

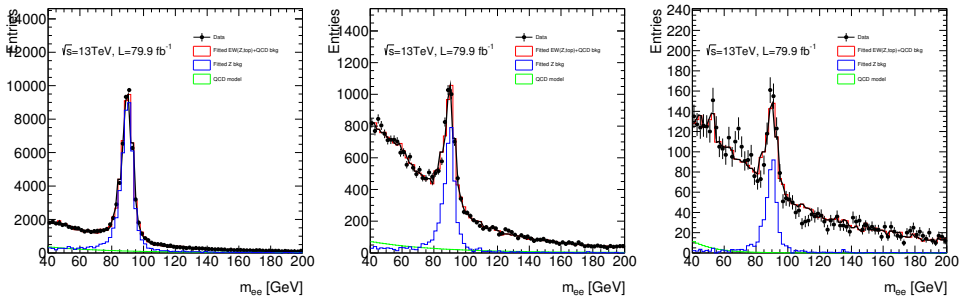

FIGURE 4.21: Same-sign dielectron mass distribution for 0-tag (a), 1-tag (b), 2-tag (c). Green histogram shows the estimated multi-jet contribution from same-sign events. The red histogram shows the fitted EW background modelled by MC plus multi-jet.

real electrons, a Z peak can still be observed. The multi-jet shape and normalization can be obtained from a fit to SS events. The fitting is performed, separately, in 0 b-tag, 1 b-tag and 2 b-tag regions (respectively, no b-tagged, 1 b-tagged and 2 b-tagged jets) to take into account any dependence on b-tagging of the MJ contamination.

Fig.(4.22) shows the di-muon mass distribution in SS events. Similarly to what said for electrons, SS-data are fit with EW background and an exponential MJ model. Tab.(4.12) and Tab.(4.13) show the MJ background fraction in opposite-sign (OS) signal regions, shown in Fig.(4.23) and Fig.(4.24). The fractions are shown in the two $m_{\ell\ell}$ regions: wider region 71 GeV<$m_{\ell\ell}$<121 GeV (ICHEP) and in the tigher selection region used in 79.8 fb^{-1} analysis 81 GeV<$m_{\ell\ell}$<101 GeV.

Assuming that the ratio OS/SS, MJ background fraction is found to be less than 1% in the enriched signal region 81 GeV<$m_{\ell\ell}$<101 GeV. Multijet background is small enough to have a negligible impact on the signal extraction and so it is not included in the profile likelihood fit. Moreover, this behaviour is not expected to change with the full Run 2 analysis.
The multijet contamination has been estimated also in the 2b-tagged $e\mu$ control region using the template method. The events are dominated by top contribution by construction with a very small $Z + jets$ contamination. The multijet model has been applied to opposite sign events with an estimate multijet contamination of 0.2% in 81 GeV<$m_{\ell\ell}$<101 GeV mass

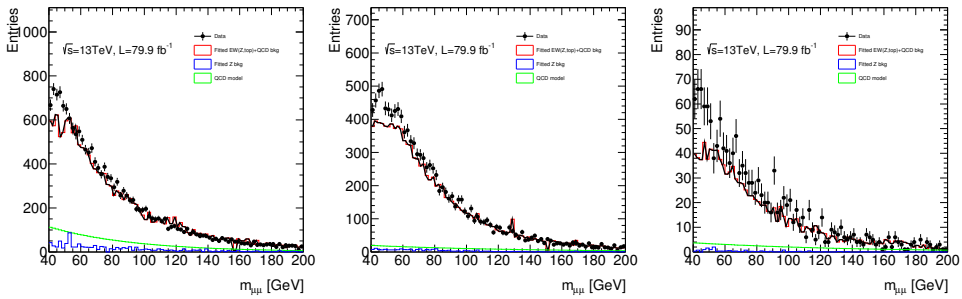

FIGURE 4.22: Same-sign di-muon mass distribution for 0-tag (a), 1-tag (b), 2-tag (c). Green histogram shows the estimated multi-jet contribution from same-sign events. The red histogram shows the fitted EW background modelled by MC plus multi-jet.

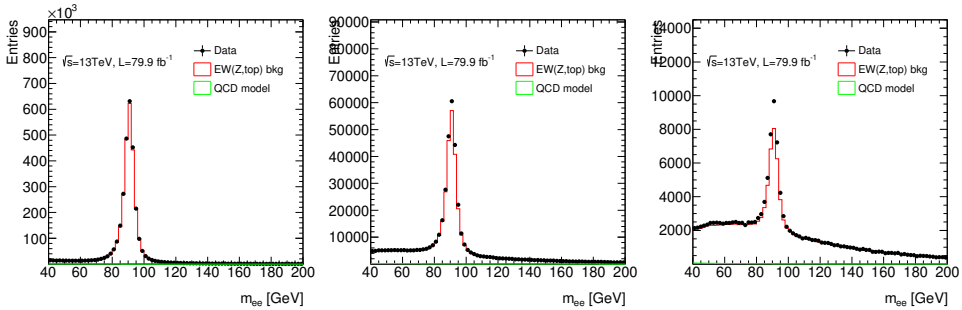

FIGURE 4.23: Opposite-sign dielectron mass distribution for 0-tag (a), 1-tag (b), 2-tag (c). Green histogram shows the estimated multi-jet contribution from same-sign events. The red histogram shows the fitted EW background modelled by MC plus multi-jet.

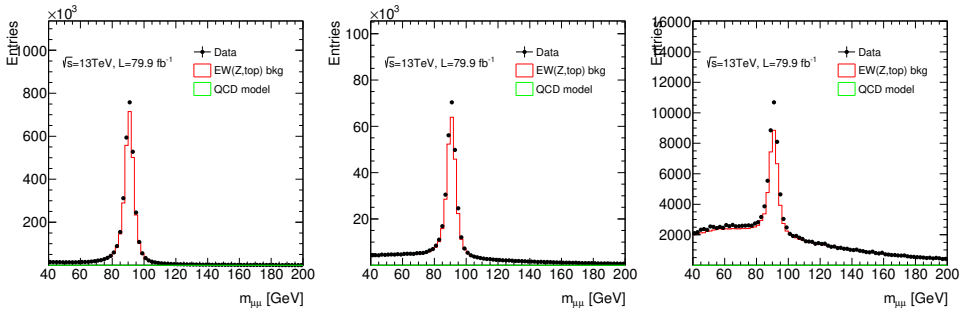

FIGURE 4.24: Opposite-sign dimuon mass distribution for 0-tag (a), 1-tag (b), 2-tag (c). Green histogram shows the estimated multi-jet contribution from same-sign events. The red histogram shows the fitted EW background modelled by MC plus multi-jet.

window. Even scaling the top background contamination to 70% of its MC predicted value, the multijet contamination is approximately 0.74%. The conclusion is that multijet contamination is negligible in the $e\mu$ CR. Fig.(4.25) shows the MJ contamination in the $2b$-tagged $e\mu$ CR in opposite sign region.

TABLE 4.12: Multijet background amout with respect to total background for 0, 1 and 2 b-tagged events in di-electron channel.

Jet Multiplicity	Multijet Fraction (71 GeV<$m_{\ell\ell}$<121 GeV)	Multijet Fraction (81 GeV<$m_{\ell\ell}$<101 GeV)
0 b-tag	0.20%	0.10%
1 b-tag	0.34%	0.19%
2 b-tag	0.02%	0.01%

TABLE 4.13: Multijet background amout with respect to total background for 0, 1 and 2 b-tagged events in di-muon channel.

Jet Multiplicity	Multijet Fraction (71 GeV<$m_{\ell\ell}$<121 GeV)	Multijet Fraction (71 GeV<$m_{\ell\ell}$<121 GeV) (81 GeV<$m_{\ell\ell}$<101 GeV)
0 b-tag	0.03%	0.02%
1 b-tag	0.08%	0.04%
2 b-tag	0.07%	0.04%

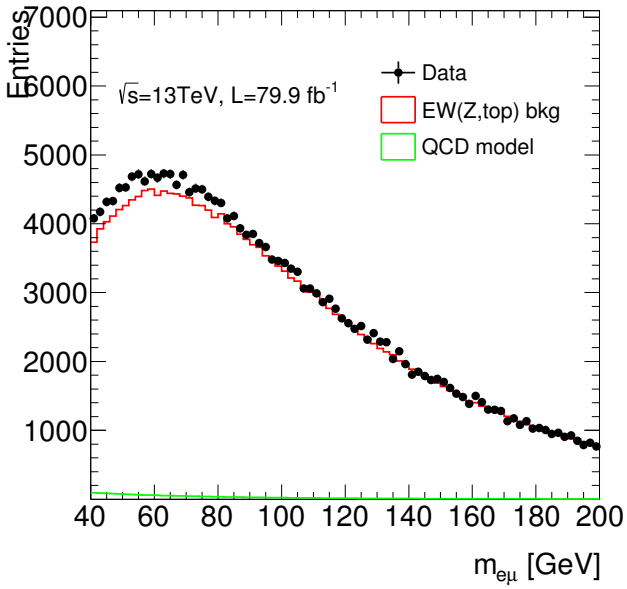

FIGURE 4.25: Multijet contamination for $e\mu$ CR in opposite sign region.

4.11.3 Study of Isolation Working Points for the 139 fb^{-1} analysis

As can be seen from Tab.(4.4) and Tab.(4.5), in the analysis iteration at 139 fb^{-1} , the lepton isolation working point have been changed in FixedCutLoose with respect to LooseTrackOnly (performance of the two working points are described for electrons in [58] and muons in [59]) used in 79.8 fb^{-1}.
In this context I have performed a study on yield and shape for the signal ZH in the 2-lepton channel both for Monte Carlo simulated samples and data with the Full Run2 statistics to verify the impact of a difference choice of isolation working point on the signal.
The difference between them can be found in 3.1.3 and in 3.2.2, respectively for muons and electrons.
The yields and shapes have been compared separately for 75 GeV<p_T^V<150 GeV and p_T^V>150 GeV, for 2 jets and $\geq$3 jets events. They are listed in Tab.(4.14) and in Tab.(4.15) together with their percentage difference. The signal considered are $qqZllH$ and $ggZllH$ (signals $qqZ\nu\nu H$ and $ggZ\nu\nu H$, corresponding to 0-lepton channel signal, and $qqWl\nu H$, corresponding to 1-lepton channel signal, have not been considered since they have be found to have negligible contributions).

TABLE 4.14: Monte Carlo event yields comparison using *FixedCutLoose* or *LooseTrackOnly* for 75 GeV<p_T^V<150 GeV for 2 jet and $\geq$ 3 jet multiplicity for the full Run2 statistics. In the last column, the percentage differences between the two can be seen.

2 jets			
Signal	*FixCutLoose*	*LooseTrackOnly*	
qqZllH	65.56 $\pm$ 0.26	65.13 $\pm$ 0.26	0.7%
ggZllH	13.73 $\pm$ 0.37	13.35 $\pm$ 0.35	2.8%
$\geq$ 3 jets			
Signal	*FixCutLoose*	*LooseTrackOnly*	
qqZllH	93.31 $\pm$ 0.30	92.39 $\pm$ 0.29	1%
ggZllH	35.00 $\pm$ 0.57	34.54 $\pm$ 0.57	1.3%

TABLE 4.15: Monte Carlo event yields comparison using *FixedCutLoose* or *LooseTrackOnly* for p_T^V>150 GeV for 2 jet and $\geq$ 3 jet multiplicity for the full Run2 statistics. In the last column, the percentage differences between the two can be seen.

2 jets			
Signal	*FixCutLoose*	*LooseTrackOnly*	
qqZllH	35.64 $\pm$ 0.07	35.42 $\pm$ 0.07	0.7%
ggZllH	8.89 $\pm$ 0.30	8.81 $\pm$ 0.30	0.9%
$\geq$3 jets			
Signal	*FixCutLoose*	*LooseTrackOnly*	
qqZllH	65.80$\pm$ 0.10	65.22$\pm$ 0.10	0.9%
ggZllH	32.82 $\pm$ 0.64	32.52 $\pm$ 0.63	0.9%

The shape comparison are shown in Fig.(4.26) (2 jets) and Fig.(4.27) ($\geq$3 jets) for the 75 GeV<p_T^V<150 GeV, while Fig.(4.28) (2 jets) and Fig.(4.29) ($\geq$3 jets) shows the same distributions for the p_T^V>150 GeV. The distribution are the invariant masses of the di-lepton pairs.
At this stage of the study, the behaviours using different working points looks very similar with differences around 1%, except for $ggZllH$ signal where there is 6% gain when using FixedCutLoose working point.
The same study has been performed on data. The yield comparisons between the two working points can be seen in Tab.(4.16) together with their percentage differences.

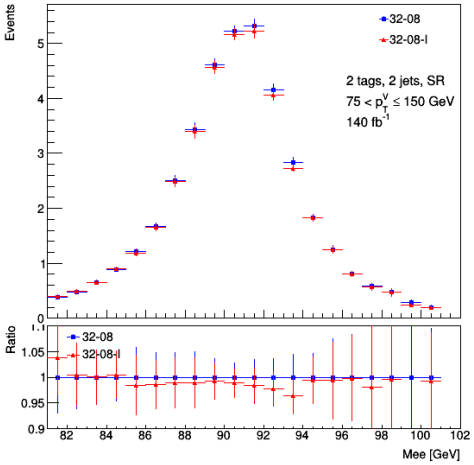

(A) Invariant di-electron mass.

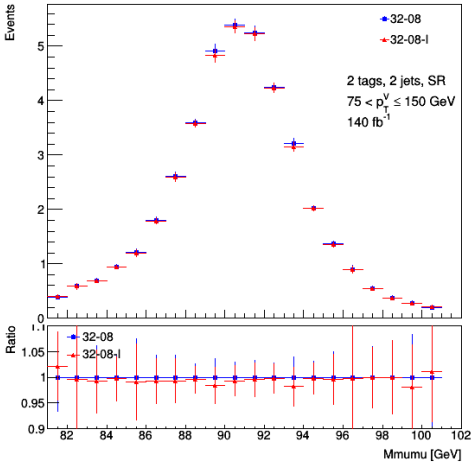

(B) Invariant di-muon mass.

FIGURE 4.26: Invariant mass of the lepton pair for the 75 GeV<p_T^V<150 GeV for 2 jets events with the full Run2 statistics. *FixedCutLoose* is shown in blue, *LooseTrackOnly* in red.

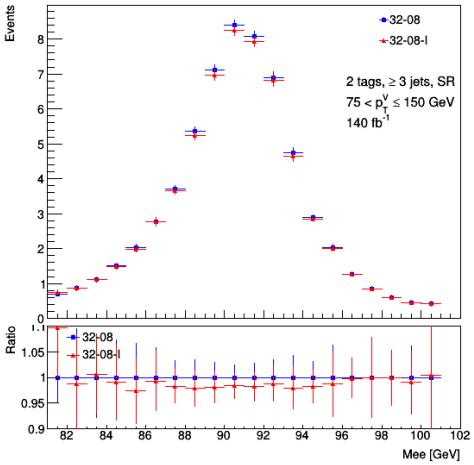

(A) Invariant di-electron mass.

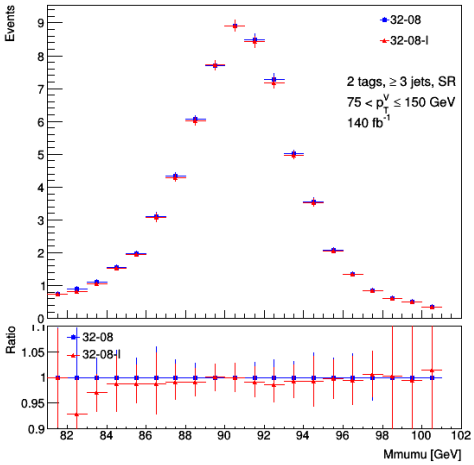

(B) Invariant di-muon mass.

FIGURE 4.27: Invariant mass of the lepton pair for the 75 GeV<p_T^V<150 GeV for $\geq$ 3 jets events with the full Run2 statistics. *FixedCutLoose* is shown in blue, *LooseTrackOnly* in red.

As can be seen, from a comparison of the results in Tab.(4.16) with what obtained from

TABLE 4.16: Data event yields comparison between the two working points for 75 GeV<p_T^V<150 GeV and p_T^V>150 GeV for 2 jet and $\geq$ 3 jet multiplicity for the full Run2 statistics. In the last column, the percentage differences between the two can be seen.

Signal Region	*FixCutLoose*	*LooseTrackOnly*	
75 GeV<p_T^V<150 GeV 2 jets	18165.00 $\pm$ 134.79	18179.00 $\pm$ 134.83	0.1%
p_T^V>150 GeV 2 jets	2606.00 $\pm$ 51.05	2625.00 $\pm$ 51.33	1.1%
75 GeV<p_T^V<150 GeV $\geq$ 3 jets	43879.00 $\pm$ 209.44	44274 $\pm$ 210.41	0.9%
p_T^V>150 GeV $\geq$ 3 jets	11932.00 $\pm$ 109.23	12066.00 $\pm$ 108.85	1.1%

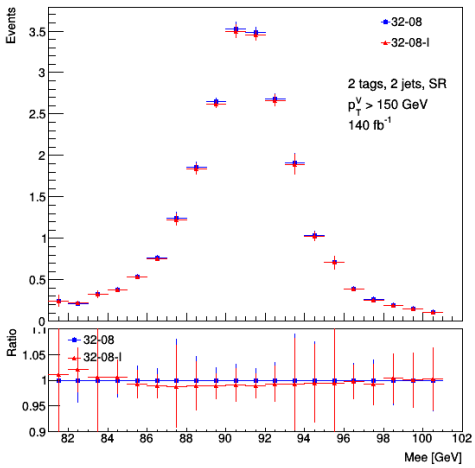

(A) Invariant di-electron mass.

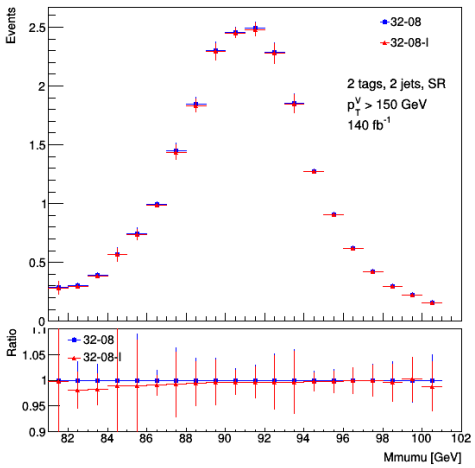

(B) Invariant di-muon mass.

FIGURE 4.28: Invariant mass of the lepton pair for the p_T^V>150 GeV for 2 jets events with the full Run2 statistics. *FixedCutLoose* is shown in blue, *LooseTrackOnly* in red.

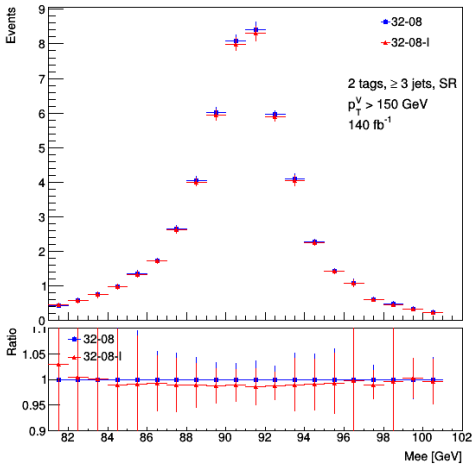

(A) Invariant di-electron mass.

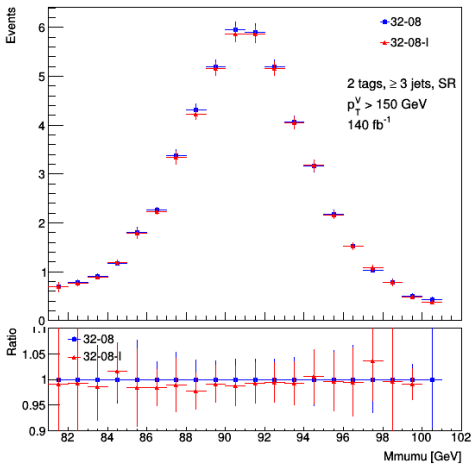

(B) Invariant di-muon mass.

FIGURE 4.29: Invariant mass of the lepton pair for the p_T^V>150 GeV for $\geq$ 3 jets events with the full Run2 statistics. *FixedCutLoose* is shown in blue, *LooseTrackOnly* in red.

Monte Carlo studies (Tab.4.14 and Tab.4.15), LooseTrackOnly slightly increases the event yields with respect to FixedCutLoose when comparing the two different working points. The differences between them in data are ∼1% in all signal regions considered.
In a final stage, it has been decided to move to FixedCutLoose working point for 2-lepton channel analysis with Full Run2 statistics because of the gain in event yield in Monte Carlo signal $ggZllH$.

4.11.4 Study of the possibility to split the high p_T^V region training at 250 GeV

One of the studies I have performed in the context of the MVA analysis has dealt with the possibility to perform separate trainings for the high p_T^V region applying a cut at 250 GeV.

As said in 4.9.2, for 2-lepton channel, three p_T^V regions enter in the profile likelihood fit in the full Run2 statistics analysis currently on going:

- 75 GeV<p_T^V<150 GeV
- 150 GeV<p_T^V<250 GeV
- p_T^V>250 GeV

The diagnostics used to test a possible improvement in using separated trainings is the study of the ROC curves. The ROC curve is a performance measurement for any classification problem. It is a probability curve and the area under it represents the separability power of the model. It provides information about how much the model is capable to distinguish between classes. In our case, as much as training and testing sample curves are similar, better is the model in distinguishing signal and background.
Fig.(4.30) shows the ROC curves (A) and the ROC ratios (ratio between the testing to training ROC) (B) for the inclusive high p_T^V (i.e. p_T^V>150 GeV), while Fig.(4.31) and Fig.(4.32) show the same plots for the other two dedicated training.

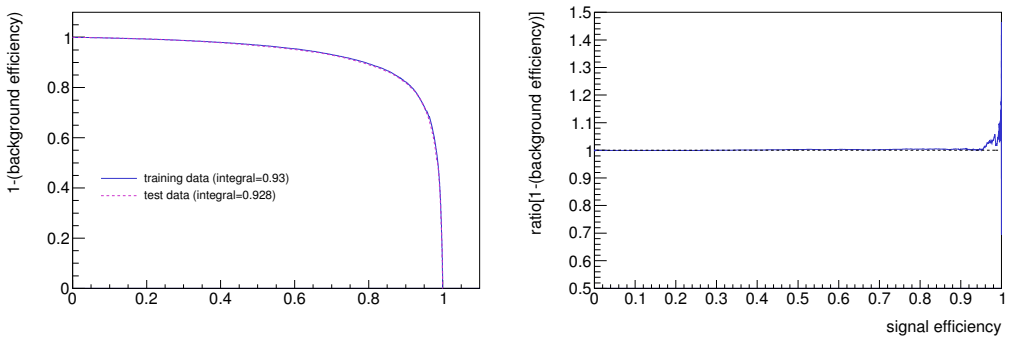

(A) ROC curves. (B) ROC ratio.

FIGURE 4.30: ROC curve and ratios for inclusive training, p_T^V>150 GeV for training and statistically independent test samples.

It can be seen, by comparing them, how the region with p_T^V>150 GeV is dominated by the 150 GeV<p_T^V<250 GeV. Overtraining is observed for the separate training with p_T^V>250 GeV resulting in a ratio between testing and training higher than 1, possibly due to the lack

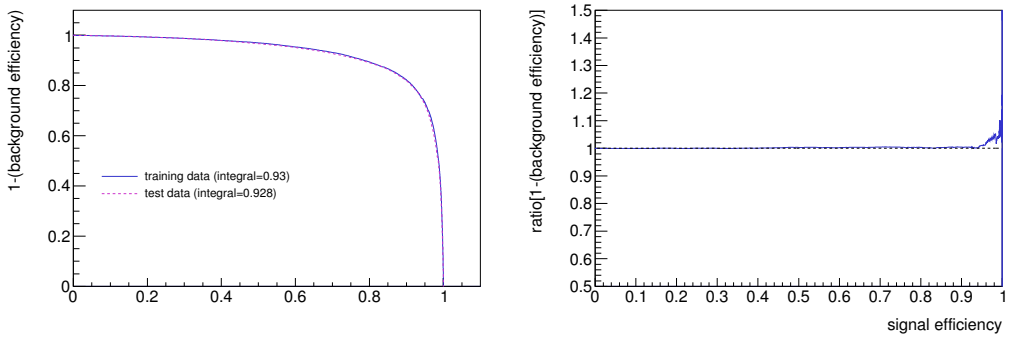

(A) ROC curves (B) ROC ratio.

FIGURE 4.31: ROC curve and ratios for 150 GeV<p_T^V<250 GeV training for training and statistically independent test sample.

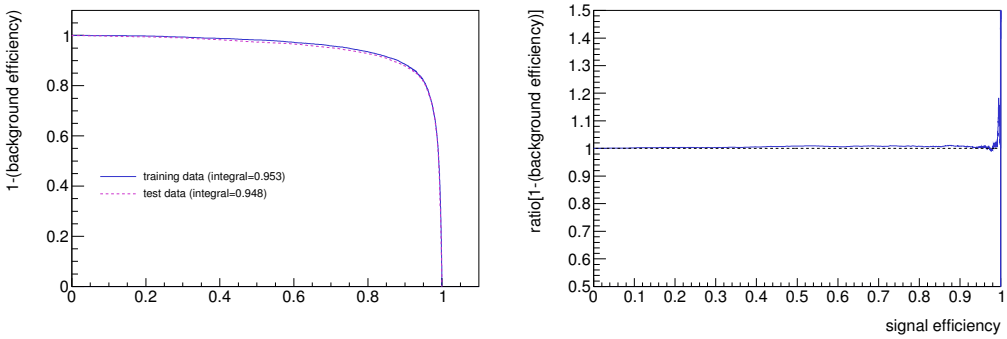

(A) ROC curves (B) ROC ratio.

FIGURE 4.32: ROC curve and ratios for p_T^V>250 GeV training for training and statistically independent test sample.

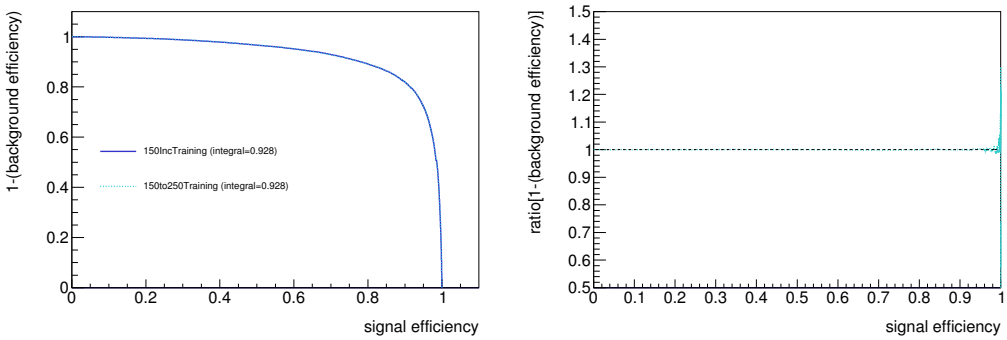

(A) ROC curves. (B) ROC ratio.

FIGURE 4.33: ROC curve and ratios for 150 GeV<p_T^V<250 GeV compared to inclusive training.

of statistics in this region, see Fig.(4.32).
Moreover, as can be seen from Fig.(4.33) and Fig.(4.34), no significant improvements are observed comparing the two separate trainings to the inclusive one.

On the basis of these studies, it is clear that no substantial gain in performance is obtained with two dedicated trainings for high p_T^V in 2-lepton channel. Similar results have been obtained also in the others two channels (0- and 1-lepton). In conclusion, no dedicated trainings will be used.

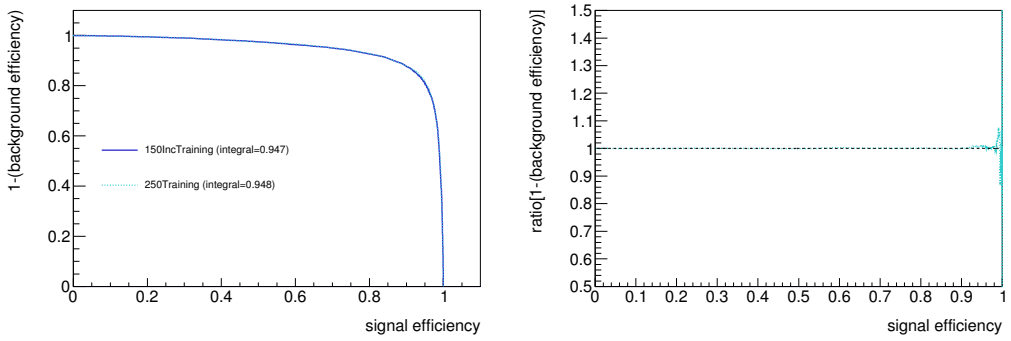

(A) ROC curves. (B) ROC ratio.

FIGURE 4.34: ROC curve and ratios for p_T^V>250 GeV compared to inclusive training.

4.11.5 Hybrid Tagging: Comparison of the MVA Performance with respect to Full Truth b-tagging

A novelty of the 139 fb^{-1} analysis is the introduction of a new tagging technique: the *hybrid tagging*. It has been developed in the attempt to solve the non negligible discrepancies between truth and direct tagged distributions for b-jets.
It consists, basically, in applying direct b-tagging to b-jets and truth tagging to other flavours. At the very stage, the jets in each event are divided in two groups, upon consideration based on their truth flavour. Direct tagging is applied to the first group, while the second group of $c-$ and $light$-jets is truth tagged. Considering an example, of a 5-jets event. One of the

jet	flavour	b-tagging score
1	b	0.99
2	b	0.74
3	c	0.24
4	c	0.16
5	$light$	0.07

2 b-jets has a b-tagging score above 70% working point, the other below, according to the recommendations listed in Tab.(3.4). The other three jets are c- and $light$ flavours. In this case, just one jet passes the b-tagging requirement of direct tagging, meaning that another b-jet is needed to make our event enter the signal region. Truth tagging is applied to the non-b-tagged group to obtain one truth jet. The jet 3 has the highest probability to be chosen so this event will enter the signal region as bc event with a weight calculated as the product of the weights from b-jets and truth-tagging weight.
As said in 4.10.3, truth b-tagging is the default strategy adopted for Monte Carlo events entering in the BDT training. Since, the simulated events entering the profile likelihood fit exploit the hybrid approach, performance using the two methods have been compared to see if there can be any gain in choosing one upon the other. From now on, *pure* truth tagging will be labelled as *full truth* in contrast with the *hybrid truth*. I personally carried on the study for the 2-lepton channel. The plots and distributions shown are referred to 2 jets multiplicity and for the inclusive high p_T^V training.

As can be see from Fig.4.35 and the comparison of the ROC curves, hybrid truth tagging shows a better performance with respect to full truth tagging since it has an higher area, but it can be also seen a small overtraining comparing training and testing ROC curves. The overtraining is confirmed by the ROC curve ratios in Fig.4.36 and by the diagnostic distributions in Fig.4.37 where differences between training and testing samples are evident.

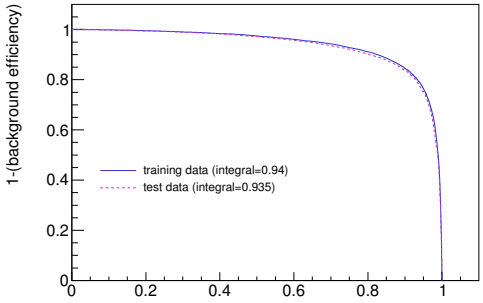

(A) ROC curves for Hybrid Truth Tagging.

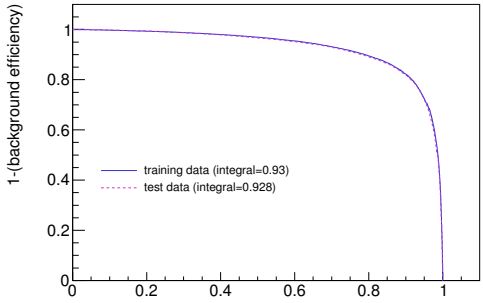

(B) ROC curve for Full Truth Tagging.

FIGURE 4.35: ROC curve for p_T^V>150 GeV training.

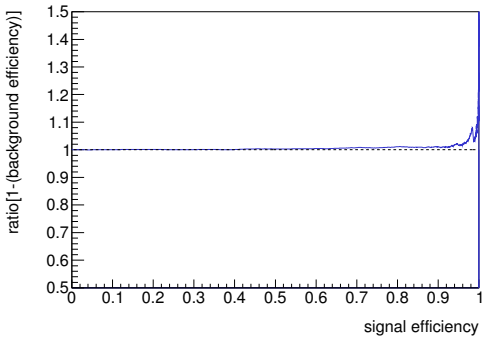

(A) ROC ratio for Hybrid Truth Tagging.

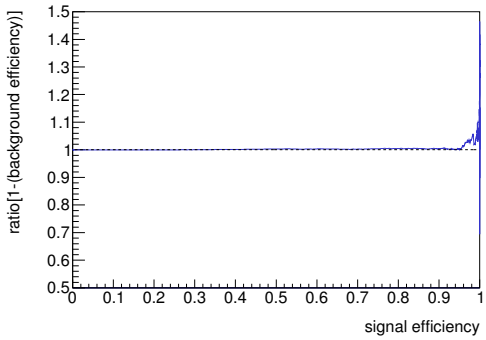

(B) ROC ratio for Full Truth Tagging.

FIGURE 4.36: ROC Ratios for p_T^V>150 GeV training.

Looking at the comparison of the training variables phase-space, no great differences are observed both for signal and background between the two different trainings, as can be seen from Fig.4.38 and Fig.4.39.

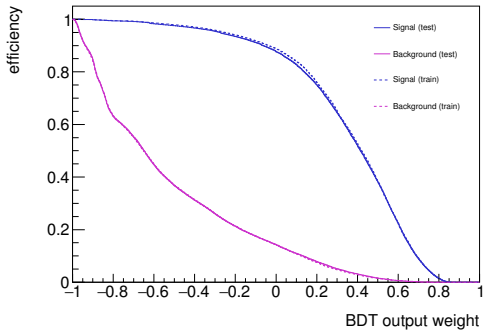

(A) BDT output score distribution.

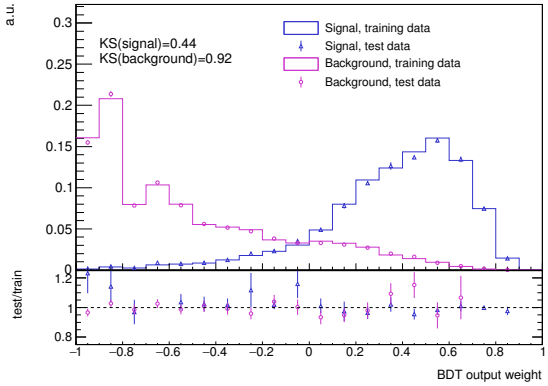

(B) Signal and Background efficiency as a function of the BDT output score.

FIGURE 4.37: Overtraining plots for training using hybrid truth tagging.

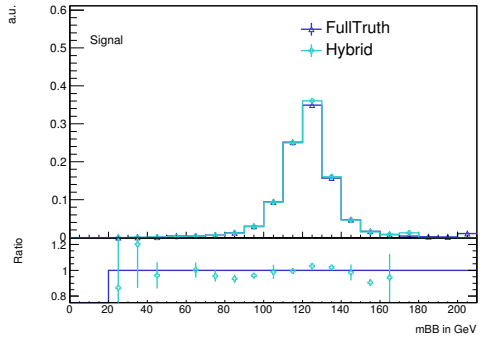

(A) m_{bb}.

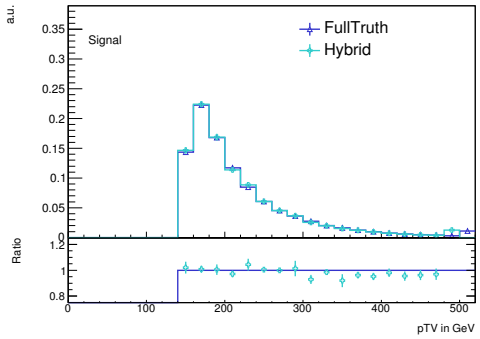

(B) p_T^V.

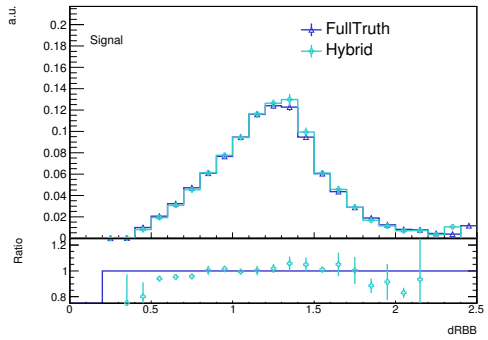

(C) dR_{bb}.

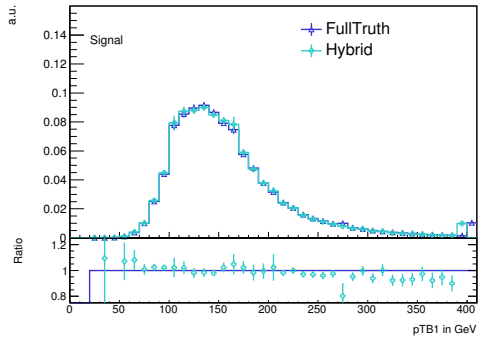

(D) p_T^{B1}.

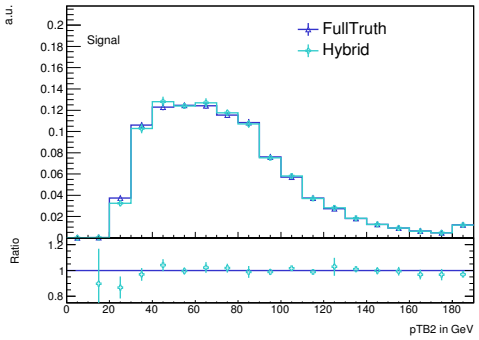

(E) p_T^{B2}.

FIGURE 4.38: Comparison of the full truth tagging (blue) training with the hybrid truth tagging (cyan) training for input variables distribution for signal.

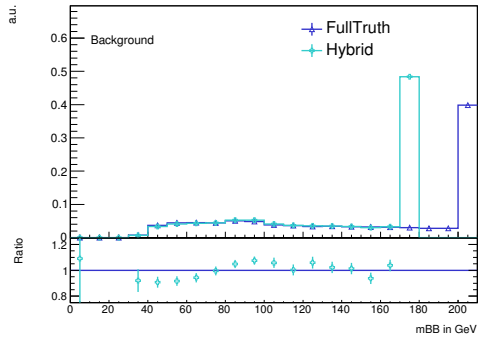

(A) m_{bb}.

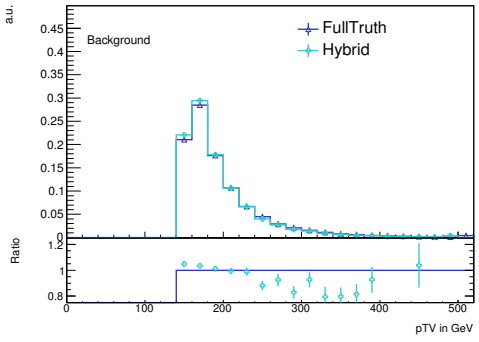

(B) p_T^V.

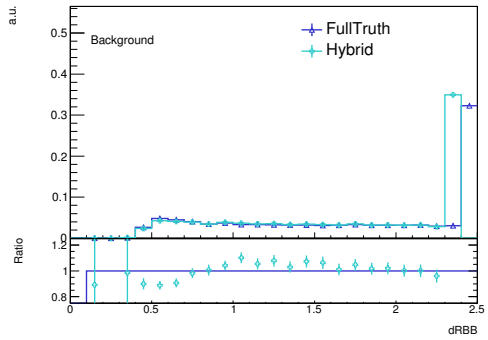

(C) dR_{bb}.

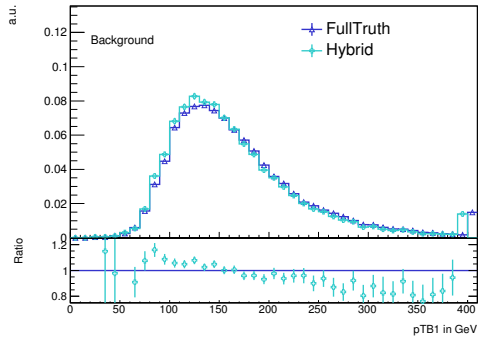

(D) p_T^{B1}.

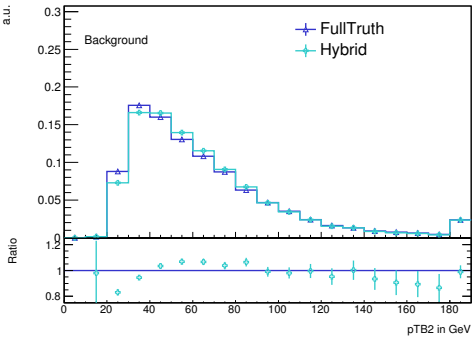

(E) p_T^{B2}.

FIGURE 4.39: Comparison of the full truth tagging (blue) training with the hybrid truth tagging (cyan) training for input variables distribution for background.

As a consequence of all these considerations it has been decided to use the full truth tagging approach for the BDT training to make use of the full statistics of Monte Carlo samples.
Similar conclusions stands also for the other two channels (0- and 1-lepton).

4.11.6 Data/Monte Carlo Comparison

In the following, pre-fit data/MC distribution will be shown. Each MC event is corrected by a series of associative calibration/correction factors to be matched to the data collected by ATLAS.

- MC Event Weights. These are the weights depending on the Matrix Element amplitude and Parton Shower procedure.
- Luminosity Weights. After the production, the effective luminosity is given by $\mathscr{L}_{MC} = \frac{N_{MC}}{\sigma_{MC}}$, where σ_{MC} corresponds to the MC estimated cross section. The events must be therefore scaled to the luminosity of the data by the weight defined as $w_{\mathscr{L}} = \frac{\mathscr{L}}{\mathscr{L}_{MC}}$.
- Pileup Reweighting. These scale factors coming from the CP::PileupReeightingTool tool and are applied event-by-event to correct the randomly generated average number of interactions per bunch-crossing to that of the period specific data distribution, see Fig.(4.40). Following this prescription, Monte Carlo samples are divided in:

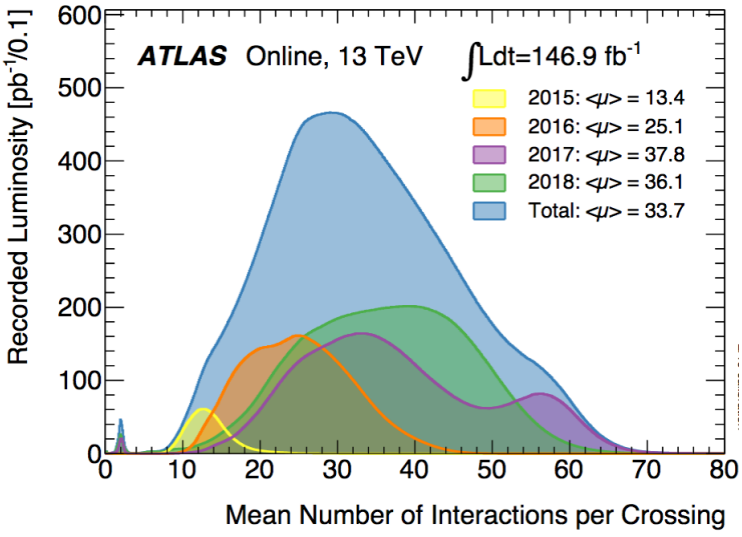

(a)

FIGURE 4.40: Recorded luminosity during Run2 with respect to the average number of interaction per bunch crossing, shown for every year of the data taking.

  - MC16a, used in conjunction with 2015+2016 data-set.
  - MC16d, used in conjuction with 2017 data-set.
  - MC16e, used in conjuction with 2018 data-set (only for 139 fb^{-1}).
- Flavour Tagging Factors. MC-to-data scale factors are introduced to correct the flavour tagging efficiency of jets generated by MC to that measured in data.
- Trigger Factors. They are applied to compensate for prescale used during data collection, trigger efficiency variation and data-to-MC trigger efficiency correction factors.

- Object Reconstruction Calibration Factors. Each reconstructed object has its own set of calibration factors to be applied to account for systematic differences of measured properties from their true value.

The Data/MC presented here is referred to the Full Run2 data taking with 139 fb^{-1}. The variables reported are m_{bb} and p_T^V, since they are the most relevant in terms of the final measurements. They are shown for the signal region and for the $e\mu$ control region for all the p_T^V under investigation and for each class of events (2jets or $\geq$3jets). As it regards the high p_T^V region, the Data/MC comparison plots are shown both without and with the split at 250 GeV. The absence of data points in the invariant mass range corresponding to a Higgs candidate in the signal region plots is due to the fact that the analysis was yet blind., see 4.1

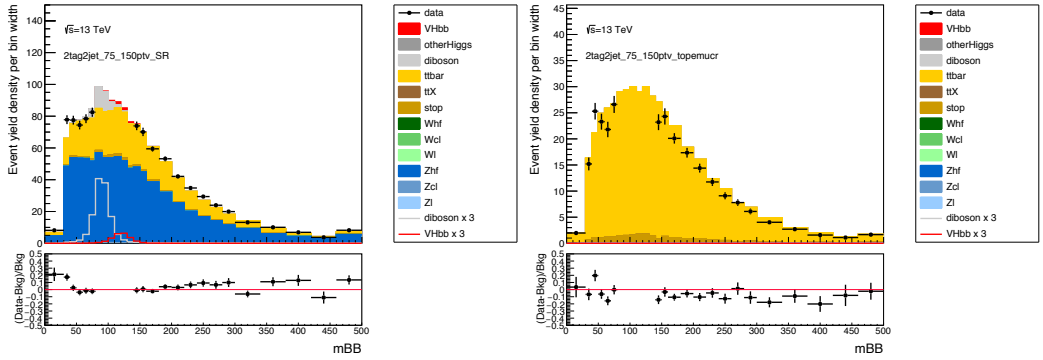

(A) m_{bb} in Signal Region.

(B) m_{bb} $e\mu$ in Control Region

(C) p_T^V in Signal Region

(D) p_T^V in Signal Region

FIGURE 4.41: Data/MC Comparison for 75 GeV<p_T<150 GeV for 2 jet (2 b-tags) events.

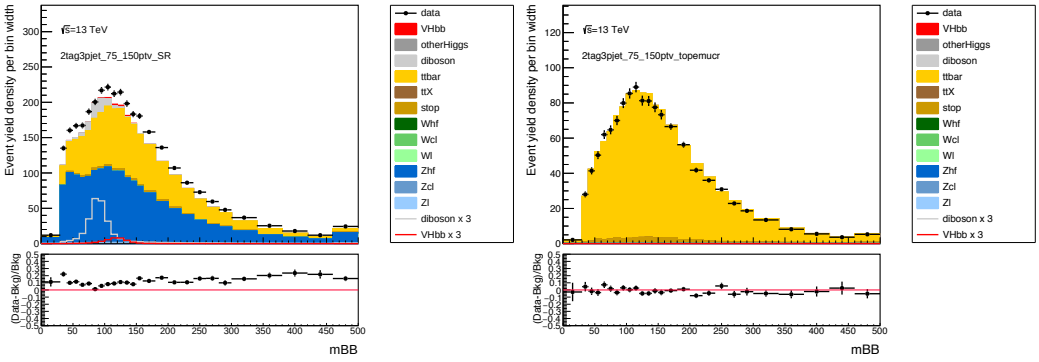

(A) m_{bb} in Signal Region.

(B) m_{bb} $e\mu$ in Control Region

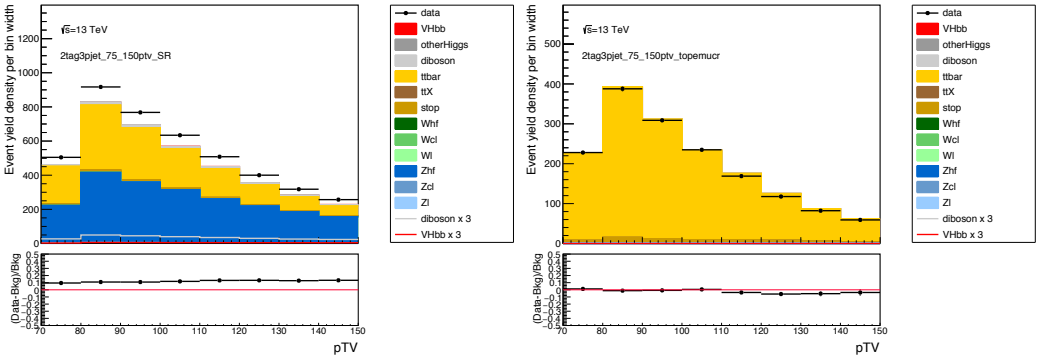

(C) p_T^V in Signal Region

(D) p_T^V in Signal Region

FIGURE 4.42: Data/MC Comparison for 75 GeV<p_T<150 GeV for $\geq$3 jets (2 b-tags) events.

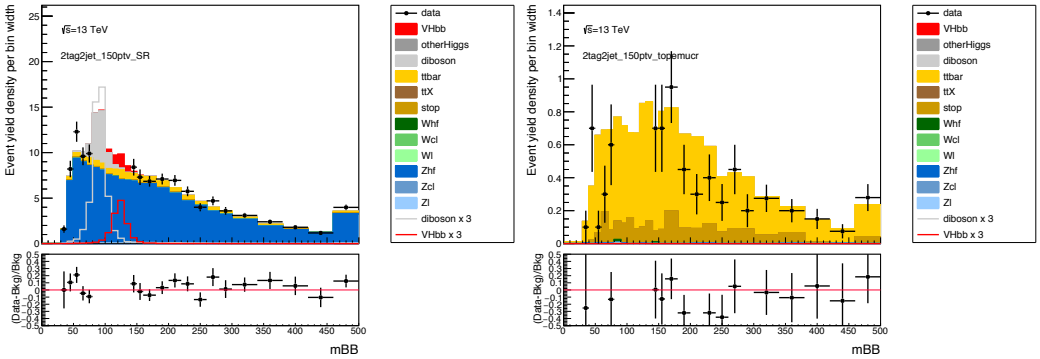

(A) m_{bb} in Signal Region.

(B) m_{bb} $e\mu$ in Control Region

(C) p_T^V in Signal Region

(D) p_T^V in Signal Region

FIGURE 4.43: Data/MC Comparison for p_T>150 GeV for 2 jets (2 b-tags) events.

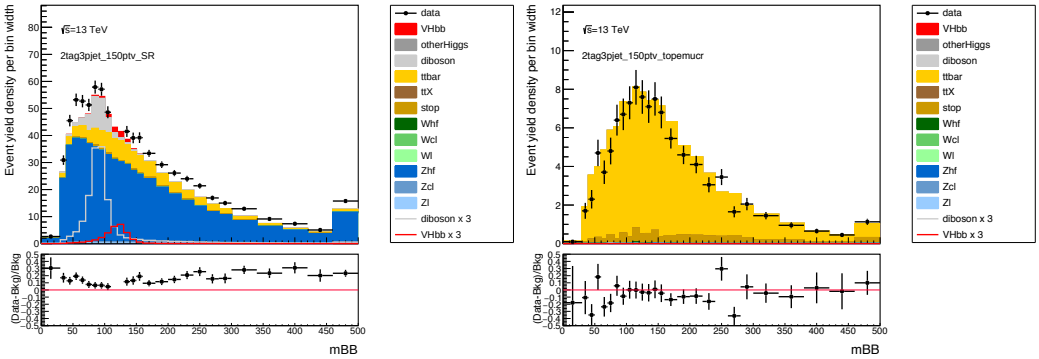

(A) m_{bb} in Signal Region.

(B) m_{bb} $e\mu$ in Control Region

(C) p_T^V in Signal Region

(D) p_T^V in Signal Region

FIGURE 4.44: Data/MC Comparison for p_T>150 GeV for $\geq$3 jets (2 b-tags) events.

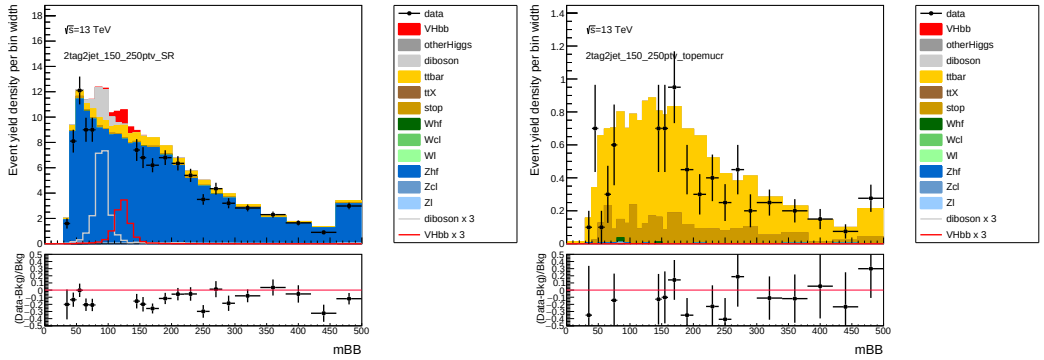

(A) m_{bb} in Signal Region.

(B) m_{bb} $e\mu$ in Control Region

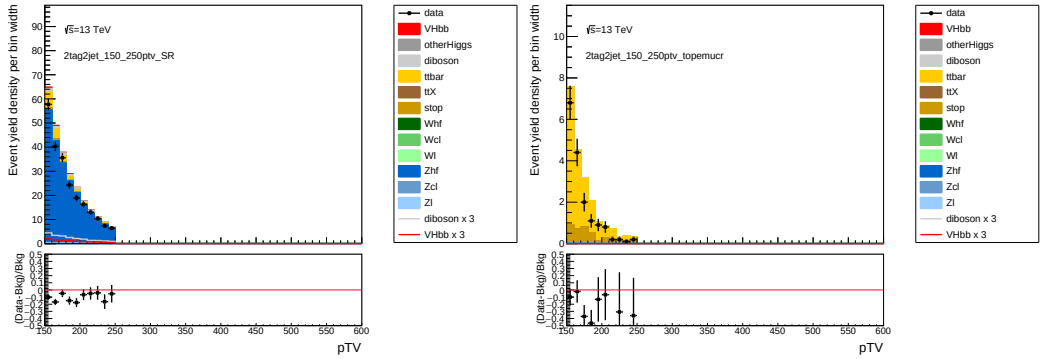

(C) p_T^V in Signal Region

(D) p_T^V in Signal Region

FIGURE 4.45: Data/MC Comparison for 150 GeV<p_T<250 GeV for 2 jets (2 b-tags) events.

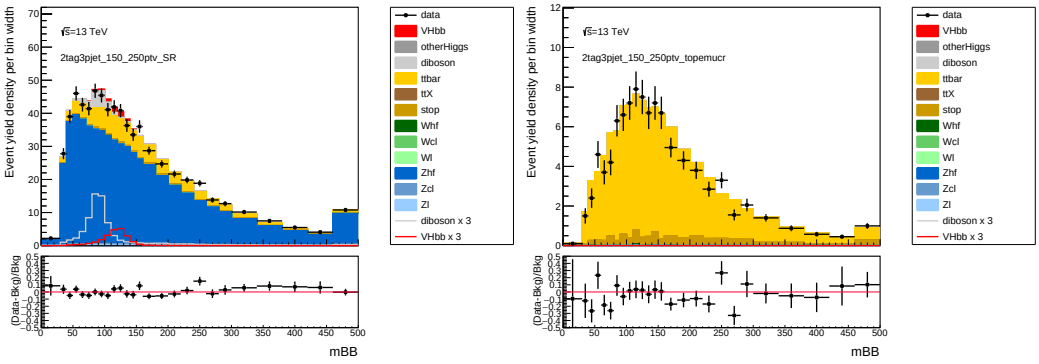

(A) m_{bb} in Signal Region.

(B) m_{bb} $e\mu$ in Control Region

(C) p_T^V in Signal Region

(D) p_T^V in Signal Region

FIGURE 4.46: Data/MC Comparison for 150 GeV<p_T<250 GeV for $\geq$3 jets (2 b-tags) events.

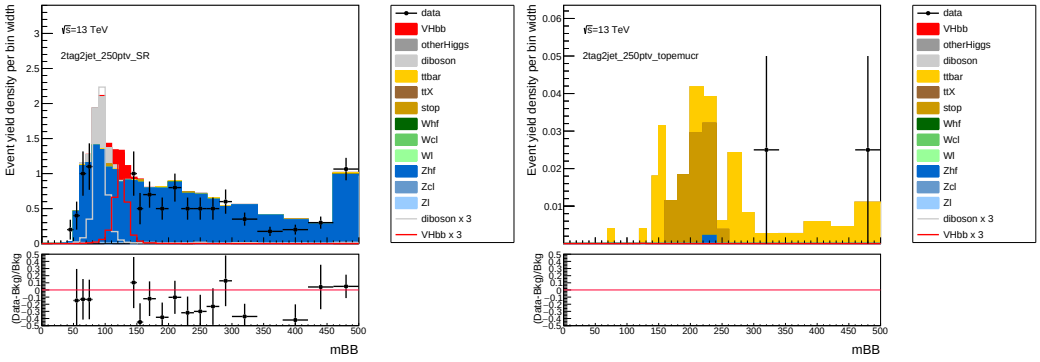

(A) m_{bb} in Signal Region.

(B) m_{bb} $e\mu$ in Control Region

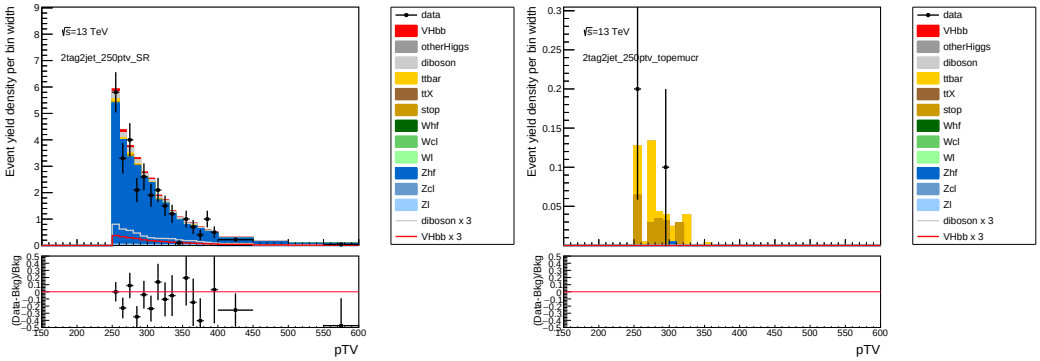

(C) p_T^V in Signal Region

(D) p_T^V in Signal Region

FIGURE 4.47: Data/MC Comparison for p_T>250 GeV for 2 jets (2 b-jets) events.

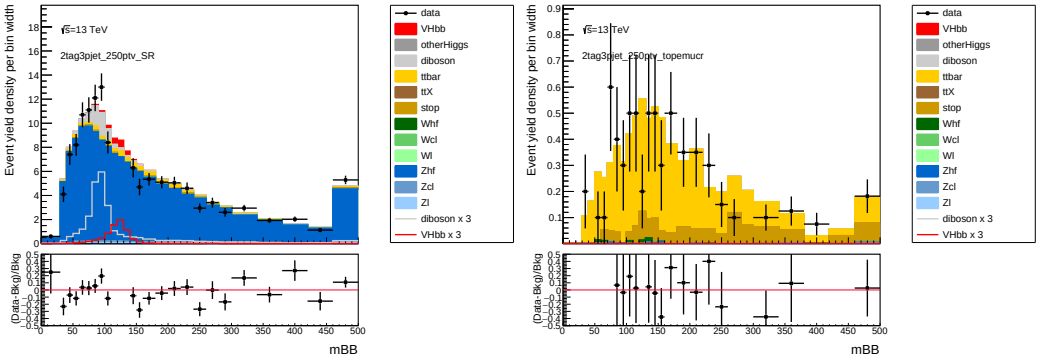

(A) m_{bb} in Signal Region.

(B) m_{bb} $e\mu$ in Control Region

(C) p_T^V in Signal Region

(D) p_T^V in Signal Region

FIGURE 4.48: Data/MC Comparison for p_T>250 GeV for $\geq$3 jets (2 b-tags) events.

As can be seen, data are well described by Monte Carlo simulation. It has also to be noted by comparing Data/MC plots with and without the split at 250 GeV how the p_T^V region is highly dominated by 150 GeV<p_T^V<250 GeV region, while p_T^V>250 GeV region suffer lack of statistics.
Moreover, it can be appreciated the high-purity of the $e\mu$ control region, with a 99% contribution from $t\bar{t}$ and single-t Wt.

4.12 Signal Extraction: Profile Likelihood Procedure

The starting point for the discovery of a new signal process is the definition of the null hypothesis H_0, which describes the known processes identified in this case as background sources, against the signal hypothesis H_1, which includes background and signal.
The method based on a significance test using *profile likelihood ratio* is used in high energy physics to claim discovery. To achieve precision, it is necessary to have a solid model for predictions of data distributions which represents the theory as much accurately as possible [73].
For each event in the signal sample, a variable x can be measured and its value can be used to construct a histogram $\mathbf{n} = (n_1, ...n_N)$ of N bins. The expectation value of n_i can be written as:

$$E[n_i] = \mu s_i + b_i \tag{4.18}$$

where s_i and b_i are:

$$s_i = \int_{bin\,i} f_s(x;\theta_s)dx \tag{4.19}$$

$$b_i = \int_{bin\,i} f_b(x;\theta_b)dx \tag{4.20}$$

representing the mean number of signal and background entries in the i-th bins, while μ is the strength of the signal process. The background only hypothesis is μ=0, the signal only μ=1. The function $f_s(x;\theta_s)$ and $f_b(x;\theta_b)$ are the probability density functions of the variable x for signal and background and θ_s and θ_b are the *nuisance parameters*, the systematic effects whose contribution is determined from data. The integrals represent the probability to find an event in the i-th bin. The nuisance parameters can be further constrained by additional measurements (for example, evaluating some kinematic variables in control regions). Such measurements provide a set of values $\mathbf{m} = (m_1, ..., m_M)$ for the number of entries and their expectation values can be written as:

$$E[m_i] = u_i(\theta) \tag{4.21}$$

where u_i are measured quantities depending on the nuisance parameters, which provides information on the background normalization b_{tot}. The normalization of the signal, s_{tot}, is usually provided by the theory.
The likelihood function is the product of Poisson probabilities for all bins:

$$\mathcal{L}(\mu,\theta) = \prod_{j=1}^{N} \frac{(\mu s_j + b_j)^{n_j}}{n_j!} e^{-(\mu s_j + b_j)} \prod_{k=1}^{N} \frac{u_k^{m_k}}{m_k!} e^{-m_k} \tag{4.22}$$

The *profile likelihood ratio* is used to test a hypothesized value of μ:

$$\lambda(\mu) = \frac{\mathcal{L}(\mu, \hat{\hat{\theta}})}{\mathcal{L}(\hat{\mu}, \hat{\theta})} \tag{4.23}$$

The numerator of Eq.(4.23) is the *profile likelihood function*. $\hat{\hat{\theta}}$ is the value of nuisance parameter vector which maximize it for a given μ: this is the *conditional* maximum-likelihood estimator of θ (function of μ). The denominator is the maximized *unconditional* likelihood function and $\hat{\mu}$ and $\hat{\theta}$ are the maximum estimators. The profile likelihood ratio can assume values between 0 and 1. When λ is close to 1, it means that there is a good agreement between the data and the hypothesis.
To fix an upper limit for μ, the statistic test q_μ is used, defined as follows:

$$q_\mu = \begin{cases} 0, & \mu < \hat{\mu} \\ -2\ln\lambda(\mu), & \mu \geq \hat{\mu} \end{cases} \tag{4.24}$$

Higher values of q_μ represent greater incompatibility between data and hypothesis. According to the central limit theorem, given enough statistics, $\lambda(\mu) \approx e^{-\chi^2/2}$ resulting in $q_\mu = \chi^2(\mu)$ for μ=$\hat{\mu}$. High values of q_μ results in high values of χ^2 giving incompatibility between the data and the test hypothesis. The level of agreement between the data and the μ coming from the hypothesis is given by the p-value:

$$p_\mu = \int_{q_{\mu obs}}^{\infty} f(q_\mu|\mu) dq_\mu \tag{4.25}$$

It is the probability, assuming the hypothesis H, of finding data of equal or greater incompatibility with the predictions of H. In Eq.(4.25), $f(q_\mu|\mu)$ is the probability density function of q_μ assuming the hypothesis of μ. In terms of upper limits, it is quoted the value of μ for which the median p-value is equal to 0.05 corresponding to 95% confidence level.
In our case μ corresponds to the signal strength. The mean value of $f(q_0|\mu = 1)$ is evaluated in order to determine the expected p-value of the measurement and it is denoted as $q_{0,exp}$. The expected value of p is:

$$p_0 = \int_{q_{0,exp}}^{\infty} f(q_0|\mu = 0) dq_0 \tag{4.26}$$

The determination of the expected p-value is shown in Fig.(4.49).

Another important quantity to introduce is the significance Z. Considering a Gaussian variable x with mean m_x, $\hat{x}$($\hat{x}$>m_x) is the value of x which an upper-tail probability equal to the p-value p. The significance is defined as the number of standard deviations of $\hat{x}$ with respect to m_x as:

$$Z = \Phi^{-1}(1 - p) \tag{4.27}$$

Φ^{-1} is the quantile of the standard Gaussian which corresponds to the inverse of the cumulative distribution.
The estimator known as *Asimov* data set has been used in the context of $H \to b\bar{b}$ to estimate the sensitivity in the expected median significance to reject different values of μ.
In the next Chapter, the results of the 79.8 fb^{-1} [71] analysis obtained from the combination of the three channels will be provided together with preliminary results from the full Run2 statistics analysis.

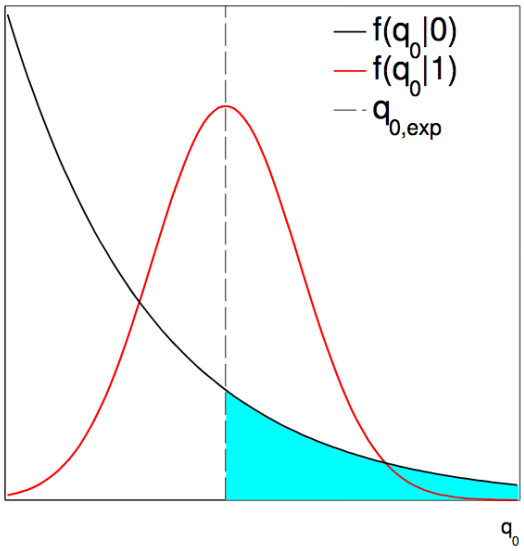

FIGURE 4.49: Diagram illustrating the extraction of the expected p-value from the distribution of q_0 with an expected signal strength of μ=1. The p-value corresponds to the integral of the cyan area.

Chapter 5

Observation of H$\rightarrow b\bar{b}$ with 79.8 fb^{-1} and Further Optimizations

In Chapter (4), the Multivariate Analysis techninque and the Profile Likelihood strategy have been described, together with the description of the object reconstruction, the event selection and the data and Monte Carlo samples description for both the analyses. The final goal is to extract the *signal strength* μ, defined as the ratio of the measured and Standard Model predicted cross sections combining all the information, as said in the description of the analysis strategy in Sec.4.1.
In the present Chapter, the result of the 79.8 fb^{-1} analysis which led to the observation of the Standard Model $H \rightarrow b\bar{b}$ decay will be presented [71]. The analysis has been performed with the combination of Run1 and Run2 results and of the other two production channels, $t\bar{t}H$ [88] [89] and VBF (vector boson fusion) [28]. These analyses are not part of my work and are therefore not presented here. The importance of such result lies in the fact that it probes the Yukawa coupling of the Higgs boson to the quark sector.
The associated production of VH has also been observed by combining the Run2 analyses results coming from $VH(H \rightarrow b\bar{b})$ with the others two main decays of VH, with $H \rightarrow ZZ^* \rightarrow 4\ell$ [90] and $H \rightarrow \gamma\gamma$ [91] (also not discussed in this thesis).
A description of the further progress of the study of $VH(H \rightarrow b\bar{b})$ with the full Run2 statistics will be provided.

5.1 Statistical Analysis

A statistical fitting procedure based on the Rootstats framework is used to extract the signal strenght of the signal from the data. A binned likelihood function $\mathcal{L}(\mu, \theta)$ is constructed as the product of the Poisson probability terms over the bin on the input distributions involving the number of the data events and the expected signal and background yields, taking into account the effects of the floating background normalisation and the systematic uncertainties. The parameter of interest is μ, the *signal strength* that multiplies the SM Higgs boson production cross section times the branching ratio into $b\bar{b}$, extracted maximizing the likelihood. The systematic uncertainties enter the likelihood as nuisance parameters θ. The signal and control regions entering the likelihood fit for the 79.8 fb^{-1} analyis are summerized in Tab.(5.1).
The primary input to the fit are the BDT$_{VH}$ discriminant in eight 2 b-tagged signal regions, defined separately for the three lepton channels, built as described in Sec.4.10.
The eight signal regions are defined according the p_T^V region and the jet multiplicity in 0-, 1- and 2-lepton analysis, as follows:

- 0-lepton analysis: one p_T^V region with p_T^V<150 GeV splitted in 2 jets and exactly 3 jets, resulting in two signal regions.

TABLE 5.1: Signal and Control regions entering the global likelihood fit for all the categories in each channel, as input to the nominal multivariate analysis for 79.8 fb^{-1}.

Channel	Region	Categories			
		75 GeV<p_T^V<150 GeV		p_T^V>150 GeV	
		2 jet	3 jet	2 jet	3 jet
0-lepton	SR	-	-	BDT	BDT
1-lepton	SR	-	-	BDT	BDT
2-lepton	SR	BDT	BDT	BDT	BDT
1-lepton	$W+HF$	-	-	Yield	Yield
2-lepton	$e\mu$	m_{bb}	m_{bb}	Yield	m_{bb}

- 1-lepton analysis: one p_T^V region with p_T^V<150 GeV splitted in 2 jets and exactly 3 jets, resulting in two signal regions.
- 2-lepton analysis: two p_T^V region with 75 GeV<p_T^V<150 GeV and p_T^V>150 GeV, each of them splitted in 2 jets and $\geq$3 jets, resulting in four signal regions.

Additionally, for the 79.8 fb^{-1}, six control regions are defined:

- Two CR for the 1-lepton channel (for each jet multiplicity category in the p_T^V>150 GeV region) to better constrain the $W+HF$ dominant background. It is defined with cuts on the top quark mass (m_t>225 GeV) and on the invariant mass of the b-jet pair (m_{bb}<75 GeV) with a 70% purity. It enters the fit as a single bin (as yields) and provides a validation of the $W+HF$ normalization.
- Four CR $e\mu$ for the 2-lepton, built as described in 4.4, with a 99% background purity, used to provide constraint on top background normalization and shape, with m_{bb} as input to the fit.

Electron and muon for the different sub-channel are summed up before entering the fit. The processes considered in the fit are:

- Signal: $VH\to Vb\bar{b}$, with $V=Z,W$ decaying in $\nu\nu$ (0-lepton), $\ell\nu$ (1-lepton) or $\ell\ell$ (2-lepton).
- Backgrounds:
  - $Z/W+jets$ (splitted into flavour components).
  - $t\bar{t}$.
  - single-t.
  - diboson: WW, WZ and ZZ
  - multijet: enters only for 1-lepton channel. It has been proved to be negligible for the other channels (see 4.11.2 for the 2-lepton channel estimation).

Before going into details of the systematic uncertainties description and their breakdown in the final fit result, it is important to briefly describe the two cross check analysis performed.

TABLE 5.2: The signal and control regions entering the global fit for all the categories in each channel, for the dijet mass analysis 79.8 fb^{-1}. For 2-lepton $e\mu$ control region the two high p_T^V region yields have been merged together to increase statistics.

Channel	Region	Categories					
		75 GeV<p_T^V<150 GeV		150 GeV<p_T^V<200 GeV		p_T^V>200 GeV	
		2 jet	3 jet	2 jet	3 jet	2 jet	3 jet
0-lepton	SR	-	-	m_{bb}	m_{bb}	m_{bb}	m_{bb}
1-lepton	SR and $W+HF$ CR	-	-	m_{bb}	m_{bb}	m_{bb}	m_{bb}
2-lepton	SR	m_{bb}	m_{bb}	m_{bb}	m_{bb}	m_{bb}	m_{bb}
2-lepton	$e\mu$	m_{bb}	m_{bb}	Yield	m_{bb}	Yield	m_{bb}

5.1.1 Di-jet Mass Analysis

The di-jet mass analysis offers a useful cross-check for the fit procedure. In this case, the BDT$_{VH}$ discriminant is replaced by the m_{bb} variable as main input for the profile likelihood fit. The number of signal regions is increased from eight to fourteen as can be seen from Tab.(5.2) where they are summerized. For the 79.8 fb^{-1} analysis the high p_T^V region has been splitted in two by an additional cut at 200 GeV for all lepton channels. .

5.1.2 Diboson Analysis

The diboson analysis is a useful cross-check for the MVA analysis and it targets the diboson production, with a Z boson decaying into a pair of b-quark and produced in association with a another vector boson (W or Z). Since the process has a similar signature to the one for the signal, it is used as validation of the main result. The cross section is about nine times larger than for the SM Higgs boson with m_H=125 GeV. Moreover, the invariant mass of the two b-tagged jets peaks at lower values and the p_T^{bb} spectrum is softer. This analysis is used for the normalisation of the diboson contribution from WW production. A Standard Model Higgs boson is included as background, with a production cross section with an uncertainty of 50%. The diboson and Higgs boson BDTs provide a good separation between the VZ and VH processes with only a weak correlation (<1%).

5.2 Systematic Uncertainties for 79.8 fb^{-1} analysis

The sources of systematic uncertainty affecting the signal strength determination can be divided into four groups:

- experimental systematic uncertainties.
- modelling of the simulated background systematic uncertainties.
- multi-jet background estimation.
- Higgs boson signal simulation.

The systematic uncertainties are encoded in the variations of BDTs, m_{bb} shapes and yields for each analysis category, for each up-and-down ($\pm\sigma$) variations.

5.2.1 Experimental Systematic Uncertainties

The dominant experimental uncertainties come from the b-tagging simulation-to-data efficiency correction factors, from jet energy scale (JES) corrections and from the modelling of the jet energy resolution (JER).

- The b-tagging simulation-to-data efficiency correction factors are derived separately for b-jets, c-jets and light-flavour jets. They depend on the jets p_T and the relative uncertainties are estimated from multiple sources, decomposed into uncorrelated components which are then treated independently. They result in three uncertainties for b-jets, c-jets and light-jets, resulting, respectively, of the order of 2%, 10% and 40% [82]. Additional uncertainties are accounted to consider the extrapolation of b-jets above p_T=300 GeV and the misidentification of hadronically decaying τ-leptons as b-jets.
  The uncertainties in the jet energy scale and resolution are based on measurements in data. The uncertainty on jet energy scale is decomposed into 21 uncorrelated components which are treated as independent.

- Uncertainties in the reconstruction, identification, isolation and trigger efficiencies of muons and electrons together with the uncertainty in their energy scale and resolution are estimated on 13 TeV data. They have been proven to have small impact on the result. The uncertainty in the energy scale and resolution of the jets and leptons are propagated to the calculation of E_T^{miss}, which also has additional uncertainties from the scale, resolution and reconstruction efficiency of the tracks, along with the modelling of the underlying event.

- An uncertainty is assigned to the E_T^{miss} trigger correction factors (relevant for 0- and 1-lepton analysis), determined from the difference between the trigger efficiency in data and simulation, to account for the statistical uncertainty in the measured correction factors and for differences between the correction factors determined from W+jets, Z+jets and $t\bar{t}$ events.

- The uncertainty on the integrated luminosity is 2.0%, determined by the Luminosity working group with the LUCID-2 detector [49], being the official provider of luminosity measurements.

- The average number of interactions per bunch-crossing is rescaled by 1.03 to improve agreement between simulation and data, based on the measurement of the visible cross-section in minimum-bias events.

5.2.2 Background Modelling Systematic Uncertainties

The modelling uncertainties enter in the global profile likelihood fit as *nuisance parameters* and they are derived from simulated samples, see Sec.(4.12). They basically regards three areas:

- normalization.

- acceptance between different phase-spaces that affect the relative normalizations between analysis regions with a common normalization.

- shapes of the differential distributions of the most important kinematic variables (typically the ones with the highest discrimating signal-background power).

The normalizations and associated uncertainties for the background processes are detailed in Tab.(5.3) and in Tab(5.4) for 79.8 fb^{-1} analysis. The normalizations of the main source of background are left floating (i.e., unconstrained) in the global profile likelihood fit. The

TABLE 5.3: Summary of the systematic uncertainties in the background modelling for Z+jets, W+jets, $t\bar{t}$, single top and multi-jet background production for 79.8 fb^{-1} analysis provided as input to the global fit. For $t\bar{t}$ background, they are uncorrelated between the three lepton channels.

Background	Normalization
Z+jets	
Z+ $\ell\ell$	18%
Z+$c\ell$	23%
Z+HF	Floating (2-jets and 3-jets)
Z+bc-to-Z+bb ratio	30-40%
Z+cc-to-Z+bb ratio	13-15%
Z+bl-to-Z+bb ratio	20-25%
0-to-2 lepton ratio	7%
m_{bb} and p_T^V	Shape
W+jets	
W+ $\ell\ell$	32%
W+$c\ell$	37%
W+HF	Floating (2-jets and 3-jets)
W+bc-to-Z+bb ratio	26% (0-lepton) and 23% (1-lepton)
W+cc-to-Z+bb ratio	15% (0-lepton) and 30% (1-lepton)
W+bl-to-Z+bb ratio	10% (0-lepton) and 30% (1-lepton)
0-to-1 lepton ratio	5%
W+HF CR to SR ratio	10% (1-lepton)
m_{bb} and p_T^V	Shape
$t\bar{t}$	
$t\bar{t}$	Floating (0-, 1-, 2-lepton)
0-to1-lepton ratio	8%
2-to-3-jet ratio	9% (0+1-lepton)
W+HF CR to SR ratio	25% (1-lepton)
m_{bb} and p_T^V	Shape
Single t	
Cross section	4.6% (s-channel), 4.4%(t-channel), 6.2% (Wt)
Acceptance 2-jet	17% (t-channel), 55%($Wt(bb)$), 24%(Wt(other))
Acceptance 2-jet	20% (t-channel), 51%($Wt(bb)$), 21%(Wt(other))
m_{bb} and p_T^V	Shape (t-channel, $Wt(bb)$, Wt(other))
Multijet (1-lepton only)	
Normalization	60-100% (2-jet) and 90-140% (3-jets)
BDT Template	Shape

systematic uncertainties in the acceptance and in the shapes are also derived from particle-level comparisons between nominal and alternative simulated samples (both with alternative generators or from alteration of the nominal values of the nominal Monte Carlo simulator) or from comparison of the data in control regions. The shape uncertainties are considered separated from each analysis region and taken from the alternative sample that differs most in shape from the nominal sample. They are evaluated only for m_{bb} and for p_T^V and this choice is due to the fact that the variation in these two variables sufficiently covers the overall shape variation of the BDT$_{VH}$.

The post-fit normalization of the unconstrained backgrounds coming from the global like-

TABLE 5.4: Summary of the systematic uncertainties in the background modelling for diboson production. Since the WW gives a small contribution (<0.1%) to the total background only a normalization is assessed.

ZZ	
Normalization	20%
0-to-2 lepton ratio	6%
Acceptance from scale variation	10-18%
Acceptance from PS/UE variations for 2 or more jets	6%
Acceptance from PS/UE variations for 2 or more jets	7% for 0-lepton and 3% for 2-lepton
m_{bb} and p_T^V from scale variations	Shape (correlated with WZ variations)
m_{bb} and p_T^V from PS/UE variations	Shape (correlated with WZ variations)
m_{bb} and p_T^V from matrix-element variations	Shape (correlated with WZ variations)
WZ	
0-to-1 lepton ratio	11%
Acceptance from scale variation	13-21%
Acceptance from PS/UE variations for 2 or more jets	4%
Acceptance from PS/UE variations for 3 jets	11%
m_{bb} and p_T^V from scale variations	Shape (correlated with ZZ variations)
m_{bb} and p_T^V from PS/UE variations	Shape (correlated with ZZ variations)
m_{bb} and p_T^V from matrix-element variations	Shape (correlated with ZZ variations)
WW	
Normalization	25%

lihood fit to the 13 TeV are reported in Tab.(5.5).

TABLE 5.5: Summary of the normalization applied to the $t\bar{t}$, $W+HF$ and $Z+HF$ backgrouds, obtained from the global likelihood fit to the 13 TeV data for the multivariate analysis, used to extract the Higgs boson signal.

Process	Normalization factor
$t\bar{t}$ 0- and 1-lepton	0.98 $\pm$ 0.08
$t\bar{t}$ 2-lepton 2jet	1.06 $\pm$ 0.09
$t\bar{t}$ 2-lepton 3jet	0.95$\pm$ 0.06
$W+HF$ 2jet	1.19$\pm$0.12
$W+HF$ 3jet	1.05$\pm$0.12
$Z+HF$ 2jet	1.37$\pm$0.11
$Z+HF$ 3jet	1.09$\pm$0.09

5.2.3 Multijet Estimation Systematic Uncertainty

In Tab.(5.3), the normalization of multijet background in 1-lepton channel is reported. Systematic effects can impact the data-driven template method for the QCD induced background model mainly in two ways:

- changing the m_W^T distributions used for the multi-jet template fit, impacting on the extracted normalization.
- directly changing the multi-jet distributions used in the profile likelihood fit.

The uncertainties are treated uncorrelated between electron and muon channels. Variations can be obtained changing the definition of the multi-jet control region and varying the normalization of the contamination from top and V+jets processes. Another variation can be the use of another disciminant variable instead of m_T^W, for example the azimuthal separation between the directions of the lepton transverse momentum, or the inclusion for the electron channel of the E_T^{miss}<30 GeV region.

5.2.4 Signal Modelling Systematic Uncertainty

The systematic uncertainties in the calculation of the VH production cross section and the $H \to b\bar{b}$ branching ratio are assigned following the recommendation of the LHC Higgs Cross Section Working Group [17]. The uncertainties on the production cross section are obtained varying the renormalization scale μ_R and the factorization scale μ_F independently to assess the effect of missing higher-order terms in QCD perturbative expansion.
The PDF+α_S uncertainty is calculated using the PDF4LHC15nnlomc set. Since the latest recommendation do not distinguish between the $qqZH$ and $ggZH$ production modes, the two related uncertainty are considered identical in the calculation of the scale uncertainties.
Another systematic uncertainty in the overall VH cross section originates from missing higher order electroweak corrections. It is estimated as the maximum variation among three quantities:

- the maximum size expected for the missing NNLO EW effects: 1%.
- the size of the NLO EW correction.
- the uncertainty in the photon-induced cross section relative to the total VH cross section.

The systematic correction in the $H \to b\bar{b}$ is 1.7%, accounting higher-order QCD and EW corrections and uncertainties on b-quark masses and α_S values.
The acceptance and shape systematic uncertainties are derived to account for missing higher-order QCD and EW corrections, for PDF+α_S uncertainty and for variations of the parton-shower and underlying event models.
The uncertainties on acceptance and shape of m_{bb} and p_T^V distributions, originating from missing higher-order terms in QCD, are estimated by comparing nominal shapes to those obtained varying factorization and renormalization scales.
The uncertainties due to parton-shower and underlying-events models are estimated by considering the difference between Powheg-MiNO+Pythia8 and Powheg-MiNLO+Herwig7 with the H7-UE-MHT tune and changing the Pythia8 parton-shower tune. It is evaluated in events generated with MadGraph5aMC@NLO showered with Pythia8 using A14 tune and its variations. The PDF+α_S uncertainty in the acceptance between regions and in the m_{bb} and p_T^V shapes is estimated applying the PDF4LHC1530 PDF set and its uncertainties. The systematic uncertainties related to signal modelling are summerized in Tab.(5.6).

TABLE 5.6: Summary of the systematic uncertainties in the signal modelling for the 79.8 fb^{-1} analysis. PS/UE points to the parton shower/underlying event.

Signal	
Cross section (scale) 0.7% (qq-production) and 27% (gg-production)	
Cross section (PDF) 1.9% ($qq \to WH$), 1.6% ($qq \to ZH$), 5% ($gg \to ZH$)	
$H \to b\bar{b}$ branching fraction	1.7%
Acceptance from scale variations	2.5%-8%
Acceptance from PS/UE variations for 2 or more jets	2.9-6.2%
Acceptance from PS/UE variations for 3 jets	1.8-11%
Acceptance from PDF+α_S variations	0.5-1.3%
m_{bb}, p_T^V from scale variation	Shape
m_{bb}, p_T^V from PS/UE variations	Shape
m_{bb}, p_T^V from PDF+α_S	Shape
p_T^V from NLO EW correction	Shape

5.2.5 Breakdown of the Systematic Uncertainties

The impact of a category of systematic uncertainties is defined as the difference in quadrature between the uncertainty in μ computed when all nuisance parameters (NP) are fitted and the one when the NPs in the category are fixed to their best-fit value. The full breakdown of the discussed systematic uncertainties on the signal strength are listed in Tab.(5.7). As can be seen from Tab.(5.7), the total experimental uncertainty is 8.8% and it is dominated

TABLE 5.7: Breakdown of the contributions to the uncertainty in μ.

Source of uncertainty	σ_μ
Total	0.259
Statistical	0.161
Systematic	0.203
Experimental Uncertainties	
Jet	0.035
E_T^{miss}	0.014
Leptons	0.009
b-tagging	0.061 b-jets
	0.042 c-jets
	0.009 light flavoured-jets
	0.008 extrapolation
Pile-up	0.007
Luminosity	0.023
Theoretical and Modelling Uncertainties	
Signal	0.094
Floating normalizations	0.035
Z+jets	0.055
W+jets	0.060
$t\bar{t}$	0.050
Single t	0.028
Diboson	0.054
Multijet	0.005
MC statistical	0.070

by jet energy scale and b-tagging uncertainty. Luminosity related uncertainty it is by far not dominant and it will be further reduced in the full Run2 analysis thanks to the ongoing ATLAS luminosity analysis which will reduce the uncertainty to $\sim$1.7% compared to 2% presently used.
The experimental uncertainty is lower with respect to the theoretical uncertainty coming from the signal and background modelling. For this reason, the careful determination of the systematic uncertainties related to $Z + jets$ background modelling, which are a relevant part of this thesis, has been crucial to better constrain this source of background for the 2-lepton analysis.

5.3 Results for 79.8 fb^{-1} analysis and Combination with Different Data-sets

Fig.(5.1) show the BDT output distributions in the high p_T^V region, which is the most sensitive. The background prediction in all post-fit distributions is obtained by normalizing the backgrounds and setting the nuisance parameters according to the results of the signal extraction fit. As can be seen in the ratio plots, in all cases the shapes and normalization of signal and background well describe the measured data.

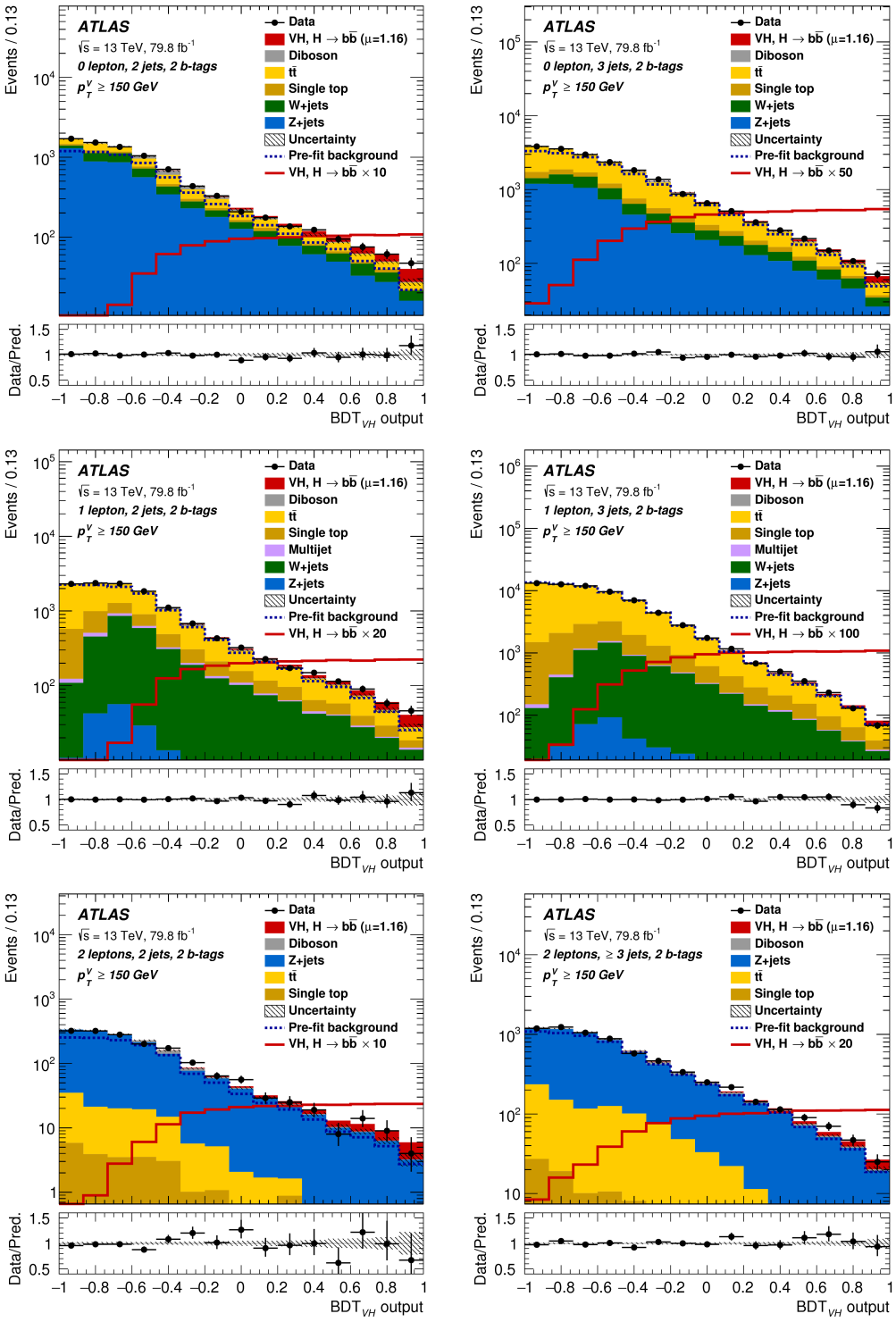

FIGURE 5.1: BDT_{VH} output post-fit distributions in the 0-lepton (top), 1-lepton (middle) and 2-lepton (bottom) channels for 2 b-tag jets events in the high p_T^V region. Left plots refers to 2-jet multiplicity, right ones to exactly 3-jets in the 0- and 1-lepton channels and to $\geq$3 jets in the 2-lepton channel. The signal, referring to a Standard Model Higgs with m_H=125 GeV, is shown as a histogram on the top of the fitted backgrounds normalizaed to the signal yield extracted from the data and unstacked as an unfilled histogram, scaled by the factor indicated in the legend. The dashed histogram shows the total pre-fit background. The size of the combined statistical and systematic uncertainty from the sum of the fitted signal and background is indicated by the hatched band. The ratio of the data to the sum of the fitted signal and background is shown in the lower panel.

For a Standard Higgs boson mass of 125 GeV, when all lepton channels are combined, the probability p_0 of obtaining a signal at least as strong as the observation from background alone is 5.3×10^{-7}, with respect to an expected value of 7.3×10^{-6}. The observation corresponds to an excess with an observed significance of 4.9 standard deviations, with respect to an expectation of 4.3 standard deviations. The signal strength extracted from the fit is:

$$\mu_{VH(H\to b\bar{b})} = 1.16^{+0.27}_{-0.25} \pm 0.16(stat)^{0.21}_{-0.19}(sys) \tag{5.1}$$

The post-fit signal and background yields are listed in Tab.(5.8).

Tab.(5.9) shows the signal strength, p_0 and significance values from the combined fit and from single channel fit. As can be seen, the single signal strength are all compatible among each other. Finally, a combined fit has also been performed with floating signal strengths for the WH and ZH production modes, separately. They have an observed (expected) significance of 2.5(2.3) and 4.0 (3.5) standard deviations, respectively for WH and ZH, as shown in Fig.(5.2). Also in this case an excellent compatibility in signal strength is found.

TABLE 5.8: The Higgs boson signal, background and data yields for each signal region category in each channel after the full selection of the multivariate analysis. The signal and background yields are normalized to the results of the global likelihood fit. All systematic uncertainties are included in the indicated uncertainties. Entries "-" points to a specific background negligible in a certain category or left zero after the full analysis selection.

Process	0-lepton		1-lepton		2-lepton			
	p_T^V>150 GeV, 2 b-tag		p_T^V>150 GeV, 2 b-tag		75 GeV<p_T^V<150 GeV, 2 b-tag		p_T^V>150 GeV, 2 b-tag	
	2-jet	3-jet	2-jet	3-jet	2-jet	$\geq$3-jet		
$Z+ll$	17±11	27±18	2±1	3±2	14±9	49±32	4±3	30±19
$Z+cl$	45±18	76±30	3±1	7±3	43±7	170±67	12±5	88±35
$Z+HF$	4770±140	5940±300	180±9	348±21	7400±120	14160±220	1421±34	5370±100
$W+ll$	20±13	32±22	31±23	65±48	<1	<1	<1	<1
$W+cl$	43±20	83±38	139±67	250±120	<1	<1	<1	<1
$W+HF$	1000±87	1990±200	2660±270	5440±670	2±0	13±2	1±0	4±1
Single top quark	368±53	1410±210	2080±290	9400±1400	188±89	440±220	23±7	93±26
$t\bar{t}$	1333±82	9150±400	6600±320	50200±1400	3170±100	8800±220	104±6	893±40
Diboson	254±49	318±90	178±47	330±110	152±32	355±68	52±11	196±35
Multi-jet e sub-channel	-	-	100±100	41±35	-	-	-	-
Multi-jet μ sub-channel	-	-	139±92	260±270	-	-	-	-
Total background	7850±90	19020±140	12110±120	66230±270	10960±100	24070±150	1620±30	6620±80
Signal (post-fit)	128±28	128±29	131±31	125±30	51±11	86±22	28±6	67±17
Data	8003	19143	12242	66348	11014	24197	1626	6686

TABLE 5.9: Measured signal strength with their combined statistical and systematic uncertainties, expected and observed p_0 and significance values in standard deviations from the combined fit with a single signal strength and from a combined fit where all the lepton channel have their own signal strength.

Single Channel or Combined	Signal Strength	p_0 expected	p_0 observed	Significance expected	Significance observed
0-lepton	$1.04^{+0.34}_{-0.32}$	9.5×10^{-4}	5.1×10^{-4}	3.1	3.3
1-lepton	$1.09^{+0.46}_{-0.42}$	8.7×10^{-3}	4.9×10^{-3}	2.4	2.6
2-lepton	$1.38^{+0.46}_{-0.42}$	4.0×10^{-3}	3.3×10^{-3}	2.6	3.4
$VH, H\to b\bar{b}$ Combination	$1.16^{+0.27}_{-0.26}$	7.3×10^{-6}	5.3×10^{-7}	4.3	4.9

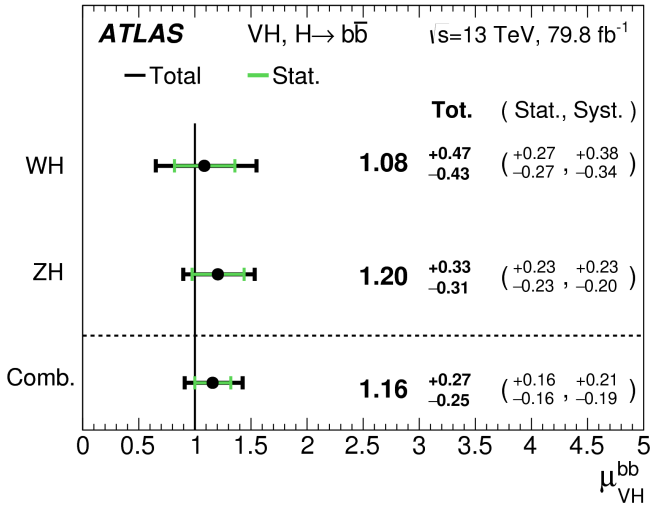

FIGURE 5.2: The fitted values of the Higgs boson signal strength $\mu_{VH\to b\bar{b}}$ for a Standard Model Higgs with m_H=125 GeV for the WH and VH processes and their combination. The single μ for WH and ZH are obtained leaving the processes floating, independently. The probability of compatibility of the individual signal strength is 84%.

5.3.1 Results from Di-jet and Diboson analysis

The result of the combined fit for the di-jet analysis (see 5.1.1), in all the channels simultaneously, is:

$$\mu_{VH(H\to b\bar{b})} = 1.06^{+0.36}_{-0.33} = 1.06 \pm 0.20(stat.)^{+0.30}_{0.26}(sys.) \tag{5.2}$$

The observed excess has a significance of 3.6 standard deviations, compared to an expectation of 3.5. Good agreement is found with the result of the nominal multivariate analysis. The m_{bb} distribution summed over all channels and p_T^V and jet multiplicity regions is shown in Fig.(5.3). It is weighted by their respective values of the ratio of fitted Higgs boson signal and background yields and after subtraction of all background except for the WZ and ZZ diboson processes. A clear excess is observed in the m_{bb} region corresponding to $H\to b\bar{b}$, reinforcing the reliability of the whole procedure. As said in 5.1.2, a measurement of VZ production based on the multiviariate analysis as been performed as validation of the Higgs boson search. The result has been found to be in agreement with the Standard Model prediction:

$$\mu_{VZ(Z\to b\bar{b})} = 1.20^{+0.20}_{-0.18} = 1.20 \pm 0.08(stat.)^{+0.19}_{0.16}(sys.) \tag{5.3}$$

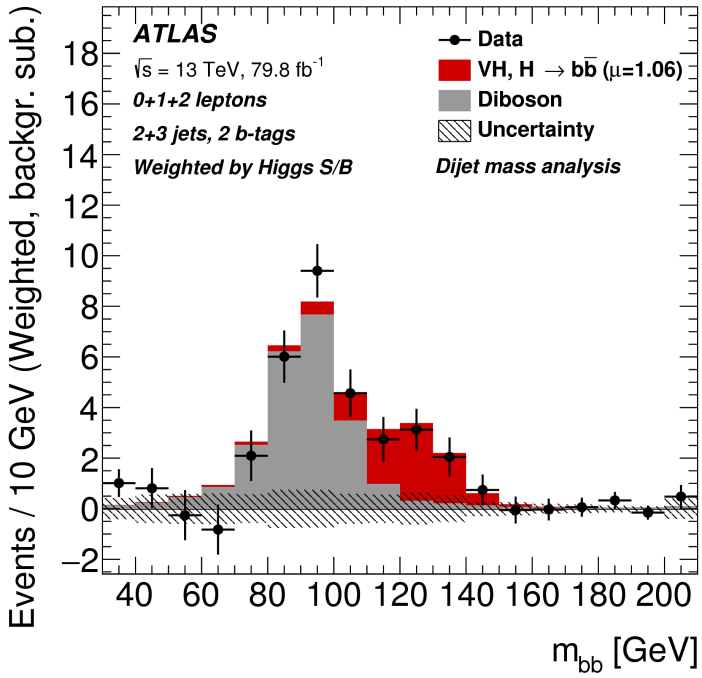

FIGURE 5.3: The distribution of the m_{bb} in data after subtraction of all backgrounds except for the WZ and ZZ diboson processes, obtained in the dijet analysis. The contributions from all lepton channels, p_T^V regions and jet multiplicity categories are summed and weighted by their respective S/B, with S being the total fitted signal and B the total fitted background in each region. The expected contribution of the associated WH and ZH prodiction is shown scaled by the measured signal strength evaluated. The size of the combined statistical and systematic uncertainty for the fitted background is indicated by the hatched band.

5.3.2 Results from Combinations with different data-sets

Three combination has been performed to obtain the final result.

1. The results obtained from the statistical analysis of the 13 TeV data are combined with those from the data recorded at 7 and 8 TeV during Run1 [92]. Studies of the impact of the correlation of systematic uncertainties between the analyses across different center of mass energies have been studies but only theory uncertainties in the Higgs boson signal (overall cross section, branching fraction and p_T^V-dependent NLO EW corrections) have been found to be relevant in that sense. The measured signal strength is:

$$\mu_{VH(H\to b\bar{b})} = 0.98^{+0.22}_{-0.21} = 0.98 \pm 0.14(stat.)^{+0.17}_{-0.16}(sys) \tag{5.4}$$

with an observed p_0 value of 5.5×10^{-7}, corresponding to an excess with a significance of 4.9 standard deviations, compared to an expectation of 5.1. The fits are also performed leaving WH and ZH production processes floating independently. The results are shown in Fig.(5.4).

2. A second combination has been performed with the results of the $H \to b\bar{b}$ decay

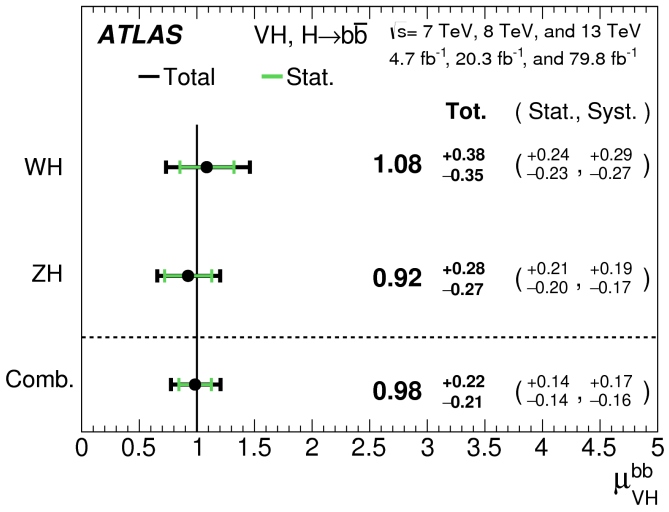

FIGURE 5.4: The fitted value of the Higgs boson signal strength μ for a Standard Model Higgs with m_H=125 GeV for the WH and ZH processes and their combination, using 7 TeV, 8 TeV and 13 TeV data.

modes in $t\bar{t}H$ [88] [89] and VBF [28] production modes coming from the Run1 and Run2 data. The combination measures the ratio of the branching fraction of the Higgs boson into b-quarks to the Standard Model prediction by constraining the cross sections of the production modes to be as predicted. For an Higgs boson mass of 125 GeV and assuming the relative production cross section as predicted by the SM, the observed significance for the $H \to b\bar{b}$ decay is 5.4 standard deviations, compared with the 5.5 expected. The fitted signal strength of the branching fraction into b-quarks is:

$$\mu_{H\to b\bar{b}} = 1.01 \pm 0.20 = 1.01 \pm 0.12(stat.)^{+0.16}_{0.15}(sys.) \tag{5.5}$$

The expected and observed significance per production mode are listed in Tab.(5.10), while in Fig.(5.5) the signal strengths obtained from a fit where the individual strengths are fitted simultaneously for the three production modes are displayed. The signal strenghts floated independently for each of the production processes in both Run1 and Run2.

TABLE 5.10: Expected and observed significances (expressed in standard deviations) for the $H \to b\bar{b}$ production modes fitted independently in the combination using 7, 8 and 13 TeV. Since the analysis targeting VBF has a sizeable contribution from gluon-gluon fusion events, it is referred as the VBF+ggF analysis.

Channel	Expected Significance	Observed Significance
VBF+ggF	0.9	1.5
$t\bar{t}H$	1.9	1.9
VH	5.1	4.9
$H \to b\bar{b}$	5.5	5.4

3. A third combination is performed also combining the Run2 $VH(H \to b\bar{b})$ result with other results in the VH production mode but considering the case of the Higgs

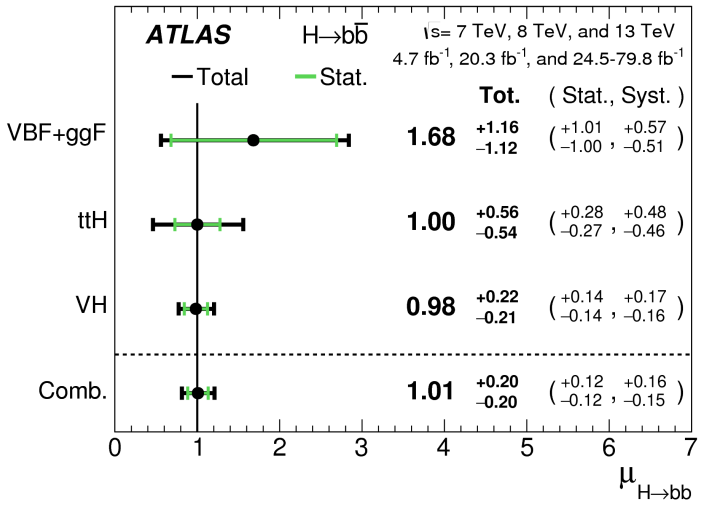

FIGURE 5.5: The fitted values of the Higgs boson signal strength $\mu_{VH(H\to b\bar{b})}$ for m_H=125 GeV for the WH and ZH processes and their combination, with the 7, 8 and 13 TeV datasets.

boson decaying into two photons [91] or via $ZZ*$ into four leptons [90]. Photons are reconstructed from calorimeter energy cluster formed using an enhanced dynamical, topological cell-clustering-based algorithm. The signal yield is extracted in each cateogory using a fit to the diphoton invariant mass distribution in the range 105-160 GeV. Also the measurement of VH production in the four-lepton final state, $H \to ZZ \to 4\ell$, where $\ell = e, \mu$, has been included. For the 79.8 fb^{-1}, the electron reconstruction have been improved and an additional event category targeting vector-boson decays that include missing transverse momentum due to the presence of one or two neutrinos in the final state have been considered [93]. This results in three VH categories, targeting the hadronic decays of the vector boson, charged leptonic decays of the vector boson and decays of the vector boson containing one or more neutrinos. The constraining of the branching fractions for the ZZ^*, diphoton and $b\bar{b}$ decays helps to measure the signal strength of the VH production modes. The observed significance for VH production is 5.3 standard deviations to be compared with an expectation of 4.8. The fitted value of the VH signal strength for all channels combined is found to be:

$$\mu_{VH(H\to b\bar{b},4\ell,\gamma\gamma)} = 1.13^{+0.24}_{-0.23} = 1.13 \pm 0.15(stat.)^{+0.15}_{-0.17}(sys.) \tag{5.6}$$

Tab.(5.11) shows the significance values for the combined likelihood fit where the four lepton ($H \to ZZ \to 4\ell$), diphoton ($H \to \gamma\gamma$) and $H \to b\bar{b}$ modes have their own signal strength for the Run2 data. From the table it is very clear that the overall significance is dominated by the $H \to b\bar{b}$ decay, reinforcing the importance of the present analysis.
Fig.(5.6) shows the signal strength obtained from the fit where individual signal strengths for the three decay modes together with their combination. As it can be noted the most precise determination of μ comes from the $b\bar{b}$ decay which sets the precision of the combined result.

TABLE 5.11: Expected and observed significance values in standard deviations for the VH decay channels.

Channel	Expected Significance	Observed Significance
$VH(H \to ZZ* \to 4\ell\ell)$	1.1	1.1
$VH(H \to \gamma\gamma)$	1.9	1.9
$VH(H \to b\bar{b})$	4.3	4.9
VH combined	4.8	5.3

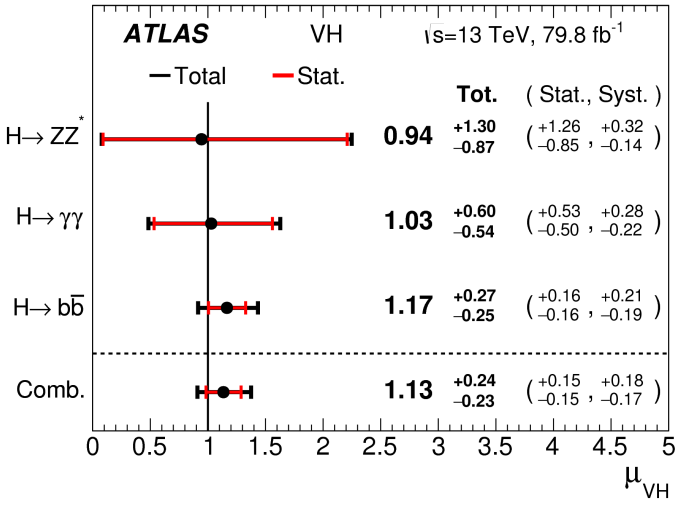

FIGURE 5.6: The fitted values of the Higgs boson signal strength $\mu_{VH(H\to b\bar{b})}$, separately for the $H \to b\bar{b}$, $H \to \gamma\gamma$ and $H \to ZZ* \to 4\ell$ decay modes, together with their combination. The probability of the individual signal strength is 96%.

Conclusions for the 79.8 fb^{-1} analysis

The search for the Standard Model Higgs boson decaying into a $b\bar{b}$ pair produced in association with a vector boson has been performed using data collected by the ATLAS experiment in proton-proton collisions from Run2 of the LHC, corresponding to an integrated luminosity of 79.8 fb^{-1}, at a center of mass energy of 13 TeV. An eccess over the expected background is being observed with a significance of 4.9 standard deviations compared to the expectation of 4.3. The corresponding measured signal strength relative to the Standard Model prediction for m_H=125 GeV has been found to be:

$$\mu_{VH(H\to b\bar{b})} = 1.16 \pm 0.16(stat.)^{+0.21}_{-0.19}(sys.) \qquad \text{Run 2} \tag{5.7}$$

Furthermore the result has been validated with two cross-checks. The first one is the diboson analysis which has provided an outcome in a good agreement with the Standard Model providing a robust validation of the background model, BDT performance and fitting stategy via the global likelihood fit. The second cross-check comes from the dijet mass analysis which has provided a signal strength:

$$\mu_{VH(H\to b\bar{b})} = 1.06^{+0.36}_{-0.33} = 1.06 \pm 0.20(stat.)^{+0.30}_{0.26}(\text{sys.}) \tag{5.8}$$

showing a good agreement with the BDT$_{VH}$ fit result, providing an efficient validation of the analysis procedure.
The result has been combined with previous results based on all the Run1 data collected at $\sqrt{s}$ of 7 TeV and 8 TeV. An excess over the expected background is observed with a significance of 4.9 standard deviations compared with an expectation of 5.1. The measured signal strength relative to the expectation has been found to be:

$$\mu_{VH(H\to b\bar{b})} = 0.98 \pm 0.14(stat.)^{+0.17}_{-0.16}(sys.) \qquad \text{Run 2+1} \tag{5.9}$$

Results for the Standard Model Higgs boson decaying into a b-quark pair in the VH, $t\bar{t}$ and VBF+ggF production modes at center of mass energies of 7 TeV, 8 TeV and 13 TeV have been combined, assuming the production cross section predicted by the model, leading to a significance of 5.4 standard deviations compared with the expected of 5.5, providing an observation of the $H \to b\bar{b}$ decay mode. The measured signal strength is:

$$\mu_{H\to b\bar{b}} = 1.01 \pm 0.12(stat.)^{+0.16}_{-0.15}(sys.) \qquad \text{Run 2+1} \tag{5.10}$$

which is consistent with the value of the Yukawa coupling to bottom quarks in the Standard Model.
The Run2 $VH(H \to b\bar{b})$ has been also combined with the other Run2 results for the Higgs boson other decays in the VH production mode. The result of the combined fit is an observed significance of 5.3 standard deviations, compared with an expectation of 4.8. The measured signal strength is:

$$\mu_{VH(H\to b\bar{b},4\ell,\gamma\gamma)} = 1.13 \pm 0.15(stat.)^{+0.18}_{-0.17}(sys.) \tag{5.11}$$

The result provides a direct observation of the Higgs boson being produced in association with a vector boson.

5.4 Further Steps: 139 fb^{-1} analysis

As said in Chapter 4, the iteration of the analysis is currently on going with the full Run2 statistics. The strategy to adopt for the statistical analysis and the extraction of the signal strength $\mu_{VH(H\to b\bar{b})}$ is the same, with some innovation in order to enhance the sensitivity. The most relevant are:

- the split of the high p_T^V region with an additional cut at p_T^V=250 GeV. The regions entering the likelihood fit for 139 fb^{-1} analysis are listed in Tab.5.13.
- the use of an hybrid truth b-tagging method (see 4.11.5).

Moreover, in the analysis iteration with the full Run2 statistics a new set of control regions have been designed, using cuts on signal efficiencies on the ΔR between the two b-tagged jets as a function of the p_T^V. They are common to the three lepton channels and orthogonal to the signal region, with negligible level of signal contamination. Lower and upper cuts are introduced, resulting in a low ΔR and high ΔR control region. They are defined following the criteria in Tab.(5.12). For 2-lepton channel where I am working on, an additional control region enriched with top-like events is considered: the $e\mu$ control region with the requirement of two leptons with different flavours.

TABLE 5.12: The distributions used in the global likelihood fit for the signal regions (SR) and controlregions (CR) for all the categories in each channel, for the nominal multivariate analysis for 139 fb^{-1}.

Channel	SR/CR	Categories					
		75 GeV<p_T^V<150 GeV		150 GeV<p_T^V<250 GeV		p_T^V>250 GeV	
		2-jet	3-jet	2-jet	3-jet	2-jet	≥3-jet
		2jet	3jet	2jet	3jet	2jet	3jet
0-lepton	CRLow	-	-	Yield	Yield	Yield	Yield
	SR	-	-	BDT	BDT		
	CRHigh	-	-	BDT	BDT	BDT	BDT
1-lepton	CRLow	-	-	Yield	Yield	Yield	Yield
	SR	-	-	BDT	BDT		
	CRHigh	-	-	Yield	Yield	Yield	Yield
2-lepton	CRLow	Yield	Yield	Yield	Yield	Yield	Yield
	SR	BDT	BDT	BDT	BDT		
	CRHigh	Yield	Yield	Yield	Yield	Yield	Yield

TABLE 5.13: Cuts defining on ΔR defining the two new Control Regions.

Category	Low ΔR CR cuts	High ΔR CR cuts
2 jet	ΔR>0.40 + $e^{0.788-0.01023}\times p_T^V$	ΔR>0.87 + $e^{1.38-0.00795}\times p_T^V$
3 jet	ΔR>0.42 + $e^{0.286-0.00809}\times p_T^V$	ΔR>0.76 + $e^{1.33-0.0073}\times p_T^V$

The main purpose of the analysis is to obtain an even more precise result in terms of signal strength and significance for the observation of $H\to b\bar{b}$ decay and VH production with the update to the analysis strategy.
Modelling of signal and background, MVA performance studies are presently on going to perform a global fit on Full Run2 statistics dataset.
As said in Chapter 4, changes have been introduced in the analysis iteration in different steps of the analysis. Two of them are the shift from truth (see 4.7) to hybrid truth tagging (4.11.5) and the introduction of new p_T^V regions by the additional cut at 250 GeV.
In terms of MVA analysis, this has led to several performance studies to understand if these two innovation would have led to better performances. The studies has been performed in the three lepton channels, separately, and I directly carried it for the 2-lepton analysis, as detailed in 4.11.4 and 4.11.5, helping in the determination of the MVA strategy to adopt.
For this analysis, it has already been performed the fit to the Asimov dataset to determine the expected significance with the full Run2 statistics. It is obtained directly from the Monte-Carlo prediction without any rescaling to data. It is referred to simply as Asimov or *pure* Asimov.
With the full Run 2 dataset, corresponding to a luminosity of 139 fb^{-1}, the expected pure Asimov significance of the $VH(H\to b\bar{b})$ signal is 6.6σ, The corresponding signal strength and its uncertainty is expected to be:

$$\mu_{VH(H\to b\bar{b})} = 1.00^{+0.122}_{-0.121}(stat.)^{+0.146}_{-0.127}(sys.) \tag{5.12}$$

while the comparison of the combined signal strength is shown in Tab.(5.14) and in Fig.(5.7).
The breakdown with 3 signal channels expected for Run2 is reported in Tab.5.14 for the expected significance and in Fig.5.7 for the signal strength.

TABLE 5.14: Expected significances for the combined and individual fits to the pure Asimov dataset.

Analysis	Expected Significance MVA VH
0-lepton	3.7
1-lepton	3.5
2-lepton	4.5
Combined	6.6

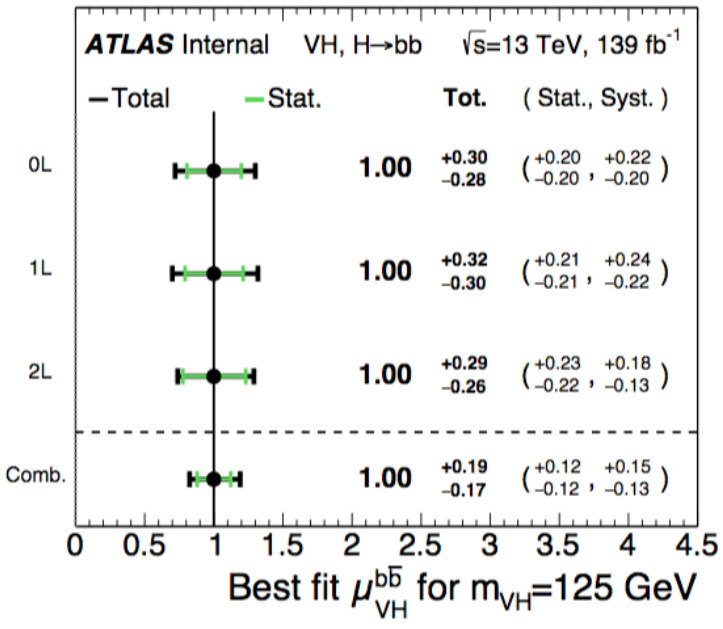

FIGURE 5.7: Best value of the signal strength $\mu_{VH(H\to b\bar{b})}$ for the 0-, 1-. 2-lepton analysis and their combination in the fit to the Asimov dataset.

Chapter 6

Phenomenological approach to Different High Energies Scenarios for Total Hadronic Cross Section and ρ-parameter

The Standard Model describes successfully the interactions between quarks and leptons but there are still many open questions to be answered such as neutrino, oscillation, matter-antimatter symmetry, dark matter and dark energy. Moreover ther are also processes within the Standard Model that are not completely understood. In particular, due to the non-Abelian nature of QCD, perturbative approach does not work for soft term calculations (i.e., for low momentum transfer) and the total hadronic cross-section evolution with energy is not properly predicted by the theory. However, there are some calculations based on very general principles, such as Dispersion Relations and Optical Theorem, which can be performed. They connect σ_{tot} and the ρ-parameter, which is defined as the ratio of the real to the imaginary parte of the elastic scattering amplitude in the forward direction. In the following, a treatment of the theoretical framework will be provided, together with the description of the σ_{tot} and ρ measurements performed in the pre-LHC and LHC eras and how they have been used to have prediction of the evolution of these two quantities with the energy.
As it will be seen in Sec.6.5, a change of perspective has been necessary after the recent TOTEM measurement at 13 TeV which seems to suggest a change of paradigm for ρ evolution (and consequently for σ_{tot}) with energy.
In Sec. 6.1, a guideline to go through my studies is provided to better understand the general flow of the work presented here.

6.1 General Description of the Studies

As anticipated in the introduction to this chapter, the main tools used for my studies are based on two physical general principles:

- the Optical Theorem which connects the total cross section σ_{tot} to the imaginary part of the elastic scattering amplitude in the forward direction.
- the Dispersion Relations which provide a relation between the real and imaginary part of a complex analytic function.

I personally developed a machinery based on ROOT, C++, Python and a dedicated library named chiron v0.55 (consisting in two C++ library for numerical calculation [94]) to perform calculation of ρ via dispersion relation. All the results presented in Sec.6.6 and Sec.6.7

were obtained in such a way.

1. In a very first stage, the basic idea was to test the validity of the two of them combined together in order to obtain a prediction on total cross section evolution with energy through a global fit of the σ_{tot} and ρ at 100 TeV, the energy regime for the possibile evolution of LHC, the *Future Circular Collider* (FCC, see 6.1). As described in Sec.6.6, one

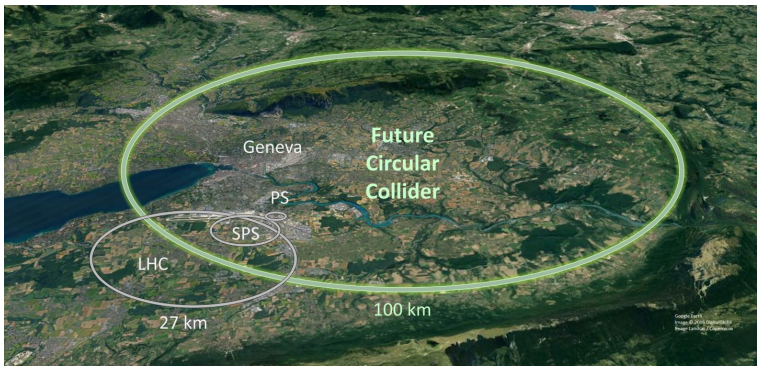

FIGURE 6.1: A skematic view of where the Future Circular Collider is proposed to be placed.

of the first steps has been the study of the impact of measurement of ρ at 14 TeV on the total cross section prediction at 100 TeV.
The next step would have been a global fit of σ_{tot} and ρ measurements but the TOTEM measurement at 13 TeV has changed the perspective, as explained below.

2. The ρ measurement published by TOTEM at 13 TeV deviates from the predictions if compared with the COMPETE model. Assuming that the cornerstones at the basis of the dispersion relations are solid, two possibility remains to understand the big difference between expectation and measurement of ρ:

   - The form of dispersion relation used up until now is not valid and this may suggest the existence of the Odderon [95].
   - Some drastic change in the σ_{tot} behaviour.

   The second approach is the one studied in this context adopting different strategies. The purpose of all of them is to see if introducing different kinds of changes in the total cross section behaviour can represent the ρ TOTEM measurement at 13 TeV, without the Odderon hypothesis.

   a. The assumption of different flattening for σ_{tot} at 20, 40 and 60 TeV, see 6.7.1.
   b. The assumption of a change of exponent at 15 TeV going from to the COMPETE preferred evolution $\sigma_{tot} \sim \ln^2(s)$ to $\sigma_{tot} \sim \ln^{1.6}(s)$, see 6.7.2.
   c. The Block and Cahn approach which introduce a tuning parameter α representing an energy scale at which the cross section change its behaviour, see 6.7.3.
   d. The KMR approach which introduces a new parametrization starting from the TeV regime, see 6.7.4.

6.2 The Total Hadronic Cross Section

The total hadronic cross-section is a fundamental parameter of strong interaction theory since it sets the size of the interaction region at a given energy. Hadronic processes are described by the *Quantum Chromodynamics* (QCD). As said in 1.1.3, QCD is a non-Abelian theory and the running nature of the coupling constant α_s sets two different regimes named *asymptotic freedom* and *confinement*. In hadron-hadron collisions, they correspond, respectively, to *hard scattering* and *soft scattering*. The former is successfully described by QCD with a perturbative approach, while for the latter ones it is not possible due to the rise of the coupling constant with the decrease of momentum transfer. The lack of pure QCD results for soft scattering processes (elastic collisions and diffractive dissociations) is a serious issue for the theoretical investigation of the total hadronic cross section.
However experimental observations may help the comprehension of a possible development of the theory in the soft sector. The total cross section σ_{tot} is defined by:

$$\sigma_{tot} = \sigma_{el} + \sigma_{inel} \tag{6.1}$$

The interpretation of σ_{tot} is both statistical and geometrical since it is connected to a probability of interaction and it represents also the effective area of interaction (usually measured in mb for hadronic scattering).
The growth of σ_{tot} with energy is hitherto an experimental fact, confirmed in every energy regime at different colliders.
We know that the total cross section is related to the elastic scattering by the *optical theorem*. The differential elastic cross section is related to the modulus squared of the elastic amplitude f_{el}, which is a complex number.

$$\frac{d\sigma_{el}}{dt} = \pi |f_{el}(\theta)|^2 \tag{6.2}$$

where t is the Mandelstam variable standing for the square of the 4-momentum transfer. As stated by the optical theorem, σ_{tot} is related to its imaginary part of $f_{el}(\theta)$ by:

$$\sigma_{tot} = \frac{4\pi}{p} \cdot Im[f_{el}(t=0)] \tag{6.3}$$

where p is the momentum of the particle. As we will see below, the optical theorem is a general law of scattering theory, which emerges from the conservation of probability using quantum mechanics. Generally, the strategy is to work with the ratio of the real to imaginary part of the amplitude in the forward direction (t=0): the ρ-parameter, defined as:

$$\rho = \left. \frac{\mathrm{Re} f_{el}(t)}{\mathrm{Im} f_{el}(t)} \right|_{t=0} \tag{6.4}$$

The ρ-parameter is related to σ_{tot} through dispersions relation, as will be explained in the following

6.2.1 The Optical Theorem and the Dispersion Relations

Dispersion relations are a fundamental mathematical tool in several area of Physics. They are based upon the *Kramers-Kronig* theorem [96] and [97]. Considering $\chi(\omega)$, a complex analytic function of the complex variable ω:

$$\chi(\omega) = \chi_1(\omega) + i\chi_2(\omega) \tag{6.5}$$

where $\chi_1(\omega)$ and $\chi_2(\omega)$ are real. Through a derivation following the Cauchy integral theorem:

$$\chi_1(\omega) = \frac{1}{\pi}\int_{\infty}\frac{\chi_2(\omega^{'})}{\omega^{'}-\omega}d\omega^{'} \tag{6.6}$$

Basically, the Kramers-Kronig theorem gives a relation between the real and imaginary part of a complex analytic function.
The first application in Particle Physics was suggested by Kronig in 1946 [98] and then applied by Gell-Mann, Goldhaber and Thirring in 1954 [99]. As it regards the first application in proton-proton scattering, it was due to Soeding in 1964 [100].
There are three cornerstones of the application of dispersion relations in particle physics:

1. Unitarity
2. Analyticity
3. Crossing Symmetry, ensured by the relativistic nature of the interaction.

Applying analyticity and crossing symmetry, one can derive the following relation [101], [102], [103], [104], [105]:

$$Ref_{+}(E) = C + \frac{E}{\pi}\int_{m}^{\infty} dE^{'}\frac{Imf_{+}(E^{'})}{E^{'}(E^{'}-E)} - \frac{Imf_{-}(E^{'})}{E^{'}(E^{'}+E)} \tag{6.7}$$

where C is a real constant. The plus sign refers to proton-proton amplitude and the minus sign to antiproton-proton amplitude. Applying unitarity, using the optical theorem, one gets:

$$Ref_{+}(E) = C + \frac{E}{4\pi^2}\int_{m}^{\infty} dE^{'}p^{'}\Big(\frac{\sigma_{+}(E^{'})}{E^{'}(E^{'}-E)} - \frac{\sigma_{-}(E^{'})}{E^{'}(E^{'}+E)}\Big) \tag{6.8}$$

where σ_{+} and σ_{-} are, respectively, proton-proton and proton-antiproton cross sections.
Eq.(6.7) is the so-called *once subtracted* integral dispersion relation which in the derivation assumes that the difference of the proton-proton to the anti-proton cross section goes to zero at high energies, following the Pomeranchuk theorem (i.e., Odderon does not contribute asymptotically) [106].
Finally, applying the ρ definition (Eq.6.4), one gets:

$$\rho_{\pm}\sigma_{\pm} = \frac{B}{p} + \frac{E}{\pi p}\int_{m_p}^{\infty}\Big[\frac{\sigma_{\pm}}{E^{'}(E^{'}-E)} - frac\sigma_{\mp}E^{'}(E^{'}+E)\Big]p^{'}dE^{'} \tag{6.9}$$

As can be seen, the integral in Eq.(6.9) has a singularity at the energy E at which ρ is calculated implying that the sensitivity to ρ on σ_{tot} is largest at this energy. Moreover, there is a sensitivity to σ_{tot} beyond the energy at which ρ is calculated. As a consequene a measurement of ρ at a given energy can be used to make predictions on total cross section at energies beyond those at wich ρ has been measured.

6.3 Measurements of Total Cross Section and ρ

In the present section, we will focus on the description of total cross section and ρ measurements [107]. The total cross section can be measured via elastic scattering using the optical theorem, (6.3). The differential elastic cross section is related to the forward amplitude by:

$$\frac{d\sigma_{el}}{dt} = \pi|f_{el}(\theta)|^2 \tag{6.10}$$

where $f_{el}(\theta)$ is a complex function:

$$f_{el}(\theta) = Ref_{el}(\theta) + iImf_{el}(\theta) \tag{6.11}$$

By the optical theorem, σ_{tot} can be expressed as:

$$\sigma^2_{tot} = \frac{16\pi}{1+\rho^2}\left|\frac{dR_{el}}{dt}\right|_{t\to 0} \tag{6.12}$$

1. *Luminosity dependent approach.*
   By expressing the differential elastic cross section in terms of elastic rate and luminosity:
   $$\frac{d\sigma_{el}}{dt} = \frac{1}{\mathscr{L}}\left(\frac{dR_{el}}{dt}\right) \tag{6.13}$$
   The total cross section becomes:
   $$\sigma^2_{tot} = \frac{16\pi}{1+\rho^2}\frac{1}{\mathscr{L}}\left(\frac{dR_{el}}{dt}\right)_{t\to 0} \tag{6.14}$$
   Eq.(6.14) represents the *luminosity dependent* approach with which σ_{tot} can be determined by measuring independently the elastic rate extrapolated at t=0 and the luminosity, while ρ is an input from the theory.

2. *Luminosity independent approach.*
   Knowing that $\sigma_{tot} = \frac{R_{tot}}{\mathscr{L}}$, Eq. (6.14) can be also expressed as:
   $$\sigma_{tot} = \frac{16\pi}{1+\rho^2}\frac{(dRel/dt)_{t\to 0}}{R_{tot}} \tag{6.15}$$
   This complementary approach is known as *luminosity independent* method. Elastic rate and total rate have to be determined simultaneously together with ρ.

3. *Coulomb-Nuclear Interference*. The Coulomb-Nuclear interference can be used to probe the nuclear component of the scattering amplitude. The amplitude describing the elastic scattering between protons can have three contributions [108]:

   - Pure QED: the amplitude is obtained by perturbative calculations as [109]:
     $$\frac{d\sigma_C}{dt} = \frac{4\pi\alpha^2}{t^2}G^4_{eff} \tag{6.16}$$
     where α is the coupling constant and G_{eff} is the *effective form factor* defined as a combination of electric and magnetic form factor:
     $$G^2_{eff} = \frac{G^2_E + G^2_M}{1+\tau} \tag{6.17}$$
     where $\tau = -\frac{t}{4m^2}$ For low momentum transfer, in the condition $t << m^2$, the contribution of the magnetic form factor is negligible while, on the other hand, if t increases with respect to m^2 the proton's magnetic momentum can no longer be neglected.

- Nuclear: at $|t| \gtrsim 0.02$ GeV^2, the effect due to Coulomb interaction are not expected to be large. As a consequence, the measured cross section is attributed to the nuclear contribution. The nuclear amplitude is parametrized as:

$$|\mathscr{A}(t)|^2 \sim \sqrt{a} exp\left(\frac{1}{2}\sum_{n=1}^{N_b} b_n t^n\right) \tag{6.18}$$

where N_b is the number of free parameters, b_1 is the nuclear slope and a the intercept of the differential cross section.

- *Coulomb-Nuclear Interference*: the simplified *West-Yennie* formula (SWY) [110] was derived in the framework of the perturbative quantum field theory by evaluating the lowest-order Feynman diagrams that comprise both nuclear and Coulomb interactions. The interference is considered as an additional phase between the Coulomb and nuclear amplitudes, as can be seen in Eq.(6.19):

$$\frac{d\sigma^{C+N}}{dt} \approx |\frac{\alpha_S}{t} G^2 e^{i\alpha\phi_{WI}(t)} + \mathscr{A}^N|^2 \tag{6.19}$$

where $\phi_{WI}(t)$ is defined as:

$$\phi_{WI} \approx -(\ln\frac{b_1(t)}{2} + \gamma) \tag{6.20}$$

where γ is the Euler constant. The Coulomb corrected differential hadronic cross section usually used for the ρ determination is:

$$\left[\frac{d\sigma}{d|t|}\right] = \left(\frac{\sigma_{tot}^2}{16\pi}\right)\left[G^4(t)\left(\frac{t_0}{t}\right)^2 \mp 2\frac{t_0}{|t|}(\rho \pm \phi_{WY}) \times G^2(t) e^{-b_1|t)/2} + (1+\rho^2) e^{-b_1|t|}\right] \tag{6.21}$$

6.3.1 Pre-LHC σ_{tot} measurements at particle accelarators

With the beginning of the accelerator era in 1950s, several total hadronic cross section measurements have been performed. The focus was the simultaneous measurement of:

- total cross section σ_{tot}.
- elastic cross section σ_{el}.
- slope of the forward elastic scattering B.
- ρ-parameter.

Since then, the study of the evolution of σ_{tot} was performed by cosmic ray experiments. The first measurements showed a decrease of the total cross section both in the case of $p\bar{p}$ (more) and in pp collision case (only slightly): all in agreement with the predictions at small momentum transfer by exchange of Regge trajectory. It was in the 1970s that the situation changed. With the first measurements at ISR, cross sections were seen to rise 6.2.

Fixed Target Experiments

The proton-nuclei cross section measurements were performed between 6 and 22 GeV, with steps of 2 GeV [111], [112]. The pp and $p\bar{p}$ cross section measurements were measured on

both hydrogen and deuterium targets. The results showed a variation of the cross section with momentum and a decrease around 12 GeV.
The method utilized was that of conventional good geometry transition experiment with scintillation counters subtending various solid angles at target liquid H_2 and D_2. Essentially, the measurements were performed following the initial and final paths of particles through a series of counters placed at subsequent intervals and covering different solid angle portions. For each set of counters, at a given solid angle, a transmission factor defined to take into consideration signals for various components and σ_{tot} at a given momentum transfer value (t) was calculated, following:

$$\sigma(t) = \frac{1}{N} \ln\left(\frac{T_E}{T_F}\right) \tag{6.22}$$

where N is the number of nuclei per cm^2 in the target, T_E and T_F the transmission factors for an empty or a full target, respectively. Partial differential cross section measured at different t-values were fitted either by a polynomial or by an exponential and extrapolation to zero.

Measurements at ISR

At ISR, several methods to determine σ_{tot} were developed and three of them were used: two of them were luminosity-dependent, one luminosity-independent. Total and/or elastic cross sections were measured by different experiments, with different strategies and in different t-regions. The measurements were performed differently with respect to fixed target experiments. An accurate estimate of the total rate, of the luminosity and/or of the elastic rate was needed together with the extrapolation to the optical point at t=0.

1. A luminosity dependent measurement (CERN-Rome group) [113] [114] of the total cross section which uses the optical point method has to count on a reliable luminosity determination and on the extrapolation of the elastic rate down to t=0. Through the optical theorem, we know that there is a quadratic dependence of the elastic differential cross section on ρ, see Eq.(6.14). However, such a method does not allow a precise determination of nuclear amplitude since at high energies (i.e., from ISR onwards), the ρ parameter is rather small, $\rho \sim 0.1$. For this reason, it is difficult to measure ρ accurately and the measurement would not determine the sign of the nuclear amplitude. Fortunately, this issue can be circumvented thanks to the interference between the Coulomb and the real part of nuclear amplitude, which allows the determination of the sign and the value of ρ. The fitting method used at ISR was the one explained by Eq.(6.21). At ISR, the measurement is performed for the region $0.001<|t|<0.01$ GeV^2.

2. The CERN-Rome group adopted an alternative approach measuring the differential cross section at small angles, but not in the Coulomb region and then extrapolated it to the optical limit [115]. The measurement was based on the parametrisation of the hadronic part of the cross section, which assumes a constant exponential t-dependence of the scattering amplitude and a parameter ρ constant in the range of t of interest.

3. Another method (Pisa-Stony Brook method) used at ISR was to measure the total cross section by determining the luminosity and the total interaction rate ($R_{el} + R_{inel}$),

through the definition [116]:

$$R(\text{number of events/second}) = \mathscr{L}[\text{cm}^{-2}\text{s}^{-1}]\sigma_{tot}[cm^{-2}] \tag{6.23}$$

4. A fourth method was adopted by combining the Pisa-Stony Brook and the CERN-Rome methods resulting in a *luminosity independent method*, see Eq.(6.15) [117], [118].

All these measurements indicated a rising total cross section. They are summarized in Tab.(6.1). The sensitivity to σ_{tot} beyond the energy at which ρ is calculated has been used

TABLE 6.1: Resulting values for σ_{tot}, ρ and B from ISR [119].

	$\sqrt{s}$ [GeV]	σ_{tot} [mb]	ρ	B [GeV^{-2}]
pp	23.5	39.65±0.22	0.022±0.014	11.80±0.30
pp	30.6	40.11±0.17	0.034±0.008	12.20±0.30
$p\bar{p}$	30.4	42.13±0.57	0.055±0.029	12.70±0.50
pp	52.8	42.38±0.15	0.077±0.009	12.87±0.14
$p\bar{p}$	52.6	43.32±0.34	0.106±0.016	13.03±0.562
pp	62.3	43.55±0.31	0.095±0.011	13.02±0.27
$p\bar{p}$	62.3	44.12±0.39	0.104±0.011	13.47±0.52

to make prediction of the energy evolution of σ_{tot} for the first time at ISR. The ρ-parameter was measured at $\sqrt{s}$ ranging from 30 to 60 GeV, with a precision of 0.01, to constrain the energy evolution of the total cross section up to at least 300 GeV. The result were obtained with a χ^2 common fit of σ_{tot} and ρ using dispersion relation (Eq(6.9)).

Measurements at Sp$\bar{p}$S

In the early 1980s, a center of mass energy of 540 GeV was reached at CERN Sp$\bar{p}$S. The total cross section was measured by experiments UA1 [120] and UA4 [121], later on followed by a combined collaboration UA2/UA4 and UA5.

1. The first measurement was performed by UA1, measuring the elastic differential cross section for 0.04<-$|t|$<0.45 GeV^2. The data were fitted by the usual exponential form:

$$\frac{dN_{el}}{dt} \propto e^{-Bt} \tag{6.24}$$

The slope parameter B was measured for two different t-ranges and the total cross section and the ratio $\frac{\sigma_{el}}{\sigma_{tot}}$ were obtained, with the determination of the integrated luminosity.

2. The UA4 also performed a first measurement, with the same approach.
In particular, UA4 experiment was specifically dedicated to the measurement of σ_{tot} and ρ. Using the luminosity independent method, two σ_{tot} values have been obtained.

   - σ_{tot} = 66 mb with a 10% statistical error.
   - σ_{tot} = 61.9 $\pm$ 1.5 mb through a cross-check with a luminosity dependent method.

   UA4 was able to measure at very small scattering angles ($\sim$ 1mrad), down to values of 0.002<$|t|$<1.5 GeV^{-2}, thanks to the Roman Pots technique.

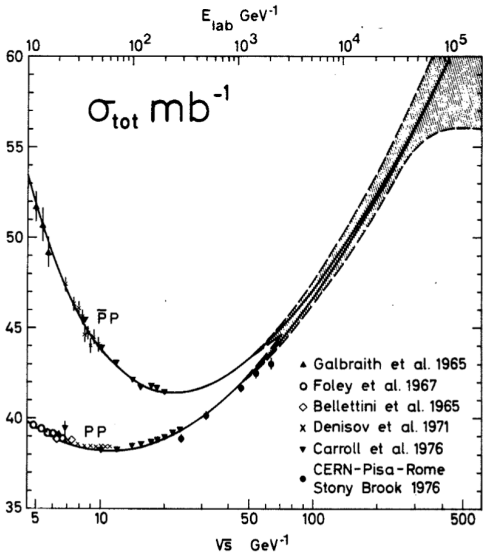

(A) Total cross section.

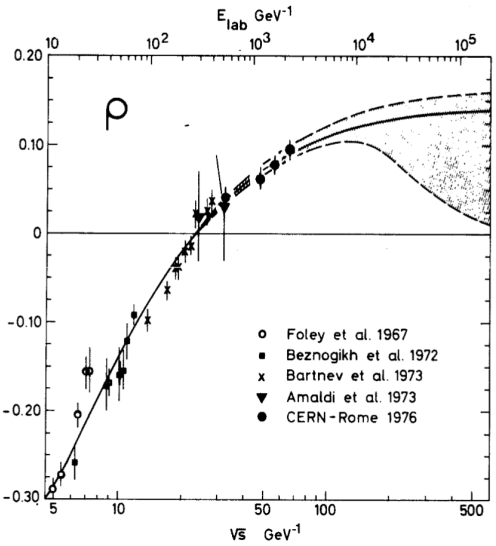

(B) The real to the imaginary part ratio of the forward elastic scattering.

FIGURE 6.2: The σ_{tot} (left) and ρ (right) measurements at low energy and at ISR. The full curves is a result of a fit, simultaneously performed on the total cross section data and on the data of ρ.

The ρ-parameter was also measured:

$$\rho = 0.24 \pm 0.4 \tag{6.25}$$

However this measurement was affected by the poor knowledge of the beam optics and by limited statistics. It was repeated by a combined UA4/UA2 collaboration [122] under very clean conditions with higher precision and better control of systematic errors, finding:

$$\rho = 0.135 \pm 0.15 \tag{6.26}$$

3. The UA5 experiment measured the $p\bar{p}$ cross section at $\sqrt{s}$=200 and 900 GeV [123], leading to:
$$\sigma_{tot}^{900\ \text{GeV}} = 65.3 \pm 0.7 \pm 1.5mb \tag{6.27}$$
which is consistent with previous measurements.

Measurements at Tevatron

At FermiLab, the Tevatron accelerator was started in 1985 for proton-antiproton scattering. The total cross section was measured by three experiments: E710, CDF(*Collider Detector Facility*) and E811.

1. At the experiment E710, the inelastic rate was measured at large and intermediate angles, at $\sqrt{s}$ = 1.8 TeV [124]. The first measurement was based on the luminosity dependent method and on the the extrapolation to zero of the usual exponential behaviour of the elastic rate in the interval 0.025<$|t|$<0.08 GeV^2. A second luminosity independent measurement was performed as cross-check.

2. CDF repeated the measurement at $\sqrt{s}$ = 546 GeV and at $\sqrt{s}$ = 1.8 TeV, using a luminosity independent method [125]. The total cross section was obtained from the measurement of the forward elastic and inelastic interaction rate. The measurement from CDF differs from the one of E710 by 3 standard deviations.

3. Because of this discrepancy, E811 repeated the measurement at very small-angle for 0.0045<$|t|$<0.036 GeV^2, using a luminosity independent method to determine simultaneously σ_{tot} and ρ [126].

The three results for σ_{tot} are listed in Tab.(6.2). The ρ parameter have been measured

TABLE 6.2: Resulting values for σ_{tot} from Tevatron.

$\sqrt{s}$ [GeV]	Experiment	σ_{tot} [mb]
546	CDF	63.3 $\pm$ 1.5 [125]
1800	E710	72.8 $\pm$ 1.63 [124]
1800	CDF	80.03 $\pm$ 2.24 [125]
1800	E811	71.42 $\pm$ 2.41 [126]

in the range 0.001$\leq|t|\leq$0.14 GeV^2 with a least square fit.

$$\rho = 0.140 \pm 0.069 \tag{6.28}$$

6.3.2 LHC Measurements during Run1: ATLAS and TOTEM

At LHC, the total cross section measurements have been performed by ATLAS with the ALFA detector [51] and by the TOTEM experiment [127]. The approach used is the usual one based on the optical theorem.
In order to reach small angles, it is necessary to be close to the beam pipe and to be afar from the Interaction point. The assembly of the quadrupoles determining the beam optics has to be optimized for a good measurement of small angle elastic scattering.
The common criteria to be satisfied both for ALFA and TOTEM are:

- The focusing at the IP has to be done in a way that the beam divergence is significantly smaller than the scattering angles to be measured. The divergence is given by $\sqrt{\frac{\epsilon}{\beta}^*}$, where ϵ is the beam emittance and β^* is the betatron function at the IP. Knowing that the typical LHC emittance is 2-3 μm, β^* has to assume values of the order of 100 m in order to achieve divergence of few μrad.

- The *parallel-to-point* focusing implies that the position trajectory in the detector is independent of the unmeasured vertex position at the IP.

- An effective lever arm, $L^{x,y}_{eff}$, between the Interaction Point and the detector can be defined as:

$$\theta_{x,y} = \frac{x,y}{L^{x,y}_{eff}} \tag{6.29}$$

  where $\theta_{x,y}$ is the scattering angle at the IP and x, y are the detector coordinates in the transverse plane. The lever arm should be large at least in one of the two transverse projection, giving a good separation at the level of the detector and, consequently, a good resolution for different scattering angles at the IP.

Both ALFA and TOTEM exploits the Roman Pots technology, pionered at ISR by CERN-Rome group in the early 1970s. A Roman Pot is a vessel that contains a detector connected to the accelarator vacuum via bellows, see Fig. (6.3). Both the experiments have two stations,

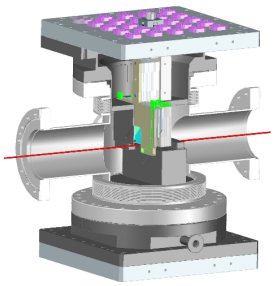

FIGURE 6.3: Two Roman Pot vessels (ALFA) which can approach the beam from above and below.

located symmetrically on each side of the IP. ALFA has been already described in Chapter 2 with a pictorial view of its configuration. The TOTEM layout (at IP5 along the LHC ring) can be seen in Fig.(6.4). The two TOTEM stations are located at about 220 m from the IP.

The TOTEM Results

TOTEM has performed four different measurements of σ_{tot} at 7 TeV and one measurement at 8 TeV.
The first measurement was based upon data taken in the first LHC run at β^*=90 m with an integrated luminosity of 1.7μb^{-1} (July 2011). The other three measurements were based upon three different methods to extract the total cross section using the same dataset of 84 μb^{-1} (October 2011). For the 8 TeV measurement the data was taken in July 2012.
The first measurement used the optical theorem through a luminosity dependent approach [128]. Although 30% of the hadronic elastic events were not collected, a $|t|$ of 0.02 GeV^{-2} was achieved. The result was:

$$\sigma_{tot} = 98.3 \pm 0.2_{stat} \pm 2.8_{sys}\text{mb} \tag{6.30}$$

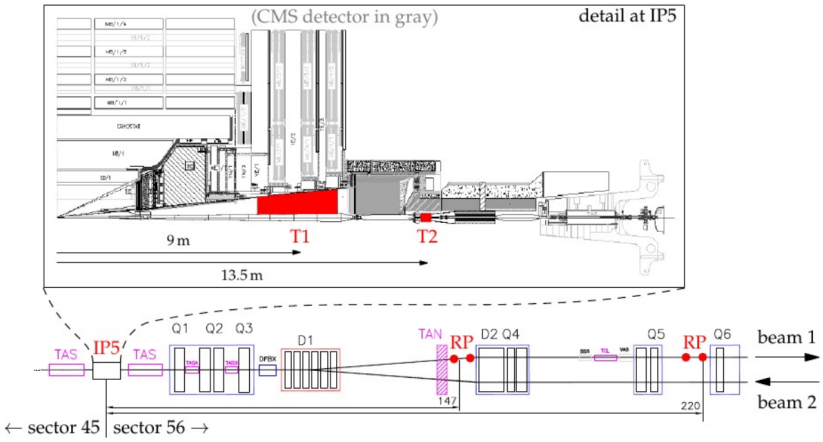

FIGURE 6.4: A schematic view of the TOTEM detector at the LHC. In the lower part, the position of the TOTEM Roman Pots in the LHC lattice is shown. T1 and T2 are the telescope used for the detection of charged particles and they are shown in red in the upper part.

with the systematic uncertainty dominated by extrapolation at t=0 and luminosity uncertainty (4%, provided by CMS).
The new data collected in October 2011 had 50 times more statistics and only 10% of hadronic elastic interaction escaping undetected. Three different sets of data were analyzed independently to better understand systematic uncertainties. Once an excellent agreement between them was found, the dataset was merged to extract the result. The differential elastic cross section was fitted in the t-range 5×10^{-3} GeV^2<$|t_{min}|$<0.2, with a simple exponential form and the extrapolation to the optical point provided the result [129]:

$$\sigma_{tot} = 98.6 \pm 2.2\text{mb} \tag{6.31}$$

The uncertainty is exclusively systematic, since the statistical uncertainty is negligible after the merging of the three datasets. Also in this case the main source of systematic is due to luminosity.
The same dataset was analyzed with a luminosity independent method, with the measurement of the inelastic rate by the two forward charged telescopes T1 and T2 [130]. The result is:

$$\sigma_{tot} = 98.0 \pm 2.5\text{mb} \tag{6.32}$$

TOTEM also employed a third method to calculate σ_{tot}. The previous ones were based upon the optical theorem and thus dependent on the value of ρ. Alternatively, σ_{tot} can be simpy calculated as the sum of σ_{inel} and σ_{el}. Using the same dataset:

$$\sigma_{tot} = 99.1 \pm 4.3\text{mb} \tag{6.33}$$

The elastic and inelastic measurements can be combined to obtain ρ^2 by:

$$\rho^2 = 16\pi \mathscr{L}_{int}^{CMS} \frac{(dN_{el}/dt)t=0}{(N_{el}+N_{inel})^2} - 1 \tag{6.34}$$

This is the first direct measurement, not an extrapolation. It yields to ρ^2 = 0.009 $\pm$ 0.056. Since it cannot be easily translated into ρ, it can be stated that at 95% confidence level ρ^2<0.10. Alternatively, one can exploit a Bayes' approach: taking a uniform prior $|\rho|$ distribution, it yields a posterior distribution with mean 0.145 and standard deviation 0.091.

In July 2012, TOTEM collected data at a center of mass energy of 8 TeV. The beam optics used was similar to the 7 TeV data taking with β^*=90 m. The luminosity independent method was used to extract the total cross-section and the inelastic rate was measured simultaneously with the elastic rate [131]. The total cross section was found to be:

$$\sigma_{tot} = 101.7 \pm 2.9\text{mb} \tag{6.35}$$

For the same dataset, ρ has been extracted via the Coulomb-nuclear interference, for the first time at LHC:

$$\rho = 0.12 \pm 0.03 \tag{6.36}$$

In 2018, TOTEM

The ATLAS Results

ATLAS reported two measurements, respectively at 7 TeV and 8 TeV. Due to the lack of coverage in the forward direction, ATLAS has chosen a luminosity dependent method to determine the total cross section. Such a choice was also due to the fact that ATLAS has a precise and reliable luminosity determination, which is the main source of systematic uncertainty as we have seen in the discussion of TOTEM results.
At 7 TeV, the data were collected in October 2011 (which is the same fill at β^* used for the second TOTEM measurement) [52]. The t-range used for the estimation was 0.01 GeV^2<$|t|$<0.1 GeV^2.
The result was:

$$\sigma_{tot} = 95.35 \pm 0.38_{stat} \pm 1.25_{sys} \pm 0.37_{extrapolation} mb \tag{6.37}$$

A total uncertainty of 2.3% is obtained for the integrated luminosity. An additional uncertainty comes from the procedure used to extrapolation to the optical region.
ATLAS has performed a measurement also at $\sqrt{s}$=8 TeV [53]. The data-taking has been collected at β^*=90 m. The strategy is the same used for the 7 TeV measurement. The differential cross section was used also to determine the nuclear slope. The absolute luminosity for this run has been determined in a dedicated analysis, taking into account the special experimental conditions with a very low number of interactions per bunch-crossing. The total cross section is:

$$\sigma_{tot} = 96.07 \pm 0.18_{stat} \pm 0.85_{exp} \pm 0.31_{extr}\text{mb} \tag{6.38}$$

where the first error is statistical, the second accounts the experimental conditions and the last is related to the extrapolation to $t \to$0.

6.4 Phenomenological Fits to Total Cross Section

Several attempt have been made to describe the pp and $p\bar{p}$ total cross section. The two described in the following were published by the Particle Data Group, before and after the start of LHC.
Fig.(6.5) show the data available before the TOTEM and ATLAS measurements, fitted with a model input from COMPETE collaboration [132].

The COMPETE program states that the region to be focused is the Coulomb-nuclear interference region and that the following theoretical inputs have to be common to all the experiments [133]:

- common parametrization of electromagnetic form factor.

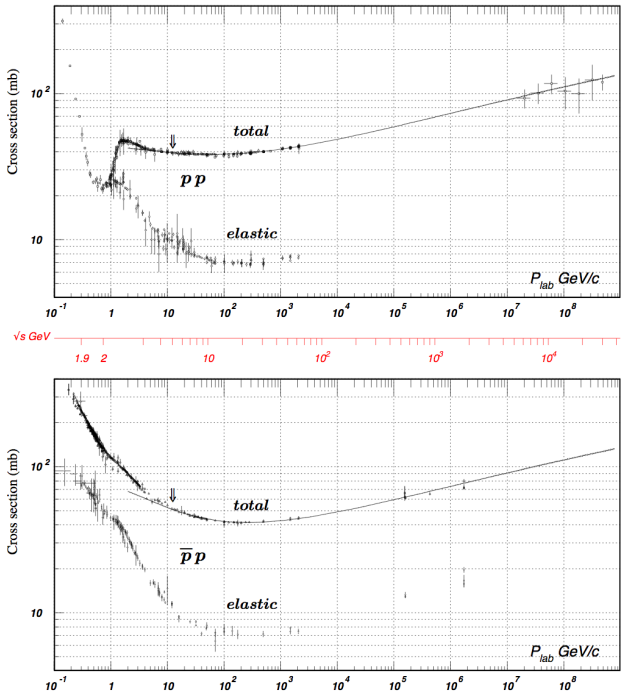

FIGURE 6.5: Total and elastic cross section as a function of the laboratory beam momentum and center of mass energy before the TOTEM and ATLAS measurements by the COMPAS collaboration for 2009.

- common procedure to analyze data in Coulomb interference region.
- common set of strong interaction elastic scattering parameters.
- common study of Regge trajectories.

The data have been fitted with the expression:

$$\sigma_{tot}(a \pm b) = H\ln^2\left(\frac{s}{s_{ab}}\right) + P^{ab} + R_1^{ab}\left(\frac{s}{s_{ab}}\right)^{-\eta_1} \pm R_2^{ab}\left(\frac{s}{s_{ab}}\right)^{-\eta_2} \tag{6.39}$$

(6.40)

where Z^{ab}, B, Y_1^{ab} are in mb, s, s_0, s_1 are in GeV^2. The scale s_1 is assumed to be 1/GeV^2, while $\sqrt{s_0} \approx 5$ GeV (i.e., the fit takes into account only measurement above this value). Eq.(6.40) can be interpreted as that the power-law terms reproduce the Regge behaviour from the imaginary part of the forward scattering amplitude, while the constant and the squared logarithmic terms reflect the Pomeron exchange. The values of the parameters are listed in Tab.(6.3)

TABLE 6.3: Fit parameters in the Pre-LHC era.

Z	35.45 mb
Y_1	42.53 mb
Y_2	33.34 mb
B	0.308 mb
η_1	0.458
η_2	0.545

In a QCD framework, the term which brings in the rise of the total cross section comes from the gluon-gluon scattering, tempered by soft gluons emitted in the initial state. The constant term is interpreted as the Pomeron which is supposed to give constant total cross section. However the cross sections only apparently goes to constant, just after the Regge descend and just before the cross section asymptotic rise.
However, there were some difficulties in making precise predictions at LHC.

- No available measurements between $\sqrt{s} \approx$ (60÷70) GeV (ISR) and $\sqrt{s} \approx$ (500÷700) (S$p\bar{p}$S).
- at Tevatron energies, $\sqrt{s} \approx 1.8$ TeV, a 2σ discrepancy between two measurements by E710 and CDF.
- t-dependence of the differential elastic cross section as $t \to 0$ may not be simply expressed as e^{Bt}, where B is assumed to be constant in t.
- large errors for total hadronic cross sections from cosmic ray measurements, due to the experimental method used to extract σ_{pp} from p-air cross section.

The final result was obtained by a combined χ^2 fit of the total cross section and ρ, via dispersion relation, and it has proved that the squared logarithmic rise was the best description with respect to the other models.
The COMPAS group has presented a new phenomenological fit and a new parametrization, adding new measurements from LHC experiments and cosmic rays. COMPAS used four terms in the hadronic cross section:

$$\sigma_{tot}(a \pm b) = H\left[\ln\left(\frac{s}{s_M^{ab}}\right)\right]^2 + P^{ab} + R_1^{ab}\left(\frac{s}{s_M^{ab}}\right)^{-eta_1} \pm R_2^{ab}\left(\frac{s}{s_M^{ab}}\right)^{-eta_2} \tag{6.41}$$

The parameters are defined as follows:

- $H = \pi/M^2$.
- scaling parameter $s_M^{ab} = (m_a + m_b + M)^2$.
- P^{ab}, the Pomeron constant.
- R_i^{ab}, the Regge trajectories.

Their values are listed below, according to the results from 2016 fit. The possible rise of total

TABLE 6.4: Fit parameters.

H	0.2720 ± 0.0024 [mb]
M	2.1206 ± 0.0094 [GeV]
P^{ab}	34.41 ± 0.13 [mb]
R_1^{ab}	13.07 ± 0.17 [mb]
R_2^{ab}	7.394 ± 0.081 [mb]
η_1	0.4473 ± 0.0077
η_2	0.5486 ± 0.0049

collision cross section in the form of squared logarithmic rise has been questioned opening the possibility to a possible faster rising form. In the form $\ln^c\left(\frac{s}{s_0}\right)$, c has been left as a free

parameter in the pp and $p\bar{p}$ fit which was performed to available total cross section and ρ-parameters in August 2015, including TOTEM points at 8 TeV. A χ^2 was performed with all data above 5 GeV and the obtained value for the exponent c was:

$$c = 1.98 \pm 0.01 \tag{6.42}$$

which is two standard deviation lower than 2, probing that up until then the universal rise prediction of the evolution of σ_{tot} was still valid. The results of the analysis are shown in Fig.(6.6).

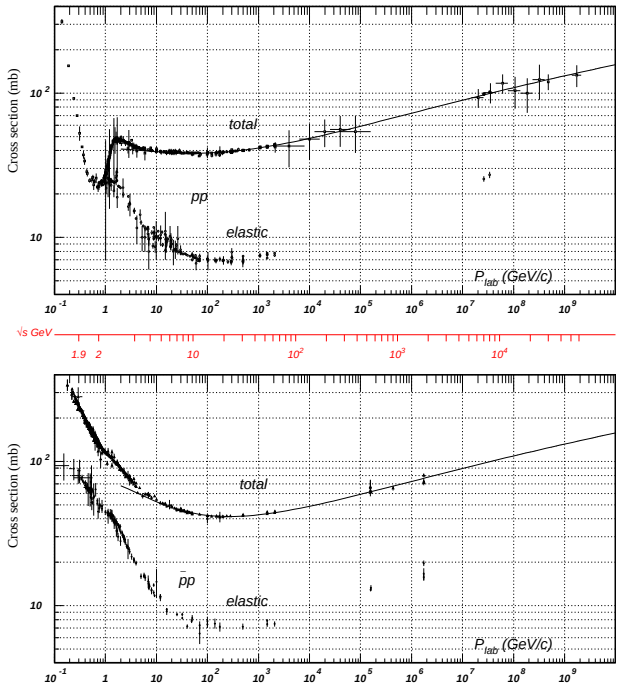

FIGURE 6.6: Total proton-proton and antiproton cross section for the 2016 COMPAS fit.

6.5 TOTEM Measurement of ρ at 13 TeV

As can be seen from Fig.(6.7), the measurement of ρ performed by pre-LHC experiments and by TOTEM at 7 and 8 TeV are in agreement with the prediction based on dispersion relation calculation.
However, in 2017 TOTEM has published two different values of ρ which deviates from the predictions, as can be seen from Fig.(6.7), [134].

- ρ = 0.09 $\pm$ 0.01
- ρ = 0.10 $\pm$ 0.01

As can be seen, the ρ values determined at 13 TeV are incompatible at a level of 4.7σ from the preferred COMPETE model.
How can this discrepancy be explained? As already said, dispersion relation are based on analiticity, crossing symmetries and unitarity. Assuming these cornerstones as solid, only two options remain to explain the big difference which can be seen in Fig.(6.7)

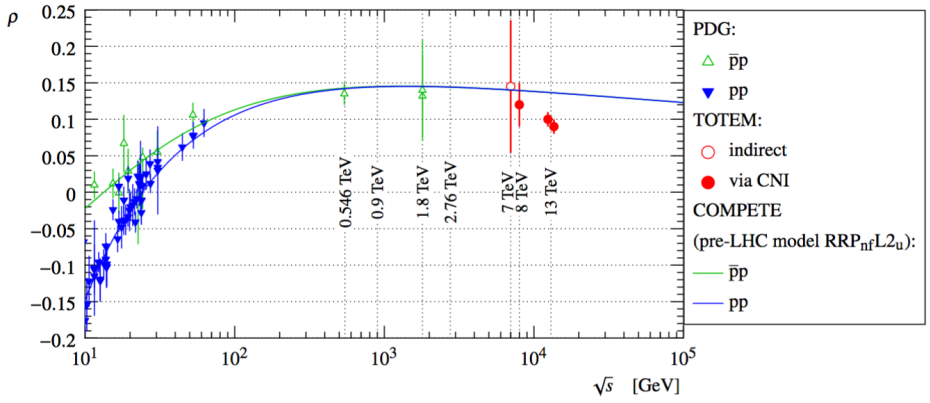

FIGURE 6.7: Dependence of the ρ parameter on energy. The pp (blue) and $p\bar{p}$ (green) are the pre-LHC measurements taken from PDG. TOTEM measurements are marked in red. The two curves corresponds to the COMPETE fit using the pre-LHC model.

1. The first one to be considered is that the form of dispersion relation (single subtracted), used at ISR and at Sp$\bar{p}$S collider, is not valid. The single subtracted dispersion relations assume that:

$$\Delta\sigma = \sigma_{pp} - \sigma_{p\bar{p}} \xrightarrow{\text{asymptotically}} 0 \tag{6.43}$$

This theorem is not valid anymore if there is a part of the elastic scattering amplitude which is odd under crossing and thus contributing with different sign for particle-particle and particle-antiparticle scattering. This can correspond, for Regge theory, to the existence of the Odderon as a partner to the Pomeron. In QCD the same phenomena is described as the possibility of a colorless three gluon compound being exchange in elastic scattering in addition to the Pomeron. However, the existence of an Odderon does not violate the generalized Pomeranchuk theorem:

$$\frac{\sigma_{pp}}{\sigma_{p\bar{p}}} \xrightarrow{\text{asymptotically}} 1 \tag{6.44}$$

2. The second possibility is that something drastic happens to σ_{tot} at energies above LHC which is the scenario explore in Sec.(6.7)

6.6 Impact of a ρ measurement at 14 TeV

At the end of 2018, LHC has been stopped for major two-year upgrade programme that will result in a renovated accelarator complex using more intense beams and high energy, reaching 14 TeV. This will be the first step toward the High-Luminosity LHC era, starting in 2025, when the instantaneous luminosity will increase of one order of magnitude and the integrated luminosity collected will be of 3000 fb^{-1}. Fig.(6.8) shows the LHC time schedule with the future plans.

In this context, I have performed a study using my code (see Sec.6.1) for the ρ estimation via dispersion relation to prove the importance of a ρ measurement at 14 TeV, during LHC Run3 (2021-2023), in terms of predictive power on the total cross section behaviour.
The underlying assumption is that there is a break point for the $\ln^2 s$ rise around 15 TeV.

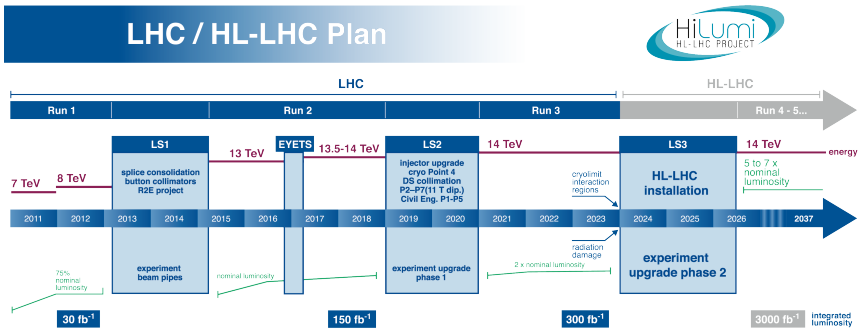

FIGURE 6.8: LHC Timeline and future plans.

Above this energy threshold, the total cross section rises with a different exponent, namely $\ln^c s$. The parametrization of σ_{tot} used is the one from 2016 COMPAS results, Eq.(6.41).
I have estimated 20 new exponent starting from c=2 and adding and subtracting Δc=0.02, at each step, for both 13 TeV and 14 TeV and calculated corresponding ρ-values. The results obtained are summarized in Tab(6.5). We assume that ρ, calculated with exponent 2, is our

TABLE 6.5: ρ calculated assuming a break point for the total cross section rise at 15 TeV for the different exponents.

Exponents	ρ(13 TeV)	ρ(14 TeV)
1.8	0.11054	0.106396
1.82	0.111951	0.10808
1.84	0.113458	0.109879
1.86	0.115069	0.111801
1.88	0.11679	0.113854
1.90	0.118629	0.116049
1.92	0.120594	0.118393
1.94	0.122692	0.120897
1.96	0.124934	0.123571
1.98	0.127328	0.126428
2.0	0.129886	0.129479
2.02	0.132617	0.132736
2.04	0.135533	0.136215
2.06	0.138647	0.13993
2.08	0.141973	0.143896
2.10	0.145523	0.14813
2.12	0.149312	0.15265
2.14	0.153358	0.157475
2.16	0.157677	0.162626
2.18	0.162287	0.168123
2.20	0.167207	0.173989

measurement for 13 TeV and 14 TeV. Furthermore, we know that the needed uncertainty on the measurement to ensure reliable prediction on σ_{tot} is $\sim$ 0.01. At this point, we can extract two new exponents by adding and subtracting this uncertainty to the ρ values calculated at 13 TeV and 14 TeV using c=2, see Fig.(6.9).

The resulting new exponents are: If we now calculate σ_{tot} at 100 TeV, using Eq.(6.41) assuming both the standard parametrization, we get σ_{tot}= 146 mb. Calculating the total cross

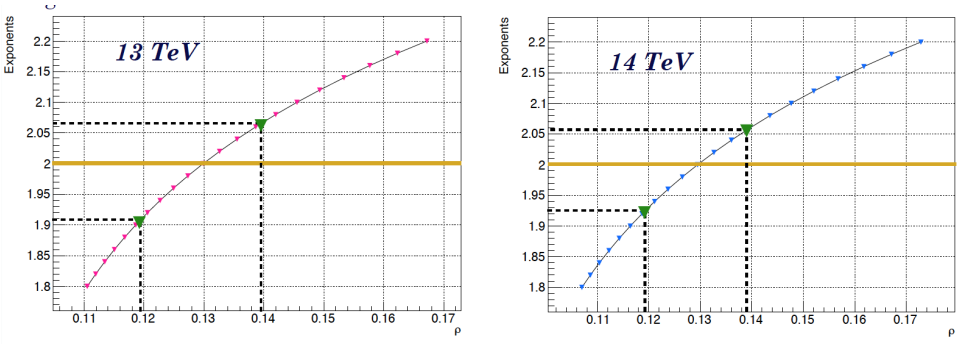

FIGURE 6.9: ρ estimated with the 20 exponents after the break at 15 TeV. Green triangles are the ρ values corresponding to ± 0.01 uncertainty.

TABLE 6.6: New exponents for 13 TeV and 14 TeV.

Scenario	ρ	c
ρ (13TeV) -0.01	0.119886	1.912
ρ (13TeV) + 0.01 0.139886	2.067	
ρ(14TeV)-0.01	0.119479	1.926
ρ(14TeV)+0.01	0.139479	2.059

section, assuming a different rise given by the new estimated exponents c listed in Tab.(6.6), we get for 13 TeV:

- σ_{tot} (c=1.912) = 136.2 mb
- σ_{tot} (c=2.067) = 155.7 mb

with a maximum spread of 19.5 mb. While for 14 TeV:

- σ_{tot} (c=1.926) = 137.5 mb
- σ_{tot} (c=2.059) = 154.5 mb

with a maximum spread of 17 mb.
The results enlighten an important fact. As can be seen from the comparison of the two scenarios, a measurement of ρ at 14 TeV with a 0.01 uncertainty ensures a predictive power on the total cross section of 15% at $\sqrt{s}$ = 100 TeV.

6.7 Different High Energy scenarios of ρ evolution assuming a change of σ_{tot}

The purpose of the studies presented here is to see if it is possible to reproduce the TOTEM ρ measurement with a drastic change of the total cross section behaviour at high energies, instead of assuming the Odderon existence. In all the plots that follows, experimental measurements are shown with a common convention for both σ_{tot} and ρ. Proton-proton and proton-antiproton measurements before LHC are shown, respectively, as full circles and empty squares. TOTEM and ATLAS measurements are shown with different colors, respectively in dark green and red. The points with large error bars corresponds to cosmic ray measurements [135], taken as reference for the beyond LHC energy behaviour.

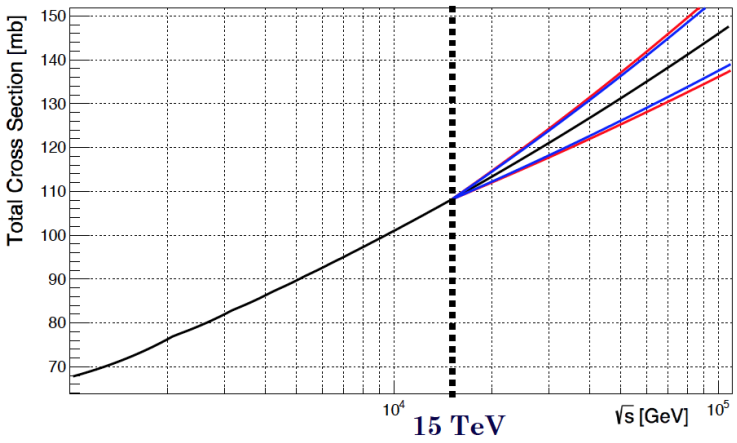

FIGURE 6.10: Comparison of the two scenarios of a measurement at 13 TeV and 14 TeV. Black line represents the σ_{tot} evolution following the standard parametrization with c=2, while red and blue line corresponds to the trends using the two exponents extracted, respectively, assuming a ρ measurement at 13 TeV or at 14 TeV, both with an uncertainty of 0.01.

6.7.1 First approach: σ_{tot} flattening

The very first approach we tried was based on the use of the latest PDG parametrization for the total cross section:

$$\sigma_{tot}(a \pm b) = H\left[\ln\left(\frac{s}{s_M^{ab}}\right)\right]^2 + P^{ab} + R_1^{ab}\left(\frac{s}{s_M^{ab}}\right)^{-eta_1} \pm R_2^{ab}\left(\frac{s}{s_M^{ab}}\right)^{-eta_2} \tag{6.45}$$

using the 2016 parametrization (corresponding values can be find in Tab.(6.4)) and assuming a simple flattening to a constant value at 20, 40 and 60 TeV, see Fig.(6.11). The corresponding ρ-value have been calculated in these three cases.
It is important to underline that Regge terms has been taken into account but their contribution at high energy has been proved to be negligible, in agreement with the Pomeranchuk theorem.

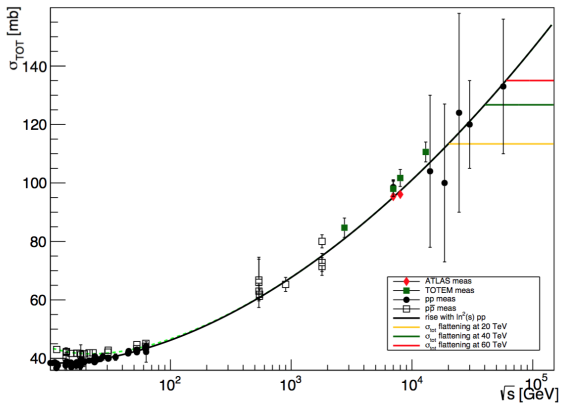

FIGURE 6.11: Total cross section calculated in different high energies scenarios. Black curve corresponds to the PDG parametrization assuming no change. Yellow, green and red curves corresponds to a change of the total cross section assuming constant value, respectively at 20, 40 and 60 TeV.

The first step was the calculation of ρ in the different scenarios, with and without flattening, at 2 TeV, 8 TeV and 13 TeV to check the sensitivity of ρ to a change in the total cross section behaviour. The results are summerized in Tab.(6.7).

TABLE 6.7: ρ values calculated via dispersion relation for different high-energies scenarios.

Scenarios	ρ at 2 TeV	ρ at 8 TeV	ρ at 13 TeV
No Flattening	0.141	0.135	0.132
Flattening at 20 TeV	0.141	0.126	0.109
Flattening at 40 TeV	0.141	0.133	0.126
Flattening at 60 TeV	0.141	0.134	0.130

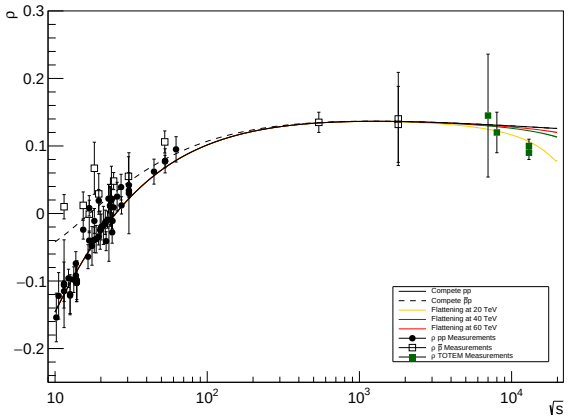

FIGURE 6.12: The ρ-parameter calculated with dispersion relation in different high energy scenarios. Black curve corresponds to scenario with no flattening. Yellow, green and red curves corresponds, respectively, to flattening at 20, 40 and 60 GeV.

As can be seen, ρ calculated at 2 TeV is independent of different high energy scenarios for σ_{tot}, while ρ at 13 TeV is the most sensitive.
After that, ρ values have been calculated at each energy value starting from 10 GeV, in steps of 1 GeV. The sensitivity of ρ to the change of scenarios is appreciable only in the TeV energy regime. The results can be seen in Fig.(6.12). As can be seen, the scenario with a flattening at 20 TeV is the most likely to describe the new TOTEM measurement at 13 TeV in this first simple approach.

6.7.2 Second approach: Change of Exponent at 15 TeV

The second tested scenario was the one considering σ_{tot} following the standard parametrization with a squared logarithmic evolution with energy up to 15 TeV. After that we consider it changing its behaviour and starting to increase with a lower speed, corresponding to a small power, see Fig.(6.13).

It was found that by changing the power to 1.6, we could bring down the ρ value to the TOTEM measurement at 13 TeV, as can be seen in Fig.6.14.

6.7.3 Block and Cahn approach

The attempts described so far demonstrate that by assuming a certain breakpoint for the total cross section behaviour at a given energy, one can reproduce the drastic change in ρ measured by TOTEM. Still it has to be underlined that such procedure is very rough and somehow unnatural. The basic message is that indeed by changing the σ_{tot} parametrization above the LHC energy range (but not far from), an impact on ρ value can be observed.
The next attempt has been to verify how σ_{tot} and ρ behave if we follow the suggestion from Block and Cahn [101], in 1985. From the results emerged from the simultaneous fit to the ISR data, it was found that they cannot be described by a simple logarithmic form as $\ln\left(\frac{s}{s_0}\right)$ but they were well described by the $\ln^2\left(\frac{s}{s_0}\right)$ rise. They introduce an α parameter to allow deviation from it, as follows:

$$\frac{\ln^2\left(\frac{s}{s_0}\right)}{\left(1+\alpha\ln^2\left(\frac{s}{s_0}\right)\right)} \tag{6.46}$$

where α is a small positive number. The smaller it is, the closer the form is to the Froissart bound [136]. The physical meaning fo α is the energy scale at which the cross section change its $\ln^2 s$ behaviour. As we know, the squared logarithmic rise is still a good description of the total cross section, as latest COMPETE fit has demonstrated but it is possible that the energy scale to see an eventual deviation it is beyond LHC energy regime.
We have investigated the effect for different α values, using the pre-LHC parametrization from COMPETE, see Sec.6.4.

$$\sigma_{tot} = 0.307\ln^2\left(\frac{s}{29.1}\right) + 35.5 + 42.6(s)^{-0.46} \pm 33.4(s)^{-0.545} \tag{6.47}$$

where the $\ln^2 s$ rise has been replaced with Eq.(6.46).
We tried with three value for the energy scale:

- α = 0.0002
- α = 0.0004
- α = 0.0006

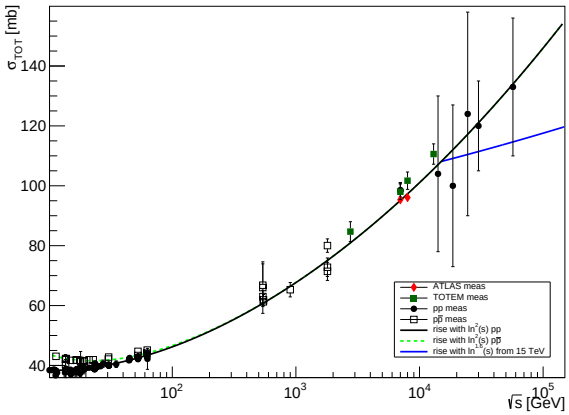

FIGURE 6.13: Total Cross Section evolution with energy together with the experimental measurements. Blu curve represent the trend with a change of exponent at 15 TeV.

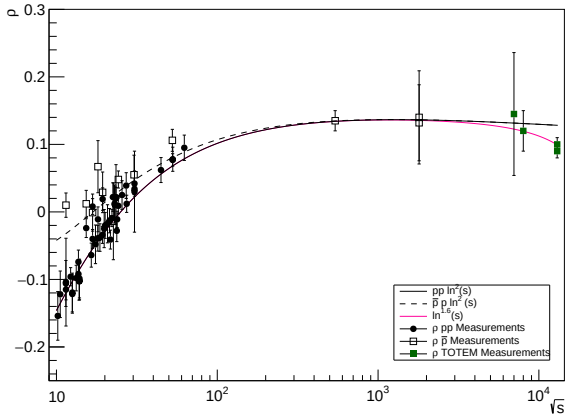

FIGURE 6.14: The ρ-parameter calculated via dispersion relation assuming a change in the total cross section parametrization at 15 TeV.

The ρ parameter has been, correspondently, evaluated by dispersion relation in steps of 1 GeV, for each α value. In Fig(6.15A) and Fig.(6.15B) can be seen the results for σ_{tot} and ρ.

The next step has been to determine σ_{tot} and ρ for different energy values, for these α values:

- α=0.00017
- α=0.00027
- α=0.00037
- α=0.00047
- α=0.00057

Tab.(6.8) and Tab.(6.9) summerize the results obtained.

Among them, α=0.00037 has been chosen to repeat the study since it is the higher value

TABLE 6.8: σ_{tot} calculated with pre LHC parametrization corrected by Eq.(6.46), varying α.

Energy [GeV]	$\sigma(\alpha$=0) [mb]	$\sigma(\alpha$=0.00017) [mb]	$\sigma(\alpha$=0.00027) [mb]	$\sigma(\alpha$=0.00037) [mb]	$\sigma(\alpha$=0.00047) [mb]	$\sigma(\alpha$=0.00057) [mb]	TOTEM [mb]	ATLAS [mb]
500	60.7	60.3	60.1	59.9	59.8	59.6	-	-
600	62.8	62.4	62.1	61.9	61.7	61.4	-	-
1960	78.2	77.2	76.6	76.9	75.6	75.04	-	-
8000	100.9	98.7	97.4	96.02	95	93.9	101.7± 2.9	96.07 ±0.9
10000	105.04	102.5	101.02	99.7	98.3	97.08	-	-
12000	108.5	105.6	104.05	102.6	101.1	99.7	-	-
13000	109.9	107.02	105.4	103.6	102.3	100.9	110.6±3.4	-
14000	111.4	108.3	106.6	105.3	103.5	102	-	-

TABLE 6.9: ρ calculated with pre LHC parametrization corrected by Eq.(6.46), varying α.

Energy [GeV]	$\rho(\alpha$=0)	$\rho(\alpha$=0.00017)	$\rho(\alpha$=0.00027)	$\rho(\alpha$=0.00037)	$\rho(\alpha$=0.00047)	$\rho(\alpha$=0.00057)	TOTEM
500	0.142	0.139	0137	0.135	0.133	0.132	-
600	0.143	0.139	0.137	0.136	0.134	0.132	-
1960	0.144	0.139	0.136	0.134	0.131	0.129	-
8000	0.138	0.132	0.128	0.125	0.121	0.118	0.12 ± 0.03
10000	0.137	0.130	0.126	0.123	0.119	0.116	-
12000	0.136	0.129	0.125	0.121	0.118	0.115	-
13000	0.135	0.128	0.124	0.121	0.117	0.114	0.09 ± 0.01 0.10 ± 0.01
14000	0.135	0.128	0.124	0.120	0.117	0.113	-

which reproduce LHC results in terms of cross section, remembering that bigger is α the

further the energy evolution is from the Froissart bound. In particular, if one looks at the σ_{tot} value for 8 TeV will see that it almost corresponds to ATLAS measurement at 8 TeV. The results can be found in Fig.6.16A for total cross section and ρ in Fig.6.16B. As can be seen from Fig.(6.16)B the predictions obtained via dispersion relation following Block-Cahn approach does not reproduce the TOTEM measurement at 13 TeV, although the change of ρ behaviour that can be observed.

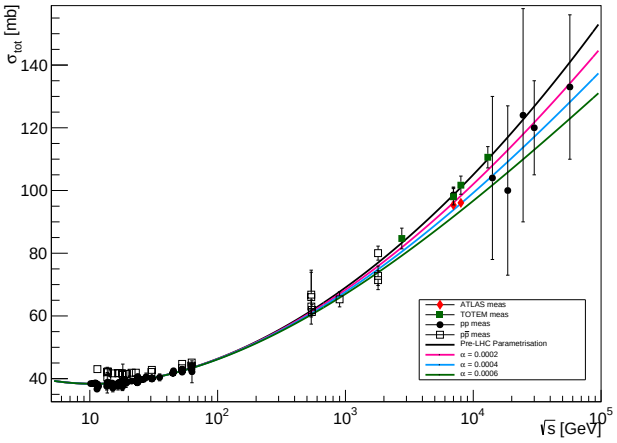

(A) Total Cross Section.

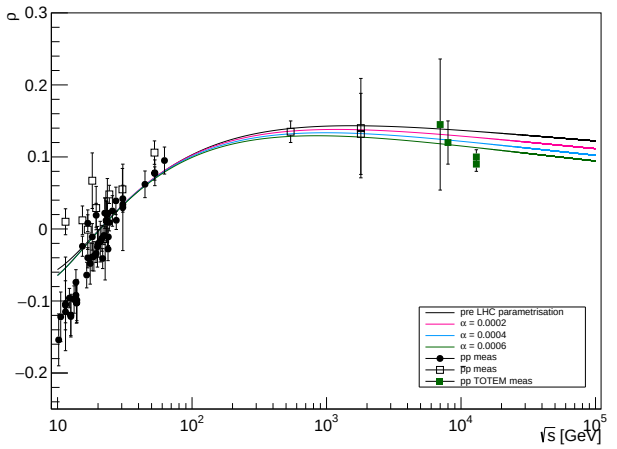

(B) The ρ-parameter.

FIGURE 6.15: Evolution of σ_{tot} and ρ, following the rise law proposed by Block and Cahn. The black line corresponds to the preLHC parametrization which the colored line to the parametrization with the introduction of the three α values.

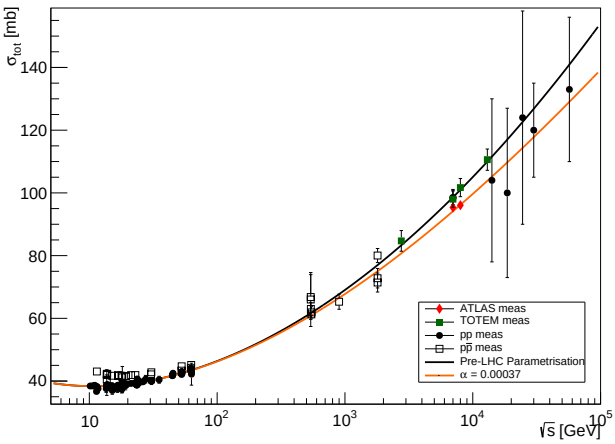

(A) Total Cross Section.

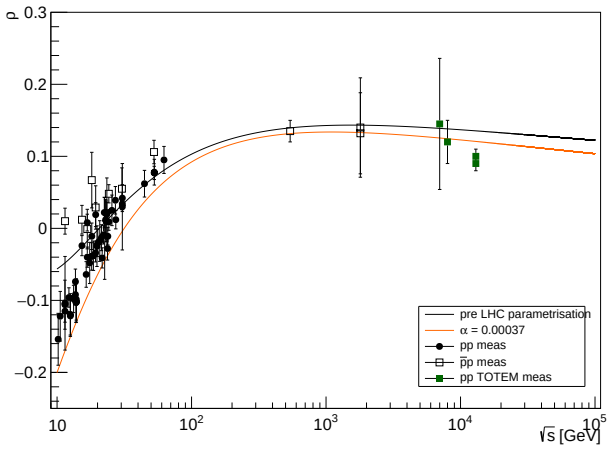

(B) The ρ-parameter.

FIGURE 6.16: Evolution of σ_{tot} and ρ, following the rise law proposed by Block and Cahn. The black line corresponds to the preLHC parametrization while the orange line to the parametrization with α=0.00037.

6.7.4 KMR approach

Another approach is based on the recent paper "Elastic scattering at LHC" by Khoze, Martin and Ryskin. Their predictions is based on a two-eikonal model [137] and take into account both the non Odderon and Odderon possibility. The authors presented the result of their calculation of ρ and σ_{tot} for 7 different energies between 100 GeV and 100 TeV and they are shown in Tab.(6.10).

From Fig.(6.17), it can be seen that the model predicts lower values of ρ also without

TABLE 6.10: The prediction of ρ and σ_{tot} [137].

Energy [TeV]	ρ	σ_{tot} [mb]
0.1	0.141	48.3
0.546	0.129	64.6
1.8	0.121	78.1
7	0.113	95.5
8	0.112	97.4
13	0.109	104.2
100	0.099	136.2

any Odderon assumption (although its inclusion can improve the description of the TOTEM measurement at 13 TeV).

In order to use the code for dispersion relation calculation and to give a prediction based

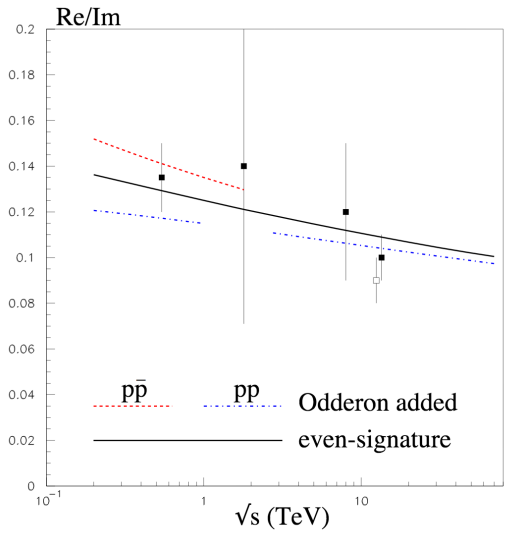

FIGURE 6.17: The energy dependence of the ρ-parameter from KMR different approaches. The first two data points corresponds to proton-antiproton scattering from E710 [124] and UA2/4 combined measurement [122]. The second two points corresponds to TOTEM measurements at 8 TeV [131] and 13 TeV [134]. The dashed line ($p\bar{p}$) and dotted-dashed (pp) curve correspon to an alternative behaviour of ρ obtained from a description of data including the Odderon while the full line represent the two-eikonal model description [137].

on the, the points from KMR predictions in Tab.(6.10) have been parametrized as follows:

$$\sigma_{tot} = 0.159\ln^2\left(\frac{s}{29.1}\right) + 2.5128ln\left(\frac{s}{29.1}\right) \tag{6.48}$$

As can be seen, the formula has the same structure of the existing parametrization as it regards the squared logarithmic term but with the addiction of a $\ln(s)$ term to properly describe the 7 points. Regge terms have been neglected since we are interested to understand the behaviour in the LHC energy range.
The results are summarized in Fig.(6.18) and Fig.(6.19).

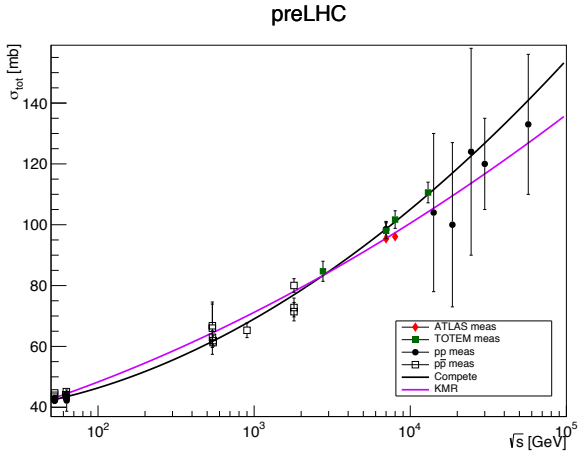

FIGURE 6.18: Evolution of σ_{tot}, following our parametrization based on KMR approach. Note that the mismodelling at low energy is due to the fact that we are neglecting Regge terms.

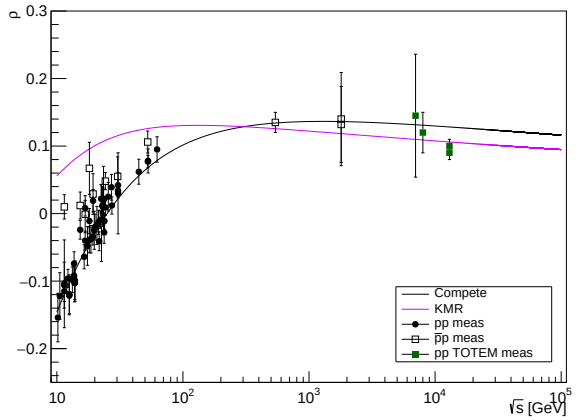

FIGURE 6.19: Evolution of ρ, following our parametrization based on KMR approach. Note that the mismodelling at low energy is due to the fact that we are neglecting Regge terms.

As can be seen from Fig.6.19, the parametrization reproduces the TOTEM measurements within their uncertainty, proving in a first stage that it is possible to give an explanation of the change of ρ evolution with energy could not be due to the Odderon presence.

Conclusion

Dispersion relations applied to high energy physics have always been a powerful tool to predict total cross section evolution with energy, due to its sensitivity to the behaviour of real

to imaginary part of the forward elastic scattering ratio, ρ. The measurement of this parameter has given prediction on the σ_{tot} behaviour well above the available center of mass energy, starting from ISR.
The new scenario opened by the TOTEM ρ measurement at 13 TeV makes really interesting the exploration of this field of physics.
In this Chapter, we have described what has been the evolution of the models and the present measurements of σ_{tot} and ρ up until now.
The purpose of my studies, which are still on going, is to verify if it is possible to understand the new ρ measurements without the assumption of the Odderon presence but instead considering a drastic change in the total cross section behaviour at high energies. The results until now look promising both using very simple approach and more complex model based methods.

Appendix A

The LUCID Detector

Luminosity is a fundamental parameter since it reflects the capability of a collider to produce a significant statistical sample of a certain class of events. A precise and reliable measurement of the luminosity is necessary both for offline analysis and for beam and performance monitoring purposes. One of the main contributions to the systematic uncertainties on some cross section measurements is the one related to luminosity that has to be therefore kept at the order of few % in particular for precision measurements such as, for example, Standard Model checks.
The ATLAS approach is redundant, exploiting several detectors and multiple algorithms. Since 2015, LUCID (*LUminosity measurements using Cherenkov Integrating Detectors*) is the reference detector for online and offline ATLAS luminosity measurements. In the next section, luminosity concept and measurements will be treated together with the description of the upgraded LUCID detector, with particular attention to what regards the upgrade of design and electronics and the gain monitoring system for the Run2 data-taking of relevance for this thesis.
I have worked to the devolopment and mantainance of a dedicated code for the analysis of the data to keep under control the stability of the sensors gain and performed on a regular basis the calibration data analysis. Morover, I have supervised the LUCID operations as run coordinator for various periods of the Run2 data-taking.

A.1 The Concept of Luminosity

The term *Luminosity*, from Latin term *lumen* (light) was for the first time introduced in particle physics by Touschek, one of the founding fathers of the AdA experiments at the Frascati Laboratory, in analogy with the astronomical definition. AdA (*Anello di Accumulazione*, i.e. storage ring) was an e^+e^- collider and the luminosity (or *source factor*, term initially used) connected the e^+e^- cross-section with the annihilation rate [138].
According to that, the most general definition of luminosity is:

$$\mathscr{L} = \frac{R}{\sigma}[\mathrm{cm}^{-2}\mathrm{s}^{-1}] \tag{A.1}$$

Eq.(A.1) represents the *instantaneous luminosity* defined as the proportionality factor between the event rate R and the cross section σ for a certain process, measured in $\mathrm{cm}^{-2}\mathrm{s}^{-1}$. For a collider, it provides information about its instantaneous performance. It may fluctuate on time scales from tens of nanoseconds to minutes and it tipically decays exponentially, following the law $\mathscr{L} = \mathscr{L}e^{-\frac{t}{\tau}}$. At LHC, τ is $\cong$ 14 h.
The integrated luminosity L is the instaneous luminosity integrated over a certain time interval.

$$L = \frac{\int R dt}{\sigma} = \frac{N}{\sigma} \tag{A.2}$$

where N is the number of produced events for a process with cross section σ, in the integration interval. It is expressed in cm^{-2} or in inverse barns [b^{-1}].
After this general introduction to the concept of luminosity, we can go through the luminosity measurements at ATLAS, with a description of the different approaches used.

A.1.1 Luminosity Measurements in ATLAS

As already explained in Chapter 2, LHC beams are not continuous but consist in *bunches* of synchronous particles. The bunch luminosity can be expressed as:

$$\mathscr{L}_b = \frac{R^b_{inel}}{\sigma_{inel}} \tag{A.3}$$

where R^b_{inel} is the rate of inelastic pp collisions in a certain bunch b (see 2.1.1) and σ_{inel} is the pp inelastic cross section. Eq.(A.3) can be re-written as:

$$\mathscr{L}_b = \frac{\mu_b f_r}{\sigma_{inel}} \tag{A.4}$$

where f_r is the LHC revolution frequency ($\sim$ 11 kHz). The instantaneous luminosity summed on all bunches is:

$$\mathscr{L} = \sum_{n_b} \mathscr{L}_b = \sum_{n_b} \frac{\mu_b f_r}{\sigma_{inel}} \tag{A.5}$$

where n_b is the total number of colliding bunches.
In Eq.(A.4), a new fundamental parameter has been introduced: μ, the average number of inelastic pp interactions per bunch-crossing (BC), also called *pile-up* parameter. What we can conclude from this expression is that the instantaneous luminosity can be determined measuring the ration $\frac{\mu}{\sigma_{inel}}$. Since μ follows the beam degradation formula $\mathscr{L} = \mathscr{L} e^{-\frac{t}{\tau}}$, the luminosity is evaluated in short time periods called *Luminosity Blocks* (LB), in which it can be considered constant. In ATLAS the typical duration of a LB is 60 s.
There are several methods for luminosity measurement which can be divided as follows:

- *Event-Counting* algorithms are based on the determination of the fraction of bunch crossing in which a specified detector registers an "event" satisfying a given selection requirement. For example, a bunch crossing contains an *event* if at least one pp interaction induced at least one observed hit in the luminosity detector.

- *Hit-Counting* algorithms are based on the counting of the number of hits in the luminosity detector. A *hit* can be for example a signal above threshold in a single electronic channel.

- *Particle Counting* algorithms are based on the measurement of quantities proportional to the instaneous particle flux in the detector (e.g., the number of tracks or vertices in the Inner Detector, the energy distribution in the calorimeters, the total ionizing current, etc.).

However, this is a *relative* luminosity determination since the detectors can only measure the average number of visible interactions, μ_{vis} depending on their efficiency and acceptance. Eq.(A.4) can be rewritten as:

$$\mathscr{L} = \frac{\mu_{vis} f_r n_b}{\epsilon \sigma_{inel}} = \frac{\mu_{vis} f_r n_b}{\sigma_{vis}} \tag{A.6}$$

where ϵ is the efficiency for detecting one inelastic pp interaction with the defined selection criteria and σ_{vis} is the *visible* cross section, the calibration constant needed to relate μ_{vis} to the *absolute* luminosity. The calibration parameter depends on the experimental conditions (i.e., colliding particles, the available center of mass energy, the pseudorapidity and the transverse momentum distribution) and on the luminometer and reconstruction algorithm.
At this point, we have made a second important distinction inside the concept of luminosity between the relative and absolute. Both of them are fundamental to convert a rate measurement to a cross section measurement.
The *absolute* luminosity is expressed in an absolute scale through an accurate calibration procedure and it directly enters in the cross section measurement. The *relative* luminosity is essential in the monitoring of relative variations in instantaneous luminosity. Diagnostic procedure with luminosity is really useful also for beam tuning and collision optimization. The overall performance of the collider is monitored keeping under control the long-term evolution of the integrated luminosity, while the *absolute specific luminosity* (luminosity per bunch and per unit bunch intensity, defined in Eq.(A.7)) provides information on beam emittances and collider optics.

$$\mathscr{L}_{spec} = \frac{\mathscr{L}_b}{n_1 n_2} = \frac{f_r}{2\pi\Sigma_x\Sigma_y} \tag{A.7}$$

where n_1 and n_2 are the bunch population, respectively for beam 1 and beam 2, whileΣ_x and Σ_y are the convolved beam widths in the transverse plane (Fig. 2.6).

ATLAS Luminosity Algorithms

The value of μ_{vis} is necessary to determine the luminosity $\mathscr{L}$ within each LB, if these two assumptions are valid:

- the number of pp interactions follows the Poisson statistics;
- the efficiency ϵ_1 to detect a single inelastic pp interaction does not change if, in the same bunch crossing, several interaction occur.

As a consequence, the efficiency ϵ_n for detecting n interactions occurring in the same bunch crossing is:

$$\epsilon_n = 1 - (1 - \epsilon_1)^n \tag{A.8}$$

In most of the experiments operating in a collider, the luminosity detectors consist in two independent parts placed symmetrically with respect to the interaction point: Forwards and Backwards, in ATLAS labelled, respectively, "A" and "C". According to the request on the hits recorded in the two sides, *Event-Counting* algorithms can be divided in two categories: *inclusive* or *coincidence* algorithms.
Event-OR is an inclusive algorithm where a bunch crossing is considered as containing an event if at least one hit is observed in the luminosity detector (either A and C or both). Under the Poissonian assumption, the probability of observing at least one event in one of the two sides is given by:

$$P_{Event-OR}(\mu_{vis}^{OR}) = \frac{N_{OR}}{N_{BC}} = 1 - e^{-\mu_{vis}^{OR}} \tag{A.9}$$

where $\mu_{vis}^{OR} = \mu\epsilon_{OR}$, with ϵ_{OR} being the single interaction detection efficiency of the detector, and N_{OR} the number of bunch-crossings, in a given LB, in which at least one pp collision satisfies the event-selection criteria of the OR algorithm over a total number of bunch-crossings N_{BC} occurred in the same time interval.

Solving Eq.(A.9) for μ_{vis}^{OR}, we get:

$$\mu_{vis}^{OR} = -\ln\left(1 - \frac{N_{OR}}{N_{BC}}\right) \tag{A.10}$$

Event-OR algorithms can be *single-side* or *double-side*, if they distinguish or not between the detector sides in which the hit is detected.
Coincidence algorithms (**Event-AND**) require both sides to record an event in the same bunch-crossing (i.e., within 25 ns at LHC). In this case, the relation between μ_{vis} and N is more complicated with respect to the inclusive algorithm because the AND condition can be satisfied both by single pp interaction or from single hits from different pp collisions in the same bunch crossing. As a consequence, three different efficiencies have to be taken into account: ϵ_A, ϵ_C and ϵ_{AND}, corresponding to having, respectively, at least one hit in the A-side, at least one hit in the the C-side and at least one hit per side. Assuming equal efficiencies and acceptances on the two sides, the probability of recording an AND event is:

$$P_{Event-AND} = \frac{N_{AND}}{N_{BC}} = 1 - 2e^{-\mu(\epsilon^{AND}+\epsilon^{OR})/2} + e^{-\mu\epsilon^{OR}} \tag{A.11}$$

Since this relation cannot be inverted analytically to determine μ_{vis}^{AND}, a numerical inversion has to be performed instead.
Event-counting algorithms loose sensitivity when μ_{vis}»1 because fewer and fewer bunch-crossings report zero observed eventes in a given time interval, implying $\frac{N_{OR}}{N_{BC}} \to 1$, condition that makes Eq.(A.9) no longer usable: this effect is know as *saturation* or *zero starvation*. In such experimental conditions, the *hit-counting* algorithm is used: the number of hits in a given detector is counted rather than just the total number of events. Under the assumption that the number of hits has a *binomial distribution* and the number of interactions per BC follows a poissonian one, the average probability of having a hit per bunch crossing in one of the detector channel can be computed as:

$$P_{HIT}(\mu_{vis}^{HIT}) = \frac{N_{HIT}}{N_{BC}N_{HIT}} = 1 - e^{-\mu_{vis}^{CH}} \tag{A.12}$$

N_{HIT} and N_{BC} are, respectively, the total number of hits and bunch crossins during a certain time interval, while N_{CH} is the number of detector channels, each having an independent probability to record a hit. It is important to underline that the binomial assumtions stands only if the probability to observe a hit in a channel is independent of the number of hits observed in the other channels. It follows that the mean number of interactions is:

$$\mu_{vis}^{HIT} = -\ln\left(1 - \frac{N_{HIT}}{N_{BC}N_{CH}}\right) \tag{A.13}$$

Despite being preferrable to event-counting in high-μ regime, the hit-counting algorithm are more sensitive with respect to the event-counting ones to instrumental effects such as threshold variations, instrumental noise, channel-to-channel efficiency variations, etc.
The validity of the poissonian assumption strictly depends on the condition expressed by Eq.(A.8) which states that the efficiency for detecting an elastic pp interaction is independent of the number of interactions that occur in each bunch crossing or, from a detector point of view, the interactions are independent of each other. Unluckily, this is intrinsically not true when a threshold is set to define a hit (and consequently one event): for example, if two pp interactions occur in the same bunch crossing, both producing signals in the detector individually below threshold but whose sum is above threshold, then the assumption in Eq.(A.8) is violated. The result is that non-linearities appear in the luminosity

measurement with increasing pile-up μ: this effect is known as *migration*. It can be reduced, but never eliminated, by lowering as much as possible the thresholds paying as a price the increase of the effeciency of the algorithm and thus lowering the saturation limit with μ. Migration becomes important in case of high pile-up parameters and, as one can expect, it affects more hit-counting methods than event-counting ones.
Another type of algorithm used is based on the measurement of observables directly proportional to the rate of particles interacting in the detector: the *particle counting algorithms*. These methods are intrinsically free from migration effects, since no threshold is used to define an event or a hit. One of the approaches used by ATLAS is the measurement of the current drawn by the readout PMTs connected to the calorimeters which is proportional to the particle flux inside the layers, which is, in turn, proportional to the luminosity. Other examples are the measurement of the energy deposit in the calorimeters or the track counting inside the inner detector.

ATLAS Online and Offline Algorithms

The online luminosity monitoring are used to provide luminosity information for machine tuning indipendently of the state of the acquisition system. In ATLAS the calculation and publication of instantaneous luminosity data is performed by the *Online Luminosity Calculator* (OLC) and the results are displayed in the ATLAS Control Room and sent to the LHC operators with a frequency of about 0.5 Hz for fast feedback on accelerator tuning. The main task of the OLC is to collect the raw information such as event and hit counts, number of colliding bunches, number of LHC orbits in time interval and then determine μ and luminosity. Due to the small time allowed for online luminosity calculation, no background subtraction is performed. The output are the instantaneous luminosities averaged on the number of colliding BCIDs, computed for all luminosity algorithms.
Most ATLAS detectors provide an LB-averaged luminosity, except for LUCID (see Fig.(A.1)) and BCM whose readout boards provide bunch-by-bunch luminosity information for each LB, as well as the luminosity per LB summed over all colliding BCIDs. For these subsystems,

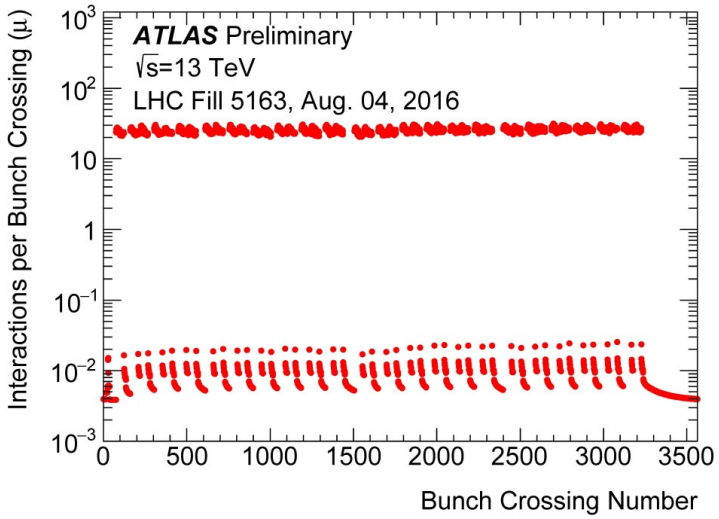

FIGURE A.1: μ measured by LUCID as a function of the bunch-crossing number averaged over the duration of the run, in a physics fill in 2016.

the OLC calculates the *bunch-integrated* luminosity using the following sum over all the colliding BCIDs:

$$\mathscr{L} = \sum_{i \in BCID} \frac{\mu_i^{vis} f_r}{\sigma_{vis}} \tag{A.14}$$

Morover the same algorithms are implemented for the offline analysis, with the advantage of the possibility to perform background subtraction and update with more precise calibrations, when available.

ATLAS Absolute Luminosity Calibration

As anticipated, each luminometer and algorithm must be calibrated to determine its visible cross section σ_{vis} to obtain the absolute luminosity. There are several methods to obtain the calibration constant. ATLAS exploits the beam-separation scans method, by measuring the *beam-overlap area* directly at the IP in dedicated runs in controlled and optimized conditions. It was first proposed by Simon van der Meer at the ISR (*Intersecting Storage Ring* at CERN) [139]. The underlying idea is to measure the parameters of the colliding bunches, namely the transverse dimensions of the beams, by varying the distance between the colliding beams in dedicated *scan sessions*. Once measured the two transverse dimensions σ_{ix} and σ_{iy} (i=1,2) and knowing the number of protons (N_1 and N_2) in the two beams, using:

$$\mathscr{L} = \frac{N_1 N_2 f_r N_b}{2\pi} / \sqrt{\sigma_{1x}^2 + \sigma_{2x}^2} \sqrt{\sigma_{1y}^2 + \sigma_{2y}^2} \tag{A.15}$$

the absolute luminosity at zero beam-separation from the beam parameters can be obtained. By comparing this luminosity with the visible interaction rate μ_{vis}, measured by the luminosity detectors, the calibration constant σ_{vis} is extracted.
Going into details, the bunch luminosity can be expressed in the transverse plane in terms of colliding beam parameters and, in case of *head-on* collisions (i.e., zero crossing angle), see Fig.(A.2), is given by:

$$\mathscr{L} = f_r n_1 n_2 \int \rho_1(x,y)\rho_2(x,y)dxdy \tag{A.16}$$

where $\rho_1(x,y)$ and $\rho_2(x,y)$ are the particles densities in the transverse plane of beam 1

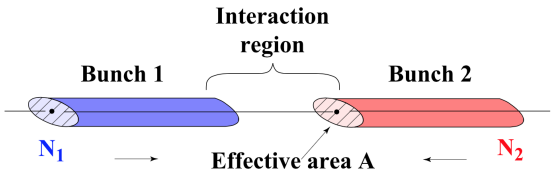

FIGURE A.2: Graphical representation of an head-on collision.

and beam 2, respectively. Assuming that the particle densities may be factorised into independent horizontal and vertical components, Eq.(A.16) becomes:

$$\mathscr{L} = f_r n_1 n_2 \Omega_x(\hat{\rho}_{x1}, \hat{\rho}_{x2}) \Omega_y(\hat{\rho}_{y1}, \hat{\rho}_{y2}) \tag{A.17}$$

where

$$\Omega_x(\hat{\rho}_{x1}, \hat{\rho}_{x2}) = \int \hat{\rho}_{x1}(x)\hat{\rho}_{x2}(x)dx \tag{A.18}$$

$$\Omega_y(\hat{\rho}_{y1}, \hat{\rho}_{y2}) = \int \hat{\rho}_{y1}(y)\hat{\rho}_{y2}(y)dx \tag{A.19}$$

which are the *beam-overlap* integrals in the two transverse directions. Considering the x direction, the integral is:

$$\Omega(\hat{\rho}_{x1}, \hat{\rho}_{x2}) = \frac{R_x(0)}{\int R_x(\delta_x)d\delta_x} \tag{A.20}$$

where $R_x(\delta_x)$ is the visible rate measured by a certain luminosity detector during a x-scan when the two beams are separated, horizontally, by the distance δ_x ($R_x(0)$ is the zero beam separation condition).
Defining the parameter Σ_x as:

$$\Sigma_x = \frac{1}{\sqrt{2\pi}} \frac{\int R_x(\delta_x)d\delta_x}{R_x(0)} \tag{A.21}$$

the bunch luminosity can be written, making the same procedure also for Σ_y, as:

$$\mathscr{L} = \frac{f_r n_1 n_2}{2\pi\Sigma_x\Sigma_y} \tag{A.22}$$

Eq.(A.22) is a general expression from which one can determine the luminosity from machine parameters by performing a pair of beam-separation scans in the x and y. Assuming a Gaussian luminosity curve, Σ_x and Σ_y coincide with the standard deviations of the horizontal and vertical distributions.
Equating the absolute luminosity obtained with this method at the peak of the scan curve to the μ_{vis} obtained by a particular algorithm, the calibration constant will be:

$$\sigma_{vis} = \mu_{vis}^{MAX} \frac{2\pi\Sigma_x\Sigma_y}{n_1 n_2} \tag{A.23}$$

It is important to underline that the van der Meer scan is a completely general calibration method. For example, in the case of non-zero crossing angle the peak luminosity is reduced by the same factor resulting in the cancelation of the increase of the measured value Σ_x by the decrease in the maximum of the distribution.

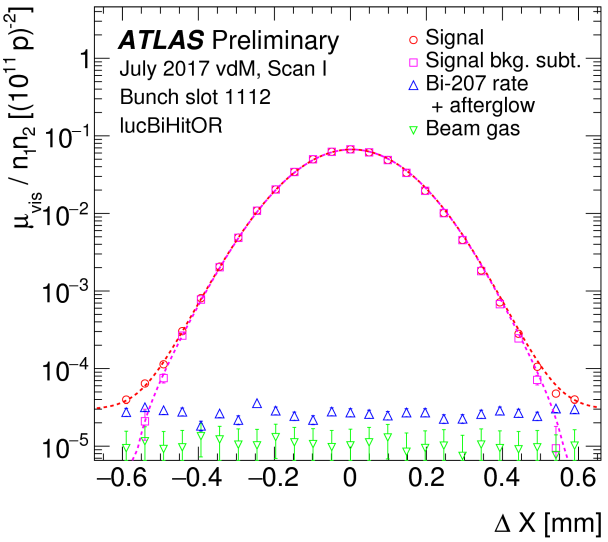

FIGURE A.3: Visible interaction rate per bunch crossing and per unit bunch-population product, for the LUCID algorithm LUCID Bi HitOR that has provided the reference ATLAS luminosity, versus the beam separation ΔX during horizontal scan 1 in the July 2017 luminosity calibration session. The total rate measured for a single colliding bunch pair located at bunch-slot number 1112 in the fill pattern is shown as red circles, and the background-subtracted rate as magenta squares. The background is dominated by random counts from the radioactive Bismuth source used for phototube gain calibration (blue triangles), as estimated from the rate measured in the preceding unfilled bunch slot. Also shown is the beam-gas background (green triangles) measured using non-colliding bunches. The beam-separation values are corrected for orbit-drift and beam-beam deflection effects. The background-subtracted rate is fitted by a Gaussian multiplied by a fourth-order polynomial plus a constant (dashed curve). The error bars are statistical only, and in most cases smaller than the size of the marker [31].

The procedure followed for the van der Meer scan is really time-consuming and challenging. Usually, it consists on the following steps:

- The horizontal scan is performed starting at zero nominal separation and moving to the maximum separation in negative direction, stepping back to zero and again to the maximum in the positive direction. The maximum separation in ATLAS is $6\sigma_b$ and it is scanned in 25 steps. Finally, it returned to the nominal zero separation.
- The same procedure is performed for vertical plane.
- In each of the 25 steps, the beams are left quiescent for about 30 s. In this time interval, relative luminosities are measured and recorded together with nominal separation, beam currents and other relavant accelerator parameters.

The other important quantity to measure is the maximum rate at zero beam separation R^{MAX}, see Fig.(A.3).

$$\sigma_{vis} = \frac{R^{MAX}}{\mathscr{L}^{MAX}} = R^{MAX} \frac{2\pi\Sigma_x\Sigma_y}{n_b f_r (n_1 n_2)^{MAX}} \tag{A.24}$$

Since the measurements in the horizontal and vertical plane are independent, R^{MAX} is the average of R_x^{MAX} and R_y^{MAX}.

A.1.2 ATLAS Luminosity Subdetectors

The ATLAS strategy to understand and control systematic uncertainties affecting the luminosity determination is to compare measurements obtainted from different detectors. The rate of inelastic pp interactions is determined using multiple event and hit counting algorithms as well as particle counting algorithms which exploit different observables.
The main detectors involved in the luminosity measurements can be seen in Fig.(A.4). A

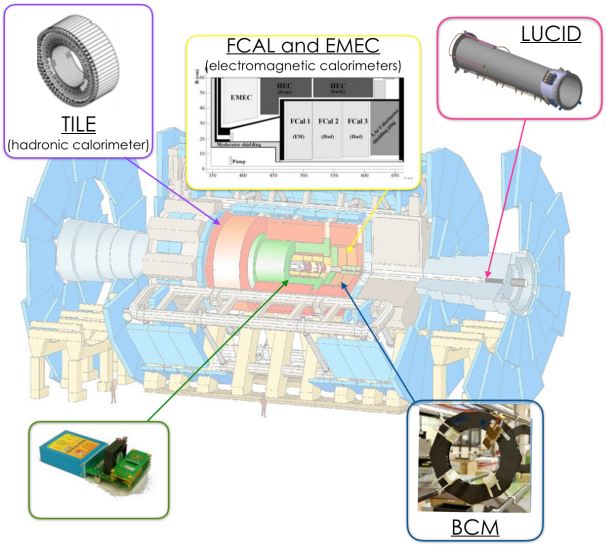

FIGURE A.4: Main ATLAS Luminosity detectors.

reliable luminosity sub-detector must fulfil three main requirements:

- To provide final absolute integrated luminosity values for offline analyses, making it available both for the full data sample and for short periods, implying that it must be measured and provided for each LB. Data are indeed used only if some quality criteria, available LB by LB, are satisfied. For this reason, LB are short in order to not discard too many data. Tipically, they last 1-2 minutes and they are uniquely identified by tags.

- To ensure fast online luminosity monitoring to LHC (1-2 seconds) for efficient beam steering and machine optimisation. Fast luminosity measurements are also used to tune the ATLAS triggers.

- To fast check the running conditions to monitor the structure of the beam and beam-induced backgrounds.

While LUCID, the ATLAS preferred detector, will be described in details in Sec.(A.2), the other detectors providing luminosity to ATLAS will be briefly treated in the following.

Inner Detector

The ATLAS Inner Detector (see 2.3.2) is used to measure the momentum of charged particles in a pseudorapidity range of $|\eta|$<2.5. The main purpose of the ID in terms of luminosity is

to count the primary vertices and the tracks produced in inelastic pp collisions during a LB, exploiting its high efficiency in tracking particles. In ATLAS it is only used as offline measurements.

BCM: Beam Condition Monitor

The main task of the *Beam Condition Monitor* (BCM) is to monitor beam losses and provide fast signals that will abort the beam safely in case of dangerous loss rates [140]. Together with LUCID (as it will be explained later), it is able to provide bunch-by-bunch luminosity measurements. It consists of two sets of four modules mounted symmetrically at a position of $z = \pm 1.84$ m and at a radius of 55 mm with respect to the beam axis, on each side of the interaction point, covering an area of $|\eta|$=4.2. The sensors are made of 500 μm thick radiation hard polycrystalline chemical vapor deposition diamonds and they are mounted with a tilt of 45 degrees with respect to the beam axis. A fast readout enables the measurement on a per-bunch level and allows to measure time of flight and pulse amplitudes. Each signal is splitted into a low and high amplitude channel. The low-level threshold channels have MIP sensitivity and they are suited to luminosity measurements. There are two readout path: one for the four horizontal modules (BCM-H), one for the four vertical ones (BCM-V), leading to two independent luminosity measurement.

Calorimeters

An independent luminosity measurement is performed by the two ATLAS calorimeters, FCAL and TileCal, to provide a cross-check of the stability and non-linearities of the main luminosity subdetectors (see 2.3.4). The current drawn in TileCal modules and across the liquid argon gaps in FCal modules are used, since they are directly proportional to the particle fluxes across the calorimeters, proportional to the luminosity. The measurements are performed over each LB. A detailed description of the two calorimeters is given in Chapter2.

A.2 LUCID-2 Detector

LUCID is the only ATLAS detector dedicated enterely to luminosity measurements. After the Run1 shutdown, it was redesigned in order to cope with new demanding experimental conditions imposed by Run2.
The old LUCID-1 has been used during the years 2009-2013 [33]. It consisted of two stations placed symmetrically with respect to the interaction point, at z=17 m. Each station was made of twenty 150 cm long Cherenkov detectors, consisting of aluminum tubes with 14 mm diameter, pointing towards the interaction region, filled with a radiation gas, C_4F_{10}, and read-out by photomultipliers PMTs. The light produced in it was collected in two different ways. The original LUCID-1 detector was designed to measure luminosity with a 5% precision up to a $\mu \leq 10$. As the μ-value was increased up to 20 in 2011, *migration* effects were noted causing a spoiling in luminosity determination. At the same time, it was observed that the particles produced enough Cherenkov light for sizeable signals, when crossing the 1.2 mm quartz windows. As a consequence the detector was operated without gas for almost all the 2011 data-taking and for the entire 2012.
This was the very first step towards the new LUCID-2 detector, as it will be explained.
The main reasons which lead to a complete redesign were:

- the LHC machine peak instaneous luminosity increase by a factor about two, from 0.77×10^{34} cm^{-2}s^{-1} for Run1 to 1.7×10^{34} cm^{-2}s^{-1} in Run2. The expected larger pileup would increase the migration and in addition some event counting algorithms were already close to saturation, or already saturated during Run1.

- the change of the LHC beam pipe material from stainless steel to aluminium. Monte Carlo simulation suggested that this would have increased the number of particles hitting LUCID by a factor of 4, impacting on luminosity algorithm saturation.
- the bunch spacing reduction from 50 ns to 25 ns called a new electronics to keep the signal duration lower than this.

For these reasons, during the long shutdown between 2013 and 2015, the LUCID-1 had been removed and it was decided to built a new LUCID-2 detector, which could meet the challenges of LHC Run2 and beyond.

A.2.1 LUCID-2 Design

LUCID-2 has been designed in 2013, installed in 2014 and commissioned in 2015 [49]. The requirements for the new detector were:

- the stability over a wide luminosity range (an average number of interaction per bunch crossing going from 10^{-3} up to 100), over a full year data-taking and in different running condition, indipendently of the type of accelerated particles, filling bunch scheme, bunch spacing, etc.
- radiation hardness to cope with the expected dose of $\sim$ 200 kGy in the full Run2.
- fast read-out electronics in order to cope with the reduced time separation between colliding bunches (from 50 ns to 25 ns) and able to provide information bunch-by-bunch and every 60 s (i.e., per LB).

LUCID-2 consists in two modules (named A and C, following the ATLAS naming convention) placed symmetrically around the beam pipe, at 17 m from the interaction point. Each module is installed on a carbon fibre cylindrical support tube surrounding the LHC beam-pipe, at a radial distance of about 10 cm from it. Fig.(A.5) shows one of the two LUCID-2 modules with the 2016 configuration. As can be seen, the active part of the detector can be divided into two groups [141]:

- The PMT detector. Four groups of PMTs per side, acting like independent detectors:
  - Bi-detector. Four Hamamatsu R760 PMTs with quartz window acting like Cherenkov medium, with a radius of 10 mm, equipped with liquid ^{207}Bi radioactive sources for gain monitoring purposes.
  - Bi2-detector. Same as Bi-detector.
  - Modified detector. Four PMTs with quartz window's radius reduced to 7 mm. Their acceptance has been reduced with the insertion of an aluminum layer masking an external ring shaped portion of the photocatode. In 2016, they were connected to the LED and laser system for the gain monitoring.
  - Spare detector. Four Hamamatsu R760 PMTs with a quartz window with radius of 10 mm used as spares in case of malfunctioning of the other ones.
- The Fiber detector. Four bundles of quartz fibers used as Cherenkov medium, read out by four PMTs, placed in a lower radiation area. The subsystem is connected to the LED and Laser system for the gain monitoring and read-out by PMTs of the same type as the other parts.

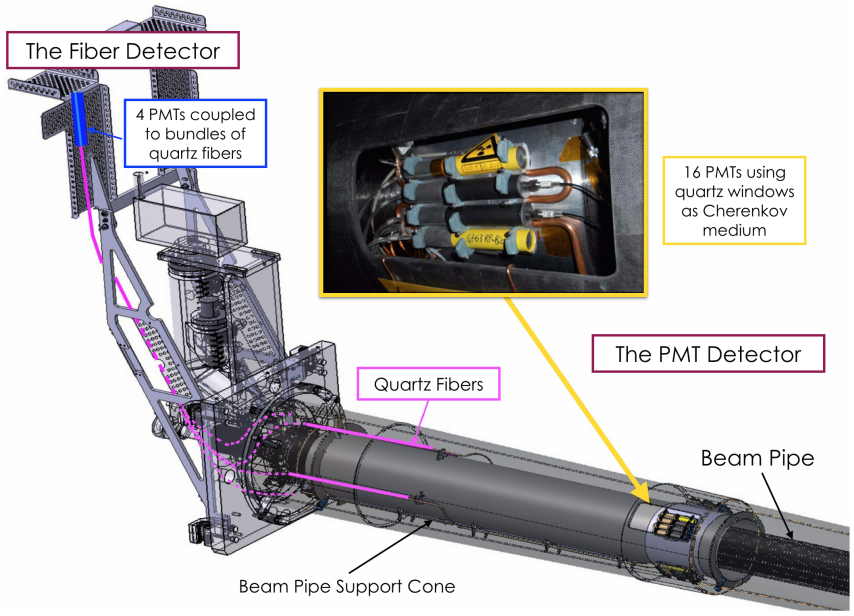

FIGURE A.5: Sketch of one module of LUCID-2 detector, with its main component enlightened.

A peculiarity of this new design is the novel and original gain monitoring system based on the ^{207}Bi radioactive sources, which will be explained in details in the following sections. It is important to underline that, during, the 2015 data-taking, it became clear that this system was superior to the LED calibration leading to the decision to equip all the PMTs with radioactive sources and therefore the LED system was dismissed except than for the fibers detector.
LUCID-2 exploits the PMT quartz window as Cherenkov medium and, knowing that its thickness is 1.2 mm, the Cherenkov kinetic energy threshold is about 175 keV. Charged particles crossing the window produce light, converted into an electrical signal in the PMT cathode and amplified by the dynode chain with a typical gain G$\sim 10^5$. Eventually, a measurable signal is produced. Analogously, quartz fibers act as Cherenkov radiators.
Since LUCID-2 is placed in a high radiation area, several studies have been done to test the PMT radiation hardness. The expected upper limit of radiation dose and neutron flux was, respectively, 200 kGy and 2.6×10^{14} n/cm^2. The PMTs have been exposed to two types of radiation:

- γ radiation from the CALLIOPE ^{60}Co source at ENEA [142].
- TAPIRO neutron facility at Enea [143].

The results lead to the conclusion that, despite the increase of dark current, there was no impact on signal shape or PMT gain. Also quartz fiber, PMT-bases and cables were irradiated and no degradation of their performances was observed.

A.2.2 LUCID Electronics

The main innovation of the new LUCID-2 electronics has been the insertion of four (two per side) custom-made VME boards called LUCROD (*LUCid Read-Out Driver*), which were entirely designed in the Electronic Laboratories of the Bologna section of the INFN. The board is schematically represented in Fig.(A.6).
A LUCROD board features 16 lemo analog inputs (each receiving the signal from 1 PMT), 16

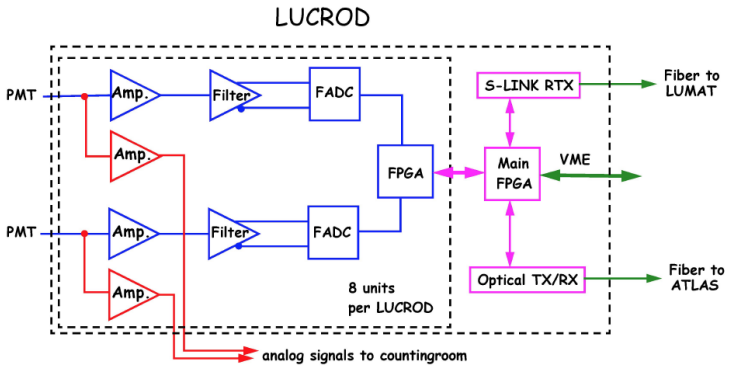

FIGURE A.6: Block diagram of the LUCROD board

lemo analog outputs, four lemo digital input/output for triggering and debugging purposes, a TTCrq to receive external synchronization signals and optical transceivers to deliver digital information. Thanks to the TTCrq, its internal clocks can be aligned with the ATLAS 40 MHz clock. Each LUCROD input is preamplified up to a factor of 16 by two independent and programmable amplifiers, one serving the analog output and one feeding a 320 MHz Flash-Analog-to-Digital Converter (FADC) with a 12-bit resolution for a 1.5 V dynaminc range.
It hosts one group of eight channel FPGAs directly connected to the inputs. In the time window of a BCID period (25 ns, corresponding to 8 clock samples), digitized inputs are summed over to provide charge information, while the maximum height is compared to a programmable threshold to define hits. While charge and hits information are accumulated in 3564-slot FIFOs, 64 samples of the digitized waveforms are made available for VME readout upon the presence of a trigger, electable between a programmable portion of the LHC orbit or the presence of a hit. This readout step allows the monitoring of the data stream with a sampling, available for each PMT waveform.
The other two FPGAs, receive charges and hits from programmable combination of the channel FPGAs, providing charge-sums, hit-sums and events sums on a BCID basis. In addition, they transmit hits to the output transceiver that feeds optical fibers connected to the other type of board, the LUMAT.
The LUCROD boards are placed about 15 m away from the photomultipliers. They are connected to them by thick and fast high-performance cables in order to avoid the signal dispersion before digitization. In such a way, the signal duration is guaranteed to be below 25 ns, the LHC bunch spacing, as can be seen in Fig.(A.7) which shows a typical ^{207}Bi signal, recorded by a LUCROD board. Since the LUCRODs are placed near to the PMTs, they are not

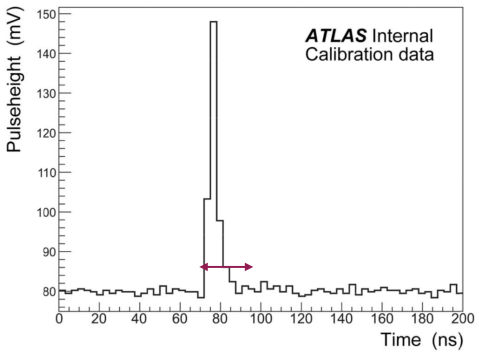

FIGURE A.7: ^{207}Bi signal recorded by a LUCROD board. As can be seen, the duration of the signal is within 25 ns, LHC bunch spacing duration.

accessible during LHC running periods. A dedicated firmware has been developed to allow reloading and changing the firmware itself, a feature necessary to recover from Single Event Upset (SEU).
The two LUMAT are 9U VME boards developed by the Bologna INFN group, as well as the

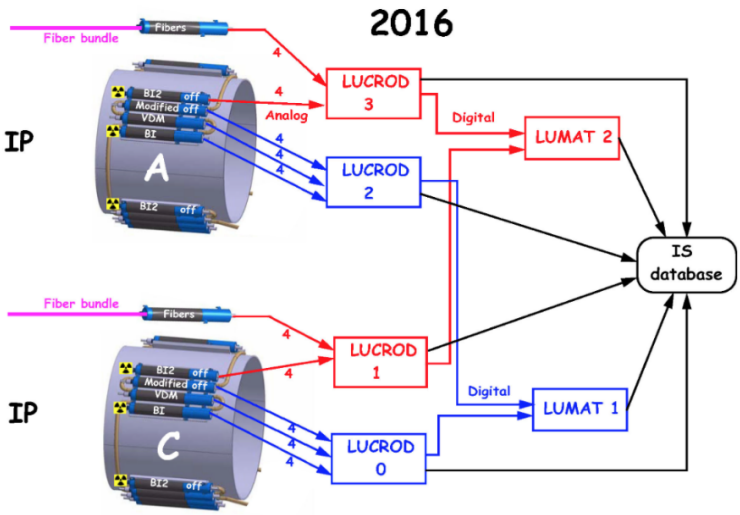

FIGURE A.8: Scheme of the LUCID electronics.

LUCRODs, and they are placed 100 m away from the detector. While the LUCROD board evaluates luminosity for single channel as well for single-side OR algorithms, the LUMAT provides luminosity measurements based on the correlation among the two sides, since it receives hits from both sides. The cumulated data read at the end of each LB is provided for further elaboration to the Information Service (IS) where data remain available for the online calculation. Fig.(A.8) shows the scheme of the LUCID electronics.

A.2.3 LUCID-2 Luminosity Algorithms

The methods generally used to measure luminosity have been already explained in A.1.1. LUCID-2 exploits both Event/Hit-counting algorithms and particle flow algorithms. LUCID Event and Hit counting algorithms are chosen according to the μ - range. Moreover, thanks to the LUCROD boards, it is possible to count the number of hits in individual PMTs which can definitely act as independent detectors.
The most important innovation for LUCID-2 in term of luminosity calculation is the *charge algorithms* implementation. This method is based on measuring the integral of photomultiplier pulses. The measured quantity Q_{TOT} is the sum of the integrals of all pulses during a luminosity block both from individual and several photomultipliers. Q_{TOT} is proportional to the luminosity, meaning that it is immune from migration effects and independent of the Poisson assumption (see A.1.1). However, charge algorithm are more sensitive to the background due to the absence of a threshold and to photomultiplier gain changes, which have to be kept under control through a reliable gain monitoring system (see A.2.4).

A.2.4 LUCID Gain Monitoring System

An essential part of providing a precise luminosity measurement is the use of a reliable method to monitor the photomultipliers gain stability over a year's running. Initially, three independent systems were designed, each exploiting a different technology and applied to

a different set of photomultipliers.
Initially, 16+16 PMTs were fed with both LED and laser light, carried by quartz optical fibers, while 4+4 were equipped with ^{207}Bi radioactive sources that produce, via internal conversion, electrons above the Cherenkov threshold in the quartz windows. Calibrations runs are performed at the end of each LHC fill to evaluate gain changes caused by the charge produced in the dynode chain. A change of 5% in gain reflects in a 1% change in the luminosity measured by hit algorithms and in a 5% change for the charge algorithms. Fig.(A.9) shows a schematic view of the two systems for one module, as it was in 2015. In the following, both the systems will be described with particular attention to the one based on radioactive sources.
My main involvement in LUCID activities during my PHD has focused on the development and the maintenance of a code for the daily monitoring of the PMTs gain stability.
The gain monitoring dedicated runs are performed before and after each physics fill, as will be explained in the next sections. The data are coherently recorded on DCS (2.3.8). My code takes them as input and analyzes charge, amplitude and high voltage values for single PMTs. The data are scaled, year per year, to a reference run typically performed at the beginning of the data taking. The offline analysis allowed to spot possible instabilities from single sensors and to perform data-quality monitoring and performance studies of the sensors. The results obtained from this analysis have been crucial both to understand which gain monitoring system had the better performance and to draw conclusion about which algorithm was more reliable for online and offline luminosity measurements.
Fig.A.10, A.13, A.14 are trend plots obtaining from my analysis of the calibration data.

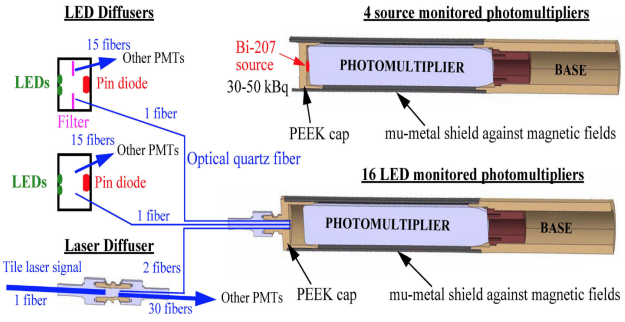

FIGURE A.9: Schematic view of the two different gain monitoring system in 2015.

The LED and Laser System

The LEDs are pulsed at the LHC orbit frequency and it can produce large signals in the PMTs. During the calibration runs, the mean value of the amplitude and the charge of the signals are used to monitor the gain stability and to allow the automatic correction by readjustments to the PMT high voltage. PIN-diodes are used to monitor LED intrinsic stability and possible light intensity fluctuations and to correct he observed signal in the PMTs. The omogeneous distribution of the light to all PMTs is ensured by a diffuser which allows a simultaneous illumination. A ring-shaped filter is placed inside the diffuser in front of the PMT calibration fibers to solve the issue due to the different sensitivity to light of the PIN-diode and the PMT, i.e. the light must be intense enough for the former but small enough for the latter to not saturate the readout electronics. The LED light is carried by fibers inserted to the PMT window through a connector. However during the data-taking, it became clear that such connectors were a major source of background, due to the material activation induced by the particle fluxes. In Fig.(A.10) the stability of the LED light monitored by

the PIN-diode is shown. As can be seen, after a drop of about 4%, a good stability has been kept for all the 2016 data-taking. As it regards the LASER system, the light is provided by the ATLAS Tile calorimeter calibration system with the monitoring of the light stability (no need for additional monitoring with PIN-diodes). Also in this case, a cylindrical diffuser was designed to distribute the light to all PMTs but collimated, contrary to the one for the LED light. It connects the single larger fiber coming from the LASER source to the bundle of smaller fibers going to PMTs, all arranged in circular geometry. Two fibers, one in the very central part of the bundle and one in the peripheral part, are used to provide light to a single PMT because the light is not radially constant. Due to the problems induced by the

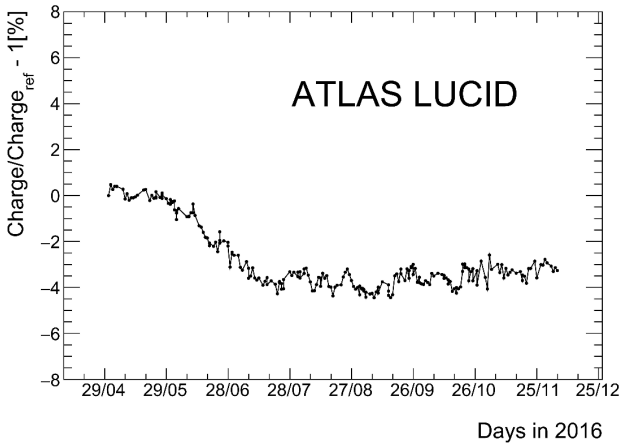

FIGURE A.10: LED light stability as monitored by PIN-diode during the 2016 data-taking. The plot has been obtained using my analysis code.

LED fiber connection and to non-fully understood results of the calibrations the LED/Laser system was abandoned towards the Bi-based calibration system (see next paragraph) with the exception of the fibers detector.

The ^{207}Bi system

The gain monitoring system based on radioactive sources of ^{207}Bi is completely new and it was used for the first time in LUCID. ^{207}Bi produces, via internal conversion (see Fig.(A.11)), electrons with an energy of 482, 554, 566, 976, 1048 or 1060 keV, all above the Cherenkov threshold in quartz. However only electrons with an energy above 900 keV can penetrate the full quartz window before being stopped. Moreover, ^{207}Bi half-time is 33 years which means that the source will not change rate significantly during the detector lifetime. Radioactive sources were obtained from the Oak Ridge laboratory (USA), while the application over the PMT windows was made at the radiological laboratory in Alberta University (Canada).

The advantage on such a method is that is free from possible instabilities of input light and from degradation of the optical fibers transporting it, since the ^{207}Bi is directly deposited on the PMT quartz window. It do not suffer from the issue of the background induced by material activation, as it is for the LED system. In addition, as can be seen from Fig.(A.12), the amplitude distribution of electrons from internal conversion is really similar to the one from LHC interactions as so is the wavelength of the photons being from Cherenkov light as the ones from particles coming from collisions. This is a particularly important feature which is not satisfied by the LED calibration system.

A critical parameter to be considered is the activity of the source because it has to be large enough to allow calibration runs and to provide enough statistics in a reasonable time,

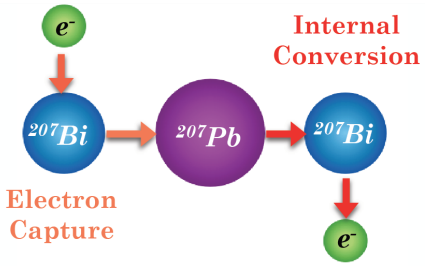

FIGURE A.11: ^{207}Bi internal conversion.

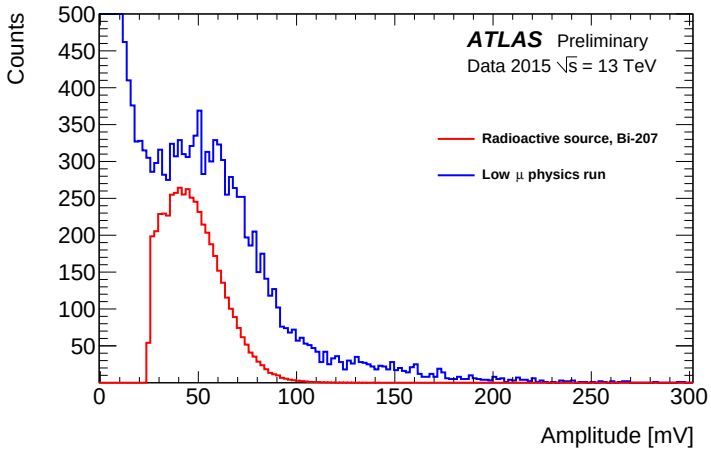

FIGURE A.12: Pulse-height distributions from a LUCID photomultiplier recorded in a 13 TeV run (blue) and in a calibration run (red) in 2015 data-taking.

but not too large to not spoil luminosity measurement during the usual data-taking. The omnipresent background from Bismuth was proved to be not worrisome during high luminosity operation but problems could arise when performing special runs in low luminosity conditions (van der Meer scans, high-β^* runs). To meet these requirements, a typical activity between 30 and 45 kBq (corresponding to a dose rate at 3 cm of 3.5 and 5.5 μSv/h) has been used.

The mean charge and the mean amplitude of signals are measured for each sensor and the values are used to estimate the PMT gain trend. In case of deviation from the reference value defined at the beginning of the data-taking, an automatic procedure varies the PMT high voltage to compensate.

This system has proved itself so successfull during the 2015/2016 data-taking that at the start of 2017, all the PMTs have been equipped with radioactive sources, with only the PMTs in the FIBER detector monitored with LED and LASER signals. In Fig.(A.13), the charge deviation relative to a reference run as a function of time for the 2016 for the Bismuth gain monitoring runs is shown, as obtained by the analysis I performed with the calibration code. The procedure has kept the mean charge constant over a whole running period and the gain decrease of 5% after a long LHC fill had been properly recovered by the HV adjustements.

However, the continuous increase of the high voltage had as a consequence a change in signal shape and in the ratio between signal charge and signal amplitude, giving sizeable effects on the efficiency of some of the luminosity algorithms. Looking at Fig.(A.14), which reports the ratio between charge and amplitude as a function of days in 2016, it can be seen that the HV increase has caused a 5% decrease of the ratio. All these features highlighted by the offline analysis of calibration data was used to optimize the calibration procedure as

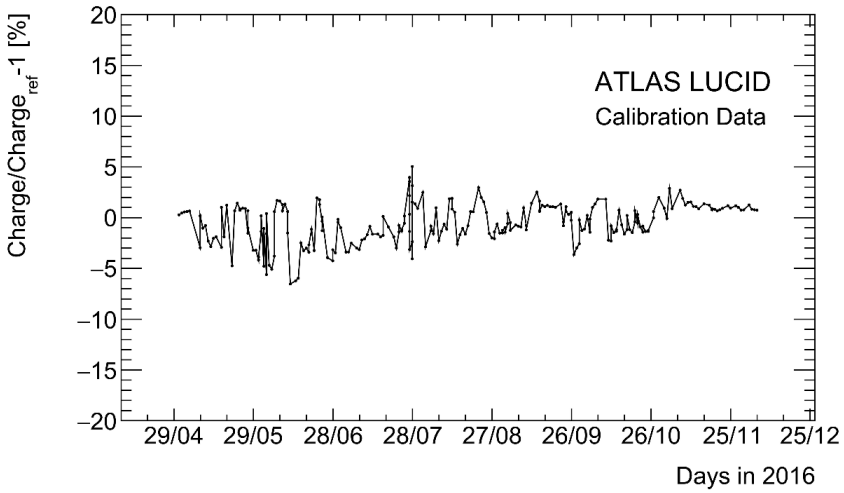

FIGURE A.13: Percentage variation of the measured mean charge relative to a reference run for one of the Bi-monitored photomultipliers in the 2016 data-taking. The plot has been obtained using my analysis code.

described below.

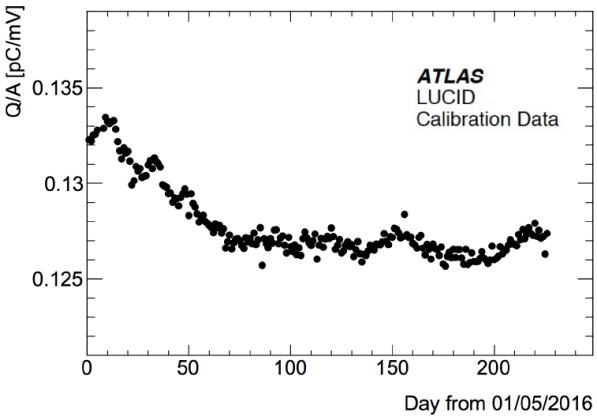

FIGURE A.14: Charge-Amplitude ratio as a function of days in 2016. The plot has been obtained using my analysis code.

Such a difference in the ratio as a function of the HV means that there is a difference in the HV adjustement depending if one tries to keep the charge or the amplitude constant. For this reason, in 2017 it has been decided that the quantity to be monitored during Bismuth sessions was the amplitude, since the main LUCID luminosity algorithms are based on counting hits over threshold, i.e. the number of times the amplitude of a signal is above that threshold.

A.3 Luminosity Measurements during Run 2

During the Run2 data-taking, the peak instantaneous luminosity has increased from 5×10^{33} $cm^{-2}s^{-1}$ to 20.1 $\times10^{33}$ $cm^{-2}s^{-1}$, as can be seen from Fig.(A.15) which shows the peak instantaneous luminosities, averaged per bunch crossing for 2015, 2016, 2017 and 2018. The

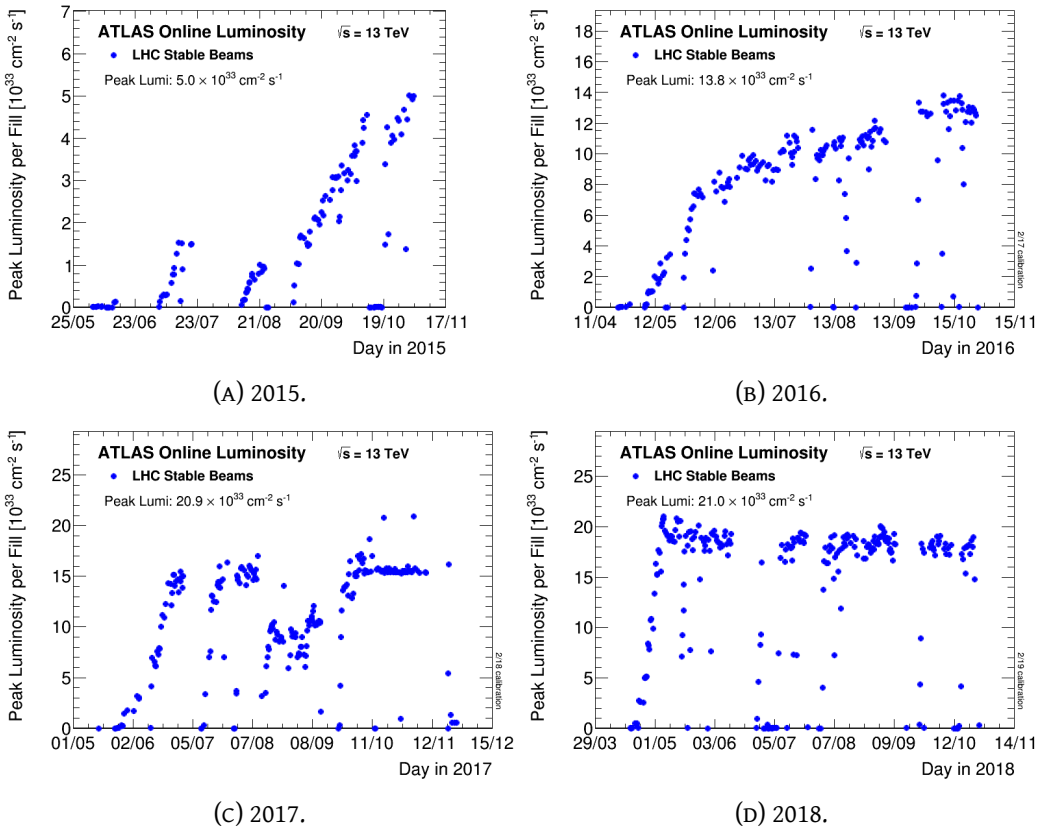

(A) 2015. (B) 2016.

(C) 2017. (D) 2018.

FIGURE A.15: The peak instantaneous luminosity delivered to ATLAS during stable beams for pp collisions at 13 TeV centre-of-mass energy shown as a function of time for 2015 (A), 2016 (B), 2017 (C) and 2018 (D) data-taking.

increase in peak instantaneous luminosity has corresponded to an increase in the average number of interactions per bunch crossing μ from 28 up to $\sim$ 80, as can be seen from Fig.(A.16) which shows average μ per fill as a function of time for the 2015, 2016, 2017, 2018 data-taking. For all the period, LUCID has been the reference detector for luminosity measurments with LUCID HitOR-Bi as preferred online and offline algorithm.
As anticipated, the ATLAS strategy for luminosity measurement is redundant with the comparison between LUCID with the calorimeters and the Inner Detector. The long term stability is monitored by the ratio between the values provided by the different luminometers. Fig.(A.17) shows the fractional difference in run-integrated luminosity between LUCID HitOR, used as reference, and TILE, EMEC, FCAL and track-counting algorithms, as a function of the cumulative delivered luminosity for 2016 and 2017 data-taking. Each point corresponds to an ATLAS run recorded with 25 ns bunch-running in 2016 and 2017 at $\sqrt{s}$ = 13 TeV. The luminosity measurements by TILE, EMEC, FCal and Tracking have been normalized to a physics run recorded on August 4th for 2016 and on July 29th for 2017 (both indicated by red arrows). In Fig.(A.18), the fractional difference in run-integrated luminosity between LUCID PMT-C12 algorithm and the TILE, EMEC, FCal and track-counting is shown as a function of the cumulated delivered luminosity (normalized to the total delivered in 2018). As said in A.2.1, single LUCID PMT sensors act as independent detector. In 2018 a significant number of PMTs stopped working during the course of the data-taking year, a single PMT on the C-side (C12) was used for the baseline luminosity measurements, because it showed good stability and gave similar results to the HitOR algorithm from the combination of the remaining seven working PMTs. Each point corresponds to an ATLAS run recorded during 25 ns bunch-train running in 2018 at $\sqrt{s}$=13 TeV. The luminosity measurements by TILE,

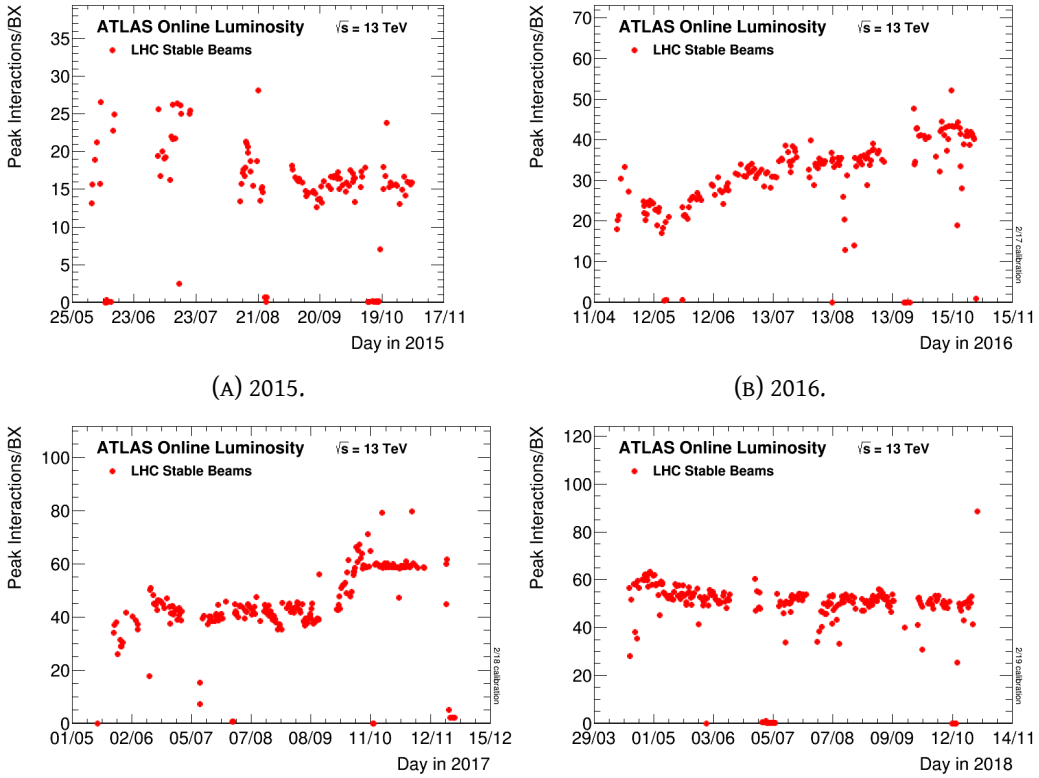

(A) 2015.

(B) 2016.

(C) 2017.

(D) 2018.

FIGURE A.16: The maximum number of inelastic collisions per bunch crossing during stable beams for pp collisions at 13 TeV centre-of-mass energy shown as a function of time for 2015 (A), 2016 (B), 2017 (C) and 2018 (D) data-taking. Luminosity measurements have been used to determine the number of interactions per bunch crossing as $\mu = \mathscr{L}_b \times \sigma_{inel}/f_r$ where $\mathscr{L}_b$ is the per-bunch instantaneous luminosity, σ_{inel} is the inelastic cross section at 13 TeV (taken to be 80 mb) and f_r is the LHC revolution frequency of 11.245 kHz. The number of interactions shown is averaged over all colliding bunch pairs and only the peak value for each fill is shown.

EMEC, FCal and Tracking have been normalized to LUCID in a reference run recorded on July 16th.

The long term stability uncertainty has been evaluated conservatively by considering a stability band which encloses the differences between LUCID and any of the other luminosity measurements. This lead to $\pm$1%, $\pm$0.7%, $\pm$1.3% amd $\pm$0.8% respectively for 2015, 2016, 2017 and 2018 data taking periods.

The long-term stability is one of the components of the overall systematic uncertainty on the luminosity measurement, together with the one related to the van der Meer scan procedure ($\sim<$ 2%), the calibration transfer due to the transition from low μ (during the dedicated calibration runs) to high μ (physics runs), typically of the order of 1%. A preliminary overall uncertainty on $\mathscr{L}$ of about 2% was achieved in each of the four years of Run2.

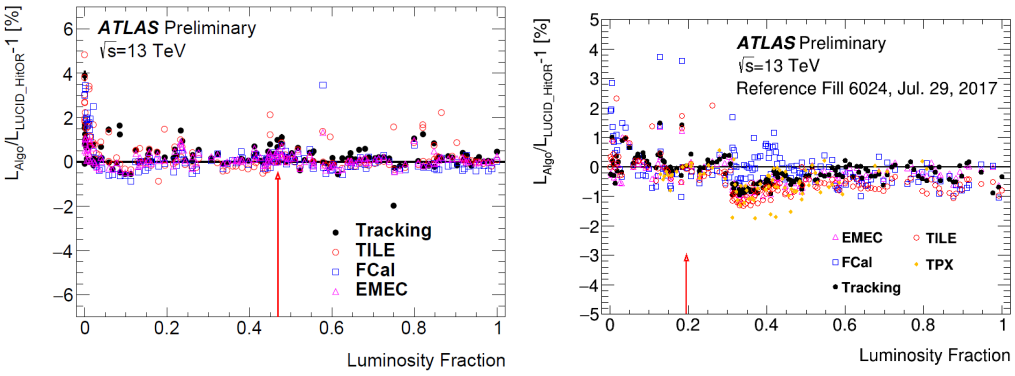

(A) 2016. (B) 2017.

FIGURE A.17: Results on time-stability of the luminosity measurements for 2016 and 2017 data-taking.

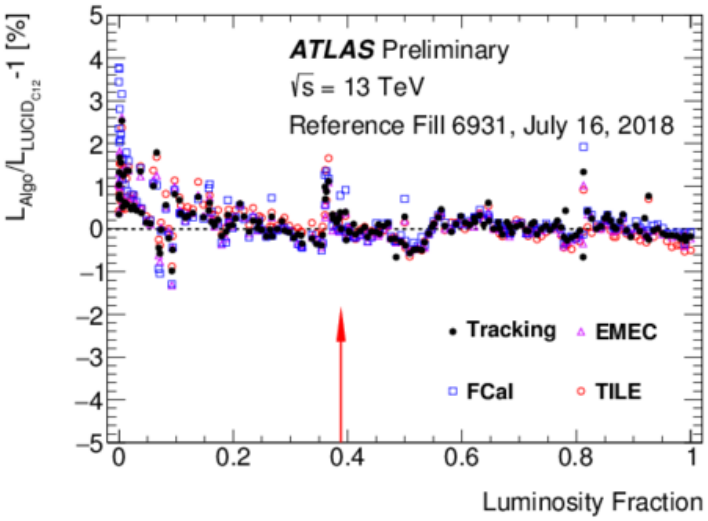

FIGURE A.18: Preliminary results on time-stability of the luminosity measurements for 2018 data-taking.

Conclusions

The Higgs boson property measurements are of great interest at LHC. In particular, the study of Higgs boson production and decays plays a key role in the confirmation the theoretical framework of the Standard Model. Among them, the Higgs decay in 2 b-quarks covers an high importance since its observation directly proves the Higgs coupling to the quark sector. In the context of this thesis, the $H \to b\bar{b}$ decay is studied in the Higgs production mode in association with a vector boson $V = Z, W$. Despite being the third production mode in terms of rate, it is the most promising channel because of the gain in accuracy of the measurement thanks to the clear signature of the final state coming from the leptonic decay of the vector boson, especially in the case of $Z \to \ell^+\ell^-$. In fact, the clear peak of the Z boson made accessible additional p_T^V phase space regions, helping to increase the statistics, and allows an almost complete rejection of the multi-jet background. A confirmation is given by the *template* fit to the residual QCD background in the $Z(Z \to \ell^+\ell^-)H$ channel, where it has been found that this source of background is negligible.
The analysis is performed in parallel in three channels, divided by the number of charged leptons in the final state coming from the vector W/Z boson decay. For each of them, the event phase space is splitted according to the vector boson transverse momentum and to the jet multiplicity. The Higgs boson is reconstructed from exactly two b-tagged jets in the final state.
In each of the resulting signal regions, a multivariate analysis is performed to provide *boosted decision tree* classifiers as input to a binned profile likelihood fit (PFL) performed on data and Monte Carlo samples to extract the signal strength, which is defined as $\mu_{VH} = \sigma_{obs}/\sigma_{SM}$, i.e. the ratio between the observed and Standard Model predicted cross section for the VH processes.
The choice of a MVA strategy is driven by the fact that an high accuracy is needed in signal and background discrimination, since the VH channel is highly affected by background sources which, as a consequence, have to be determined as precisely as possible. The main sources of background for the analysis are $Z + HF$, $t\bar{t}$ and $W + HF$ and they enter the PFL fit as floating normalization, meaning that they are determined from the fit to data thanks to high statistics used. However, a crucial part of the analysis is the assessment of the backgroung related systematic uncertainties, entering the fit to provide a better constraint to the background normalization.

- As we have seen, the systematic uncertainties related to background are highly dominated by the theoretical uncertainties. One of my contributions to the 79.8 fb^{-1} analysis has concerned the determination of the uncertainties related to different phase-space acceptance and flavour compositions of the jets for the $Z + HF$ background, which is irreducible for the 2-lepton channel, by comparing the nominal Monte Carlo event generator with several internal variations and an alternative simulator.

The first measurement presented in this thesis has been performed with data collected by the ATLAS detector at a center of mass energy of $\sqrt{s}$=13 TeV. The data were collected during 2015, 2016 and 2017 data-taking corresponding to an integrated luminosity of 79.8 fb^{-1}. The

analysis, performed in the three different analysis channels, has produced the following results:

$$\mu_{ZH\to\nu\nu b\bar{b}} = 1.04^{+0.34}_{-0.32} \quad \text{with an observed significance of } 3.3\sigma(\text{exp.}3.1\sigma)$$

$$\mu_{WH\to\ell\nu b\bar{b}} = 1.09^{+0.46}_{-0.42} \quad \text{with an observed significance of } 2.6\sigma(\text{exp. } 2.4\sigma)$$

$$\mu_{ZH\to\ell\ell b\bar{b}} = 1.38^{+0.46}_{-0.42} \quad \text{with an observed significance of } 3.4\sigma(\text{exp. } 2.6\sigma)$$

while the signal strength coming from the combined analysis in the three channels is:

$$\mu_{VH(H\to b\bar{b})} = 1.16^{+0.27}_{-0.26} \quad \text{exp. } 4.9\sigma(\text{exp. } 4.3\sigma)$$

The MVA and fit strategy have been validated performing two orthogonal analysis:

- Dijet analysis as validation of fit procedure, with result:

$$\mu_{VH(H\to b\bar{b})} = 1.06^{+0.36}_{-0.33} = 1.06 \pm 0.20(stat.)^{+0.30}_{-0.26}(sys.)$$

- Diboson analysis as validation of the MVA analysis, with result:

$$\mu_{VZ(Z\to b\bar{b})} = 1.20^{+0.20}_{-0.18} = 1.20 \pm 0.08(stat.)^{+0.19}_{-0.16}(sys.)$$

Three combinations, with different data-set, has been also performed:

1. The results obtained from the 13 TeV analysis has been combined with the ones obtained at 7 and 8 TeV in Run1. The measured signal strenght is:

$$\mu_{VH(H\to b\bar{b})} = 0.98^{+0.22}_{-0.21} = 0.98 \pm 0.14(stat.)^{+0.17}_{-0.16}(sys) \tag{A.25}$$

   with an observed significance of 4.9σ (with respect to an expectation of 5.1σ).

2. The results obtained for $H \to b\bar{b}$ decay obtained in the VH analysis has been combined with the ones obtained from other production modes, $t\bar{t}H$ and VBF, for Run1 and Run2 data. The combination measures the ratio of the branching fraction of the Higgs boson into b-quarks to the Standard Model predictions, constraining the cross sections of the production modes to be as predicted. The observed significance for $H \to b\bar{b}$ is 5.4σ, compared to expectation of 5.5σ. The corresponding signal strenght is:

$$\mu_{H\to b\bar{b}} = 1.01 \pm 0.20 = 1.01 \pm 0.12(stat.)^{+0.16}_{0.15}(sys.)$$

3. The third combination is performed combining the VH analysis result with the ones obtained during Run2 for others decay modes, namely $H \to \gamma\gamma$ and $H \to ZZ^*$. The observed significance for the VH production is 5.3σ, with respect to an expected of 4.8. The result for signal strength is:

$$\mu_{VH(H\to b\bar{b},4\ell,\gamma\gamma)} = 1.13^{+0.24}_{-0.23} = 1.13 \pm 0.15(stat.)^{+0.15}_{-0.17}(sys.) \tag{A.26}$$

   The importance of this last combinations lies in the fact that it has allowed to observe for the first time the Higgs associated production with a vector boson.

An iteration of the $VH(H \to b\bar{b})$ analysis is currently on going exploiting the Full Run 2 statistics, corresponding to an integrated luminosity of 139 fb^{-1}.
The main purpose of the iteration of the analysis is to obtain an even more precise result in terms of signal strength and significance for the observation of $H \to b\bar{b}$ decay and VH

production. Although the general strategy of the analysis is the same described above, several changes have been introduced in order to obtain an even better sensitivity to signal. In this context, I have studied the performances of various isolation working points for the leptons. The new isolation working points, which applies fixed cut on calorimeter and track information, has proved to increase the Monte Carlo statistics in signal sample generation. An additional cut at 250 GeV has been applied to study the high p_T^V region (p_T^V<150 GeV) which is the most sensitive to new physics event. Even more precise results in this region can provide a further confirmation of the Standard Model or possibly point to new physics. Another innovation worked on regards the b-tagging strategy which has a high relevance since it is a crucial point for Higgs candidate reconstruction. A *hybrid* truth tagged approach has been chosen, over the *full truth* method used as default for the previous analysis.
Performance MVA studies have been carried to test the effects of these two changes in three analysis channel and I personally carried the studies for 2-lepton channel. These studies have been crucial in the definition of the more effective MVA strategy.
The analysis is still on going but the preliminary result of the fit on the Asimov dataset shows that the expected significance is of about 6.6σ, looking really promising for the further step, consisting in a profile likelihood fit on data and Monte Carlo samples with the full Run2 statistics.

Due to the non-Abelian nature of the QCD, it is not possible to apply a perturbative approach in the soft part calculation of the inelastic interactions, resulting in a lack of the theory in predicting the total proton-proton cross section evolution with energy. This can be circumvented using very general principles such as the Optical Theorem and the Dispersion Relations: the first one connects the total hadronic cross section with the forward scattering amplitude, while the second one provides a relation between the real and the imaginary part of the scattering amplitude (considered as a complex analytic function in the scattering theory). The two of them combined together help us to have a relation called *one-subtracted dispersion relation* which allows us to make predictions on σ_{tot} by means of estimating ρ (defined as the real to imaginary part of the forward elastic scattering amplitude), which is sensitive to σ_{tot} evolution with energy well above the energy at which it is calculated, and *viceversa*. However, the recent TOTEM measurements of ρ obtained at 13 TeV, by fitting the Coulomb-Nuclear Interference region at small angles, have changed the paradigm since lower values have been observed with respect to the predictions from dispersion relations. There are two possibilities to explain it:

1. the form of the dispersion relations used until now are no longer valid and this may suggest the existence of the Odderon exchange.

2. some change occurs in the energy-dependence of σ_{tot} behaviour above LHC energy range.

The second scenario is the one I studied using both very simple approaches and model-based methods, under the assumption that the low ρ values can be explained without the Odderon presence. The study is still on goind but as can be seen from the preliminary results, an alternative explanation, with respect to the Odderon existence, of the TOTEM measurements is possible, at least qualitatively, in the context of dispersion relations.

Finally a description of my technical work within the luminosity measurement with the LUCID detector is described. My contribution in this context has been to develop and mantain the code aimed to analyze the LUCID calibration data, needed to both keep constant

the operating conditions of the detector (PMT-gain) so to ensure an appropriate long-term stability of the luminosity measurement and to study the detectors performances.

Bibliography

[1] M. et al. Tanabashi. "Review of Particle Physics". In: *Phys. Rev. D* 98 (3 2018), p. 030001. DOI: 10.1103/PhysRevD.98.030001. URL: https://link.aps.org/doi/10.1103/PhysRevD.98.030001.

[2] Francis Halzen and Alan Martin. *Quarks & Leptons: An introductory course in modern particle physics*. New York, USA: John Wiley & Sons, 1984.

[3] O Nachtmann. *Elementary particle physics: concepts and phenomena*. Texts and monographs in physics. Trans. of : Phänomena und Konzepte der Elementarteilchenphysik, publ. by Vieweg Verlag. Berlin: Springer, 1990. DOI: 10.1007/978-3-642-61281-7. URL: https://cds.cern.ch/record/114154.

[4] Alexandre Deur, Stanley Jerome Brodsky, and Guy F. de Téramond. "The QCD Running Coupling". In: 2016.

[5] Donald Hill Perkins. *Introduction to high energy physics; 4th ed.* Cambridge: Cambridge Univ. Press, 2000. DOI: 10.1017/CBO9780511809040. URL: https://cds.cern.ch/record/396126.

[6] Claude Cohen-Tannoudji, Jacques Dupont-Roc, and Gilbert Grynberg. *Photons and atoms: introduction to quantum electrodynamics*. Trans. of : Photons et atomes. Paris, InterEditions, 1987. New York, NY: Wiley, 1989. URL: https://cds.cern.ch/record/113864.

[7] Peter W. Higgs. "Broken Symmetries and the Masses of Gauge Bosons". In: *Phys. Rev. Lett.* 13 (16 1964), pp. 508–509. DOI: 10.1103/PhysRevLett.13.508. URL: https://link.aps.org/doi/10.1103/PhysRevLett.13.508.

[8] F. Englert and R. Brout. "Broken Symmetry and the Mass of Gauge Vector Mesons". In: *Phys. Rev. Lett.* 13 (9 1964), pp. 321–323. DOI: 10.1103/PhysRevLett.13.321. URL: https://link.aps.org/doi/10.1103/PhysRevLett.13.321.

[9] T W B Kibble. "Spontaneous symmetry breaking in gauge theories". In: *Philos. Trans. R. Soc. Lond. A* 373.2032 (2014), 20140033. 12 p. DOI: 10.1098/rsta.2014.0033. URL: https://cds.cern.ch/record/2295084.

[10] G. Aad et al. "Measurements of Higgs boson production and couplings in diboson final states with the ATLAS detector at the LHC". In: *Physics Letters B* 726.1-3 (2013), 88–119. ISSN: 0370-2693. DOI: 10.1016/j.physletb.2013.08.010. URL: http://dx.doi.org/10.1016/j.physletb.2013.08.010.

[11] "Combination of standard model Higgs boson searches and measurements of the properties of the new boson with a mass near 125 GeV". In: (2013).

[12] "Search for the Standard Model Higgs boson at LEP". In: *Physics Letters B* 565 (2003), pp. 61 –75. ISSN: 0370-2693. DOI: https://doi.org/10.1016/S0370-2693(03)00614-2. URL: http://www.sciencedirect.com/science/article/pii/S0370269303006142.

[13] S. Dittmaier et al. "Handbook of LHC Higgs Cross Sections: 1. Inclusive Observables". In: (2011). DOI: 10.5170/CERN-2011-002. arXiv: 1101.0593 [hep-ph].

[14] S. Dittmaier et al. “Handbook of LHC Higgs Cross Sections: 2. Differential Distributions”. In: (2012). DOI: 10.5170/CERN-2012-002. arXiv: 1201.3084 [hep-ph].

[15] J R Andersen et al. “Handbook of LHC Higgs Cross Sections: 3. Higgs Properties”. In: (2013). Ed. by S Heinemeyer et al. DOI: 10.5170/CERN-2013-004. arXiv: 1307.1347 [hep-ph].

[16] D. de Florian et al. “Handbook of LHC Higgs Cross Sections: 4. Deciphering the Nature of the Higgs Sector”. In: (2016). DOI: 10.2172/1345634, 10.23731/CYRM-2017-002. arXiv: 1610.07922 [hep-ph].

[17] *LHC Higgs Cross Section Working Group*. URL: https://twiki.cern.ch/twiki/bin/view/LHCPhysics/LHCHXSWG.

[18] H. M. Georgi et al. “Higgs Bosons from Two-Gluon Annihilation in Proton-Proton Collisions”. In: *Phys. Rev. Lett.* 40 (11 1978), pp. 692–694. DOI: 10.1103/PhysRevLett.40.692. URL: https://link.aps.org/doi/10.1103/PhysRevLett.40.692.

[19] D. Graudenz, M. Spira, and P. M. Zerwas. “QCD corrections to Higgs-boson production at proton-proton colliders”. In: *Phys. Rev. Lett.* 70 (10 1993), pp. 1372–1375. DOI: 10.1103/PhysRevLett.70.1372. URL: https://link.aps.org/doi/10.1103/PhysRevLett.70.1372.

[20] S. Dawson. “Radiative corrections to Higgs boson production”. In: *Nucl. Phys.* B359 (1991), pp. 283–300. DOI: 10.1016/0550-3213(91)90061-2.

[21] V. Ravindran, J.ohn Smith, and W. Neerven. “NNLO corrections to the total cross section for Higgs boson production in hadron-hadron collisions”. In: *Nuclear Physics B - NUCL PHYS B* 665 (Feb. 2003). DOI: 10.1016/S0550-3213(03)00457-7.

[22] Charalampos Anastasiou et al. “High precision determination of the gluon fusion Higgs boson cross-section at the LHC”. In: *JHEP* 05 (2016), p. 058. DOI: 10.1007/JHEP05(2016)058. arXiv: 1602.00695 [hep-ph].

[23] M. Carena and H.E. Haber. “Higgs Boson theory and phenomenology”. In: *Progress in Particle and Nuclear Physics* 50.1 (2003), 63–152. ISSN: 0146-6410. DOI: 10.1016/s0146-6410(02)00177-1. URL: http://dx.doi.org/10.1016/S0146-6410(02)00177-1.

[24] W. Beenakker et al. “Higgs radiation off top quarks at the Tevatron and the LHC”. In: *Phys. Rev. Lett.* 87 (2001), p. 201805. DOI: 10.1103/PhysRevLett.87.201805. arXiv: hep-ph/0107081 [hep-ph].

[25] Philipp Maierhöfer and Andreas Papaefstathiou. “Higgs Boson pair production merged to one jet”. In: *JHEP* 03 (2014), p. 126. DOI: 10.1007/JHEP03(2014)126. arXiv: 1401.0007 [hep-ph].

[26] A. DJOUADI. “HIGGS PARTICLES AT FUTURE HADRON AND ELECTRON-POSITRON COLLIDERS”. In: *International Journal of Modern Physics A* 10.01 (1995), pp. 1–63. DOI: 10.1142/S0217751X95000024. eprint: https://doi.org/10.1142/S0217751X95000024. URL: https://doi.org/10.1142/S0217751X95000024.

[27] Emidio Gabrielli et al. “Higgs boson production in association with a photon in vector boson fusion at the LHC”. In: *Nuclear Physics B* 781.1-3 (2007), 64–84. ISSN: 0550-3213. DOI: 10.1016/j.nuclphysb.2007.05.010. URL: http://dx.doi.org/10.1016/j.nuclphysb.2007.05.010.

[28] M. Aaboud et al. “Search for the Standard Model Higgs boson produced by vector-boson fusion and decaying to bottom quarks in s = 8

$$\sqrt{s} = 8$$

TeV pp collisions with the ATLAS detector". In: *Journal of High Energy Physics* 2016.11 (2016). ISSN: 1029-8479. DOI: 10.1007/jhep11(2016)112. URL: http://dx.doi.org/10.1007/JHEP11(2016)112.

[29] *Search for Higgs boson production via weak boson fusion and decaying to $b\bar{b}$ in association with a high-energy photon in the ATLAS detector*. Tech. rep. ATLAS-CONF-2016-063. Geneva: CERN, 2016. URL: http://cds.cern.ch/record/2206201.

[30] The CDF Collaboration et al. *Updated Combination of CDF and D0 Searches for Standard Model Higgs Boson Production with up to 10.0 fb-1 of Data*. 2012. arXiv: 1207.0449 [hep-ex].

[31] *Luminosity Public Results Run-2*. URL: https://twiki.cern.ch/twiki/bin/view/AtlasPublic/LuminosityPublicResultsRun2.

[32] *Luminosity determination in pp collisions at $\sqrt{s} = 13$ TeV using the ATLAS detector at the LHC*. Tech. rep. ATLAS-CONF-2019-021. Geneva: CERN, 2019. URL: http://cds.cern.ch/record/2677054.

[33] G. Aad et al. "The ATLAS Experiment at the CERN Large Hadron Collider". In: *JINST* 3 (2008), S08003. DOI: 10.1088/1748-0221/3/08/S08003.

[34] G. Aad et al. "The ATLAS Inner Detector commissioning and calibration". In: *The European Physical Journal C* 70.3 (2010), 787–821. ISSN: 1434-6052. DOI: 10.1140/epjc/s10052-010-1366-7. URL: http://dx.doi.org/10.1140/epjc/s10052-010-1366-7.

[35] F. Hügging. "The ATLAS Pixel Insertable B-layer (IBL)". In: *Nuclear Instruments and Methods in Physics Research Section A: Accelerators, Spectrometers, Detectors and Associated Equipment* 650.1 (2011), 45–49. ISSN: 0168-9002. DOI: 10.1016/j.nima.2010.12.113. URL: http://dx.doi.org/10.1016/j.nima.2010.12.113.

[36] *ATLAS magnet system: Technical Design Report, 1*. Technical Design Report ATLAS. Geneva: CERN, 1997. URL: https://cds.cern.ch/record/338080.

[37] Djamel Eddine Boumediene. *ATLAS calorimeters: Run-2 performances and Phase-II upgrades*. Tech. rep. ATL-CAL-PROC-2017-001. Geneva: CERN, 2017. DOI: 10.22323/1.314.0485. URL: https://cds.cern.ch/record/2288402.

[38] Henric Wilkens and the ATLAS LArg Collaboration. "The ATLAS Liquid Argon calorimeter: An overview". In: *Journal of Physics: Conference Series* 160 (2009), p. 012043. DOI: 10.1088/1742-6596/160/1/012043. URL: https://doi.org/10.1088%2F1742-6596%2F160%2F1%2F012043.

[39] Ana Maria Henriques Correia. *The ATLAS Tile Calorimeter*. Tech. rep. ATL-TILECAL-PROC-2015-002. Geneva: CERN, 2015. DOI: 10.1109/ANIMMA.2015.7465554. URL: https://cds.cern.ch/record/2004868.

[40] *ATLAS muon spectrometer: Technical Design Report*. Technical Design Report ATLAS. Geneva: CERN, 1997. URL: https://cds.cern.ch/record/331068.

[41] Adele Rimoldi. "The ATLAS muon trigger chamber system". In: *Nuclear Instruments and Methods in Physics Research Section A: Accelerators, Spectrometers, Detectors and Associated Equipment* 409.1 (1998), pp. 669 –674. ISSN: 0168-9002. DOI: https://doi.org/10.1016/S0168-9002(97)01348-X. URL: http://www.sciencedirect.com/science/article/pii/S016890029701348X.

[42] *L1 Muon Trigger Public Results*. URL: https://twiki.cern.ch/twiki/bin/view/AtlasPublic/L1MuonTriggerPublicResults.

[43] U Bratzler. "The ATLAS muon precision chamber system11This paper is based on a talk presented on behalf of the ATLAS Muon Collaboration (CERN, Geneva, Switzerland)." In: *Nuclear Instruments and Methods in Physics Research Section A: Accelerators, Spectrometers, Detectors and Associated Equipment* 409.1 (1998), pp. 29 –32. ISSN: 0168-9002. DOI: https://doi.org/10.1016/S0168-9002(97)01228-X. URL: http://www.sciencedirect.com/science/article/pii/S016890029701228X.

[44] N. Soni. *ATLAS Forward Detectors and Physics*. 2010. arXiv: 1006.5426 [hep-ex].

[45] ATLAS Collaboration. "ATLAS Forward Detectors". General Photo. 2018. URL: https://cds.cern.ch/record/2627582.

[46] Bruschi, M. "Diffraction and Forward Physics in ATLAS: results and perspectives". In: *EPJ Web of Conferences* 90 (2015), p. 06003. DOI: 10.1051/epjconf/20159006003. URL: https://doi.org/10.1051/epjconf/20159006003.

[47] S. Roesler, R. Engel, and J. Ranft. "The Monte Carlo Event Generator DPMJET-III". In: *Advanced Monte Carlo for Radiation Physics, Particle Transport Simulation and Applications* (2001), 1033–1038. DOI: 10.1007/978-3-642-18211-2_166. URL: http://dx.doi.org/10.1007/978-3-642-18211-2_166.

[48] G. Aad et al. "Rapidity gap cross sections measured with the ATLAS detector in pp collisions at $\sqrt{s} = 7$ TeV". In: *The European Physical Journal C* 72.3 (2012). ISSN: 1434-6052. DOI: 10.1140/epjc/s10052-012-1926-0. URL: http://dx.doi.org/10.1140/epjc/s10052-012-1926-0.

[49] G. Avoni et al. "The new LUCID-2 detector for luminosity measurement and monitoring in ATLAS". In: *JINST* 13.07 (2018), P07017. DOI: 10.1088/1748-0221/13/07/P07017.

[50] Peter Jenni, Marzio Nessi, and Markus Nordberg. *Zero Degree Calorimeters for ATLAS*. Tech. rep. CERN-LHCC-2007-001. LHCC-I-016. Geneva: CERN, 2007. URL: https://cds.cern.ch/record/1009649.

[51] S. Abdel Khalek et al. "The ALFA Roman Pot detectors of ATLAS". In: *Journal of Instrumentation* 11.11 (2016), P11013–P11013. ISSN: 1748-0221. DOI: 10.1088/1748-0221/11/11/p11013. URL: http://dx.doi.org/10.1088/1748-0221/11/11/P11013.

[52] G. Aad et al. "Measurement of the total cross section from elastic scattering in pp collisions ats=7 TeVwith the ATLAS detector". In: *Nuclear Physics B* 889 (2014), 486–548. ISSN: 0550-3213. DOI: 10.1016/j.nuclphysb.2014.10.019. URL: http://dx.doi.org/10.1016/j.nuclphysb.2014.10.019.

[53] Morad Aaboud et al. "Measurement of the total cross section from elastic scattering in pp collisions at $\sqrt{s} = 8$ TeV with the ATLAS detector". In: *Phys. Lett.* B761 (2016), pp. 158–178. DOI: 10.1016/j.physletb.2016.08.020. arXiv: 1607.06605 [hep-ex].

[54] S. Grinstein. "The ATLAS Forward Proton Detector (AFP)". In: *Nuclear and Particle Physics Proceedings* 273-275 (2016). 37th International Conference on High Energy Physics (ICHEP), pp. 1180 –1184. ISSN: 2405-6014. DOI: https://doi.org/10.1016/j.nuclphysbps.2015.09.185. URL: http://www.sciencedirect.com/science/article/pii/S2405601415006744.

[55] "The ATLAS Data Acquisition and High Level Trigger system". In: *Journal of Instrumentation* 11.06 (2016), P06008–P06008. DOI: 10.1088/1748-0221/11/06/p06008. URL: https://doi.org/10.1088%2F1748-0221%2F11%2F06%2Fp06008.

[56] Aranzazu Ruiz-Martinez and ATLAS Collaboration. *The Run-2 ATLAS Trigger System*. Tech. rep. ATL-DAQ-PROC-2016-003. Geneva: CERN, 2016. DOI: 10.1088/1742-6596/762/1/012003. URL: https://cds.cern.ch/record/2133909.

[57] K Lantzsch et al. "The ATLAS Detector Control System". In: *Journal of Physics: Conference Series* 396.1 (2012), p. 012028. DOI: 10.1088/1742-6596/396/1/012028. URL: https://doi.org/10.1088%2F1742-6596%2F396%2F1%2F012028.

[58] M. Aaboud et al. "Electron reconstruction and identification in the ATLAS experiment using the 2015 and 2016 LHC proton–proton collision data at $\sqrt{s}$ = 13 TeV". In: *The European Physical Journal C* 79.8 (2019). ISSN: 1434-6052. DOI: 10.1140/epjc/s10052-019-7140-6. URL: http://dx.doi.org/10.1140/epjc/s10052-019-7140-6.

[59] Nicolas Maximilian Koehler et al. *Muon Efficiency Measurements on the Full Run 2 dataset*. Tech. rep. ATL-COM-PHYS-2019-176. Geneva: CERN, 2019. URL: https://cds.cern.ch/record/2665704.

[60] N. Eldik et al. "The ATLAS muon spectrometer: calibration and pattern recognition". In: (Jan. 2006).

[61] M. Aaboud et al. "Performance of missing transverse momentum reconstruction with the ATLAS detector using proton–proton collisions at $\sqrt{s}$=13 TeV". In: *The European Physical Journal C* 78.11 (2018). ISSN: 1434-6052. DOI: 10.1140/epjc/s10052-018-6288-9. URL: http://dx.doi.org/10.1140/epjc/s10052-018-6288-9.

[62] Gavin P. Salam. "Towards jetography". In: *The European Physical Journal C* 67.3-4 (2010), 637–686. ISSN: 1434-6052. DOI: 10.1140/epjc/s10052-010-1314-6. URL: http://dx.doi.org/10.1140/epjc/s10052-010-1314-6.

[63] Matteo Cacciari, Gavin P Salam, and Gregory Soyez. "The anti-ktjet clustering algorithm". In: *Journal of High Energy Physics* 2008.04 (2008), 063–063. ISSN: 1029-8479. DOI: 10.1088/1126-6708/2008/04/063. URL: http://dx.doi.org/10.1088/1126-6708/2008/04/063.

[64] Steven Schramm. "ATLAS Jet Reconstruction, Energy Scale Calibration, and Tagging of Lorentz-boosted Objects". In: (2017). URL: https://cds.cern.ch/record/2284807.

[65] *Tagging and suppression of pileup jets*. Tech. rep. ATL-PHYS-PUB-2014-001. Geneva: CERN, 2014. URL: https://cds.cern.ch/record/1643929.

[66] G. Aad et al. "Performance of pile-up mitigation techniques for jets in pp collisions at $\sqrt{s} = 8$ TeV using the ATLAS detector". In: *The European Physical Journal C* 76.11 (2016). ISSN: 1434-6052. DOI: 10.1140/epjc/s10052-016-4395-z. URL: http://dx.doi.org/10.1140/epjc/s10052-016-4395-z.

[67] Pádraig Cunningham and Sarah Jane Delany. *k-Nearest Neighbour Classifiers*. 2007.

[68] D. Schouten, A. Tanasijczuk, and M. Vetterli. *ATLAS Jet Energy Scale*. 2012. arXiv: 1201.2429 [hep-ex].

[69] Atlas Collaboration. "Performance of b-Jet Identification in the ATLAS Experiment". In: 2015.

[70] *Expected performance of the ATLAS b-tagging algorithms in Run-2*. Tech. rep. ATL-PHYS-PUB-2015-022. Geneva: CERN, 2015. URL: https://cds.cern.ch/record/2037697.

[71] M. Aaboud et al. "Observation of $H \to b\bar{b}$ decays and VH production with the ATLAS detector". In: *Physics Letters B* 786 (2018), 59–86. ISSN: 0370-2693. DOI: 10.1016/j.physletb.2018.09.013. URL: http://dx.doi.org/10.1016/j.physletb.2018.09.013.

[72] M. Aaboud et al. "Evidence for the $H \to b\bar{b}$ decay with the ATLAS detector". In: *Journal of High Energy Physics* 2017.12 (2017). ISSN: 1029-8479. DOI: 10.1007/jhep12(2017)024. URL: http://dx.doi.org/10.1007/JHEP12(2017)024.

[73] Glen Cowan et al. "Asymptotic formulae for likelihood-based tests of new physics". In: *The European Physical Journal C* 71.2 (2011). ISSN: 1434-6052. DOI: 10.1140/epjc/s10052-011-1554-0. URL: http://dx.doi.org/10.1140/epjc/s10052-011-1554-0.

[74] C. Oleari. "The POWHEG BOX". In: *Nuclear Physics B - Proceedings Supplements* 205-206 (2010), 36–41. ISSN: 0920-5632. DOI: 10.1016/j.nuclphysbps.2010.08.016. URL: http://dx.doi.org/10.1016/j.nuclphysbps.2010.08.016.

[75] Torbjörn Sjöstrand. *The PYTHIA Event Generator: Past, Present and Future*. 2019. arXiv: 1907.09874 [hep-ph].

[76] Enrico Bothmann et al. "Event generation with Sherpa 2.2". In: *SciPost Physics* 7.3 (2019). ISSN: 2542-4653. DOI: 10.21468/scipostphys.7.3.034. URL: http://dx.doi.org/10.21468/SciPostPhys.7.3.034.

[77] Manuel Bähr et al. "Herwig++ physics and manual". In: *The European Physical Journal C* 58.4 (2008), 639–707. ISSN: 1434-6052. DOI: 10.1140/epjc/s10052-008-0798-9. URL: http://dx.doi.org/10.1140/epjc/s10052-008-0798-9.

[78] Johan Alwall et al. "MadGraph 5: going beyond". In: *Journal of High Energy Physics* 2011.6 (2011). ISSN: 1029-8479. DOI: 10.1007/jhep06(2011)128. URL: http://dx.doi.org/10.1007/JHEP06(2011)128.

[79] S. Agostinelli et al. "GEANT4: A Simulation toolkit". In: *Nucl. Instrum. Meth.* A506 (2003), pp. 250–303. DOI: 10.1016/S0168-9002(03)01368-8.

[80] Jon Butterworth et al. "PDF4LHC recommendations for LHC Run II". In: *Journal of Physics G: Nuclear and Particle Physics* 43.2 (2016), p. 023001. ISSN: 1361-6471. DOI: 10.1088/0954-3899/43/2/023001. URL: http://dx.doi.org/10.1088/0954-3899/43/2/023001.

[81] *ATLAS simulation of boson plus jets processes in Run 2*. Tech. rep. ATL-PHYS-PUB-2017-006. Geneva: CERN, 2017. URL: https://cds.cern.ch/record/2261937.

[82] M. Aaboud et al. "Measurements of b-jet tagging efficiency with the ATLAS detector using $t\bar{t}$ events at $\sqrt{s}$=13 TeV". In: *Journal of High Energy Physics* 2018.8 (2018). ISSN: 1029-8479. DOI: 10.1007/jhep08(2018)089. URL: http://dx.doi.org/10.1007/JHEP08(2018)089.

[83] Pushpa Bhat. "Multivariate Analysis Methods in Particle Physics *". In: *Annual Review of Nuclear and Particle Science* 61 (Nov. 2011), pp. 281–309. DOI: 10.1146/annurev.nucl.012809.104427.

[84] A. Hoecker et al. *TMVA - Toolkit for Multivariate Data Analysis*. 2007. arXiv: physics/0703039 [physics.data-an].

[85] Tilmann Gneiting and Peter Vogel. *Receiver Operating Characteristic (ROC) Curves*. 2018. arXiv: 1809.04808 [stat.ME].

[86] Stefano Catani et al. "QCD Matrix Elements + Parton Showers". In: *Journal of High Energy Physics* 2001.11 (2001), 063–063. ISSN: 1029-8479. DOI: 10.1088/1126-6708/2001/11/063. URL: http://dx.doi.org/10.1088/1126-6708/2001/11/063.

[87] Tatsuya Masubuchi et al. *Search for a Standard Model Higgs boson produced in association with a vector boson and decaying to a pair of b-quarks*. Tech. rep. ATL-COM-PHYS-2016-1724. Geneva: CERN, 2016. URL: https://cds.cern.ch/record/2235437.

[88] G. Aad et al. "Search for the Standard Model Higgs boson produced in association with top quarks and decaying into b in pp collisions at $\sqrt{s}$ = 8 TeV with the ATLAS detector". In: *The European Physical Journal C* 75.7 (2015). ISSN: 1434-6052. DOI: 10.1140/epjc/s10052-015-3543-1. URL: http://dx.doi.org/10.1140/epjc/s10052-015-3543-1.

[89] M. Aaboud et al. "Search for the standard model Higgs boson produced in association with top quarks and decaying into a $b\bar{b}$ pair in pp collisions at $\sqrt{s}$=13 TeV with the ATLAS detector". In: *Physical Review D* 97.7 (2018). ISSN: 2470-0029. DOI: 10.1103/physrevd.97.072016. URL: http://dx.doi.org/10.1103/PhysRevD.97.072016.

[90] *Measurements of the Higgs boson production, fiducial and differential cross sections in the 4ℓ decay channel at $\sqrt{s}$=13 TeV with the ATLAS detector*. Tech. rep. ATLAS-CONF-2018-018. Geneva: CERN, 2018. URL: http://cds.cern.ch/record/2621479.

[91] *Measurements of Higgs boson properties in the diphoton decay channel using 80 fb^{-1} of pp collision data at $\sqrt{s}$ = 13 TeV with the ATLAS detector*. Tech. rep. ATLAS-CONF-2018-028. Geneva: CERN, 2018. URL: http://cds.cern.ch/record/2628771.

[92] G. Aad et al. "Search for the $b\bar{b}$ decay of the Standard Model Higgs boson in associated (W/Z)H production with the ATLAS detector". In: *Journal of High Energy Physics* 2015.1 (2015). ISSN: 1029-8479. DOI: 10.1007/jhep01(2015)069. URL: http://dx.doi.org/10.1007/JHEP01(2015)069.

[93] *Combined measurements of Higgs boson production and decay using up to 80 fb^{-1} of proton-proton collision data at $\sqrt{s}$ = 13 TeV collected with the ATLAS experiment*. Tech. rep. ATLAS-CONF-2018-031. Geneva: CERN, 2018. URL: http://cds.cern.ch/record/2629412.

[94] Johan Bijnens. "CHIRON: a package for ChPT numerical results at two loops". In: *The European Physical Journal C* 75.1 (2015). ISSN: 1434-6052. DOI: 10.1140/epjc/s10052-014-3249-9. URL: http://dx.doi.org/10.1140/epjc/s10052-014-3249-9.

[95] Evgenij Martynov and Basarab Nicolescu. "Discovery of the Odderon by TOTEM experiments and the FMO approach". In: *EPJ Web of Conferences* 206 (2019). Ed. by A. Yang et al., p. 06001. ISSN: 2100-014X. DOI: 10.1051/epjconf/201920606001. URL: http://dx.doi.org/10.1051/epjconf/201920606001.

[96] *Atti. Congr. Intern. Fis.,Como,2,545,(1927)*.

[97] R. de L. Kronig. "On the Theory of Dispersion of X-Rays". In: *J. Opt. Soc. Am.* 12.6 (1926), pp. 547–557. DOI: 10.1364/JOSA.12.000547. URL: http://www.osapublishing.org/abstract.cfm?URI=josa-12-6-547.

[98] R. Kronig. "A supplementary condition in Heisenberg's theory of elementary particles". In: *Physica* 12.8 (1946), pp. 543 –544. ISSN: 0031-8914. DOI: https://doi.org/10.1016/S0031-8914(46)80078-8. URL: http://www.sciencedirect.com/science/article/pii/S0031891446800788.

[99] M. Gell-Mann, M. L. Goldberger, and W. E. Thirring. "Use of Causality Conditions in Quantum Theory". In: *Phys. Rev.* 95 (6 1954), pp. 1612–1627. DOI: 10.1103/PhysRev.95.1612. URL: https://link.aps.org/doi/10.1103/PhysRev.95.1612.

[100] P. Söding. "Real part of the proton-proton and proton-antiproton forward scattering amplitude at high energies". In: *Physics Letters* 8.4 (1964), pp. 285 –287. ISSN: 0031-9163. DOI: https://doi.org/10.1016/S0031-9163(64)91897-9. URL: http://www.sciencedirect.com/science/article/pii/S0031916364918979.

[101] M. M. Block and R. N. Cahn. "High-energy $p\bar{p}$ and pp forward elastic scattering and total cross sections". In: *Rev. Mod. Phys.* 57 (2 1985), pp. 563–598. DOI: 10.1103/RevModPhys.57.563. URL: https://link.aps.org/doi/10.1103/RevModPhys.57.563.

[102] M.L Goldberger, Y Nambu, and R Oehme. "Dispersion relations for nucleon-nucleon scattering". In: *Annals of Physics* 2.3 (1957), pp. 226 –282. ISSN: 0003-4916. DOI: https://doi.org/10.1016/0003-4916(57)90030-1. URL: http://www.sciencedirect.com/science/article/pii/0003491657900301.

[103] Ugo Amaldi et al. "The Real Part Of The Forward Proton-proton Scattering Amplitude Measured At The Cern Intersecting Storage Rings". In: *Phys. Lett. B* 66.PRINT-77-0078-CERN. 4 (2000), 390–400. 10 p. DOI: 10.1016/0370-2693(77)90022-3. URL: https://cds.cern.ch/record/438822.

[104] C. Augier et al. "Predictions on the total cross section and real part at LHC and SSC". In: *Physics Letters B* 315.3 (1993), pp. 503 –506. ISSN: 0370-2693. DOI: https://doi.org/10.1016/0370-2693(93)91647-6. URL: http://www.sciencedirect.com/science/article/pii/0370269393916476.

[105] J R Cudell, E S Martynov, and O V Selyugin. *Integral and derivative dispersion relations in the analysis of the data on pp and $\bar{p}p$ forward scattering*. Tech. rep. hep-ph/0307254. 2003. URL: https://cds.cern.ch/record/629857.

[106] T. N. Truong and W. S. Lam. "Proof of the Pomeranchuk Theorem and Related Theorems Deduced from Unitarity". In: *Phys. Rev. D* 6 (10 1972), pp. 2875–2883. DOI: 10.1103/PhysRevD.6.2875. URL: https://link.aps.org/doi/10.1103/PhysRevD.6.2875.

[107] Giulia Pancheri and Y. N. Srivastava. "Introduction to the physics of the total cross-section at LHC". In: *Eur. Phys. J.* C77.3 (2017), p. 150. DOI: 10.1140/epjc/s10052-016-4585-8. arXiv: 1610.10038 [hep-ph].

[108] G. Antchev et al. "Measurement of the elastic pp scattering at $\sqrt{s}$=8 TeV in the Coulomb-nuclear interference region: determination of the ρ parameter and the total cross-section". In: *The European Physical Journal C* 76.12 (2016). ISSN: 1434-6052. DOI: 10.1140/epjc/s10052-016-4399-8. URL: http://dx.doi.org/10.1140/epjc/s10052-016-4399-8.

[109] Jan Kaspar. "Elastic scattering at the LHC". Presented 10 Apr 2012. 2011. URL: http://cds.cern.ch/record/1441140.

[110] Geoffrey B. West and D. R. Yennie. "Coulomb Interference in High-Energy Scattering". In: *Phys. Rev.* 172 (5 1968), pp. 1413–1422. DOI: 10.1103/PhysRev.172.1413. URL: https://link.aps.org/doi/10.1103/PhysRev.172.1413.

[111] A. Citron et al. "Structure in the Pion-Proton Total Cross Section between 2 and 7 GeV/c". In: *Phys. Rev.* 144 (1966), pp. 1101–1114. DOI: 10.1103/PhysRev.144.1101.

[112] G. Bellettini et al. "Proton-nuclei cross sections at 20 GeV". In: *Nucl. Phys.* 79 (1966), pp. 609–624. DOI: 10.1016/0029-5582(66)90267-7.

[113] U. Amaldi et al. "Measurements of small angle proton proton elastic scattering at the cern intersecting storage rings". In: *Phys. Lett.* 36B (1971), pp. 504–508. DOI: 10.1016/0370-2693(71)90542-9.

[114] U. Amaldi et al. "Measurements of the proton proton total cross-sections by means of Coulomb scattering at the Cern intersecting storage rings". In: *Phys. Lett.* 43B (1973), pp. 231–236. DOI: 10.1016/0370-2693(73)90277-3.

[115] U. Amaldi et al. “The Real Part of the Forward Proton Proton Scattering Amplitude Measured at the CERN Intersecting Storage Rings”. In: *Phys. Lett.* 66B (1977), pp. 390–394. DOI: 10.1016/0370-2693(77)90022-3.

[116] S. R. Amendolia et al. “Measurement of the total proton proton cross-section at the ISR”. In: *Phys. Lett.* 44B (1973), pp. 119–124. DOI: 10.1016/0370-2693(73)90316-X.

[117] U. Amaldi et al. “New Measurements of Proton Proton Total Cross-Section at the CERN Intersecting Storage Rings”. In: *Phys. Lett.* 62B (1976), pp. 460–466. DOI: 10.1016/0370-2693(76)90685-7.

[118] U. Amaldi et al. “Precision Measurement of Proton Proton Total Cross-section at the CERN Intersecting Storage Rings”. In: *Nucl. Phys.* B145 (1978), pp. 367–401. DOI: 10.1016/0550-3213(78)90090-1.

[119] Norman A. Amos et al. “Comparison of Small Angle $\bar{p}p$ and p p Elastic Scattering at the CERN Intersecting Storage Rings”. In: *Phys. Lett.* 128B (1983), pp. 343–348. DOI: 10.1016/0370-2693(83)90272-1.

[120] G. Arnison et al. “Elastic and total cross-section measurement at the CERN proton-antiproton collider”. In: *Phys. Lett.* 128B (1983). [,15(1983)], p. 336. DOI: 10.1016/0370-2693(83)90271-X.

[121] R. Battiston et al. “Measurement of the Proton - Anti-proton Elastic and Total Cross-section at a Center-of-mass Energy of 540-GeV”. In: *Phys. Lett.* 117B (1982), pp. 126–130. DOI: 10.1016/0370-2693(82)90888-7.

[122] C. Augier et al. “A Precise measurement of the real part of the elastic scattering amplitude at the S anti-p p S”. In: *Phys. Lett.* B316 (1993). [,7(1993)], pp. 448–454. DOI: 10.1016/0370-2693(93)90350-Q.

[123] G. J. Alner et al. “Antiproton-proton cross sections at 200 and 900 GeV c.m. energy”. In: *Z. Phys.* C32 (1986), pp. 153–161. DOI: 10.1007/BF01552491.

[124] Norman A. Amos et al. “Measurement of the $\bar{p}p$ Total Cross-Section at $\sqrt{s}$ = 1.8-TeV”. In: *Phys. Rev. Lett.* 63 (1989), p. 2784. DOI: 10.1103/PhysRevLett.63.2784.

[125] F. Abe et al. “Measurement of the $\bar{p}p$ total cross-section at $\sqrt{s} = 546$ GeV and 1800-GeV”. In: *Phys. Rev.* D50 (1994), pp. 5550–5561. DOI: 10.1103/PhysRevD.50.5550.

[126] C. Avila et al. “A Measurement of the proton-antiproton total cross-section at $\sqrt{s}$ = 1.8 TeV”. In: *Phys. Lett.* B445 (1999), pp. 419–422. DOI: 10.1016/S0370-2693(98)01421-X.

[127] The Collaboration et al. “The TOTEM Experiment at the CERN Large Hadron Collider”. In: *Journal of Instrumentation* 3.08 (2008), S08007–S08007. DOI: 10.1088/1748-0221/3/08/s08007. URL: https://doi.org/10.1088%2F1748-0221%2F3%2F08%2Fs08007.

[128] Gueorgui Antchev et al. “Elastic Scattering and Total Cross-Section in p+p reactions measured by the LHC Experiment TOTEM at $\sqrt{s}$ = 7 TeV”. In: *Progress of Theoretical Physics Supplement* 193 (Apr. 2012). DOI: 10.1143/PTPS.193.180.

[129] G. Antchev et al. “Measurement of proton-proton elastic scattering and total cross-section at $\sqrt{s}$= 7 TeV”. In: *EPL* 101.2 (2013), p. 21002. DOI: 10.1209/0295-5075/101/21002.

[130] G. Antchev et al. “Luminosity-independent measurements of total, elastic and inelastic cross-sections at $\sqrt{s} = 7$ TeV”. In: *EPL* 101.2 (2013), p. 21004. DOI: 10.1209/0295-5075/101/21004.

[131] G. Antchev et al. "Measurement of elastic pp scattering at $\sqrt{s}$ = 8 TeV in the Coulomb–nuclear interference region: determination of the ρ parameter and the total cross-section". In: *Eur. Phys. J.* C76.12 (2016), p. 661. DOI: 10.1140/epjc/s10052-016-4399-8. arXiv: 1610.00603 [nucl-ex].

[132] Claude Amsler et al. "Review of Particle Physics". In: *Phys. Lett.* B667 (2008), pp. 1–1340. DOI: 10.1016/j.physletb.2008.07.018.

[133] V. V. Ezhela et al. "Overview of the compete program". In: *Diffraction 2002: Interpretation of the new diffractive phenomena in quantum chromodynamics and in the S matrix theory. Proceedings, NATO Advanced Research Workshop, Alushta, Ukraine, August 31-September 6, 2002*. 2002, pp. 47–61. arXiv: hep-ph/0212398 [hep-ph].

[134] G. Antchev et al. "First determination of the ρ parameter at $\sqrt{s}$ = 13 TeV probing the existence of a colourless three-gluon bound state". In: *Phys. Rev. D* arXiv:1812.04732 (2017). Submitted to Phys.Rev., 28 p. DOI: 10.1140/epjc/s10052-019-7223-4. URL: https://cds.cern.ch/record/2298154.

[135] Rasha Abbasi. "Measurements of the proton-air cross section with high energy cosmic ray experiments". In: *EPJ Web of Conferences* 120 (Jan. 2016), p. 04005. DOI: 10.1051/epjconf/201612004005.

[136] Marcel Froissart. "Asymptotic Behavior and Subtractions in the Mandelstam Representation". In: *Phys. Rev.* 123 (3 1961), pp. 1053–1057. DOI: 10.1103/PhysRev.123.1053. URL: https://link.aps.org/doi/10.1103/PhysRev.123.1053.

[137] V.A. Khoze, A.D. Martin, and M.G. Ryskin. "Elastic and diffractive scattering at the LHC". In: *Physics Letters B* 784 (2018), 192–198. ISSN: 0370-2693. DOI: 10.1016/j.physletb.2018.07.054. URL: http://dx.doi.org/10.1016/j.physletb.2018.07.054.

[138] P. Grafström and W. Kozanecki. "Luminosity determination at proton colliders". In: *Progress in Particle and Nuclear Physics* 81 (2015), pp. 97 –148. ISSN: 0146-6410. DOI: https://doi.org/10.1016/j.ppnp.2014.11.002. URL: http://www.sciencedirect.com/science/article/pii/S0146641014000878.

[139] S van der Meer. *Calibration of the effective beam height in the ISR*. Tech. rep. CERN-ISR-PO-68-31. ISR-PO-68-31. Geneva: CERN, 1968. URL: https://cds.cern.ch/record/296752.

[140] V Cindro et al. "The ATLAS Beam Conditions Monitor". In: *Journal of Instrumentation* 3.02 (2008), P02004–P02004. DOI: 10.1088/1748-0221/3/02/p02004. URL: https://doi.org/10.1088%2F1748-0221%2F3%2F02%2Fp02004.

[141] G.L. Alberghi et al. "Choice and characterization of photomultipliers for the new ATLAS LUCID detector". In: *Journal of Instrumentation* 11.05 (2016), P05014–P05014. DOI: 10.1088/1748-0221/11/05/p05014. URL: https://doi.org/10.1088%2F1748-0221%2F11%2F05%2Fp05014.

[142] *Gamma irradiation Calliope facility at ENEA-Casaccia Research Centre (Rome, Italy)*. URL: http://openarchive.enea.it//handle/10840/9845.

[143] Juan Esposito, G Rosi, and S Agosteo. "The new hybrid thermal neutron facility at TAPIRO reactor for BNCT radiobiological experiments". In: *Radiation protection dosimetry* 126 (Feb. 2007), pp. 69–73. DOI: 10.1093/rpd/ncm015.